

# **Thermoplastic Forming and Related Studies of the Supercooled Liquid Region of Metallic Glasses**

Thesis by

**Aaron Wiest**

In Partial Fulfillment of the Requirements for the Degree of

Doctor of Philosophy



California Institute of Technology

Pasadena, California

2010

(Submitted November 16, 2009)

© 2010

Aaron Wiest

All Rights Reserved

## Acknowledgments



Dr. Johnson is a one of a kind advisor. He gives his students the freedom to pursue avenues of research that interest them and is always available to visit in his office (or on the roof) and provide valuable insight and scientific breakthroughs. He fosters an atmosphere of invention and trust and happiness and gave me the education I had dreamed of for graduate school.

My thesis defense committee (Dr. Fultz, Dr. Ravichandran, Dr. Atwater, Dr. Conner) was thorough and insightful. They gave me good suggestions to improve the presentation of my work and I thank them for their time, knowledge and instruction during my time at Caltech.

Many thanks to my fellow group members for sharing their latest breakthroughs and the excitement those discoveries bring. They were always there with equipment expertise, scientific know how and great conversation topics.

My family is the best! They were always excited to hear about my work and often provided new ways of thinking about problems that led to the answers I needed. They cheered me on, understood my strange hours and even helped in lots of my midnight jaunts to the lab. Special thanks to my proof reader and best sounding board – my mom.

It has been a great four years!

**Abstract**

The thermoplastic formability (TPF) of metallic glasses was found to be related to the calorimetrically measured crystallization temperature minus the glass transition temperature,  $T_g - T_x = \Delta T$ . Alloy development in the ZrTiBe system identified a composition with  $\Delta T = 120$  °C. Many alloys with  $\Delta T > 150$  °C and one alloy,  $Zr_{35}Ti_{30}Be_{27.5}Cu_{7.5}$ , with  $\Delta T = 165$  °C were discovered by substituting Be with small amounts of fourth alloying elements. The viscosity as a function of temperature,  $\eta(T)$ , and time temperature transformation (TTT) measurements for the new alloy are presented and combined to create  $\eta$ TT plots (viscosity time transformation) that are useful in determining what viscosities are available for a required processing time.  $\eta$ TT plots are created for many alloys used in TPF in the literature and it is found that for processes requiring 60 - 300 s,  $Zr_{35}Ti_{30}Be_{27.5}Cu_{7.5}$  provides an order of magnitude lower viscosity for processing than the other metallic glasses. Injection molding is demonstrated with  $Zr_{35}Ti_{30}Be_{27.5}Cu_{7.5}$  and the part shows improved mechanical properties over die cast specimens of the same geometry. Changes of slope in  $\eta(T)$  measurements were observed and investigated in some quaternary compositions and found to be present in ternary compositions as well. Traditionally metallic glasses show a single discontinuity in heat capacity at the glass transition temperature. Alloys with the changes in slope of  $\eta(T)$  were found to show two discontinuities in heat capacity with the changes in slope of  $\eta(T)$  roughly correlating with the observed  $T_g$  values. These two  $T_g$  values were assumed to arise from two glassy phases present in the alloy. Further heat capacity analysis found systematic trends in the magnitude of the heat capacity discontinuities with composition and the single phase compositions of a metastable miscibility gap were discovered.

Microscopic evidence of the two phases is lacking so we must limit our claims to evidence of two relaxation phenomena existing and can't definitively claim two phases.

The alloy development led to the discovery of alloys with densities near Ti that are among the highest strength to weight ratio materials known. Alloys with corrosion resistances in simulated sea water 10x greater than other Zr based glasses and commonly used marine metals were discovered. Glasses spanning 6 orders of magnitude in corrosion resistance to 37% w/w HCl were discovered. Corrosion fatigue in saline environments remains a problem for these compositions and prevents their utility as biomaterials despite good evidence of biocompatibility in *in vitro* and *in vivo* studies.

## Table of Contents

<b>Copyright</b>		ii
<b>Acknowledgments</b>		iii
<b>Abstract</b>		iv
<b>Table of Contents</b>		vi
<b>List of Figures</b>		ix
<b>List of Tables</b>		xv
<b>Chapter 1</b>	<b>Introduction</b> .....	1.1
	1.1 History .....	1.1
	1.2 Physics of Metallic Glasses .....	1.2
	1.3 Applied Physics (for processing) in Metallic Glasses .....	1.11
	1.4 Advantages of Thermoplastic Processing and State of the Field in 2005 .....	1.14
	1.5 Alloy Development Strategies .....	1.20
	1.6 What To Do with All These Alloys .....	1.24
	1.6.1 Biocompatible Beryllium???	1.32
	1.7 Introduction Summary .....	1.37
	Chapter 1 References .....	1.38
<b>Chapter 2</b>	<b>Lightweight Ti-based Bulk Glassy Alloys Excluding Late Transition Metals</b> .....	2.1
	Chapter 2 References .....	2.9
<b>Chapter 3</b>	<b>ZrTi Based Be Bearing Glasses Optimized for High Thermal Stability and Thermoplastic Formability</b> .....	3.1
	3.1 Introduction .....	3.1
	3.2 Experimental Method .....	3.3
	3.3 Results and Discussion .....	3.5
	3.3.1 Quaternary Alloys .....	3.8
	3.4 Conclusion .....	3.13
	Chapter 3 References .....	3.15

<b>Chapter 4</b>	<b>Bulk Metallic Glass with Benchmark Thermoplastic Processability</b>	4.1
	4.1 Experimental Method	4.12
	Chapter 4 References	4.13
<b>Chapter 5</b>	<b>Injection Molding Metallic Glass</b>	5.1
	Chapter 5 References	5.12
<b>Chapter 6</b>	<b>Relaxation Phenomena in the ZrTiBe System</b>	6.1
	6.1 Abstract	6.1
	6.2 Introduction	6.1
	6.3 Experimental Method	6.3
	6.4 Results and Discussion	6.6
	6.4.1 Heat Capacity Measurements	6.6
	6.4.2 Rheology	6.11
	6.4.3 Shear Modulus	6.14
	6.4.4 Microscopy	6.16
	6.5 Conclusion	6.18
	Chapter 6 References	6.20
<b>Chapter 7</b>	<b>Conclusion</b>	7.1
	7.1 Future Research Directions	7.3
	Chapter 7 References	7.6
<b>Appendix 1</b>	<b>Corrosion Properties of ZrTiBe + Me Alloys in HCl</b>	A1.1
	A1.1 Abstract	A1.2
	A1.2 Introduction	A1.3
	A1.3 Experimental Method	A1.4
	A1.4 Results and Discussion	A1.5
	A1.5 Conclusion	A1.10
	Appendix 1 References	A1.11

<b>Appendix 2</b>	<b>One Year Rabbit Implantation Study of a Zirconium Based Beryllium Bearing Metallic Glass</b>	A2.1
	A2.1 Abstract	A2.2
	A2.2 Introduction	A2.2
	A2.3 Experimental Method	A2.4
	A2.4 Preliminary Tests and Results	A2.4
	A2.5 Long Term Implantation Study	A2.9
	A2.6 Conclusion	A2.12
	Appendix 2 References	A2.13
<b>Appendix 3</b>	<b>Corrosion and Corrosion Fatigue of Vitreloy Glasses Containing Low Fractions of Late Transition Metals</b>	A3.1
	Appendix 3 References	A3.10
<b>Appendix 4</b>	<b>Derivations</b>	A4.1
	Derivation 1 Fourier Heat Equation	A4.1
	Derivation 2 Implications of Slope Change in Thermodynamic Variables	A4.2
	Derivation 3 Stephan's Equation for Parallel Plate Viscometer	A4.2
	Derivation 4 Vogel-Fulcher-Tammann Viscosity	A4.4
	Derivation 5 Viscosity of BMG from Potential Energy Landscape Perspective	A4.4
	Derivation 6 Thermoplastic Formability Parameter	A4.6
	Derivation 7 Composition Counting	A4.7
	Derivation 8 Limiting Cases of Two Phase Liquid Flow	A4.10
	Derivation 9 Modulus of Rupture Equation for Rectangular Beam	A4.14
	Appendix 4 References	A4.15

<b>List of Figures</b>	<b>Page</b>
<b>Figure 1.1</b> DSC scan of $Zr_{44}Ti_{11}Cu_{20}Be_{25}$ showing heat capacity features characteristic of metallic glasses. Inset region on left shows glass transition region and maintains axis units of large plot.	1.3
<b>Figure 1.2</b> TTT diagram upon heating ( $\blacktriangle$ ) and cooling ( $\blacksquare$ ) for $Zr_{41.2}Ti_{13.8}Cu_{12.5}Ni_{10}Be_{22.5}$ .	1.6
<b>Figure 1.3</b> Schematic TTT plot shown with high mobility (kinetics) and low driving force (thermodynamics) at high temperature and low atom mobility with high thermodynamic driving force at low temperature creating a nose in the TTT curve at intermediate temperatures.	1.6
<b>Figure 1.4</b> $\eta$ TT plot for $Zr_{41.2}Ti_{13.8}Cu_{12.5}Ni_{10}Be_{22.5}$ using heating TTT data ( $\blacktriangle$ ) and cooling TTT data ( $\blacksquare$ ). This plot looks upside down compared to Figure 1.2 because lower viscosities occur at higher temperatures.	1.12
<b>Figure 1.5</b> Schematic of squish test proposed by Schroers.	1.13
<b>Figure 1.6</b> Thermoplastic forming demonstrations 2005-2007 [30-31, 36-37].	1.16
<b>Figure 1.7</b> $\eta$ TT plots for alloys commonly used in TPF processes. GFA for the Pt alloy is insufficient to obtain the entire cooling TTT curve. No cooling TTT data is available for $Zr_{44}Ti_{11}Cu_{10}Ni_{10}Be_{25}$ . Conflicting heating TTT data for the Pd alloy is not presented. Data taken from [1, 5, 7, 40-41].	1.19
<b>Figure 1.8</b> Quaternary alloy with 5% Cu plotted at bottom of figure. This quaternary alloy could be thought of as 5% substitution of Cu for Zr, Ti, or Be in the ternary alloys going top down. $Zr_{35}Ti_{30}Be_{35}$ has a SCLR most similar to the quaternary alloy so Cu substitution for Be is the most useful way to think of these alloys to maximize $\Delta T$ .	1.23
<b>Figure 1.9</b> Time to crystallization versus viscosity plot for four thermoplastically processable alloys. This plot combines TTT and viscosity versus time data to show available processing time for a given viscosity for the alloys [7, 37, 40-41, 56]. Figure reproduced in Chapter 5.	1.26
<b>Figure 1.10</b> Photograph of the polished injection molded part prior to final sectioning for three-point bend testing.	1.27
<b>Figure 1.11</b> Apparent two $T_g$ phenomenon seen in 20 K/min DSC scan of $Zr_{35}Ti_{30}Be_{27.5}Cu_{7.5}$ .	1.28

<b>Figure 1.12</b>	DSC and viscosity curve plotted against temperature for $Zr_{30}Ti_{30}Be_{40}$ which shows about 60% of the low $T_g$ phase and 40% of the high $T_g$ phase. The viscosity plot shows two flow regions roughly corresponding to the discontinuities in heat capacity seen in the DSC.	1.29
<b>Figure 1.13</b>	Plot of $\Delta c_{p1}/(\Delta c_{p1} + \Delta c_{p2})$ versus Zr concentration gives fraction of phase 1 assuming two glassy phases with similar fragilities. Linear fits indicate rule of mixtures analysis is appropriate and suggests a metastable miscibility gap in SCLR.	1.30
<b>Figure 2.1</b>	Pictures of amorphous 6mm diameter rod of $Ti_{45}Zr_{20}Be_{35}$ (S1), 7mm diameter rod of $Ti_{45}Zr_{20}Be_{30}Cr_5$ (S2) and 8mm diameter rod of $Ti_{40}Zr_{25}Be_{30}Cr_5$ (S3) prepared by the copper mold casting method are presented in (a). The X-ray diffraction patterns (b) verify the amorphous nature of the corresponding samples.	2.4
<b>Figure 2.2</b>	DSC scans of the amorphous $Ti_{45}Zr_{20}Be_{35}$ (S1), $Ti_{45}Zr_{20}Be_{30}Cr_5$ (S2), and $Ti_{40}Zr_{25}Be_{30}Cr_5$ (S3) alloys at a constant heating rate of 0.33 K/s. The marked arrows represent the glass transition temperatures.	2.6
<b>Figure 2.3</b>	Compressive stress-strain curves for the $Ti_{45}Zr_{20}Be_{35}$ and $Ti_{40}Zr_{25}Be_{30}Cr_5$ 3mm amorphous rods.	2.7
<b>Figure 3.1</b>	Bulk glass forming regions shown on ZrTiBe phase diagram.	3.5
<b>Figure 3.2</b>	Ternary ZrTiBe phase diagram showing the region originally explored by Tanner for ribbon forming glasses (dashed line), the isothermal cross sections showing the liquid phase at various temperatures (shaded triangles), and the alloys recreated in this experiment (letters).	3.6
<b>Figure 3.3</b>	20 K/min DSC scans of several alloys in the ternary ZrTiBe system. Crystallization is seen as a single exothermic peak suggesting that these alloys tend to crystallize by simultaneous crystal growth at that heating rate. Inset: Magnified view of glass transitions (temperature axes aligned); vertical order of alloys maintained.	3.8
<b>Figure 3.4</b>	(a) The effect of Cu substitution for Be in $Zr_{35}Ti_{30}Be_{35}$ (Alloy K). (b) The effect of Co substitution for Be in $Zr_{35}Ti_{30}Be_{35}$ (Alloy K). (c) The effect of Fe substitution for Be in $Zr_{35}Ti_{30}Be_{35}$ (Alloy K). All insets contain magnified view of glass transitions (temperature axes aligned) with vertical order of alloys maintained.	3.10

- Figure 3.5** Bar graph showing the compositions with the largest  $\Delta T$  from each quaternary family. Alloys with  $\Delta T$  values as large as 165.1 °C are shown.  $Zr_{44}Ti_{11}Be_{25}Cu_{10}Ni_{10}$  (Vitreloy 1b) is shown for reference. 3.13
- Figure 4.1** DSC scans of three typical bulk metallic glasses with excellent glass forming ability and extremely high thermal stability. The marked arrows represent the glass transition temperatures. 4.4
- Figure 4.2** The temperature dependence of equilibrium viscosity of several metallic glass forming liquids:  $Zr_{41.2}Ti_{13.8}Ni_{10}Cu_{12.5}Be_{22.5}$  (Vitreloy 1) ( $\Delta$ );  $Zr_{46.25}Ti_{8.25}Cu_{7.5}Ni_{10}Be_{27.5}$  (Vitreloy 4) ( $\circ$ );  $Zr_{35}Ti_{30}Cu_{8.25}Be_{26.75}$  ( $\blacksquare$ );  $Pd_{43}Ni_{10}Cu_{27}P_{20}$  ( $\times$ );  $Pt_{60}Ni_{15}P_{25}$  ( $\diamond$ ). It is shown that the viscosity of  $Zr_{35}Ti_{30}Cu_{8.25}Be_{26.75}$  in the thermoplastic processing region is at least two orders of magnitude lower than that of Vitreloy 1 or Vitreloy 4 and is comparable to that of Pd based metallic glass and polymer glasses. 4.6
- Figure 4.3** TTT diagrams for  $Zr_{35}Ti_{30}Cu_{8.25}Be_{26.75}$  upon heating ( $\blacksquare$ ), and cooling ( $\square$ ). The data were measured by electrostatic levitation for cooling measurements. TTT upon heating measurements were done by processing in graphite crucibles after heating from the amorphous state. At 683 K, where the equilibrium viscosity is about  $8 \cdot 10^4$  Pa-s, a 600 s thermoplastic processing window is available. 4.8
- Figure 4.4** Demonstration of the strong thermoplastic processability of the  $Zr_{35}Ti_{30}Cu_{8.25}Be_{26.75}$  metallic glass. The ingot in (a) is pressed over a dime at 643 K for 45 s at 25 MPa to form the negative imprint of a United States dime shown in (b). A diamond shaped microindentation pattern was placed in the flame on the dime (c) and was successfully replicated in the negative imprint (d) as well. 4.9
- Figure 4.5** Squish test proposed by Schroers [28] performed on four alloys traditionally used in TPF and the new large  $\Delta T$  alloy. The largest diameter after the squish test is obtained by using the  $Zr_{35}Ti_{30}Cu_{7.5}Be_{27.5}$  alloy suggesting that it will exhibit the best flow properties in TPF processes requiring large strains. 4.11
- Figure 5.1** Time to crystallization versus viscosity plot for four thermoplastically processable alloys. This plot combines TTT and viscosity versus time data found in references [6-9] to show available processing time for a given viscosity for the alloys. 5.3

<b>Figure 5.2</b>	2a - 20 °C/min DSC scans of feedstock material and injection molded specimen. The injection molding process appears to have had little effect on the thermodynamic properties measured in the DSC. Inset 2b - Schematic drawing of the modified injection molding setup consisting of a plunger, gates, and a heated mold and reservoir. The dimensions of the mold cavities are 2mm x 10mm x 20mm and 1.5mm x 10mm x 20mm.	5.5
<b>Figure 5.3</b>	Photograph of injection molded parts. The top part (5.3a) was processed at 410 °C with an applied pressure of 140 MPa but the plunger jammed. The second part (5.3b) was processed at 385 °C with an applied pressure of 300 MPa for 3 minutes. The third part (5.3c) was processed at 420 °C with an applied pressure of 300 MPa for two minutes. The fourth part (5.3d) made of polyethylene was processed at 210 °C with an applied pressure of 35 MPa for one minute.	5.8
<b>Figure 5.4</b>	Plot of modulus of rupture values for injection molded and die cast samples. Die cast modulus of rupture = $(2.879 \pm 0.240)$ GPa. Injection molding modulus of rupture = $(2.923 \pm 0.065)$ GPa.	5.11
<b>Figure 6.1</b>	20 K/min DSC scan of $Zr_{30}Ti_{30}Be_{40}$ showing double discontinuity in heat capacity in SCLR. $\Delta c_p$ and $T_g$ determination method illustrated.	6.4
<b>Figure 6.2</b>	Plot of $\Delta c_{p1}/(\Delta c_{p1} + \Delta c_{p2})$ versus Zr concentration gives fraction of phase 1 assuming two glassy phases with similar fragilities. Linear fits indicate rule of mixtures analysis is appropriate and suggests a metastable miscibility gap in SCLR.	6.7
<b>Figure 6.3</b>	20 K/min DSC scans of alloys predicted to show only one phase from rule of mixtures analysis and one intermediate two phase composition.	6.9
<b>Figure 6.4</b>	Sketch of the metastable miscibility gap in SCLR of $(Zr_aTi_{1-a})_{60}Be_{40}$ . Endpoint compositions are known, but temperature bounds are not.	6.10

- Figure 6.5**  $\eta(T)$  plots for three alloys with differing fractions of phase 1, showing apparent double glass transition. The test specimens were 1mm diameter x 1.8mm tall rods of  $Zr_{20}Ti_{40}Be_{40}$  (38% phase 1),  $Zr_{25}Ti_{35}Be_{40}$  (48% phase 1), and  $Zr_{30}Ti_{30}Be_{40}$  (61% phase 1) deformed under a force of 1400 mN at 5 K/min in a TMA. Region 1 corresponds to a solid-solid mixture with no deformation. Region 2 corresponds to solid-liquid mixture and minimal deformation indicated by shallow slope of  $\eta(T)$ . Region 3 is a liquid-liquid mixture with the greatest deformation rate indicated by the steepest  $\eta(T)$  slope. The scatter in first and second glass transitions as measured in 5 K/min DSC scans shown by parallel black vertical lines. 6.13
- Figure 6.6**  $\eta(T)$  plots for as-cast and annealed samples of  $Zr_{30}Ti_{30}Be_{32}Cu_8$ . The test specimens were 3mm diameter x 3mm tall rods deformed under a force of 1400 mN at 5 K/min in a TMA. The annealed sample was heated to 410 °C for 100 s and shows a slightly lower viscosity than the as-cast sample in region 2. Both samples show similar flow behavior in the SCLR. The flow regions and glass transitions do not align for these samples as was observed for the  $(Zr_aTi_{1-a})_{60}Be_{40}$  compositions in Figure 6.5. 6.14
- Figure 6.7** In situ  $G(T)$  measurements on an annealed sample of  $Zr_{30}Ti_{30}Be_{32}Cu_8$  showing two slope changes. These slope changes are indicative of two relaxation events in the alloy. The  $G(T)$  and  $\eta(T)$  relaxation temperatures do not correlate well for this sample. 6.15
- Figure 6.8** Dimple ground and ion milled sample imaged in TEM. Bright field and dark field images show no evidence of two phases. The diffraction pattern is characteristic of an amorphous alloy. 6.17
- Figure 7.1** Heating and forming times achievable using rapid discharge forming, RF heating, and conventional heating depicted along the x axis.  $\eta_{TT}$  data for a marginal glass former is schematically represented with the dashed line.  $\eta_{TT}$  data for the Pd alloy is sketchy because it is estimated from constant heating experiments in [1-2] but shows a change in slope as the melting temperature is approached.  $\eta_{TT}$  data for Pt alloy found in [2-3], and for the Zr alloy in [2, 4]. 7.4
- Figure A1.1** Corrosion rate as a function of Zr content in  $Zr_{65-x}Ti_xBe_{35}$  alloys. Squares are 2mm diameter amorphous rods. The triangle is a crystallized 2mm diameter sample. A1.5

<b>Figure A1.2</b>	Plot of corrosion rate versus standard half cell potential $E^0$ of quaternary alloying element. Table A1.2 gives compositions.	A1.7
<b>Fig A1.3</b>	High resolution XPS scans of $Zr_{35}Ti_{30}Be_{35}$ after sitting in air for 24 hours (blue) and after being immersed in 12M HCl for 12 hr resulting in 3% mass loss (pink).	A1.9
<b>Figure A3.1</b>	Cyclic anodic polarization curves of $Zr_{52.5}Cu_{17.9}Ni_{14.6}Al_{10}Ti_5$ , $Zr_{35}Ti_{30}Be_{29}Co_6$ , and $Zr_{35}Ti_{30}Be_{35}$ in 0.6M NaCl solution at a scan rate of 0.167 mV/s.	A3.4
<b>Figure A3.2</b>	Fatigue performance in air ( $\blacktriangle$ $Zr_{52.5}Cu_{17.9}Ni_{14.6}Al_{10}Ti_5$ , $\blacksquare$ $Zr_{35}Ti_{30}Be_{29}Co_6$ , and $\bullet$ $Zr_{35}Ti_{30}Be_{35}$ ) and in 0.6M NaCl ( $\Delta$ $Zr_{52.5}Cu_{17.9}Ni_{14.6}Al_{10}Ti_5$ , $\square$ $Zr_{35}Ti_{30}Be_{29}Co_6$ , and $\circ$ $Zr_{35}Ti_{30}Be_{35}$ ) at a frequency of 10 Hz and $R = 0.1$ . $Zr_{52.5}Cu_{17.9}Ni_{14.6}Al_{10}Ti_5$ is tested in four-point bending geometry (data taken from [9]). $Zr_{35}Ti_{30}Be_{29}Co_6$ and $Zr_{35}Ti_{30}Be_{35}$ are tested in compression-compression geometry (present study).	A3.5
<b>Figure A4.1</b>	Thermoplastic formability parameter $\delta$ found by integrating as shown.	A4.6
<b>Figure A4.2</b>	Squish test data for 5 TPF candidate alloys shows $\delta$ is a decent predictor of TPF potential.	A4.6
<b>Figure A4.3</b>	All possible three component compositions with 5% composition steps found at line intersections.	A4.7
<b>Figure A4.4</b>	Four component phase diagram is an equilateral pyramid / tetrahedron.	A4.8
<b>Figure A4.5</b>	Five component phase diagram is a 4D equilateral hyperpyramid.	A4.8
<b>Figure A4.6</b>	Case 1 showing laminae of two fluids orthogonal to shear direction.	A4.10
<b>Figure A4.7</b>	Case 2 showing laminae of two fluids parallel to shear direction.	A4.11
<b>Figure A4.8</b>	Additive fluidity cases and additive viscosity cases on three flow regions of a glass with 60% low $T_g$ phase are shown. It is interesting to note that the theoretical additive viscosity case resembles the flow seen in figure 6.5 suggesting that we may approach the immiscible fluids resisting indefinite extension case proposed in [1] on page 87.	A4.14

<b>List of Tables</b>	<b>Page</b>
<b>Table 2.1</b> Density, thermal and elastic properties of representative lightweight TiZrBe and Vitreloy type glassy alloys.	2.5
<b>Table 3.1</b> Thermodynamic data of the alloys listed in Figure 3.1.	3.7
<b>Table 3.2</b> Thermodynamic data for quaternary variants of $Zr_{35}Ti_{30}Be_{35}$ (Alloy K) obtained by substituting Cu, Co, Fe, Al for Be.	3.9
<b>Table 3.3</b> Thermodynamic data for quaternary variants of large $\Delta T$ ternary compositions obtained by substituting Cu for Be.	3.12
<b>Table 4.1</b> Thermal, mechanical, and rheological properties of various BMG forming alloys.	4.5
<b>Table 5.1</b> Effects of rod diameter and overheating above melt temperature on $\Delta T$ as well as variation in arc melted button $\Delta T$ are tabulated. Temperatures given in $^{\circ}C$ .	5.7
<b>Table 6.1</b> DSC data for alloys considered in this article. Data shown in parentheses taken at 5 K/min. Other data taken at 20 K/min. Temperatures in $^{\circ}C$ . $\Delta c_{p1}$ values in $J/(g \cdot K)$ .	6.8
<b>Table A1.1</b> Mass loss and ICPMS measurements of NaOH solution after 3 months. Solution acidified to 2% w/w $HNO_3$ as required for ICPMS.	A1.2
<b>Table A1.2</b> Alloy compositions and corrosion rates measured in 12M HCl.	A1.6
<b>Table A2.1</b> Muscle and bone implant histological grading criteria.	A2.14
<b>Table A2.2</b> 3 Month Muscle Implants: Significance of Material Type vs Parameter.	A2.15
<b>Table A2.3</b> 3 Month Bone Implants: Significance of Material Type vs Parameter.	A2.15
<b>Table A2.4</b> 6 Month Muscle Implants: Significance of Material Type vs Parameter.	A2.15
<b>Table A2.5</b> 6 Month Bone Implants: Significance of Material Type vs Parameter.	A2.16
<b>Table A2.6</b> 12 Month Muscle Implants: Significance of Material Type vs Parameter.	A2.16

<b>Table A2.7</b>	12 Month Bone Implants: Significance of Material Type vs Parameter.	A2.16
<b>Table A2.8</b>	Fibrosis Thickness Interaction Analysis: Muscle Implants by Time, Finish, and Material.	A2.17
<b>Table A2.9</b>	Intracapsular Inflammation Interaction Analysis: Muscle Implants by Time, Finish, and Material.	A2.17
<b>Table A2.10</b>	Degeneration Interaction Analysis: Muscle Implants by Time, Finish, and Material.	A2.17
<b>Table A2.11</b>	Extracapsular Inflammation Grade Interaction Analysis: Muscle Implants by Time, Finish, and Material.	A2.18
<b>Table A2.12</b>	Extracapsular Inflammation Distance Interaction Analysis: Muscle Implants by Time, Finish, and Material.	A2.18
	Supplementary tables for Appendix 2.	A2.19 – A2.30
<b>Table A3.1</b>	Data for corrosion and corrosion fatigue in 0.6M NaCl. Fatigue values are the stress amplitudes at which the samples endured $10^7$ loading cycles normalized by the material yield strength. The yield strengths of $Zr_{35}Ti_{30}Be_{35}$ , $Zr_{35}Ti_{30}Be_{29}Co_6$ , and $Zr_{52.5}Cu_{17.9}Ni_{14.6}Al_{10}Ti_5$ are 1850 MPa [22], 1800 MPa [22], and 1700 MPa [7], respectively. Corrosion data for 18/8 Stainless Steel, annealed Monel, and Alclad 24S-T are taken from [10], while data for fatigue in air and 0.6M NaCl are taken from [11-15].	A3.4
<b>Table A4.1</b>	All possible two component compositions with 5% composition steps.	A4.7
<b>Table A4.2</b>	Combinatorics for 3 - 5 element alloys.	A4.9

## **Chapter 1 - Introduction**

### **1.1 History**

Metallic glasses have some amazing properties that captured my imagination and determined my path for grad school. In APh 110, Winter term 2003-2004, Dr. William L. Johnson gave a seminar lecture describing his research with an enthusiasm that was intoxicating. He described amorphous metals, materials having a random arrangement of atoms that were frozen in a liquid configuration because of a clever choice of alloying elements. These elements were chosen to have large negative heats of mixing and near eutectic compositions meaning the elements were much happier mixed than separate. The atomic sizes of alloying elements were also chosen so that many different sized spheres can log jam efforts of the mixture to crystallize upon cooling from the molten state.

Dr. Johnson's most famous alloy is a ZrTiCuNiBe composition called Vitreloy 1. This alloy was so resistant to crystallization that 1 inch thick samples could be cooled amorphous. The material conducted electricity like a metal, had strength in tension and hardness as high as the best steels with elastic limits ten times greater than crystalline metals. It could be die cast like aluminum because the melting temperature of the alloy was half that of steel and it had an interesting softening behavior at the glass transition temperature that opened possibilities of processing the material like a plastic.

To recap: There is a material as strong and hard as cutting edge steels with the ability to be formed like a plastic. This is something I had to study!

The metamorphosis of this theoretical possibility, plastically processing a metallic glass, into reality, provided endless hours in my laboratory playground pursuing interesting avenues of research that made for a wonderful grad school experience.

## 1.2 Physics of Metallic Glasses

Below the glass transition temperature, metallic glasses are liquids stuck in one configuration. They are formed by rapidly quenching molten material. As the material cools, a competition between thermodynamics and kinetics ensues. Thermodynamics requires that materials exist in the lowest energy state at a given temperature. Below the melting temperature, the lowest energy state for materials is a crystal. To form a crystal however, the atoms must move into a crystalline configuration. As a liquid cools, the viscosity of the liquid increases or stated another way, the mobility of the atoms decreases. If a material can be cooled quickly enough to limit atom mobility and frustrate crystallization, a glass is formed. The speed at which an alloy must be cooled to frustrate crystallization is called its glass forming ability (GFA). Due to the slower cooling rate of thicker samples, another measure of GFA is an alloy's critical casting thickness. Critical casting thickness is the maximum diameter a cylindrical sample can be cast amorphous (see Derivation 1).

A glass at room temperature can be reheated above  $T_g$  to a viscous liquid state where the mobility of the atoms increases as a function of temperature. This increased mobility allows the glass, which bypassed crystallization when originally cooled from the melt, to sample various configurations and eventually the crystalline state is found. Most heating processes are too slow to bypass crystallization of metallic glasses, but one alloy very resistant to crystallization, PdNiCuP, has been cooled from the molten state to room temperature and then reheated to the molten state with no crystallization [1].

These thermodynamic properties can be measured in a Differential Scanning Calorimeter (DSC). The amount of heat required to equalize the temperatures of an

empty reference crucible and a crucible with a known weight of sample is measured as a function of temperature. The heat difference divided by the mass of the sample is the heat capacity of the sample. A plot of the heat capacity as a function of temperature for a typical metallic glass (MG) is a good starting point to discuss the thermodynamics of these materials. Figure 1.1 shows a typical DSC scan for a MG. The glass transition temperature,  $T_g$ , the crystallization temperature,  $T_x$ , the solidus temperature,  $T_s$ , and the liquidus temperature,  $T_L$ , are shown along with the enthalpy of crystallization,  $H_x$ , the enthalpy of fusion,  $H_f$  and the magnitude of the discontinuity in heat capacity  $\Delta c_p$ .

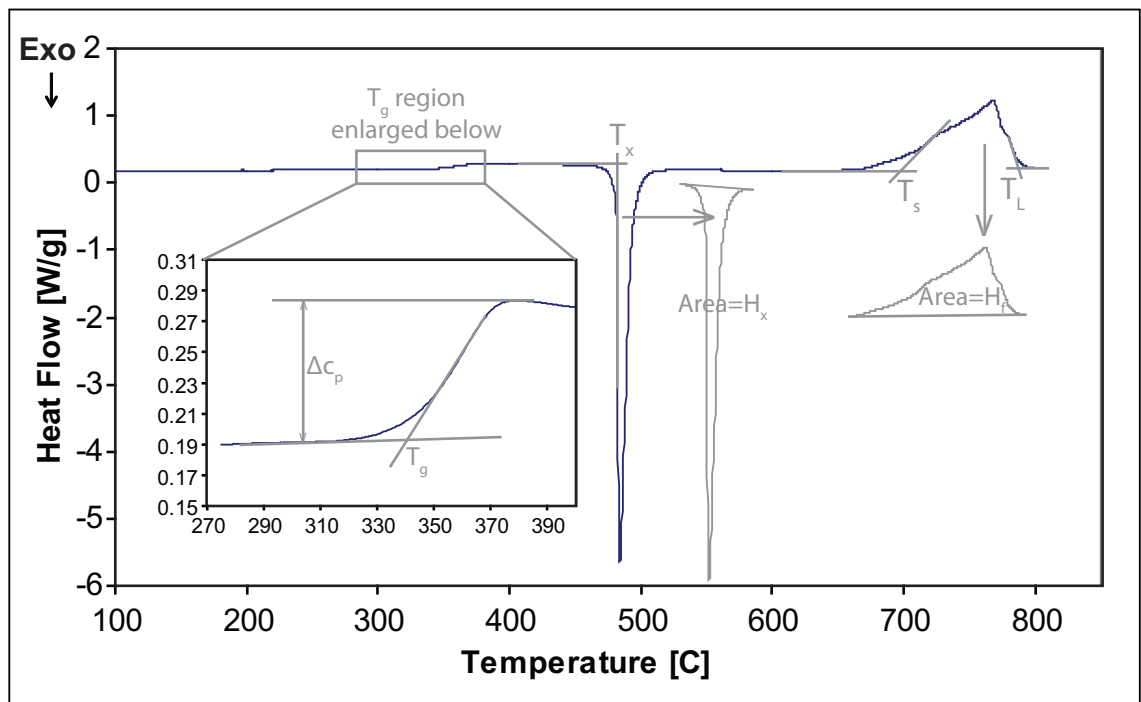


**Figure 1.1:** DSC scan of  $Zr_{44}Ti_{11}Cu_{20}Be_{25}$  showing heat capacity features characteristic of metallic glasses. Inset region on left shows glass transition region and maintains axis units of large plot.

These variables need further explanation. The glassy sample begins at room temperature and is heated above its glass transition temperature. The physics of the glass transition is still being debated. Some claim that it is a second order phase transition [2]

and that glasses are a unique phase of matter. The less controversial explanation follows the kinetics argument above and defines  $T_g$  as the temperature at which the material begins to flow. The glass transition is visible as a discontinuous jump in heat capacity =  $\Delta c_p$ . In the kinetics argument,  $\Delta c_p$  arises from changes in the slope of the volume, entropy, and enthalpy curves at the glass transition due to the kinetic freezing of the liquid [2] (see Derivation 2). Above  $T_g$ , the mobility of the atoms in the undercooled liquid increases and at  $T_x$  a crystalline configuration is found and the sample reaches the desired thermodynamic low energy crystalline state. As the sample transitions from a high energy liquid to a low energy crystal, heat must be released and the exothermic crystallization peak is observed. The total heat released in the crystallization process is  $H_x$ . The temperatures at which melting begins and ends are  $T_s$  and  $T_L$  respectively. In an elemental solid, melting peaks are very sharp and theoretically  $T_s = T_L$ . Melting a solid is an endothermic process meaning that heat input is required to cause the phase change from crystal to liquid. The amount of heat required to melt the crystal =  $H_f$ . If the sample was heated quickly enough, crystallization and melting would not have occurred and the glass could be taken back above the crystalline melting temperature with only a discontinuity in heat capacity.

The ability of a metallic glass to resist crystallization at temperatures above  $T_g$  is called its thermal stability. This is of course a time and temperature dependant parameter. The longer a MG is left at a temperature above  $T_g$ , the more configurations the atoms can explore and eventually the sample will crystallize. Additionally, the atoms move more quickly and explore configurations more quickly at higher temperatures. Both  $T_g$  and  $T_x$  as measured in a DSC will depend on heating rate. Exact values for  $T_g$

and  $T_x$  are impossible to obtain because they are tied to the kinetics of the atoms. In much of the scientific literature on MG and for most of this thesis, thermodynamic data is collected at heating rates of 20 K/min. The value  $T_x - T_g = \Delta T$  is one measure of the thermal stability of a MG.  $\Delta T$  is also called the width of the supercooled liquid region (SCLR), so named because the material has regained flow properties of a liquid, but exists at “super cooled” temperatures well below the melting temperature.

Another quantitative measure of the thermal stability of an alloy is summarized in a time temperature transformation (TTT) diagram. TTT diagrams depict the results of rapidly bringing a MG to a given temperature and then measuring the time to the onset of crystallization at that temperature. Asymmetries exist in TTT diagrams constructed by cooling molten material and waiting for crystallization vs ones constructed by heating glassy material and waiting for crystallization [3]. The authors of [3] discuss the asymmetry in terms of classical nucleation theory and suggest that crystal nuclei are formed upon cooling and then grow at different rates upon heating above  $T_g$ . Heating and cooling TTT diagrams for the Zr based alloy with the highest known GFA,  $Zr_{41.2}Ti_{13.8}Cu_{12.5}Ni_{10}Be_{22.5}$  [3-5], are presented in Figure 1.2. Notice the rounded shape of the cooling TTT curve. The shortest time is marked  $T_n$  on the temperature axis indicating the “nose temperature.” At this temperature, the thermodynamic driving force to crystallize and mobility of the atoms combine to be optimal for crystallizing in the shortest possible time. At temperatures higher than  $T_n$ , the mobility of atoms is greater, but there is less thermodynamic driving force to crystallize. At temperatures lower than  $T_n$ , the thermodynamic driving force is higher, but the mobility of the atoms is too low. These concepts are shown in Figure 1.3.

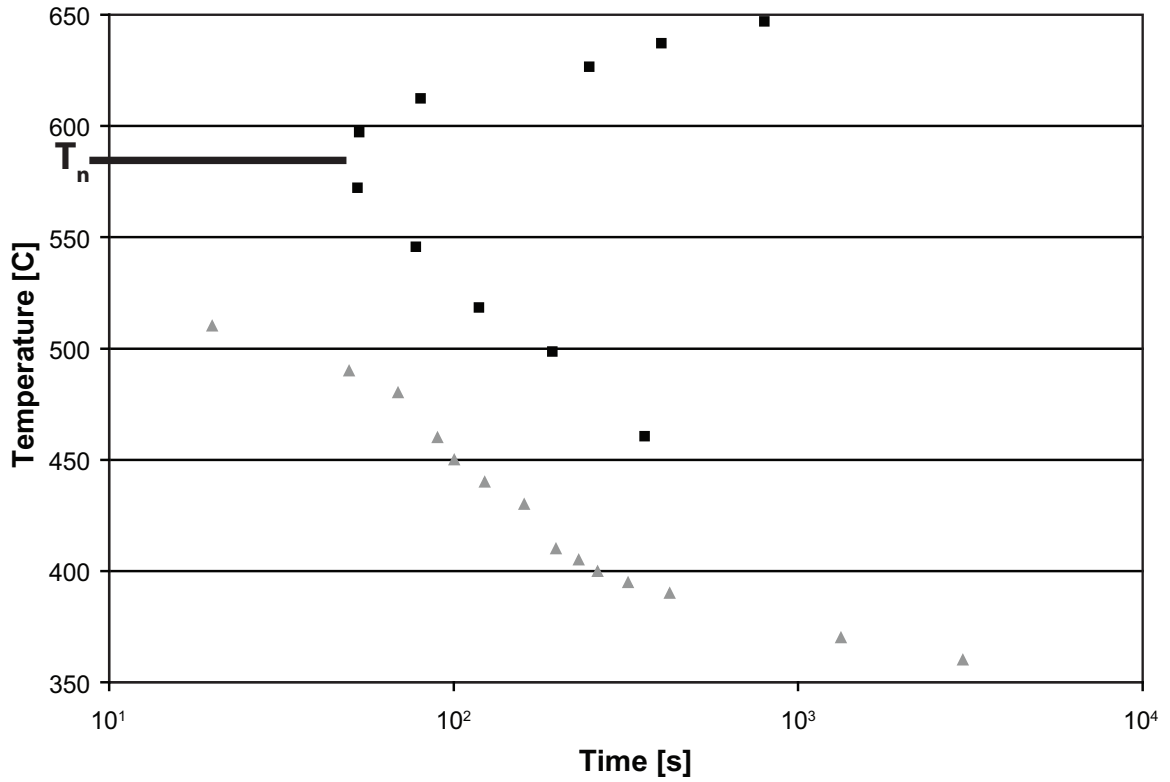


Figure 1.2: TTT diagram upon heating ( $\blacktriangle$ ) and cooling ( $\blacksquare$ ) for  $Zr_{41.2}Ti_{13.8}Cu_{12.5}Ni_{10}Be_{22.5}$ .

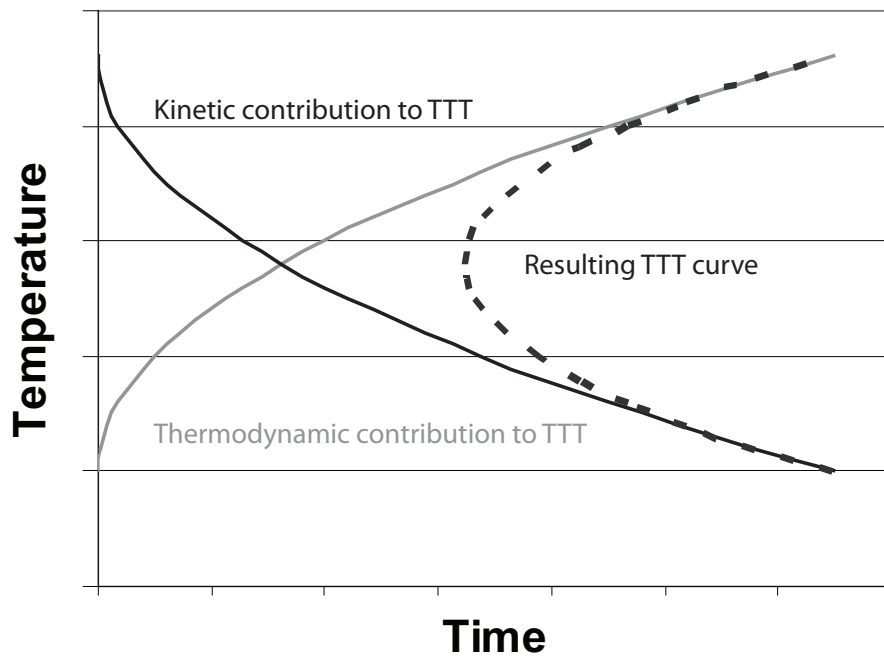


Figure 1.3: Schematic TTT plot shown with high mobility (kinetics) and low driving force (thermodynamics) at high temperature and low atom mobility with high thermodynamic driving force at low temperature creating a nose in the TTT curve at intermediate temperatures. The thermodynamic driving force would go to zero (infinite time) above the liquidus temperature.

We know that a MG begins to flow at  $T_g$  and stops flowing at  $T_x$  (liquid to solid transition) upon heating. Flow can be thought of in terms of shear stresses, i.e., how does one layer of material move with respect to another as they slide across each other. The fundamental equation governing viscosity is  $\frac{dv}{dr} = \frac{F}{\eta}$  where  $F$  is the applied shear stress,  $\eta$  is the viscosity, and  $dv/dr$  is the spatial derivative of the velocity orthogonal to the shear direction. This equation can be solved for many testing geometries. The parallel plate geometry is solved in Derivation 3. Measurements of viscosity as a function of temperature are also possible and a good mathematical fit to  $\eta(T)$  data is achieved using the Vogel-Fulcher-Tammann (VFT) equation presented in Derivation 4 [6].

The physics of MG flow has been a subject of much interest in the MG community [7]. Johnson et al. examined flow of MG from a microscopic perspective. Given that MG are multicomponent alloys, there should be a smallest length scale at which the properties of the glass are observable. In crystals, this length scale is the unit cell and a periodic arrangement of unit cells recreates the crystal and its properties. In MG a “unit cell” is most closely approximated by a shear transformation zone, STZ. Experiments suggest that STZ may be as small as 200 atoms [7]. One can not periodically arrange STZ because they approximate fundamental units of an amorphous material and are not space filling. There are compatibility stresses required to place STZ in space. As the name suggests, an STZ will shear given an appropriate temperature and stress and accommodate movement in the SCLR. Analysis of flow assuming a distribution of STZ sizes and energy wells each STZ sits in is contained in Derivation 5.

The result is an equation with less fitting parameters than the VFT equation that better fits  $\eta(T)$  data of MG. The equation is:

$$\frac{\eta}{\eta_{\infty}} = \text{Exp} \left[ A \left( \frac{T_g}{T} \right)^{m/A} \right]$$

Where  $\eta$  is the temperature dependant viscosity,  $\eta_{\infty}$  is the high temperature viscosity or can be approximated by the plank limit viscosity  $\sim 10^{-5}$  Pa-s,  $A = \text{Log}(\eta_g/\eta_{\infty})$  where  $\eta_g = 10^{12}$  Pa-s, and  $m = \text{Angell fragility}$ .

The Angell fragility is defined as follows:

$$m = \frac{\partial \text{Log}(\eta)}{\partial (T_g/T)}$$

The Angell fragility gives the slope of the  $\text{Log}(\eta(T_g/T))$  curve. This is a valuable parameter because it determines how steep the  $\eta(T)$  plot will be. Fragile liquids or materials with high  $m$  soften quickly above their glass transition temperature and exhibit steeper  $\eta(T)$  relationships.

The physics of the SCLR in some alloys is even more complicated than we have discussed so far. Phase separation in metallic glasses has been claimed in many glass forming alloy systems including AuPbSb [8-9], ZrCu [10], ZrTiBe [11-14], ZrTiCuNiBe [15-17], MgCuYLi [18], CuZrAlAg [19], TiYAlCo and ZrYAlCo [20]. X-ray scattering has shown splitting of the broad amorphous spectrum in as-cast AuPbSb glass [8].

Additionally Small Angle Neutron Scattering (SANS), Small Angle X-ray Scattering (SAXS), Anomalous Small Angle X-ray Scattering (ASAXS), observation with Transmission Electron Microscopy (TEM), rheology measurement anomalies, resistivity measurement anomalies, and Differential Scanning Calorimetry (DSC) measurements showing apparent double glass transitions are some of the techniques used to support the

claims of phase separation. Some AuPbSb and ZrTiBe glasses are thought to have two glasses in as-quenched samples. Other alloy systems are thought to phase separate upon annealing.

Much of the work on phase separation in the Vitreloy (ZrTiNiCuBe) system is relevant to this thesis. Johnson and collaborators conducted SANS experiments on Vitreloy compositions after various annealing times and temperatures [15-17]. As-cast samples exhibited only background scattering, but after annealing, the maximum scattering intensity was peaked about  $q = 0.5 \text{ \AA}^{-1}$  and indicated a quasiperiodic arrangement of scattering inhomogeneities. SAXS and ASAXS experiments determined that the annealing led to the segregation of the alloy into Zr rich and Ti rich amorphous phases. This composition variation was found to happen at a length scale of about 13nm. After this amorphous phase separation, the crystallization pathway becomes quite complex. Kelton found a stable icosahedral phase in the TiZrNi phase diagram from ab initio calculations [21]. Evidence of the icosahedral phase has been found in various Vitreloy compositions by indexing X-ray diffraction patterns of alloys crystallized by isothermal annealing in the SCLR [22-24]. TEM observation of quasicrystal phases has also been accomplished [23-24]. The SANS peak is seen to shift as a function of annealing temperature as predicted by the Cahn-Hilliard theory for spinodal decomposition. Annealing at temperatures higher than the amorphous phase decomposition region causes spinodal decomposition of the alloy into nanocrystalline regions [15-17]. Some postulate that the quasicrystals phase precipitates from the phase separated glass and later provides the nucleation site for other crystal phases [22-24]. Slight coarsening of the nanocrystals has been observed with annealing, but the length

scale only increased to about 40nm [17]. Other compositions in the same Vitreloy alloy family did not phase separate into amorphous phases upon annealing [16]. Johnson and collaborators proposed a miscibility gap and a spinodal decomposition region in the SCLR of the ZrTiNiCuBe phase diagram and proposed rough composition boundaries.

Tanner and Ray examined the ZrTiBe system for glass forming compositions and found many alloys could be made amorphous in 100 $\mu$ m thick ribbons [11-14]. Heat capacity measurements conducted in a DSC on some of the compositions revealed two discontinuities in heat capacity in the supercooled liquid region (SCLR). A glassy material is expected to exhibit one discontinuity in heat capacity at the glass transition temperature as the material transitions from solid-like to liquid-like behavior and becomes able to flow [2]. Two jumps in heat capacity, and an apparent double glass transition temperature are unusual. Tanner proposed that this anomalous feature in the heat capacity was due to the presence of two glassy phases.

There are some in the metallic glass community who dispute the existence of the two phases in many of these systems and attempt to explain the data in alternative ways [25-28]. Perhaps the most controversial alloy thought to show two phases is  $Zr_{36}Ti_{24}Be_{40}$ . Hono showed that TEM work done by Tanner supporting the existence of two phases in the  $Zr_{36}Ti_{24}Be_{40}$  alloy was flawed and proved that the observed “phases” were in fact etching artifacts [27]. The apparent double glass transition has been suggested to be a single glass transition with a neighboring exothermic ordering event prior to crystallization [26]. This explanation could be plausible given the evidence of quasi crystal formation in the more complicated Vitreloy system, especially in light of TEM work showing what appear to be ordered phases after deformation of the in the

SCLR of the  $Zr_{36}Ti_{24}Be_{40}$  alloy [25]. Discussion and experiments supporting the two phase glass argument in the ZrTiBe system will be discussed further in Chapter 6.

### **1.3 Applied Physics (for processing) in Metallic Glasses**

Armed with the concepts of viscosity, thermal stability and TTT diagrams we can consider what properties a metallic glass must possess to be a good candidate for processing like a plastic in the SCLR. The plastic forming process we sought to replicate was injection molding. A simple injection molding process requires feedstock material, a heated reservoir in which the material is softened, a nozzle, a mold and a plunger to force the softened material from the reservoir through the nozzle into the mold. Typical plastic injection molding occurs at temperatures of 180 - 340 °C and viscosities of  $10^2 - 10^3$  Pa-s. Time is a minimal constraint because polymers and plastics typically have enormous thermal stabilities due to the long tangled molecular chains that kinetically resist organization into a crystalline structure. 60 - 300 s is a reasonable time to thermally equilibrate the feedstock material and inject it into the mold.

A metallic glass must have good enough GFA to make macroscopic specimens to be a viable candidate for feedstock material. The metallic glass community calls an alloy a bulk metallic glass (BMG) if the GFA is high enough to allow 1mm diameter rods to be cast fully amorphous. BMG forming alloys also have the advantage of having better thermal stability on cooling as compared to alloys with poorer GFA.

Processing a BMG using a method similar to injection molding in the SCLR however, requires high thermal stability of the glass upon heating. In order to look at the relevant parameters for processing in the SCLR we invented a new kind of plot for metallic glasses. Because temperature is the easiest parameter to vary in the injection

molding process, we combined the TTT data upon heating with  $\eta(T)$  data for an alloy of interest eliminating the temperature variable. This created an  $\eta$ TT or viscosity time transformation plot. An  $\eta$ TT plot is shown in Figure 1.4 for the well known  $Zr_{41.2}Ti_{13.8}Cu_{12.5}Ni_{10}Be_{22.5}$ , Vitreloy 1, composition. TTT and  $\eta(T)$  data is only tabulated for a few alloys in the literature because the measurements are very time consuming. Therefore another parameter is needed to compare the majority of BMG forming alloys.

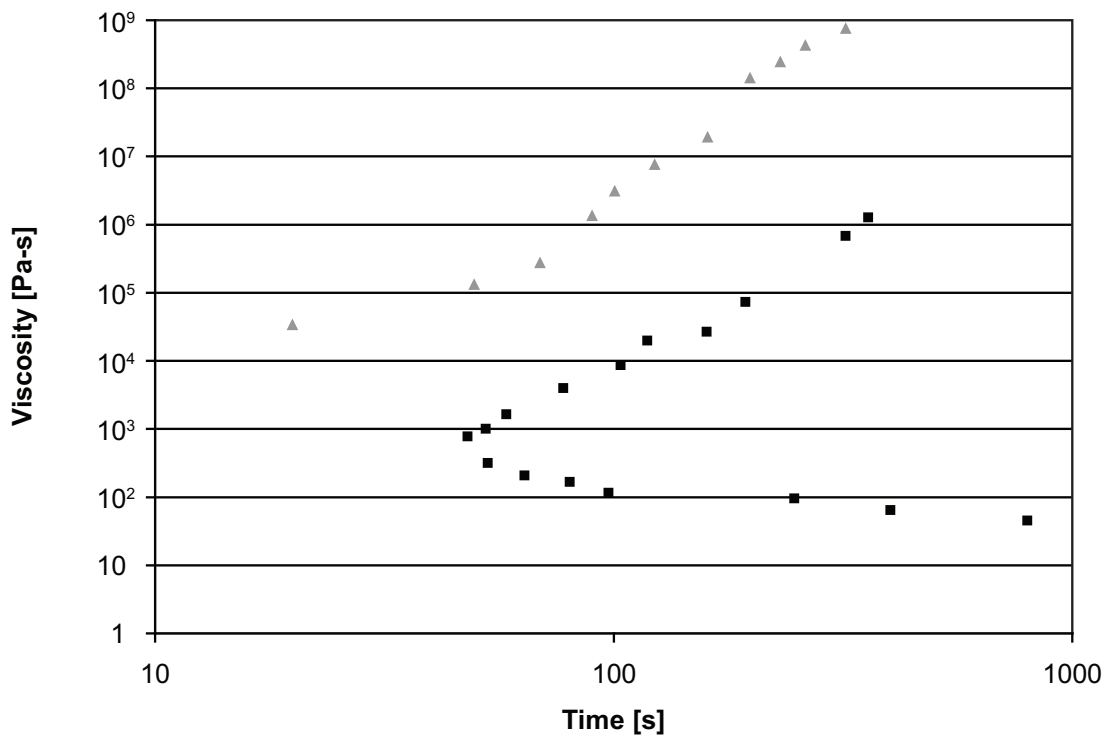


**Figure 1.4:**  $\eta$ TT plot for  $Zr_{41.2}Ti_{13.8}Cu_{12.5}Ni_{10}Be_{22.5}$  using heating TTT data (▲) and cooling TTT data (■). This plot looks upside down compared to Figure 1.2 because lower viscosities occur at higher temperatures.

If an oversimplification is made and all BMG are assumed to have similar fragilities, then the dominant term predicting the lowest available processing viscosity in the  $\eta(T)$  equation derived by Johnson et al. [7] is  $T_x - T_g = \Delta T$ .  $\Delta T$  is also a measure of an alloy's thermal stability upon heating. Measurement of  $\Delta T$  for a BMG forming alloy

takes less than one hour and  $\Delta T$  data is tabulated for many compositions. This could be a simple way of eliminating many compositions from consideration as potential alloys for plastic forming processes in the SCLR.

Another method to measure formability of glassy alloys in the SCLR was suggested by Schroers [29]. Schroers proposed that  $0.1\text{cm}^3$  of material could be compressed between parallel plates under a specified load at a constant heating rate through the SCLR until crystallization of the glassy material stopped the flow. A schematic diagram illustrating this test is presented in Figure 1.5 (modified from Chapter 4). The diameter of the squished disk would be a measure of the formability with larger diameters indicating higher formability in the SCLR. This method closely resembles viscosity determination in a parallel plate rheometer, but explores the entire SCLR in one measurement. For alloys with known fragility, a parameter to predict formability can be derived from the Johnson  $\eta(T)$  equation [7] coupled with the ideas behind the squish test method proposed by Schroers. The basic idea is to integrate the area between the infinite temperature viscosity line and the  $\eta(T)$  equation over the SCLR. The parameter is presented in Derivation 6.

## Formability Characterization

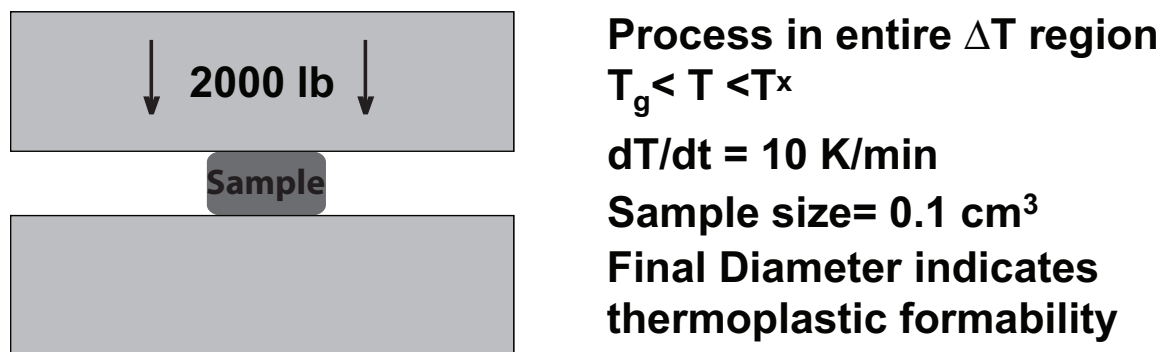


**Figure 1.5:** Schematic of squish test proposed by Schroers.

#### **1.4 Advantages of Thermoplastic Processing and State of the Field in 2005**

Most practical applications of MG demand near net-shaping process in manufacturing. The most common method of obtaining metallic glass parts is die casting wherein molten alloy is injected into a mold and then cooled below the glass transition temperature sufficiently fast to avoid crystallization. Die casting requires the molten alloy to be quickly introduced into the mold and then rapidly quenched before the onset of crystallization. This processing route takes advantage of the thermodynamic stability of the alloy at temperatures above the crystallization nose,  $T_n$  in the TTT diagram showed in Figure 1.2. At the temperature  $T_n$ , an alloy has the minimum time to crystallization. Porosity is introduced into the sample due to the high inertial forces in relation to the surface tension forces realized during the injection of the molten liquid, which gives rise to a Rayleigh-Taylor instability and consequent flow breakup resulting in void entrapment. Porosity is also found in the center of die cast parts because parts are cooled through contact with a mold from the outside in and cavities nucleate in the center due to large negative pressures present in the center of parts cooled in this manner. The cooling requirements of die casting bound the dimensions of die cast parts to no larger than can be cooled sufficiently fast to avoid crystallization and no smaller than can be quickly filled. Parts with complex geometries, thin sections, and high aspect ratios are difficult to obtain with die casting.

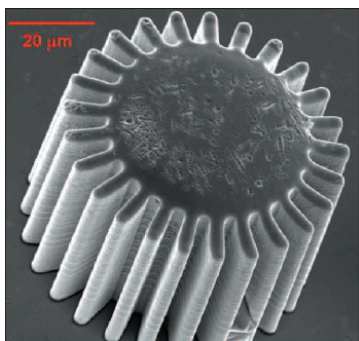
The unique advantages of injection molding, blow molding, micro replication, and other thermoplastic technologies are largely responsible for the widespread uses of plastics such as polyethylene, polyurethane, PVC, etc., in a broad range of engineering applications. Powder Injection Molding (PIM) of metals represents an effort to apply

similar processing to metals, but requires blending of the powder with a plastic binder to achieve net shape forming and subsequent sintering of the powder. Given suitable materials, thermoplastic forming (TPF) would be the method of choice for manufacturing of metallic glass components because TPF decouples the forming and cooling steps by processing glassy material at temperatures above  $T_g$  and below  $T_x$  followed by cooling to ambient temperature [30-31]. To clear up some terminology difficulties it should be noted that forming in the SCLR, thermoplastic forming, and plastic processing all refer to the same process of applying pressure to deform an alloy heated to a temperature in the SCLR. A polymer or plastic material made up of long carbon chains also exhibits a  $T_g$  and is processed in this manner, thus the terminology “plastic” processing.

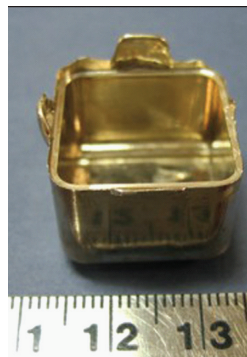
Thermoplastic forming methods take advantage of the kinetic stability of an alloy at temperatures below the crystallization nose. TPF decouples the fast cooling and forming of MG parts inherent in die casting and allows for the replication of small features and thin sections of metals with high aspect ratios. TPF methods also take advantage of lower processing temperatures resulting in relatively lower oxidation rates. TPF has several advantages over conventional die casting, including smaller solidification shrinkage, less porosity of the final product, more flexibility on possible product sizes, and a robust process that does not sacrifice the mechanical properties of the material. TPF methods include the forming of amorphous metal sheets [32], the compaction of amorphous powders [33], the extrusion of amorphous feedstock into a die [34], and the imprinting of amorphous metal [35]. Most of these routes reduce the porosity of the processed amorphous part but have limitations. Forming of amorphous metal sheets limits the thickness of the final sample and the available part geometries.

Powder compaction methods usually produce parts having micro or nano dispersed porosity which often results in inferior mechanical properties compared to homogeneously solidifying parts. Free extrusion, or extrusion into a die only allows parts with simple geometries to be fabricated. Imprinting methods enable very small features to be replicated, but are incapable of producing bulk parts. Figure 1.6 gives a pictorial summary of some of the parts created with thermoplastic forming techniques. It is easily seen in Figure 1.6 that fabrication of the depicted parts required relatively small strains. In fact, all the parts formed using TPF methods prior to the work described in Chapter 5 of this thesis were limited to small strains.

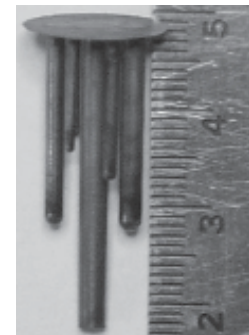
## Overview of Plastic Processing Methods



Micro Forming



Powder/Pellet  
Compaction



Extrusion



Imprinting



Blow Molding

**Figure 1.6:** Thermoplastic forming demonstrations 2005-2007 [30-31, 36-37].

The goal of injection molding is to use the ability of metallic glasses to flow homogeneously at temperatures between  $T_g$  and  $T_x$  to enable pressurized injection of the alloy into a mold to produce a homogenous bulk part with no size restrictions. This method would require higher strains than previously achieved by any of the thermoplastic forming methods prior to 2005.

A perfect BMG forming alloy that could be swapped for polymer plastics in injection molding and similar plastic forming processes would have the following properties:

- Thermal stability in the SCLR for 60 - 300 s
- A viscosity of  $10^2 - 10^3$  Pa-s
- A processing temperature of 180 - 340 °C

In 2005 when my graduate studies began, there were hundreds of BMG forming compositions to choose from. Metallic glass forming alloy compositions are given in atomic percent unless otherwise stated and the family to which a particular alloy belongs is determined by the element with the highest atomic percentage. Some of the families we considered were Au, Pd, Pt, Zr, Ti, Ce, Y, La, Mg, Ca, Co, and Fe based alloys [38-39]. Y, La, Co, and Fe based alloys are known for low fracture toughness and are therefore mechanically undesirable. Ce, Ca, and Mg based glasses are often prone to corrosion. Au based alloys have very high fragility but often the  $T_g$  is near room temperature and the alloys crystallize readily. Zr, Ti, Pd, and Pt based BMG were examined for suitability to forming processes in the SCLR.

A literature search revealed many attempts at forming in the SCLR prior to 2005. Some of the best results to date are presented in Figure 1.6. The favored alloys were

$\text{Pd}_{43}\text{Ni}_{10}\text{Cu}_{27}\text{P}_{20}$ ,  $\text{Pt}_{57.5}\text{Ni}_{5.3}\text{Cu}_{14.7}\text{P}_{22.5}$ ,  $\text{Zr}_{41.2}\text{Ti}_{13.8}\text{Cu}_{12.5}\text{Ni}_{10}\text{Be}_{22.5}$  (Vitreloy 1), and  $\text{Zr}_{44}\text{Ti}_{11}\text{Cu}_{10}\text{Ni}_{10}\text{Be}_{25}$  (Vitreloy 1b). TTT diagrams and  $\eta(T)$  measurements had been published prior to 2005 for many of these alloys and DSC data existed for all of them. The alloys all had large  $\Delta T$  values ranging from the smallest value for  $\Delta T_{\text{Vit 1}} = 65$  °C to  $\Delta T_{\text{Vit 1b}} = 135$  °C. The Pd and Pt based glasses have smaller  $\Delta T$  values, but higher fragilities making all these alloys good candidates for TPF. In the last four years, publications from other research groups, and work within the Johnson group has fleshed out the data necessary to construct  $\eta$ TT plots for all these compositions. Figure 1.7 contains heating and cooling  $\eta$ TT plots for the good TPF candidate alloys. It is quickly seen that the alloys are limited to viscosities greater than  $10^5$  Pa-s for the processing times required for injection molding and similar TPF processes using the  $\eta$ TT plots for heating. Only a cooling  $\eta$ TT plot for  $\text{Pd}_{43}\text{Ni}_{10}\text{Cu}_{27}\text{P}_{20}$  is presented. There are multiple conflicting sets of data for heating the Pd alloy. The Pd alloy differs from other alloys because Pd based alloys are able to be fluxed and cleaned with  $\text{B}_2\text{O}_3$ . Fluxing Pd based alloys with  $\text{B}_2\text{O}_3$  under inert gases allows the alloys greater thermal stability and resistance to crystallization. Fluxed and unfluxed samples have very different TTT plots because unfluxed alloys crystallize at much shorter times for a given temperature than their fluxed counterparts. In an injection molding process conducted in air, the unfluxed behavior is what would be observed. The Pd based alloy shows the most promise for TPF of the alloys examined so far, but falls short of what would be needed to replace a plastic.

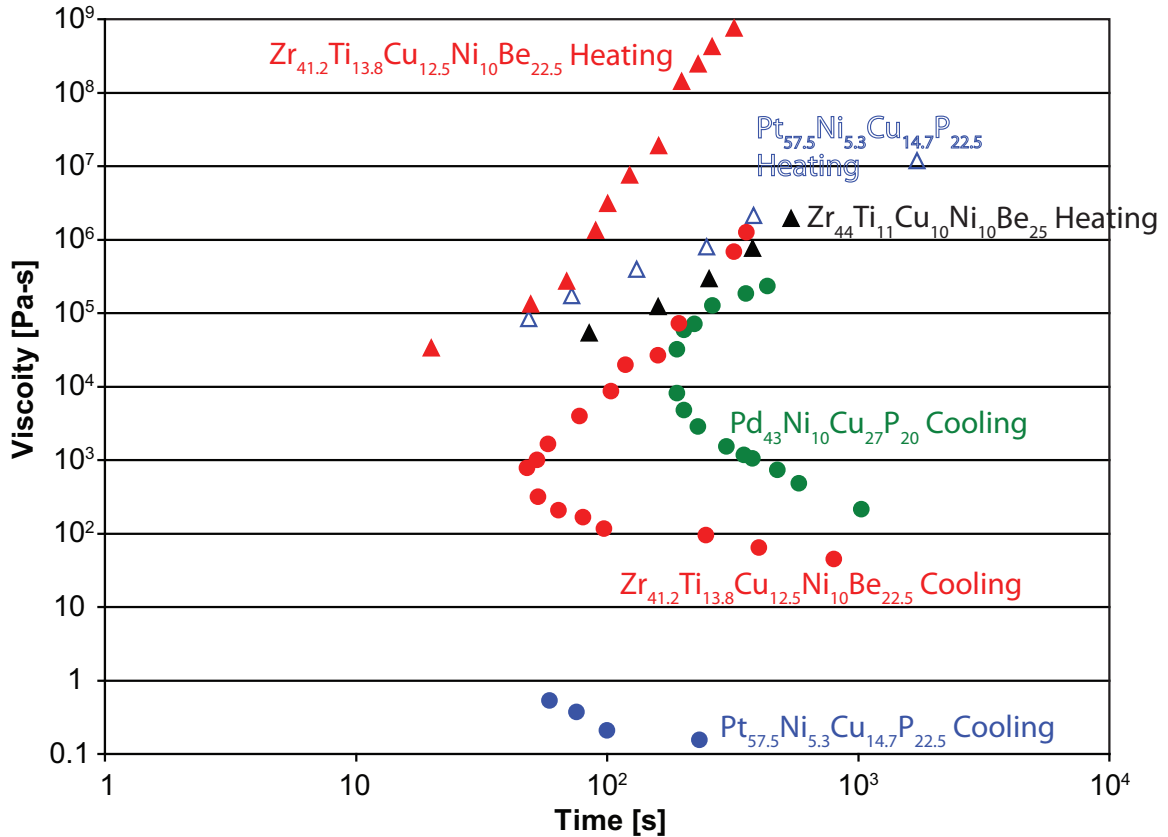


**Figure 1.7:**  $\eta$ TT plots for alloys commonly used in TPF processes. GFA for the Pt alloy is insufficient to obtain the entire cooling TTT curve. No cooling TTT data is available for  $Zr_{44}Ti_{11}Cu_{10}Ni_{10}Be_{25}$ . Conflicting heating TTT data for the Pd alloy is not presented. Data taken from [1, 5, 7, 40-41].

From a processing point of view, BMG alloys with an extremely large supercooled liquid region (excellent thermal stability against crystallization), which can provide lower processing viscosities and exhibit smaller flow stress, would be desirable for use in conjunction with a TPF process. In addition, excellent GFA and low glass transition temperature ( $T_g$ ) are also preferred properties for MG used in TPF processes. Unfortunately, among the published metallic glasses, no suitable alloys existed [42-44]. Zr based metallic glasses, especially the Vitreloy series, are much less expensive than Pt and Pd based alloys, have exceptional glass forming ability, but they have low fragilities and low processing viscosities are unattainable in the SCLR [45-48].

Accordingly, a need exists for a new family of inexpensive MG that can be incorporated into a thermoplastic processing application.

### 1.5 Alloy Development Strategies

The value of  $\Delta T$  was the easiest parameter to measure and seemed to give a good indication of TPF potential so we set out to find alloys with larger  $\Delta T$  values. Without a strategy, success in alloy development can be as likely as winning the lottery.

Approaching the problem scientifically and not just rolling the dice was the key. Even then, it took a few iterations before finding the right method.

The first strategy to find alloys with larger  $\Delta T$  values that met with limited success was based on the phase separation work discussed in Section 1.2 in the ZrTiCuNiBe, Vitreloy, system. Given that some of the Vitreloy compositions showed phase separation upon annealing in the SCLR which led to formation of a quasicrystal phase and eventual nanocrystallization, it was thought that we could increase  $\Delta T$  by suppressing the quasicrystalline phase. Kelton's work predicted a stable TiZrNi quasicrystal [21]. The simplest solution to suppress a TiZrNi phase is to remove all Ni from the alloys.

The alloy with the largest  $\Delta T$  found by this method was the all Cu version of Vitreloy 1b,  $Zr_{44}Ti_{11}Cu_{20}Be_{25}$ . Unfortunately,  $\Delta T_{vit\ 1b\ all\ Cu} = 135\ ^\circ C$ . We hadn't lost anything in  $\Delta T$  by removing all the Ni, but also hadn't gained anything.

Exploring quinary composition space in the Vitreloy system is very cumbersome. Assuming we coarse grained the system into 5% composition steps, we would need to create 10626 alloys to tile the composition space. The combinatorics for 1 - 5 component alloys is included in Derivation 7. It takes approximately 2 hours per alloy to weigh,

melt, cast and run a DSC scan. This task could be accomplished in just over 10 years of 40 hour work weeks. If we explored a ternary composition space, we would only need 231 alloys to tile the system. Tanner explored the ZrTiBe system in the 1970s [11-14] and found that compositions with 30 – 60% Be could be made amorphous in thin foils. Additional work by Tanner using the CALPHAD method to predict ternary phase diagrams from binary phase diagram data found the region of composition space expected to have the lowest melting temperature alloys [49]. This near eutectic region occupied a triangle with 30 - 45% Be. Using this prior work by Tanner and the ternary phase space simplification, we were able to significantly diminish the number of alloys necessary to explore the composition space. The ternary alloy development is detailed in Chapter 3 of this thesis.

The next alloy development strategy challenged many of the assumptions about GFA in the Vitreloy family held in the BMG community in 2005. It was assumed because of the work by Tanner that alloys in the ZrTiBe system were limited in GFA to thin foils 10 - 100 $\mu$ m thick [11-14, 50-51]. Thanks to Dr. Peker's work and patent it was also assumed that the GFA of Vitreloy type alloys was only attainable by adding late transition metals (LTM) from the columns containing Mn, Fe, Co, Ni, or Cu on the periodic table [4, 52]. Both these assumptions turned out to be false. In order to stay outside the Peker patent, only alloys free of LTM were tested. ZrTiBe compositions with GFA high enough to cast 1 - 6mm diameter rods were found. This means that the critical cooling rates required to create amorphous ZrTiBe samples were 100 - 1000 times lower than previously thought. Additions of V, Nb, and Cr were found to raise the GFA of alloys to as high as 8mm diameter casting thickness. Bulk glass forming alloys with

densities as low as crystalline Titanium were discovered having compressive yield strengths as high as Vitreloy compositions [53-54]. Some of the highest strength to weight ratio metals in existence are among these alloys. The low density and no LTM alloy development details and hallmark alloys are more thoroughly discussed in Chapter 2 of this thesis. The alloy with largest  $\Delta T$  value discovered using this strategy of alloy development,  $Zr_{35}Ti_{30}Be_{35}$ , only had  $\Delta T = 120$  °C.

It became clear that our last option was to venture back into Peker patent territory by adding LTM to the ternary compositions. It is important to have a mental picture of what each alloying addition accomplishes to know what direction to move for further improvement. For instance the alloy  $Zr_{35}Ti_{30}Be_{30}Cu_5$  could be thought of as

- 5% Cu substitution of Zr in  $Zr_{40}Ti_{30}Be_{30}$
- 5% Cu substitution of Ti in  $Zr_{35}Ti_{35}Be_{30}$
- 5% Cu substitution of Be in  $Zr_{35}Ti_{30}Be_{35}$

The property we sought to maximize was  $\Delta T$ . Adding a LTM to the alloys had the added bonus of increasing GFA. DSC plots of the ternary alloys and quaternary alloy which could be thought of as Cu substitution for the various elements are included in Figure 1.8. Figure 1.8 suggests that LTM substitution should be thought of as a fourth element being substituted for Be in order to maximize  $\Delta T$ .

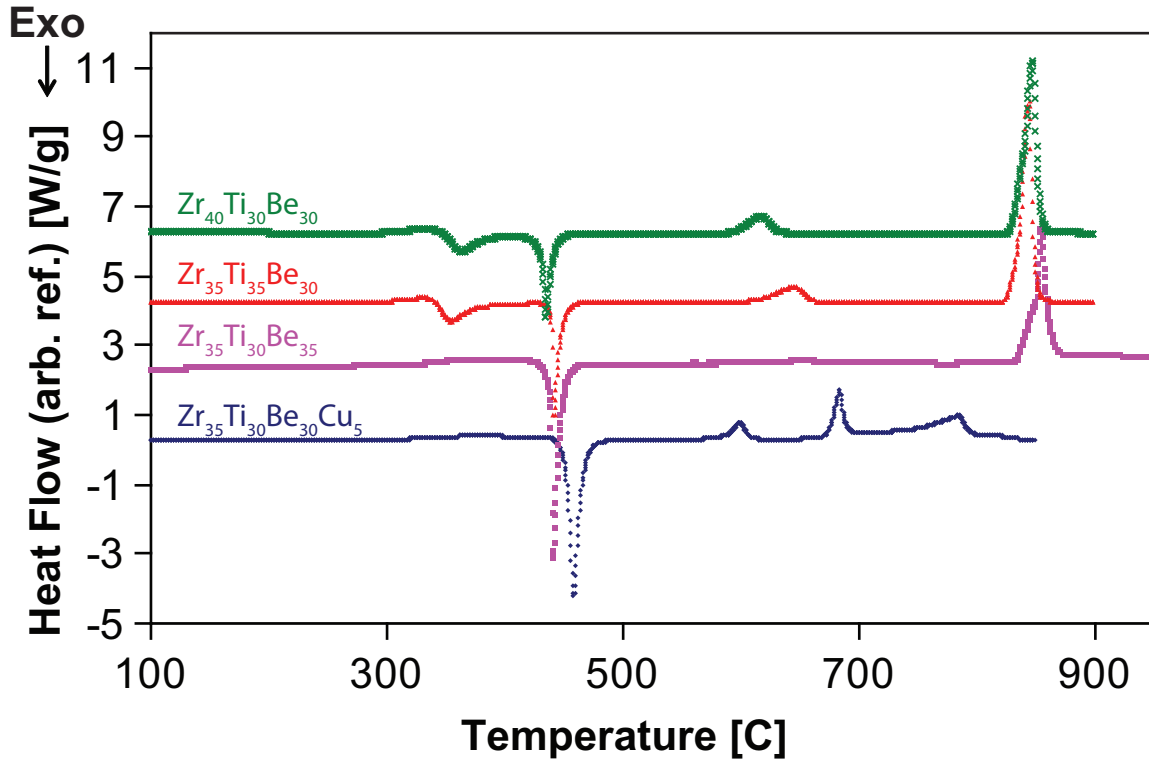


**Figure 1.8:** Quaternary alloy with 5% Cu plotted at bottom of figure. This quaternary alloy could be thought of as 5% substitution of Cu for Zr, Ti, or Be in the ternary alloys going top down.  $Zr_{35}Ti_{30}Be_{35}$  has a SCLR most similar to the quaternary alloy so Cu substitution for Be is the most useful way to think of these alloys to maximize  $\Delta T$ .

We identified the ternary compositions with the largest  $\Delta T$  and replaced Be with increasing amounts of LTM until  $\Delta T$  stopped increasing. This strategy was extremely successful. We tried Co, Fe, Ni, and Cu substitution for Be and found Cu to be the best alloying addition. We found 12 alloys with  $\Delta T$  larger than 150 °C and three alloys with  $\Delta T$  larger than 160 °C. An alloy based on the ternary composition with the largest  $\Delta T$  turned out to be the optimal alloy for our purposes.  $Zr_{35}Ti_{30}Be_{27.5}Cu_{7.5}$  had  $\Delta T = 165$  °C. Our work in alloy development increased the thermal stability of Vitreloy type glasses by over 20% and opened up possibilities for injection molding a metal. The addition of LTM to create quaternary alloys with the largest known  $\Delta T$  values of any metallic glass is detailed in Chapter 3 of this thesis.

## 1.6 What To Do with All These Alloys

Grad students often daydream about being one of those scientists so accomplished they get equations or physical constants or even elements named after them. Einstein, Curie, Fermi, Nobel, Mendel, Bohr, Lawrence, Rutherford, Meitner, and Seaborg all made it to the Periodic Table of the Elements. Some of us in the Johnson group wished to play a hand in our scientific immortality and decided to name alloys after ourselves. Elements have the suffix “ium” added after the name and in order to differentiate our alloys from elements, we had to come up with a new suffix. Indisputably Amorphous Metal, “IAM,” seemed like a good suffix that would sound elemental. It further amused because of the biblical reference in Exodus, and because the plural, IAMS, could be confused for a dog food. Just to make sure these alloys are in print and not limited to oral histories of the Johnson research group they are recorded here.

- Aaroniam  $Zr_{35}Ti_{30}Be_{29}Co_6$
- Marioniams A class of Ni and Cu free Pd glasses [55]
- O’Reillyam / O’Reilliam  $Zr_{35}Ti_{30}Be_{30}Al_5^*$

\*In honor of my favorite news commentator, I have named a cutting edge alloy after Bill O’Reilly. This alloy, O’Reillyam (O’Reilliam) is less dense than others in its family and can withstand a corrosive environment 1,000,000 times longer than its precious-metal sister.

After inventing and naming the alloys, some of the properties needed to be studied. The squish test proposed by Schroers, as a way to rank thermoplastic formability of different alloys, was performed on the alloys favored for TPF in the literature, namely,  $Pd_{43}Ni_{10}Cu_{27}P_{20}$ ,  $Pt_{57.5}Ni_{5.3}Cu_{14.7}P_{22.5}$ ,  $Zr_{41.2}Ti_{13.8}Cu_{12.5}Ni_{10}Be_{22.5}$  (Vitreloy 1), and

$Zr_{44}Ti_{11}Cu_{10}Ni_{10}Be_{25}$  (Vitreloy 1b) as well as the alloy we invented with the largest  $\Delta T$ ,  $Zr_{35}Ti_{30}Be_{27.5}Cu_{7.5}$ . The squish test indicated that  $Zr_{35}Ti_{30}Be_{27.5}Cu_{7.5}$  had the best potential for TPF of any of the alloys tested. Details of the squish test are included in Chapter 4 of this thesis.

$\eta(T)$  and TTT measurements for  $Zr_{35}Ti_{30}Be_{27.5}Cu_{7.5}$  were taken to quantitatively determine the TPF. Details of these experiments in Chapter 4 reveal a surprisingly high fragility was calculated for this alloy that does not fit well with other Vitreloy alloy data. It has been neglected so far, but many of the ternary alloys showed the double discontinuity in heat capacity that Tanner proposed was evidence of two glasses. Many of the quaternary compositions based on the “two  $T_g$ ” ternaries also showed the double jump in heat capacity. A more detailed study of the flow properties of these materials with the two  $T_g$  events is included in Chapter 6 of this thesis. The unusual flow properties of these materials may be the reason for the high fragility calculated for  $Zr_{35}Ti_{30}Be_{27.5}Cu_{7.5}$  which exhibits the two  $T_g$  phenomenon. A plot in Chapter 5 of  $\eta(T)$  (using heating data) for the commonly used TPF alloys and the newly invented  $Zr_{35}Ti_{30}Be_{27.5}Cu_{7.5}$  verify as the squish tests did that  $Zr_{35}Ti_{30}Be_{27.5}Cu_{7.5}$  is the best available for TPF applications like injection molding. That plot is reprinted here as Figure 1.9.

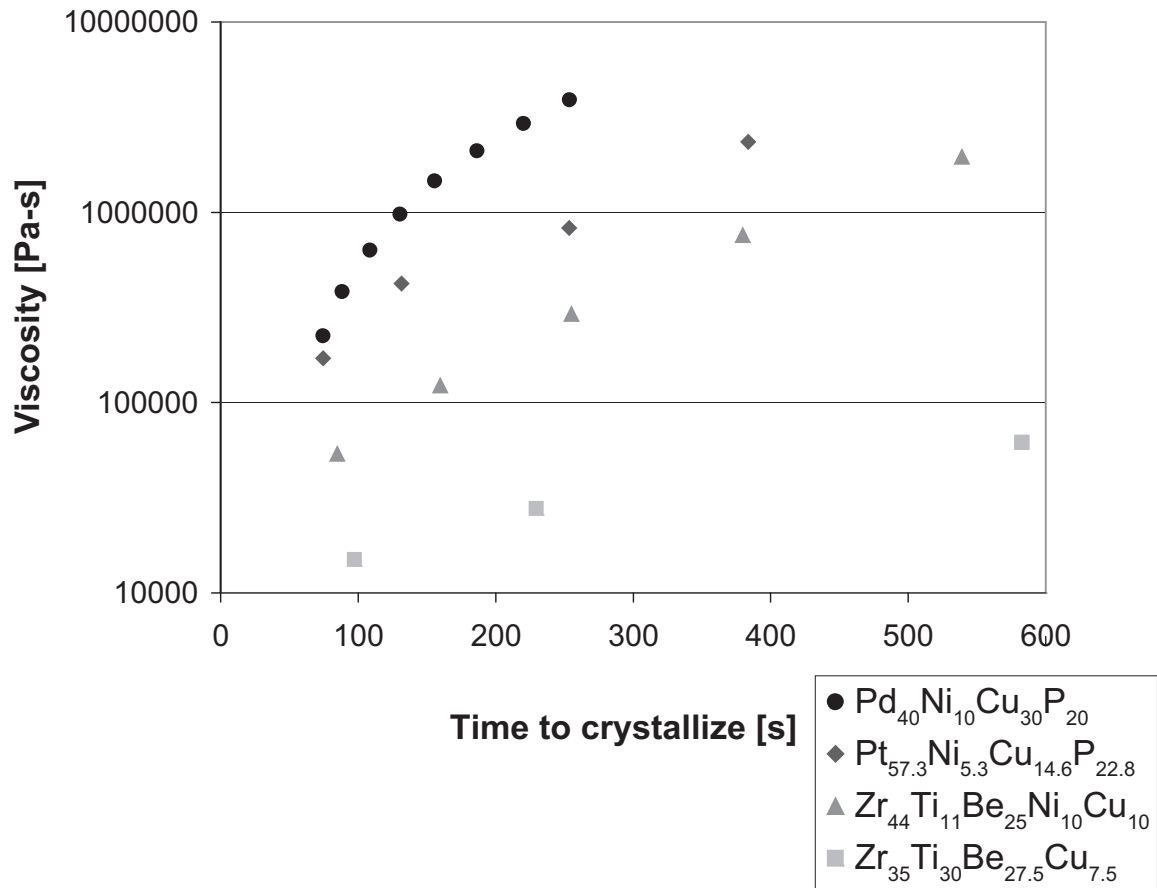


**Figure 1.9:** Time to crystallization versus viscosity plot for four thermoplastically processable alloys. This plot combines TTT and viscosity versus time data to show available processing time for a given viscosity for the alloys [7, 37, 40-41, 56]. Figure reproduced in Chapter 5.

A TPF process like injection molding takes 60 - 300 s. If we look at Figure 1.9, we see that  $Zr_{35}Ti_{30}Be_{27.5}Cu_{7.5}$  has 10 times lower processing viscosities in that time frame than any other metallic glass. This is a huge alloy development success, but unfortunately not a candidate to replace plastics in injection molding because plastics process at  $10^2 - 10^3$  Pa-s while this alloy only reaches viscosities of  $10^4$  Pa-s at the times required for injection molding.

Determined to have some success after this much work, we modified an injection molding setup to maximize the nozzle diameter, increase the available force, and heat the feedstock to temperatures higher than those used for processing plastics. As we tried to

make  $Zr_{35}Ti_{30}Be_{27.5}Cu_{7.5}$  feedstock we ran into additional problems. Alloys are melted on an arc melter and if the ingot cools amorphous, the value of  $\Delta T \sim 165$  °C. If the alloy is remelted and cast into a mold,  $\Delta T$  decreases. We tried various temperatures and hold times while melting the alloy in quartz tubes and water quenching and the value of  $\Delta T$  decreased. The details of this study are included in Chapter 5.

Finally we decided that amorphous ingots from the arc melter must be used as feedstock material. The bottom of the ingots however had a thin crystalline layer because of direct contact with the cooled hearth and had to be cut off with a diamond saw. After verifying that the ingots were completely amorphous, multiple attempts at injection molding were made using varying temperatures and pressures. The modifications were successful and the first ever injection molded metallic glass part was created. A figure showing the polished injection molded part from Chapter 5 is included below as Figure 1.10. The injection molded part had superior mechanical properties to a die cast specimen of the same dimensions. Details can be found in Chapter 5.



**Figure 1.10:** Photograph of the polished injection molded part prior to final sectioning for three-point bend testing.

Viscosity measurements performed on  $Zr_{35}Ti_{30}Be_{27.5}Cu_{7.5}$  had some unusual characteristics that were neglected in the push to be the first person to injection mold a metallic glass. A DSC scan of the SCLR of  $Zr_{35}Ti_{30}Be_{27.5}Cu_{7.5}$  is magnified to show the

apparent two  $T_g$  phenomenon in Figure 1.11. Viscosity measurements of this alloy would show small deformation for the first 50 °C after the calorimetric  $T_{g1}$  and then the deformation rate would increase dramatically after the calorimetric  $T_{g2}$ . After successfully injection molding this alloy, curiosity prompted a revisiting of the ternary alloys that showed the most prominent discontinuities in heat capacity.

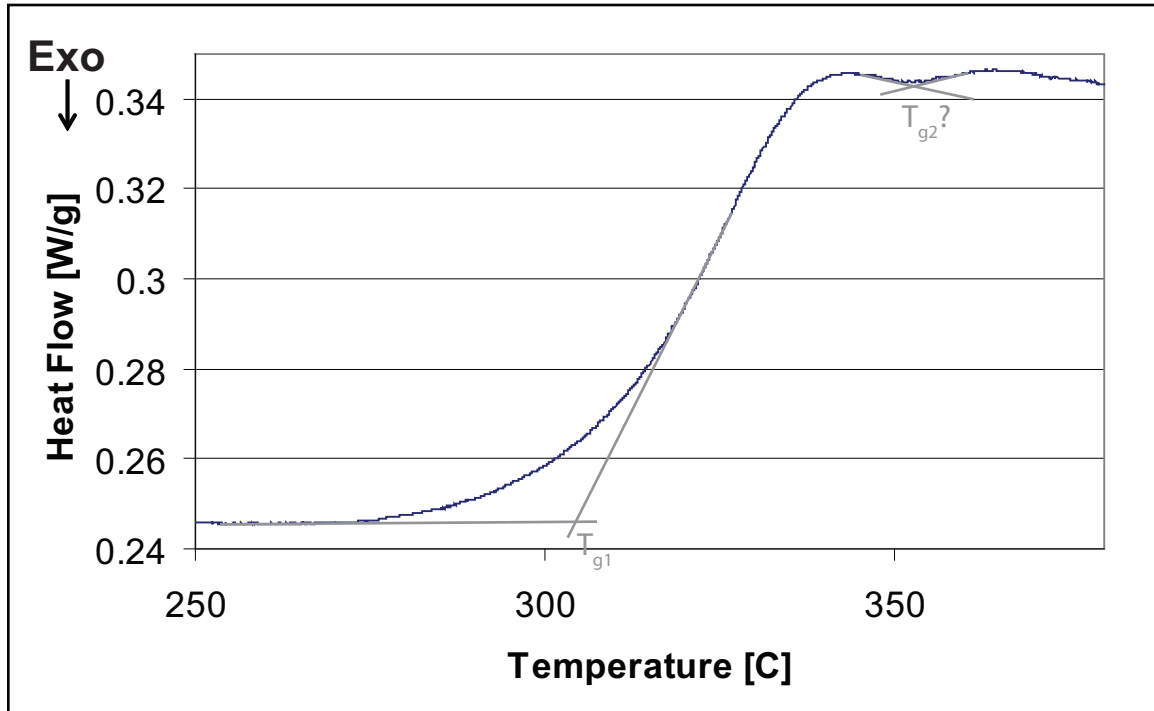


**Figure 1.11:** Apparent two  $T_g$  phenomenon seen in 20 K/min DSC scan of  $Zr_{35}Ti_{30}Be_{27.5}Cu_{7.5}$ .

The ternary alloys with the most prominent double heat capacity discontinuities lay along the  $(Zr_aTi_{1-a})_{60}Be_{40}$  composition line. Three regions of flow were observed in these alloys with discontinuities in the slope of the  $\eta(T)$  measurements roughly correlating to the  $T_g$  values measured in the DSC. Figure 1.12 shows a representative viscosity curve superimposed with a DSC curve for this composition line. The alloy should have about 60% of the low  $T_g$  phase and 40% of the high  $T_g$  phase. Viscosity is plotted on the left vertical axis, temperature is along the x axis and the heat capacity is

along the right vertical axis. Although there is some controversy in the BMG community over the existence of two phases in these alloys, the flow behavior can be nicely explained with the two phase assumption. In region 1, both phases are below their glass transition temperatures and would behave like solids. In region 2, the phase with the lower  $T_g$  softens and the other phase is still below its  $T_g$  so a solid + liquid flow is observed. In region 3, the second glass softens at temperatures above  $T_{g2}$  and we get liquid + liquid flow, where the two liquids have different viscosities. A large body of theoretical work has been done on two phase flow and with some hefty assumptions, a qualitative picture of what a two phase glass  $\eta(T)$  plot should look like is included in Derivation 8. The analysis predicts changes of slope in  $\eta(T)$  as observed experimentally.

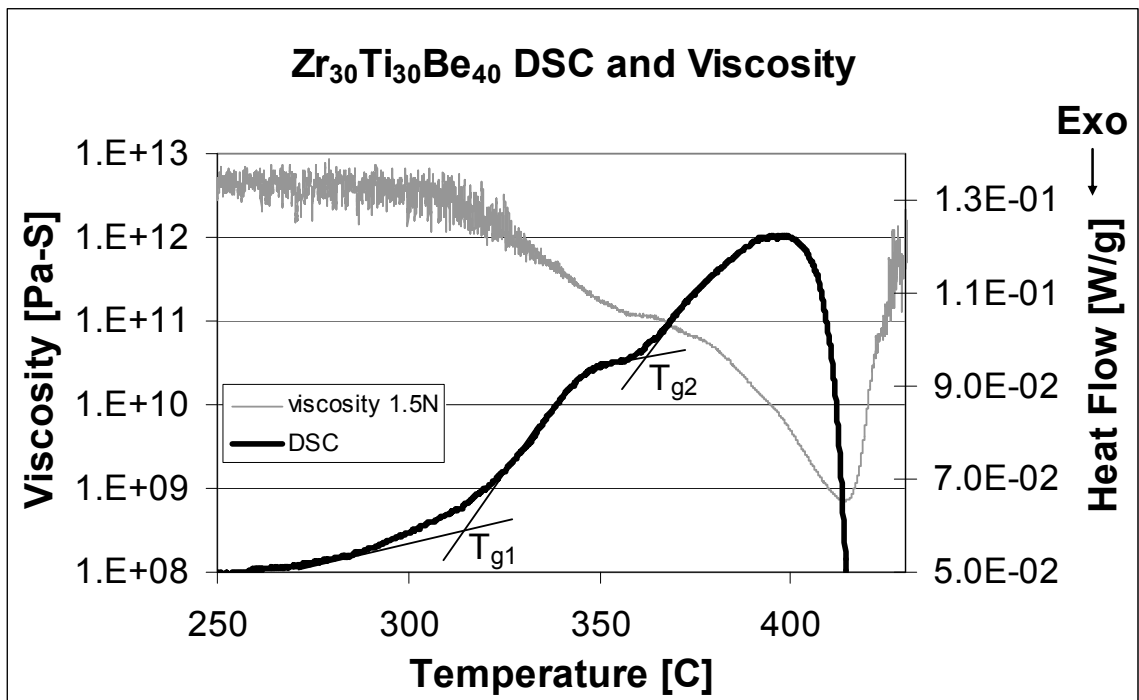


**Figure 1.12:** DSC and viscosity curve plotted against temperature for  $Zr_{30}Ti_{30}Be_{40}$  which shows about 60% of the low  $T_g$  phase and 40% of the high  $T_g$  phase. The viscosity plot shows two flow regions roughly corresponding to the discontinuities in heat capacity seen in the DSC.

If we assume that the magnitude of the discontinuities in heat capacities,  $\Delta c_{p1}$  and  $\Delta c_{p2}$ , are directly correlated to the fraction of each phase, we can look at how composition affects phase fraction. Figure 1.13 is reproduced in Chapter 6 where the two  $T_g$  story is thoroughly presented, but is necessary to illustrate this concept. A linear relationship was found between Zr concentration in the alloy and the fraction of phase 1  $= \Delta c_{p1}/(\Delta c_{p1} + \Delta c_{p2})$ . The linear relationship of these variables viewed in the context of a rule of mixtures analysis predicts a metastable miscibility gap in the SCLR. This is similar to the phenomenon seen in the phase separating Vitreloy glasses studied by Johnson et al. [15-17] described in Section 1.2, but no annealing is required to cause phase separation. Using a fit to the Zr concentration vs  $\Delta c_{p1}/(\Delta c_{p1} + \Delta c_{p2})$  data presented in Chapter 6, we can predict the compositions that should show all phase 1 or all phase 2 by setting  $\Delta c_{p1}/(\Delta c_{p1} + \Delta c_{p2}) = 1$  or 0 respectively. Amorphous samples of these compositions showed only single discontinuities in heat capacity as expected from single phase glasses. If this two phase analysis is correct, the endpoints of the miscibility gap have been discovered and the phases into which the alloy separates are known.

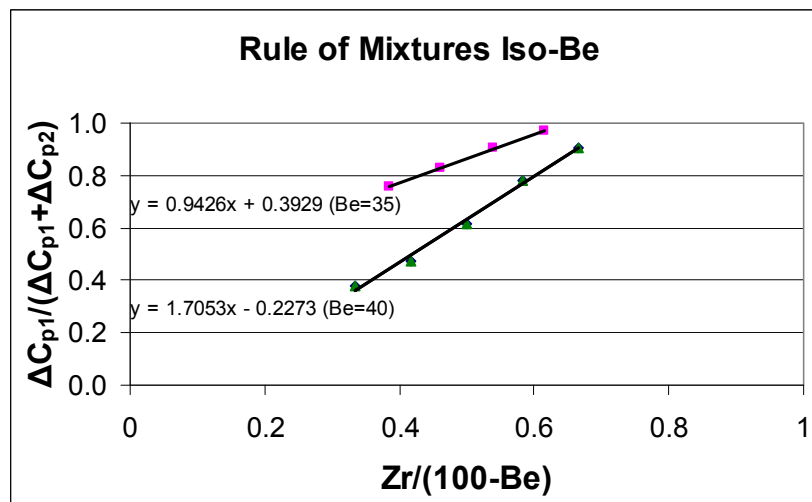


**Figure 1.13:** Plot of  $\Delta c_{p1}/(\Delta c_{p1} + \Delta c_{p2})$  versus Zr concentration gives fraction of phase 1 assuming two glassy phases with similar fragilities. Linear fits indicate rule of mixtures analysis is appropriate and suggests a metastable miscibility gap in SCLR.

The alloy calculated to contain only phase 1 was  $Zr_{43}Ti_{17}Be_{40}$ . The alloy calculated to contain only phase 2 was  $Zr_8Ti_{52}Be_{40}$ . If phase separation into these single phase compositions existed in the two  $T_g$  alloys, Z contrast imaging in the SEM seemed like a good way to prove their existence. SEM failed to observe the phases suggesting that perhaps the scale of phase separation was too small. This was plausible because Johnson et al. calculated the scale of phase separation was 13nm in Vitreloy compositions from SANS data [15]. TEM work also failed to reveal the two phases. Bright field (BF) and dark field (DF) images showed no evidence of phase separation at nm length scales. Diffraction patterns may have had broadening of the amorphous halo, but were not distinct enough to prove phase separation. Composition analysis was also inconclusive. If the phase separation is very small, on the order of 3 - 5nm or the size of an STZ, the electron interactions with multiple phase regions would be averaged over the thickness of the sample and would mask BF or DF contrast.

It is disheartening not to have microscopic evidence of the two phases. Ternary samples had limited GFA so preparation of a sample for SANS is difficult. SAXS is a good technique for observing composition fluctuations that we are pursuing at Argonne National Labs. We discovered that these samples could be doped with up to 2% Fe without diminishing the apparent two  $T_g$  effect and hoped that Mössbauer spectroscopy might reveal two local environments. We doped the two endpoint compositions expected to contain only one phase with 2% Fe and observed two distinct spectra. Two intermediate compositions showing the two  $T_g$  phenomenon were also doped with 2% Fe. The two intermediate compositions had Mössbauer spectra identical to the  $Zr_8Ti_{52}Be_{40}$  alloy. Various annealing times and temperatures were tried on the two  $T_g$  alloys with no

change in the spectra. If we had microscopic evidence of the two phases, we could argue that all the Fe went to the Ti rich phase and therefore all spectra looked like the  $Zr_8Ti_{52}Be_{40}$  alloy except the  $Zr_{43}Ti_{17}Be_{40}$  composition where the Fe was forced into the Zr rich phase because there was no Ti rich phase present. This explanation seems implausible given the entropic driving force to dissolve impurities in a phase. Additionally there seems to be no insolubility of Fe in the FeZr phase diagram.

The anomalous flow behavior of alloys with an apparent two  $T_g$  event was observed and the steeper slope of  $\eta(T)$  in the “liquid + liquid” region 3 may be the reason for the higher than expected fragility calculated for  $Zr_{35}Ti_{30}Be_{27.5}Cu_{7.5}$  reported in Chapter 4. Chapter 6 clearly shows the presence of two relaxation phenomena in the SCLR of these alloys, but fails to convincingly establish the presence of two phases.

### 1.6.1 Biocompatible Beryllium???

Appendices A1, A2, and A3 were a digression from the thermodynamics, flow properties and TPF theme of this work, but represent efforts to commercialize a few of the more amazing alloys and led to some important discoveries.

ZrTiBe alloys have high strength, high hardness, good wear characteristics, high corrosion resistance, high elastic limit, and low Young's modulus [57-59]. They fail catastrophically in tension and can show some compressive plasticity in compression [57, 60]. They are less dense than steel, more dense than Al and some compositions approach the density of Ti [57]. The fatigue properties were wonderful according to some groups in 2005 and terrible according to other groups [61-62]. One promising application we saw for these alloys was as orthopaedic hardware.

Hip replacements have some characteristic failure mechanisms. Wear debris can be created as the ball and socket material rub together [63]. This wear debris migrates into the surrounding tissue and causes inflammation. The hardness and good wear characteristics of ZrTiBe glasses could diminish the likelihood of this failure mechanism. Another problem is called stress shielding [64]. The commonly used implant materials have stiffnesses or Young's moduli much higher than bone. As a result, the load on the hip is carried mainly by the metallic implant material and not the bone surrounding it. As a result of this stress shielding, the body decreases the unused bone's density, the implant loosens, and fracture can result. The Young's modulus of ZrTiBe BMG is much lower than the commonly used implant materials and could diminish stress shielding. Another failure mechanism is fatigue cracking [65]. The size and type of artificial hip is determined prior to surgery. If a person gains weight and stresses the hip more than was estimated, fatigue conditions accelerate and the socket joint can fail catastrophically. The good corrosion resistance and high strength of ZrTiBe glasses along with some of the promising fatigue data made us hopeful that the newly discovered alloys would be unaffected by this failure mechanism as well.

The newly invented alloys showed promise to solve some of the mechanical failure mechanisms of hip joints or more broadly orthopaedic hardware, but biocompatibility of these alloys was unknown. Zr and Ti are well known for their biocompatibility. Many alloys free of Ni and Cu had been invented and Ni and Cu are known for poor biocompatibility. Beryllium is a known respiratory toxin, but very little data on cytotoxicity of Be containing alloys was found in the literature. A good indicator of biocompatibility is corrosion resistance [66]. Zr based BMG compositions are known

to have good corrosion resistances in saline environments [67] and biologically relevant solutions [68] and this suggested they might show good biocompatibility.

With limited equipment to test corrosion at Caltech, we chose four highly corrosive solutions, (37% w/w HCl, 0.6M NaCl, 50% w/w NaOH, and 10x phosphate buffered saline (PBS)), to test the corrosion resistance of three metallic glass compositions, ( $Zr_{35}Ti_{30}Be_{35}$ ,  $Zr_{35}Ti_{30}Be_{29}Co_6$ , and  $Zr_{44}Ti_{11}Cu_{10}Ni_{10}Be_{25}$ ), and three commonly used alloys for biomedical applications (Ti-6Al-4V, 316L Stainless Steel, and CoCrMo). Mass loss measurements were conducted at 1 week, 1 month, and 3 months. Inductively coupled plasma mass spectrometry (ICPMS) measurements were used to analyze the solution for dissolved elements. Details of this study are included in Appendix A1. It was determined from mass loss data that all alloys had excellent corrosion resistance in all solutions except for HCl. ICPMS data was inconclusive for some of the solutions because the amount of dissolved material was below the detection limit.

Corrosion rates in HCl were enormous for most of the alloys tested.  $Zr_{44}Ti_{11}Cu_{10}Ni_{10}Be_{25}$  dissolved in under 10 minutes. Most of the other alloys were completely dissolved in 1 week,  $Zr_{35}Ti_{30}Be_{35}$  survived for almost 1 month, and the only alloy to survive the full 3 months was CoCrMo which lost 12% of its mass. Corrosion rates in HCl were seen to vary by many orders of magnitude depending on composition. We sought to find the most corrosion resistant BMG for biological applications and given that this was an acidic chloride containing environment, we saw an opportunity to quickly differentiate corrosion resistances in a possibly biologically relevant accelerated corrosion environment.

Zr<sub>35</sub>Ti<sub>30</sub>Be<sub>35</sub> quaternary variants showed the most promise for injection molding so the bulk of the corrosion testing focused on those compositions. Depending on the fourth alloying element, the corrosion rate varied from 10<sup>7</sup> MPY to 50 MPY where MPY is a corrosion penetration rate that measures .001 in / year thickness loss. A plot of standard hydrogen electrode (SHE) half cell potential of the fourth alloying element vs Log(MPY) gave a fairly linear relationship. This was unexpected and has not been satisfactorily explained. The most noble alloying element Pd, when substituted for 4% Be, caused the highest corrosion rate while Al, which has the most anodic half cell potential, when substituted for 5% Be, caused the lowest corrosion rate of the ZrTiBe compositions tested in HCl. The problem with Al addition was that it raised T<sub>g</sub> and decreased GFA and ΔT (see Chapter 3). More details can be found in Appendix A1.

Zr<sub>35</sub>Ti<sub>30</sub>Be<sub>35</sub> and Zr<sub>35</sub>Ti<sub>30</sub>Be<sub>29</sub>Co<sub>6</sub> were chosen for further biocompatibility testing. Zr<sub>35</sub>Ti<sub>30</sub>Be<sub>35</sub> exhibited one of the best corrosion resistances in HCl, had moderate GFA = 6mm, had a moderate ΔT = 120 °C and good strength to weight ratio. Zr<sub>35</sub>Ti<sub>30</sub>Be<sub>29</sub>Co<sub>6</sub> had good corrosion resistance, but much better GFA = 15mm, ΔT = 155 °C, and showed good potential for TPF. Samples were sent to a testing company NAMSA and short term *in vitro* and *in vivo* studies were done to assess biocompatibility. Both alloys performed as well as the control specimen and were considered biocompatible in these short term trials. I took a semester long cell culture class at PCC and had the opportunity to test the cytotoxicity of the 10x PBS solutions in which the metals were tested for corrosion resistance. The solution was diluted to regular 1x strength and no visible damage to the cells resulted after they were exposed to the media and allowed to reach 90% confluence. We became aware of extensive biocompatibility testing performed for Liquidmetal

Technologies on samples of Vitreloy 1 and a glassy composite material called LM2 in an effort to obtain FDA approval. The testing showed that both Vitreloy and the Be containing LM2 were viable as biomaterials and had even passed 1 year *in vivo* studies in New Zealand White Rabbits. The results of the biocompatibility testing are more thoroughly discussed in Appendix A2.

Discussions with Liquidmetal Technologies revealed that the FDA approval process had been abandoned temporarily not because of biocompatibility issues, but because of corrosion fatigue issues with these alloys. Given our improvements in ZrTiBe alloy corrosion resistance we arranged a collaboration with Dr. Liaw at the University of Tennessee, Knoxville and provided  $Zr_{35}Ti_{30}Be_{35}$  and  $Zr_{35}Ti_{30}Be_{29}Co_6$  samples for corrosion testing in NaCl solutions and corrosion fatigue testing. Our newly invented alloys showed more than an order of magnitude increase in corrosion resistance in simulated sea water solutions as compared to other ZrTi based BMG compositions and even better than other crystalline alloys commonly used in marine environments. Corrosion fatigue results however, were unimproved over other ZrTi based glass forming compositions.

X-ray photoelectron spectroscopy, XPS, studies of the surface chemistry of these new compositions revealed a fully oxidized surface that likely acts as an effective corrosion barrier in static corrosion testing. This oxide layer is expected to have low fracture toughness if the fracture toughnesses of Zr, Ti, or Be oxides are representative of the alloy's surface oxide fracture toughness. As a result of the applied stresses in corrosion fatigue testing, the surface layer cracks allowing the corrosive solution access

to the unoxidized inner material, resulting in a corrosion couple between the inner material and cracked surface layer. More details of this study are found in Appendix A3.

### 1.7 Introduction Summary

The thermoplastic formability (TPF) of metallic glasses was found to be related to the calorimetrically measured crystallization temperature minus the glass transition temperature,  $T_g - T_x = \Delta T$ . Alloy development in the ZrTiBe system identified a composition with  $\Delta T = 120$  °C. Many alloys with  $\Delta T > 150$  °C and one alloy,  $Zr_{35}Ti_{30}Be_{27.5}Cu_{7.5}$ , with  $\Delta T = 165$  °C were discovered by substituting Be with small amounts of fourth alloying elements. The viscosity as a function of temperature,  $\eta(T)$ , and time temperature transformation (TTT) measurements for the new alloy are presented and combined to create  $\eta$ TT plots (viscosity time transformation) that are useful in determining what viscosities are available for a required processing time.  $\eta$ TT plots are created for many alloys used in TPF in the literature and it is found that for processes requiring 60 - 300 s,  $Zr_{35}Ti_{30}Be_{27.5}Cu_{7.5}$  provides an order of magnitude lower viscosity for processing than the other metallic glasses. Injection molding is demonstrated with  $Zr_{35}Ti_{30}Be_{27.5}Cu_{7.5}$  and the part shows improved mechanical properties over die cast specimens of the same geometry. Changes of slope in  $\eta(T)$  measurements were observed and investigated in some quaternary compositions and found to be present in ternary compositions as well. Traditionally metallic glasses show a single discontinuity in heat capacity at the glass transition temperature. Alloys with the changes in slope of  $\eta(T)$  were found to show two discontinuities in heat capacity with the changes in slope of  $\eta(T)$  roughly correlating with the observed  $T_g$  values. These two  $T_g$  values were assumed to arise from two glassy phases present in the alloy. Further heat capacity analysis found

systematic trends in the magnitude of the heat capacity discontinuities with composition and the single phase compositions of a metastable miscibility gap were discovered.

Microscopic evidence of the two phases is lacking so we must limit our claims to evidence of two relaxation phenomena existing and can't definitively claim two phases.

The alloy development led to the discovery of alloys with densities near Ti that are among the highest strength to weight ratio materials known. Alloys with corrosion resistances in simulated sea water 10x greater than other Zr based glasses and commonly used marine metals were discovered. Glasses spanning 6 orders of magnitude in corrosion resistance to 37% w/w HCl were discovered. Corrosion fatigue in saline environments remains a problem for these compositions and prevents their utility as biomaterials despite good evidence of biocompatibility in *in vitro* and *in vivo* studies.

### Chapter 1 References

- [1] J. Schroers, W.L. Johnson, R. Busch, Appl. Phys. Lett. 77 (2000) 1158.
- [2] S.R. Elliott, Physics of Amorphous Materials, second ed., John Wiley & Sons Inc., New York, 1990, pp. 29-69.
- [3] J. Schroers, A. Masuhr, W.L. Johnson, R. Busch, Phys. Rev. B 60 (1999) 11855.
- [4] A. Peker, W.L. Johnson, Appl. Phys. Lett. 63 (1993) 2342.
- [5] Y.J. Kim, R. Busch, W.L. Johnson, A.J. Rulison, W.K. Rhim, Appl. Phys. Lett. 68 (1996) 1057.
- [6] H. Vogel, Z. Phys. 22 (1921) 645.
- [7] W.L. Johnson, M.D. Demetriou, J.S. Harmon, M.L. Lind, K. Samwer, MRS Bull. 32 (2007) 644.
- [8] M.C. Lee, J.M. Kendall, W.L. Johnson, Appl. Phys. Lett. 40 (1982) 382.
- [9] W.L. Johnson, Amorphe Metallische Werkstoffe 14, Metalltagung in der DDR (1981) 183.
- [10] R. Schulz, K. Samwer, W.L. Johnson, J. Non-Cryst. Solids 61 & 62 (1984) 997.
- [11] L.E. Tanner, R. Ray, Scripta Metal. 11 (1977) 783.
- [12] R. Hasegawa, L.E. Tanner, Phys. Rev. B 16 (1977) 3925.
- [13] L.E. Tanner, R. Ray, Acta Metall. 27 (1979) 1727.
- [14] L.E. Tanner, R. Ray, Scripta Metall. 14 (1980) 657.
- [15] S. Schneider, P. Thiyagarajan, U. Geyer, W.L. Johnson, MRS Technical Report DOI 10.2172/510428 (1996).
- [16] S. Schneider, P. Thiyagarajan, U. Geyer, W.L. Johnson, Physica B 241 (1998) 918.

- [17] S. Schneider, U. Geyer, P. Thiyagarajan, W.L. Johnson, *Materials Science Forum* Vols. 235-238 (1997) 337.
- [18] W. Liu, W.L. Johnson, S. Schneider, U. Geyer, P. Thiyagarajan, *Phys. Rev. B* 59 (1999) 11755.
- [19] Q. Zhang, W. Zhang, G. Xie, A. Inoue, *Mater. Sci. Eng. B* 148 (2008) 97.
- [20] B.J. Park, H.J. Chang, D.H. Kim, W.T. Kim, K. Chattopadhyay, T.A. Abinandanan, S. Bhattacharyya, *Phys. Rev. Lett.* 96 (2006) 245503.
- [21] R.G. Hennig, A.E. Carlsson, K.F. Kelton, C.L. Henley, *Phys. Rev. B* 71 (2005) 144103.
- [22] X.P. Tang, J.F. Löffler, W.L. Johnson, Y. Wu, *J. Non-Cryst. Solids* 317 (2003) 118.
- [23] B. Van de Moortele, T. Epicier, J.L. Soubeyroux, J.M. Pelletier, *Phil. Mag. Lett.* 84 (2004) 245.
- [24] G. Wang, J. Shen, J.F. Sun, B.D. Zhou, J.D. Fitz Gerald, D.J. Llewellyn, Z.H. Stachurski, *Scripta Mater.* 53 (2005) 641.
- [25] J.H. Na, Y.C. Kim, W.T. Kim, D.H. Kim, *Met. Mater. Int.* 14 (2008) 553.
- [26] G. Kumar, D. Nagahama, M. Ohnuma, T. Ohkubo, K. Hono, *Scripta Mater.* 54 (2006) 801.
- [27] D. Nagahama, T. Ohkubo, K. Hono, *Scripta Mater.* 49 (2003) 729.
- [28] T. Abe, M. Shimono, K. Hashimoto, K. Hono, H. Onodera, *Scripta Mater.* 55 (2006) 421.
- [29] J. Schroers, *Acta Mater.* 56 (2008) 471.
- [30] J. Schroers, *JOM* 57 (2005) 35.
- [31] J. Schroers, N. Paton, *Adv. Mater. Processes* 164 (2006) 61.
- [32] T. Masumoto, A. Inoue, N. Nishiyama, H. Horimura, T. Shibata, *US Patent #6027586*.
- [33] T. Masumoto, A. Inoue, J. Nagahora, K. Kita, *US Patent #5209791*.
- [34] K.S. Lee, Y.W. Chang, *Mater. Sci. Eng. A* 399 (2005) 238.
- [35] Y. Saotome, K. Imai, S. Shioda, S. Shimizu, T. Zhang, A. Inoue, *Intermetallics* 10 (2002) 1241.
- [36] J. Schroers, Q. Pham, A. Peker, N. Paton, R.V. Curtis, *Scripta Mater.* 57 (2007) 341.
- [37] G. Duan, A. Wiest, M.L. Lind, J. Li, W.K. Rhim, W.L. Johnson, *Adv. Mater.* 19 (2007) 4272.
- [38] Y. Li, S.J. Poon, G.J. Shiflet, J. Xu, D.H. Kim, J.F. Löffler, *MRS Bull.* 32 (2007) 624.
- [39] A.L. Greer, E. Ma, *MRS Bull.* 32 (2007) 611.
- [40] B.A. Legg, J. Schroers, R. Busch, *Acta Mater.* 55 (2007) 1109.
- [41] T. Waniuk, J. Schroers, W.L. Johnson, *Phys. Rev. B* 67 (2003) 184203.
- [42] J. Schroers, W.L. Johnson, *Appl. Phys. Lett.* 84 (2004) 3666.
- [43] G.J. Fan, H.J. Fecht, E.J. Lavernia, *Appl. Phys. Lett.* 84 (2004) 487.
- [44] J.P. Chu, H. Wijaya, C.W. Wu, T.R. Tsai, C.S. Wei, T.G. Nieh, J. Wadsworth, *Appl. Phys. Lett.* 90 (2007), 034101.
- [45] A. Masuhr, T.A. Waniuk, R. Busch, W.L. Johnson, *Phys. Rev. Lett.* 82 (1999) 2290.
- [46] R. Busch, W.L. Johnson, *Appl. Phys. Lett.* 72 (1998) 2695.

- [47] F. Spaepen, *Acta Metall.* 25 (1977) 407.
- [48] J. Lu, G. Ravichandran, W.L. Johnson, *Acta Mater.* 21 (2003) 3429.
- [49] L. Kaufman, L.E. Tanner, *CALPHAD* 3 (1979) 91.
- [50] L.E. Tanner, R. Ray, C.F. Cline, US Patent #3989517.
- [51] L.E. Tanner, R. Ray, C.F. Cline, US Patent #4050931.
- [52] A. Peker, W.L. Johnson, US Patent #5288344.
- [53] G. Duan, A. Wiest, W.L. Johnson, US Patent Application #20080121316.
- [54] G. Duan, A. Wiest, M.L. Lind, A. Kahl, W.L. Johnson, *Appl. Phys. Lett.* 90 (2007) 211901.
- [55] M.D. Demetriou, A. Wiest, W.L. Johnson, US Patent Application #20090162629.
- [56] J.F. Löffler, J. Schroers, W.L. Johnson, *Appl. Phys. Lett.* 77 (2000) 681.
- [57] G. Duan, A. Wiest, M.L. Lind, A. Kahl, W.L. Johnson, *Scripta Mater.* 58 (2008) 465.
- [58] A. Wiest, G.Y. Wang, L. Huang, S. Roberts, M.D. Demetriou, P.K. Liaw, W.L. Johnson, *Scripta Mater.* in review.
- [59] M.Z. Ma, R.P. Liu, Y. Xiao, D.C. Lou, L. Liu, Q. Wang, W.K. Wang, *Mater. Sci. Eng. A* 386 (2004) 326.
- [60] D.C. Hofmann, J.Y. Suh, A. Wiest, G. Duan, M.L. Lind, M.D. Demetriou, W.L. Johnson, *Nature* 451 (2008) 1085.
- [61] G.Y. Wang, P.K. Liaw, A. Peker, B. Yang, M.L. Benson, W. Yuan, W.H. Peter, L. Huang, M. Freels, R.A. Buchanan, C.T. Liu, C.R. Brooks, *Intermetallics* 13 (2005) 429.
- [62] C.J. Gilbert, J.M. Lippmann, R.O. Ritchie, *Scripta Mater.* 38 (1998) 537.
- [63] C.R. McMillin, in: B.D. Ratner, A.S. Hoffman, F.J. Schoen, J.E. Lemons (Eds.), *Biomaterials Science: An Introduction to Materials in Medicine*, Academic Press, California, 1996, pp. 267-271.
- [64] J. Black, *Biological Performance of Materials: Fundamentals of biocompatibility*, fourth ed., CRC Press, Florida, 2006.
- [65] M. Niinomi, T. Hattori, T. Kasuga, H. Fukui, in: G.E. Wnek, G.L. Bowlin (Eds.), *Encyclopedia of Biomaterials and Biomedical Engineering*, second ed., Informa Healthcare USA, Inc., New York, 2008, pp. 2876-2892.
- [66] G.L. Burke, *Can. Med. Assoc. J.* (1940) 125.
- [67] M.L. Morrison, R.A. Buchanan, P.K. Liaw, B.A. Green, G.Y. Wang, C.T. Liu, J.A. Horton, *Mater. Sci. Eng. A* 467 (2007) 198.
- [68] M.L. Morrison, R.A. Buchanan, R.V. Leon, C.T. Liu, B.A. Green, P.K. Liaw, J.A. Horton, *J. Biomed. Mater. Res. Part A* 74 (2005) 430.

**Chapter 2 - Lightweight Ti-based Bulk Glassy Alloys Excluding Late Transition Metals**

This chapter draws heavily on the article, “Lightweight Ti-based Bulk Glassy Alloys Excluding Late Transition Metals,” published in Scripta Materialia [G. Duan, A. Wiest, M.L. Lind, A. Kahl, W.L. Johnson, Scripta Mater. 58 (2008) 465]. It discusses lightweight Ti based bulk amorphous metals with more than double the specific strength of conventional titanium alloys discovered in the course of alloy development in the ZrTiBe system. Thermal, elastic, and mechanical properties of these metallic glasses were studied and presented. These amorphous alloys exhibit good glass forming ability, exceptional thermal stability, and high strength. The research results have important implications on designing and developing bulk metallic glasses (BMG). The technological potential of this class of lightweight Ti based glassy alloys as structural metals is very promising.

Owing to their high glass forming ability (GFA), good processing ability, and exceptional stability with respect to crystallization along with many promising properties such as high strength, elastic strain limit, wear resistance, fatigue resistance, and corrosion resistance, BMG have garnered considerable attention in the past 20 years scientifically and technically [1-2]. To date, families of binary and multi-component systems have been designed and characterized to be BMG formers [3-15] among which highly processable ZrTiCuNiBe BMG (Vitreloy series) have been used commercially for items such as sporting goods and electronic casings [3, 16].

Prior research results teach that Be bearing amorphous alloys (Vitreloy series) require the presence of at least one early transition metal (ETM) and at least one late transition metal (LTM) in order to form BMG. It is believed that BMG containing

certain LTM (e.g., Fe, Ni, Cu) have potential advantages including better glass forming ability, higher strength and elastic modulus, and lower materials cost. However, because of the high density of LTM, glassy alloys containing LTM will have higher densities than alloys excluding LTM. Vitreloy alloys have densities of about  $\sim 6$  g/cc [17] and are therefore limited in their uses in structural applications requiring low density and high specific strength materials. The elimination of LTM would make this class of materials ideal for structural applications where specific strength and specific modulus are key figures of merit. We discovered that Be bearing alloys excluding LTM are excellent bulk metallic glass formers and have a 20% to 40% advantage over Vitreloy alloys in density while still possessing high strength and high elastic modulus.

Conventional titanium alloys have been widely used in the aerospace industry due to their resource availability, low density and high specific strength. However no Ti based BMG with density comparable to that of pure titanium or Ti-6Al-4V alloy have been discovered yet, although researchers have developed several Ti based glass forming systems [13, 18-20]. Recently BMG forming alloys in the form of glassy ingots were discovered in TiZrNiCuBe system [13]. Up to 14mm amorphous rods could be successfully produced. For a typical  $\text{Ti}_{40}\text{Zr}_{25}\text{Ni}_3\text{Cu}_{12}\text{Be}_{20}$  alloy, a density of  $\sim 5.4$  g/cc was obtained. In this chapter we report a class of Ti based bulk amorphous alloys with high GFA, exceptional thermal stability, and low density ( $\sim 4.59$  g/cc) comparable to that of pure titanium, as well as very high specific strength.

Tanner reported that some TiBe, ZrBe and TiZrBe compositions could be made amorphous at very high cooling rates of  $\sim 10^6$  K/s [21-24]. These cooling rates are achievable using splat quenching or melt spinning techniques, which limits the thickness

of the alloys to 30 - 100 $\mu\text{m}$ . However, no bulk glass formers have been identified in the ternary TiZrBe system. This research discovered that TiZrBe compositions are not limited to 30 - 100 $\mu\text{m}$  thick foils, but many compositions can be cast into bulk samples of 1 - 6mm thickness. This discovery reveals alloys can be cooled amorphous 1000 times slower than reported by Tanner [21-24].

Mixtures of elements of purity ranging from 99.9% to 99.99% were alloyed in an arc melter with a water cooled copper plate under a Ti-gettered argon atmosphere. Each ingot was flipped over and remelted at least three times in order to obtain chemical homogeneity. After the alloys were prepared, the materials were cast into machined copper molds under high vacuum. These copper molds have internal cylindrical cavities of diameters ranging from 1 - 10mm. A Philips X'Pert Pro X-ray Diffractometer and a Netzsch 404C Pegasus Differential Scanning Calorimeter (DSC) with graphite crucibles performed at a constant heating rate 20 K/min were utilized to verify the amorphous natures and to examine the thermal behavior of these alloys. We evaluated the elastic properties of the samples using ultrasonic measurements along with density measurements. The pulse-echo overlap technique was used to measure the shear and longitudinal wave speeds at room temperature for each of the samples. 25 MHz piezoelectric transducers and a computer controlled pulser/receiver were used to produce and measure the acoustic signal. The signal was measured using a Tektronix TDS 1012 oscilloscope. Sample density was measured by the Archimedean technique according to the American Society of Testing Materials standard C 693-93. Cylindrical rods 3mm in diameter x 6mm in height were used to measure mechanical properties of the lightweight Ti based bulk glassy alloys on an Instron testing machine at a strain rate of  $1 \times 10^{-4} \text{ s}^{-1}$ .

Before these mechanical tests, both ends of each specimen were examined with X-ray diffraction to make sure that the rod was fully amorphous and that no crystallization occurred due to unexpected factors.

It was recently found that in the CuZrBe alloy system, the shear modulus,  $G$ , and Poisson's ratio,  $\nu$ , are very sensitive to composition changes, where  $G$  decreases linearly with the increasing total Zr concentration [25]. Extensive regions in the TiZrBe phase diagram were systematically examined. The best glass forming region was found along the pseudo-binary line,  $Ti_xZr_{(65-x)}Be_{35}$ . Figure 2.1(a) shows pictures of three as-cast rods,  $Ti_{45}Zr_{20}Be_{35}$  (S1),  $Ti_{45}Zr_{20}Be_{30}Cr_5$  (S2) and  $Ti_{40}Zr_{25}Be_{30}Cr_5$  (S3), having diameters of 6, 7, and 8mm, respectively. Their as-cast surfaces appear smooth and no apparent volume reductions can be recognized on their surfaces. The X-ray diffraction patterns of S1, S2, and S3 are presented in Figure 2.1(b). S1 and S2 have X-ray patterns indicative of fully amorphous samples and S3 has a very small Bragg peak on an otherwise amorphous background indicating that the critical casting diameter has been reached. Glassy rods up to 8mm diameter are formed by the addition of 5% Cr into the ternary TiZrBe alloys.

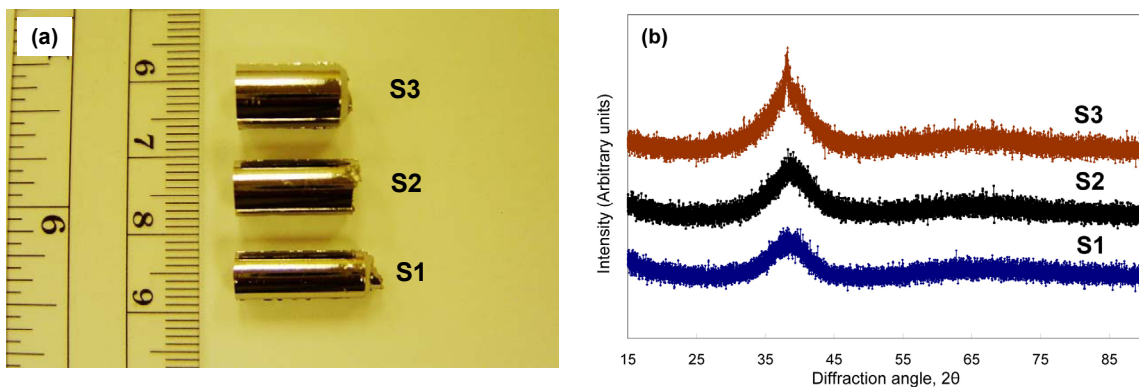


**Figure 2.1:** Pictures of amorphous 6mm diameter rod of  $Ti_{45}Zr_{20}Be_{35}$  (S1), 7mm diameter rod of  $Ti_{45}Zr_{20}Be_{30}Cr_5$  (S2) and 8mm diameter rod of  $Ti_{40}Zr_{25}Be_{30}Cr_5$  (S3) prepared by the copper mold casting method are presented in (a). The X-ray diffraction patterns (b) verify the amorphous nature of the corresponding samples.

Thermal behavior of these glassy alloys was measured using DSC at a constant heating rate of 20 K/min. The characteristic thermal parameters including the variations of supercooled liquid region,  $\Delta T$ , ( $\Delta T = T_x - T_g$ , in which  $T_x$  is the onset temperature of the first crystallization event and  $T_g$  is the glass transition temperature) and reduced glass transition temperature  $T_{rg}$  ( $T_{rg} = T_g/T_L$ , where  $T_L$  is the liquidus temperature) are evaluated and listed in Table 2.1. The DSC scans are shown in Figure 2.2.

**Table 2.1:** Density, thermal and elastic properties of representative lightweight TiZrBe and Vitreloy type glassy alloys.

Materials	$\rho$ [g/cm <sup>3</sup> ]	d [mm]	$T_g$ [K]	$T_x$ [K]	$T_L$ [K]	$\Delta T$ [K]	$T_g/T_L$	G [Gpa]	B [Gpa]	Y [Gpa]	$\nu$
Ti <sub>45</sub> Zr <sub>20</sub> Be <sub>35</sub>	4.59	6	597	654	1123	57	0.53	35.7	111.4	96.8	0.36
Ti <sub>40</sub> Zr <sub>25</sub> Be <sub>35</sub>	4.69	6	598	675	1125	76	0.53	37.2	102.7	99.6	0.34
Ti <sub>45</sub> Zr <sub>20</sub> Be <sub>30</sub> Cr <sub>5</sub>	5.76	7	602	678	1135	77	0.53	39.2	114.5	105.6	0.35
Ti <sub>40</sub> Zr <sub>25</sub> Be <sub>30</sub> Cr <sub>5</sub>	4.89	8	599	692	1101	93	0.54	35.2	103.1	94.8	0.35
Zr <sub>65</sub> Cu <sub>12.5</sub> Be <sub>22.5</sub>	6.12	4	585	684	1098	99	0.53	27.5	111.9	76.3	0.39
Zr <sub>41.2</sub> Ti <sub>13.8</sub> Cu <sub>12.5</sub> Ni <sub>10</sub> Be <sub>22.5</sub>	6.07	>20	623	712	993	89	0.63	37.4	115.9	101.3	0.35
Zr <sub>46.75</sub> Ti <sub>8.25</sub> Cu <sub>7.5</sub> Ni <sub>10</sub> Be <sub>27.5</sub>	6.00	>20	625	738	1185	113	0.53	35.0	110.3	95.0	0.36

Upon heating, these amorphous alloys exhibit a clear endothermic glass transition followed by a series of exothermic events characteristic of crystallization. It appears that Cr delays the exothermic peaks, indicating a suppression of the kinetics of crystal nucleation and growth. In the TiZrBe ternary alloy system, the critical casting diameter of Ti<sub>45</sub>Zr<sub>20</sub>Be<sub>35</sub> and Ti<sub>40</sub>Zr<sub>25</sub>Be<sub>35</sub> is 6mm (see Table 2.1). The addition of Cr increases the crystallization temperature, stabilizes the supercooled liquid, thereby increasing the GFA. It is known that the GFA of the present lightweight TiZrBe glassy alloys would be dramatically improved with Ni and Cu additions as indicated in [13].

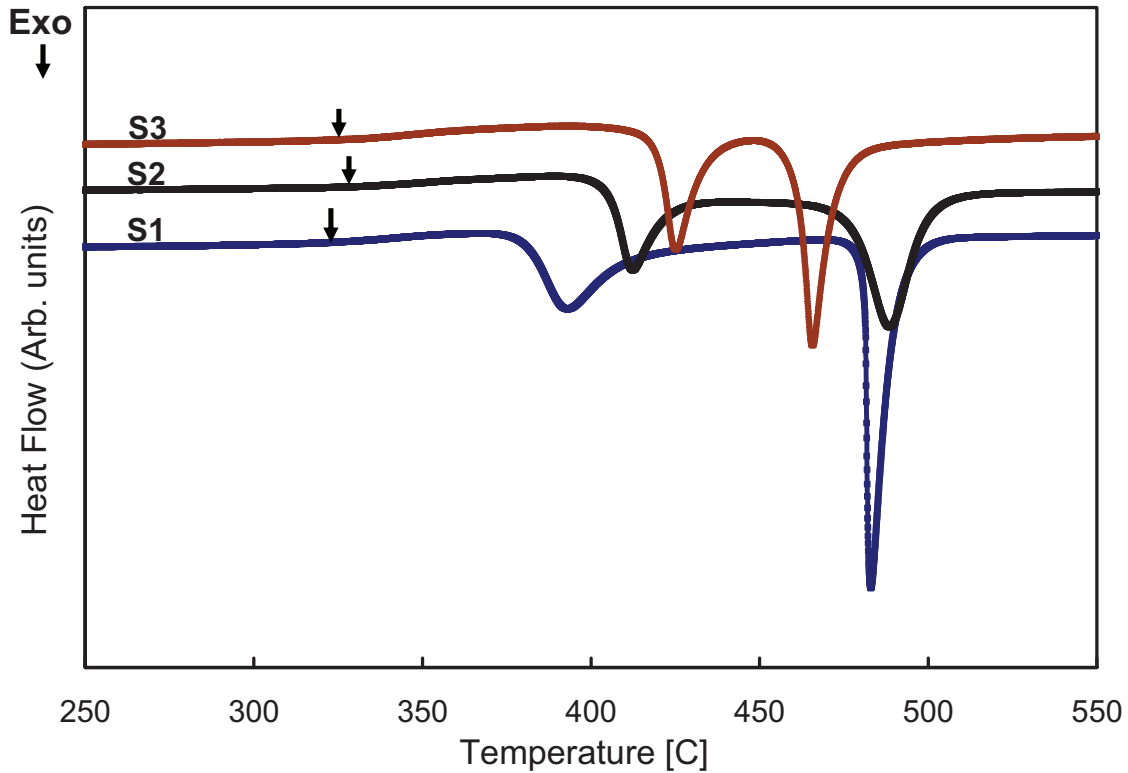


**Figure 2.2:** DSC scans of the amorphous  $\text{Ti}_{45}\text{Zr}_{20}\text{Be}_{35}$  (S1),  $\text{Ti}_{45}\text{Zr}_{20}\text{Be}_{30}\text{Cr}_5$  (S2), and  $\text{Ti}_{40}\text{Zr}_{25}\text{Be}_{30}\text{Cr}_5$  (S3) alloys at a constant heating rate of 0.33 K/s. The marked arrows represent the glass transition temperatures.

Table 2.1 also presents the density, thermal and elastic properties of representative glassy alloys in ZrCuBe ternary systems and other Vitreloy type BMG. The value of  $T_{\text{rg}}$  gives a good first order approximation of GFA. The newly developed low density TiZrBe glassy alloys show very good thermal stability against crystallization. The best glass former  $\text{Ti}_{40}\text{Zr}_{25}\text{Be}_{30}\text{Cr}_5$  possesses a large supercooled liquid region of 93 K, among the highest in the known Ti based BMG. It is noted that the glass transition temperatures of TiZrBe amorphous alloys fall into the same range as those of ZrCuBe glasses with the same total Zr + Ti concentration. High Ti content alloys exhibited higher G values than are typical for Vitreloy type alloys. Another interesting observation is that ZrTi based Be bearing glassy alloys have to be Zr rich to exhibit a low G and a high  $v$ .

Figure 2.3 presents typical compressive stress-strain curves for 3mm diameter amorphous rods of the lowest density alloy,  $\text{Ti}_{45}\text{Zr}_{20}\text{Be}_{35}$ , and the best glass former,  $\text{Ti}_{40}\text{Zr}_{25}\text{Be}_{30}\text{Cr}_5$ . Compression tests indicate that  $\text{Ti}_{45}\text{Zr}_{20}\text{Be}_{35}$  shows fracture strength of  $\sim 1860$  MPa, with total strain of  $\sim 2.2\%$  (mainly elastic).  $\text{Ti}_{40}\text{Zr}_{25}\text{Be}_{30}\text{Cr}_5$  yields at  $\sim 1720$  MPa, with an elastic strain limit of  $\sim 1.9\%$ , and ultimately fractures at a strength of  $\sim 1900$  MPa, with a plastic strain of  $\sim 3.5\%$ .

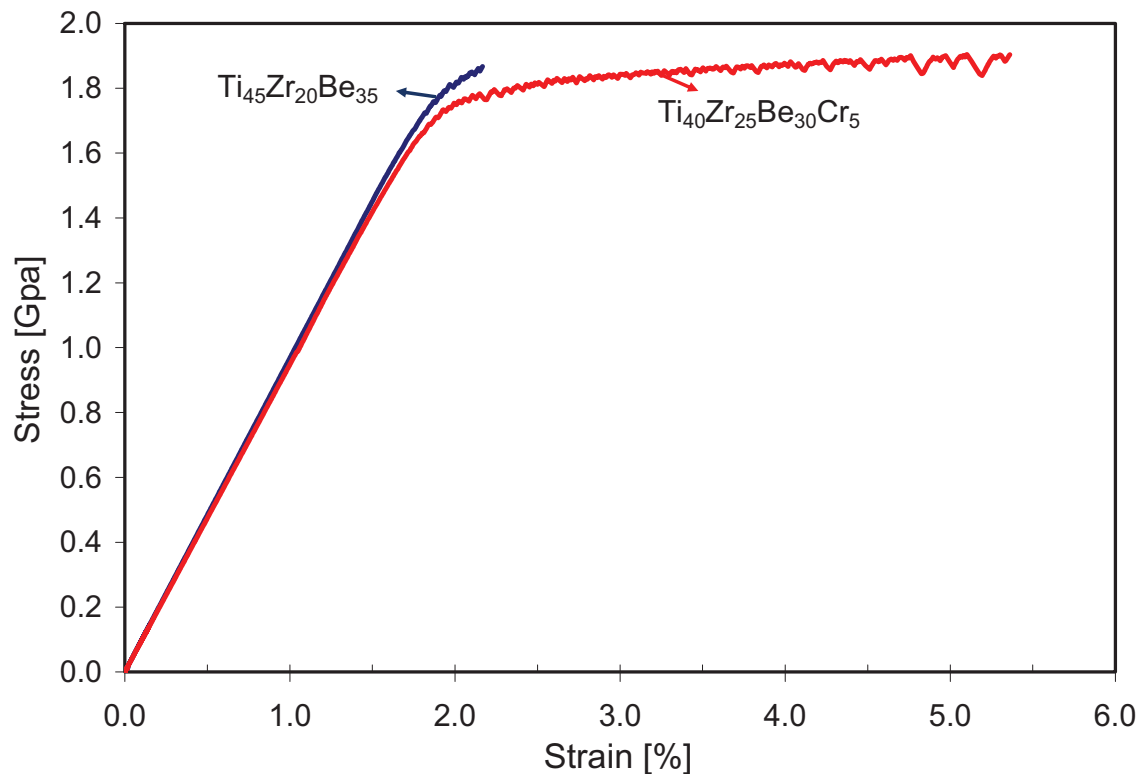


**Figure 2.3:** Compressive stress-strain curves for the  $\text{Ti}_{45}\text{Zr}_{20}\text{Be}_{35}$  and  $\text{Ti}_{40}\text{Zr}_{25}\text{Be}_{30}\text{Cr}_5$  3mm amorphous rods.

The current study resulted in a class of bulk amorphous alloys with high GFA, good processing ability and exceptional thermal stability with mass densities significantly lower than those of the Vitreloy alloys and comparable to those of pure titanium and Ti-6Al-4V alloy (see Table 2.1).  $\text{Ti}_{45}\text{Zr}_{20}\text{Be}_{35}$  and  $\text{Ti}_{40}\text{Zr}_{25}\text{Be}_{30}\text{Cr}_5$  show low densities of  $\sim 4.59$  and  $\sim 4.76$  g/cc respectively. Compared to Vitreloy alloys, a 20 - 40% higher

specific strength is observed in the lightweight TiZrBe compositions. These lightweight Ti based bulk amorphous alloys also exhibit higher specific strengths than crystalline Ti alloys. For example, commercial Ti-6Al-4V exhibits a specific strength of 175 J/g, while bulk amorphous  $\text{Ti}_{45}\text{Zr}_{20}\text{Be}_{35}$  is calculated to have a specific strength of 405 J/g. The specific strength of Vitreloy 1 ( $\text{Zr}_{41.2}\text{Ti}_{13.8}\text{Ni}_{10}\text{Cu}_{12.5}\text{Be}_{22.5}$ ) is about 305 J/g. Thus, this class of amorphous alloys is ideal for structural applications where specific strength and specific modulus are key figures of merit.

In summary, lightweight Ti based bulk amorphous structural metals with low mass density comparable to that of pure titanium have been discovered. These amorphous alloys exhibit high GFA, exceptional thermal stability, and very high specific strength. The research results have important implications on designing and developing bulk metallic glasses.

The authors acknowledge the support from the MRSEC Program (Center for the Science and Engineering Materials, CSEM) of the National Science Foundation under Award Number DMR-0520565.

**Chapter 2 References**

- [1] W.L. Johnson, *MRS Bull.* 24 (1999) 42.
- [2] A. Inoue, *Acta Mater.* 48 (2000) 279.
- [3] A. Peker, W.L. Johnson, *Appl. Phys. Lett.* 63 (1993) 2342.
- [4] V. Ponnambalam, S.J. Poon, G.J. Shiflet, *J. Mater. Res.* 19 (2004) 1320.
- [5] V. Ponnambalam, S.J. Poon, G.J. Shiflet, *J. Mater. Res.* 19 (2004) 3046.
- [6] Z.P. Lu, C.T. Liu, J.R. Thompson, W.D. Porter, *Phys. Rev. Lett.* 92 (2004) 245503.
- [7] D.H. Xu, G. Duan, W.L. Johnson, C. Garland, *Acta Mater.* 52 (2004) 3493.
- [8] B. Zhang, D.Q. Zhao, M.X. Pan, W.H. Wang A.L. Greer, *Phys. Rev. Lett.* 94 (2005) 205502.
- [9] F.Q. Guo, S.J. Poon, G.J. Shiflet, *Appl. Phys. Lett.* 84 (2004) 37.
- [10] D.H. Xu, G. Duan, W.L. Johnson, *Phys. Rev. Lett.* 92 (2004) 245504.
- [11] F.Q. Guo, S.J. Poon, G.J. Shiflet, *Appl. Phys. Lett.* 83 (2003) 2575.
- [12] G. Duan, D.H. Xu, W.L. Johnson, *Metall. Mater. Trans. A* 36A (2005) 455.
- [13] F.Q. Guo, H.J. Wang, S.J. Poon, G.J. Shiflet, *Appl. Phys. Lett.* 86 (2005) 091907.
- [14] F.Q. Guo, S.J. Poon, X.F. Gu, G.J. Shiflet, *Scripta Mater.* 56 (2007) 689.
- [15] G. Duan, D.H. Xu, Q. Zhang, G.Y. Zhang, T. Cagin, W.L. Johnson, W.A. Goddard, *Phys. Rev. B* 71 (2005) 224208.
- [16] A.J. Peker, W.L. Johnson, US Patent #5288344.
- [17] M.L. Lind, G. Duan, W.L. Johnson, *Phys. Rev. Lett.* 97 (2006) 015501.
- [18] C.L. Ma, S. Ishihara, H. Soejima, N. Nishiyama, A. Inoue, *Mater. Trans.* 45 (2004) 1802.
- [19] H. Men, S.J. Pang, A. Inoue, T. Zhang, *Mater. Trans.* 46 (2005) 2218.
- [20] J.J. Oak, D.V. Louzguine-Luzgin, A. Inoue, *J. Mater. Res.* 22 (2007) 1346.
- [21] L.E. Tanner, R. Ray, *Scripta Metall.* 11 (1977) 783.
- [22] R. Hasegawa, L.E. Tanner, *Phys. Rev. B* 16 (1977) 3925.
- [23] L.E. Tanner, R. Ray, *Acta Metall.* 27 (1979) 1727.
- [24] L.E. Tanner, R. Ray, *Scripta Metall.* 14 (1980) 657.
- [25] G. Duan, M.L. Lind, K. De Blauwe, A. Wiest, W.L. Johnson, *Appl. Phys. Lett.* 90 (2007) 211901.

### **Chapter 3 - ZrTi Based Be Bearing Glasses Optimized for High Thermal Stability and Thermoplastic Formability**

We flesh out the details of the alloy development story in this chapter with a thorough exploration of the ZrTiBe system and the large  $\Delta T$  quaternary compositions. This chapter draws heavily on the article “ZrTi based Be bearing glasses optimized for high thermal stability and thermoplastic formability” published in Acta Materialia [A. Wiest, G. Duan, M.D. Demetriou, L.A. Wiest, A. Peck, G. Kaltenboeck, B. Wiest, W.L. Johnson, Acta Mater. 56 (2008) 2625].

A new class of ZrTi based Be bearing (Vitreloy) glass forming compositions that exhibit high thermal stability and good glass forming ability is reported. Optimized ternary compositions were obtained by reexamining the ZrTiBe phase diagram for regions that produce glasses having high thermal stability and modest glass forming ability. By incorporating a fourth element in the optimized ternary compositions, quaternary alloys were obtained having thermal stabilities twice that of  $Zr_{41.2}Ti_{13.8}Ni_{10}Cu_{12.5}Be_{22.5}$  (Vitreloy 1) while exhibiting good glass forming abilities. Optimized quaternary alloys exhibiting critical casting thicknesses exceeding 15mm and thermal stabilities as high as 165 °C are reported herein. The good thermal stability of these alloys renders them attractive for forming processes that can be performed thermoplastically in the supercooled liquid region, in a manner similar to the forming of polymers.

#### **3.1 Introduction**

Over the last decade, families of bulk glass forming metallic systems exhibiting remarkable glass forming ability (GFA) have been discovered [1-3]. These relatively

new materials are known to exhibit attractive mechanical properties, including high (near theoretical) yield strengths, high elastic limits, and good wear resistance. More interestingly, the ability of amorphous metals to soften and flow upon relaxation at the glass transition gives rise to a viscoplastic flow behavior enabling unique forming capabilities that resemble those of plastics and conventional glasses [4-6]. Essentially, such thermoplastic forming ability arises as a result of the supercooled liquid thermal stability and fragility.

The liquid thermal stability can be defined as the resistance of a glassy sample to crystallize upon heating above the glass transition temperature,  $T_g$ , and is typically quantified by the temperature region bounded between  $T_g$  and  $T_x$ , i.e.,  $\Delta T = T_g - T_x$ , where  $T_x$  is the temperature at which a sample crystallizes at a certain heating rate. This temperature region is typically referred to as the supercooled liquid region (SCLR). The glass fragility ( $m$ ) is referred to as the steepness of the equilibrium temperature dependent viscosity at  $T_g$  [7]. Given that the viscosity of liquids is a hyper-Arrhenius function of temperature, one can reasonably assume that the higher the  $m$  and  $\Delta T$  for a given glass, the lower the accessible viscosities in the SCLR that could be utilized for forming.

Many forming processes have been attempted with metallic glasses in the SCLR. Micro and nano replication [8-9], powder consolidation [10], extrusion [11], and recently blow molding [12] have been demonstrated. These processes are collectively referred to as thermoplastic forming processes. The success and feasibility of these and similar processes are dependant on the processing time available at the accessible viscosities in the SCLR. Very few alloys are known to exhibit the combination of thermal stability and fragility necessary for successful thermoplastic forming. The most commonly used

alloys in thermoplastic forming applications are the fragile  $\text{Pd}_{43}\text{Ni}_{10}\text{Cu}_{27}\text{P}_{20}$  and  $\text{Pt}_{57.5}\text{Ni}_{5.3}\text{Cu}_{14.7}\text{P}_{22.5}$  glasses and the thermally stable  $\text{Zr}_{44}\text{Ti}_{11}\text{Cu}_{10}\text{Ni}_{10}\text{Be}_{25}$  (Vitreloy 1b), but even these alloys require high pressures and undergo only limited thermoplastic strains due to the high viscosities and limited processing times available.

In the present work, optimization of ZrTi based Be bearing glasses for large thermal stability is attempted. Measurement of the liquid fragility of these alloys will be the subject of future investigation. Several quaternary ZrTi based Be bearing glasses with high  $\Delta T$  and good GFA will be presented. The alloy optimization was approached by examining the ternary ZrTiBe system for compositions exhibiting large  $\Delta T$  and modest GFA. Some of the ternary compositions investigated here for bulk glass forming ability include those investigated previously by Tanner [13], who focused primarily on their amorphous ribbon forming ability. An appropriate fourth “solute element” at an optimum fraction was added to the ternary compositions, and in most cases, both  $\Delta T$  and glass forming were seen to increase until too high a concentration of solute precipitated additional phases. Late transition metals were found to be the optimum solute element. Ni was not considered a viable solute atom as ample evidence in the literature suggests that the NiTi rich quasicrystal is the first phase to nucleate in Vitreloy glasses, providing nucleation sites for other crystals that eventually crystallize the alloy [14-15]. This is the approach that led to the development of the recently reported  $\text{Zr}_{35}\text{Ti}_{30}\text{Cu}_{8.25}\text{Be}_{26.75}$  alloy [16], having  $\Delta T = 159$  °C and a processing viscosity prior to crystallization of  $\sim 10^4$  Pa-s.

### **3.2 Experimental Method**

Alloys were prepared using elements of >99.9% purity. The elements were weighed to within  $\pm 0.1\%$  of the calculated mass to ensure accurate compositions, and

were ultrasonically cleaned in acetone and ethanol prior to melting. Typically 6 g ingots were arc melted on a Cu plate in a Ti-gettered argon atmosphere and flipped at least three times to ensure chemical homogeneity. The mass was again measured after melting to ensure proper composition, and alloys with greater than  $\pm 0.1\%$  deviation from the originally weighed mass were discarded.

Rods were cast under an argon atmosphere using an Edmund Buhler mini arc melter suction casting setup or by injecting inductively molten alloy from quartz nozzles into a copper mold. The largest diameter rod for which each alloy casts fully amorphous is reported as critical casting thickness or GFA. The amorphous nature of the rods was verified using a Philips X'Pert Pro X-ray Diffractometer and thermodynamic data was collected in graphite crucibles at 20 K/min using a Netzsch 404C Pegasus Differential Scanning Calorimeter (DSC).  $T_g$ ,  $T_x$ , solidus temperature ( $T_s$ ), liquidus temperature ( $T_L$ ) and enthalpy of crystallization ( $\Delta H_x$ ) are reported.

Casting techniques introduced a large variability into the DSC results. Thermodynamic data is reported from DSC scans of mini arc melter cast specimens. For different segments of a mini arc melter cast rod (top, middle, bottom), there was less than 3 °C variation in  $T_g$ ,  $T_x$ ,  $T_s$ , and  $T_L$ , while  $\Delta H_x$  showed less than 5% variability. Variability between rods of the same alloy cast using identical casting methods was also minimal. Critical casting measurements necessitated the use of die casting into large diameter copper molds. Die casting from quartz nozzles into copper molds occasionally lowered the  $T_x$  value by as much as 10 °C and larger diameter rods were seen to have lower  $T_g$  values than smaller diameter rods. Error bars are  $\pm 3$  °C on temperatures and  $\pm 5\%$  on  $\Delta H_x$ .

### 3.3 Results and Discussion

The ZrTiBe system was investigated in the 1970s by Tanner, who discovered that amorphous ribbons (10-100 $\mu$ m thick) could be produced by means of melt spinning at cooling rates of  $10^5$  -  $10^6$  K/s [17]. Ternary phase diagrams showing isothermal sections of the composition space are published, but very little of the thermodynamic data on the glasses is available [18].

In this study, many of the alloys reported to be glassy ribbons were recreated, primarily those in the low melting temperature regions given by the isothermal cross section phase diagrams. Several bulk glasses with critical casting thicknesses between 1mm and 6mm were identified from those compositions. Bulk GFA regions are shown in Figure 3.1. The ternary phase diagram showing the Tanner glassy ribbons region is presented in Figure 3.2. Twenty-two bulk glass forming compositions are outlined in the diagram. The thermodynamic data for these compositions are listed in Table 3.1.

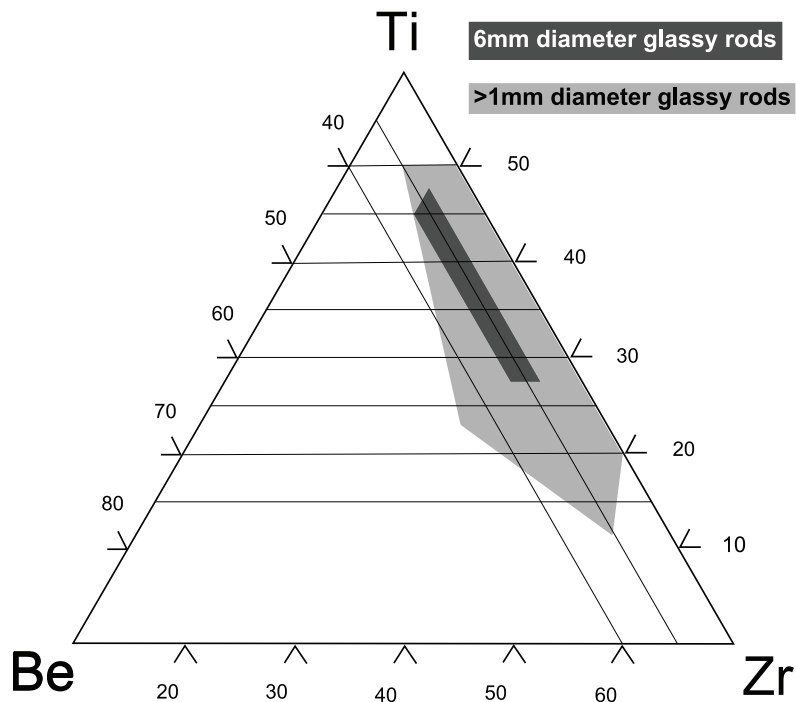


**Figure 3.1:** Bulk glass forming regions shown on ZrTiBe phase diagram.

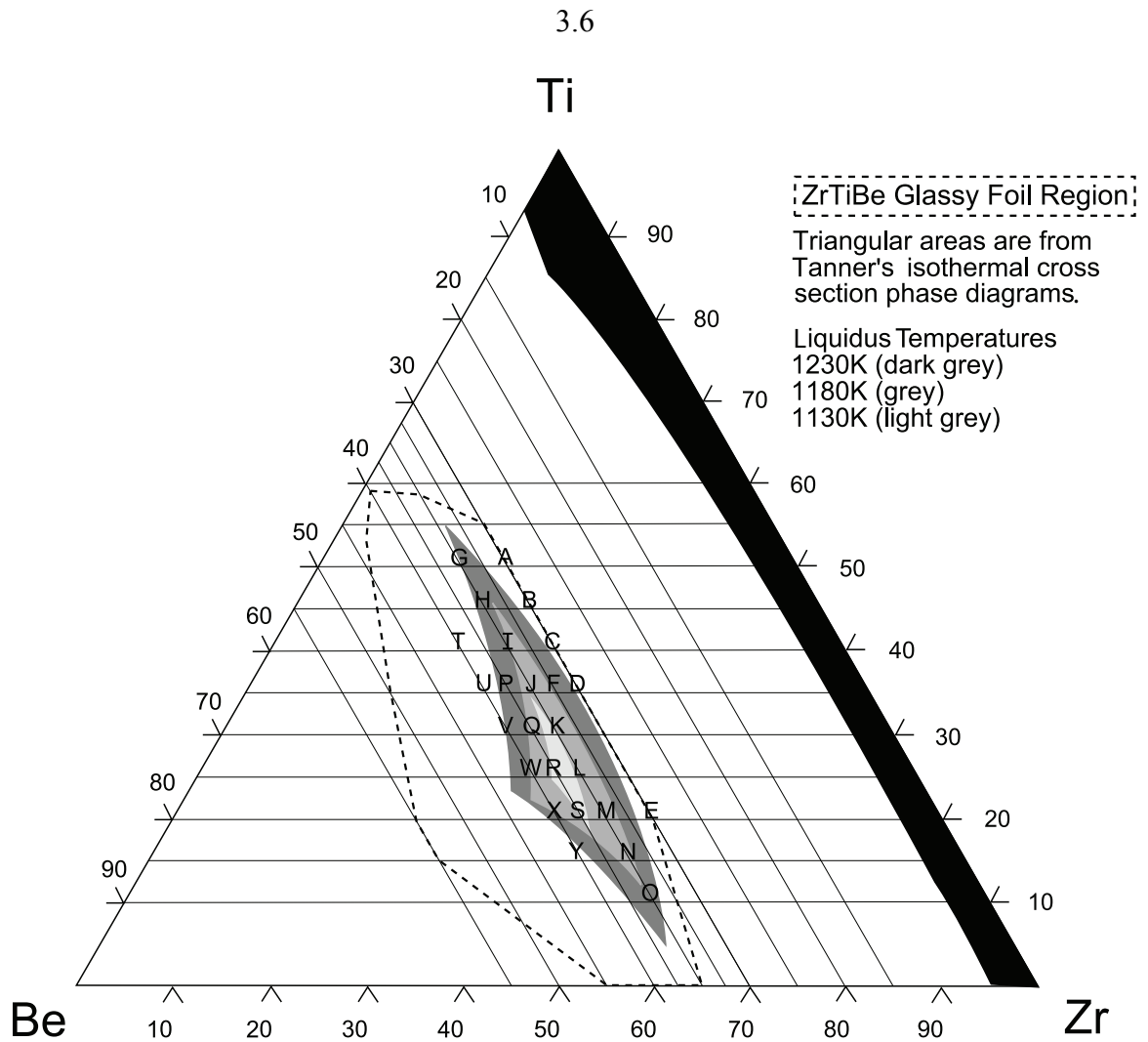


**Figure 3.2:** Ternary ZrTiBe phase diagram showing the region originally explored by Tanner for ribbon forming glasses (dashed line), the isothermal cross sections showing the liquid phase at various temperatures (shaded triangles), and the alloys recreated in this experiment (letters).

Alloys H, I, J and K are found to have a critical casting thickness of 6mm [19].

This is rather surprising, considering the extensive investigation previously performed in this system. The work of Peker and Johnson [20] indicates that addition of at least one late transition metal was necessary to form a bulk glass in this system. Tanner on the other hand, explored the ZrTiBe system and concluded that glass formation required cooling rates of  $10^5 - 10^6$  K/s, which limited the dimension of amorphous samples to  $\sim 100\mu\text{m}$  thick. The presence of bulk glass formers in the ternary system facilitated the

optimization of quaternary alloys for large  $\Delta T$  by allowing a large range of additional elements to be added without concern for GFA.

**Table 3.1:** Thermodynamic data of the alloys listed in Figure 3.2.

Alloy	Composition	$T_g$ [C]	$T_{x1}$ [C]	$T_{x2}$ [C]	$\Delta T$	$\Delta H_x$ [J/mol]	$T_s$ [C]	$T_L$ [C]	GFA
A	Zr <sub>20</sub> Ti <sub>50</sub> Be <sub>30</sub>	288.2	331.4	464.9	43.2	5610	829	>950	>1mm
B	Zr <sub>25</sub> Ti <sub>45</sub> Be <sub>30</sub>	308	348.1	454.2	40.1	4121	846	850.2	>1mm
C	Zr <sub>30</sub> Ti <sub>40</sub> Be <sub>30</sub>	293.7	339.2	439.5	45.5	6177	838	848.9	>1mm
D	Zr <sub>35</sub> Ti <sub>35</sub> Be <sub>30</sub>	292.2	349	431.3	56.8	6244	842	853.5	>1mm
E	Zr <sub>50</sub> Ti <sub>20</sub> Be <sub>30</sub>	292.3	362.9	422.3	70.6	6003	881	>900	>1mm
F	Zr <sub>32.5</sub> Ti <sub>35</sub> Be <sub>32.5</sub>	299.4	378.5	444.6	79.1	6477	870	922.1	>1mm
G	Zr <sub>15</sub> Ti <sub>50</sub> Be <sub>35</sub>	313.4	366.1	503.2	52.7	5484	830	914.5	>0.5mm
H	Zr <sub>20</sub> Ti <sub>45</sub> Be <sub>35</sub>	319.9	380.5	481.2	60.6	6265	836	848.5	6mm
I	Zr <sub>25</sub> Ti <sub>40</sub> Be <sub>35</sub>	322.3	401.7	469.8	79.4	6690	845	850.6	6mm
J	Zr <sub>30</sub> Ti <sub>35</sub> Be <sub>35</sub>	308	412.8	454	105	6964	838	845	6mm
K	Zr <sub>35</sub> Ti <sub>30</sub> Be <sub>35</sub>	319	439.2	-	120	6284	849	861.5	6mm
L	Zr <sub>40</sub> Ti <sub>25</sub> Be <sub>35</sub>	300.2	409	429	109	5796	838	934.3	>1mm
M	Zr <sub>45</sub> Ti <sub>20</sub> Be <sub>35</sub>	304.7	402.7	423.4	98	6421	877	>950	>1mm
N	Zr <sub>50</sub> Ti <sub>15</sub> Be <sub>35</sub>	302.4	398	418	95.6	6613	879	>950	>1mm
O	Zr <sub>55</sub> Ti <sub>10</sub> Be <sub>35</sub>	306.9	389.4	415.1	82.5	6747	905	>950	>0.5mm
P	Zr <sub>27.5</sub> Ti <sub>35</sub> Be <sub>37.5</sub>	317.4	440.2	456.5	123	7167	833	843	>1mm
Q	Zr <sub>32.5</sub> Ti <sub>30</sub> Be <sub>37.5</sub>	314.2	427.5	441.8	113	6469	837	846.8	>1mm
R	Zr <sub>37.5</sub> Ti <sub>25</sub> Be <sub>37.5</sub>	314.1	413.2	431.4	99.1	6800	831	857.7	>1mm
S	Zr <sub>42.5</sub> Ti <sub>20</sub> Be <sub>37.5</sub>	314.8	405.4	424.4	90.6	6382	845	880.8	>1mm
T	Zr <sub>20</sub> Ti <sub>40</sub> Be <sub>40</sub>	314.3	433.2	488.8	119	6542	829	853	>0.5mm
U	Zr <sub>25</sub> Ti <sub>35</sub> Be <sub>40</sub>	322.2	444.7	449.6	123	7104	831	842.8	>1mm
V	Zr <sub>30</sub> Ti <sub>30</sub> Be <sub>40</sub>	330.1	447.4	-	117	6659	826	844.1	>1mm
W	Zr <sub>35</sub> Ti <sub>25</sub> Be <sub>40</sub>	325.5	432.4	-	107	6422	837	850	>1mm
X	Zr <sub>40</sub> Ti <sub>20</sub> Be <sub>40</sub>	324.8	415.9	-	91.1	6323	842	907.2	>1mm
Y	Zr <sub>45</sub> Ti <sub>15</sub> Be <sub>40</sub>	326.4	411.8	-	85.4	7242	880	>900	>1mm

Error bars are  $\pm 3$  °C on temperatures and  $\pm 5\%$  on  $\Delta H_x$ .

Many alloys with large  $\Delta T$  are found in the ternary system. The 20 K/min DSC scans of some of the ternary alloys are shown in Figure 3.3. It is interesting to note that the scans of the alloys of Figure 3.3 reveal a single exothermic peak following the glass transition, suggesting that these alloys tend to crystallize by simultaneous crystal growth. Many other alloys revealed a small additional exothermic event before or after the main

crystallization event indicating that for these alloys the crystallization was nearly simultaneous. It was found that replacing small fractions of Be with certain late transition metals in alloys that exhibited simultaneous or nearly simultaneous crystal growth had the most beneficial effect on increasing the thermal stability of the alloys.

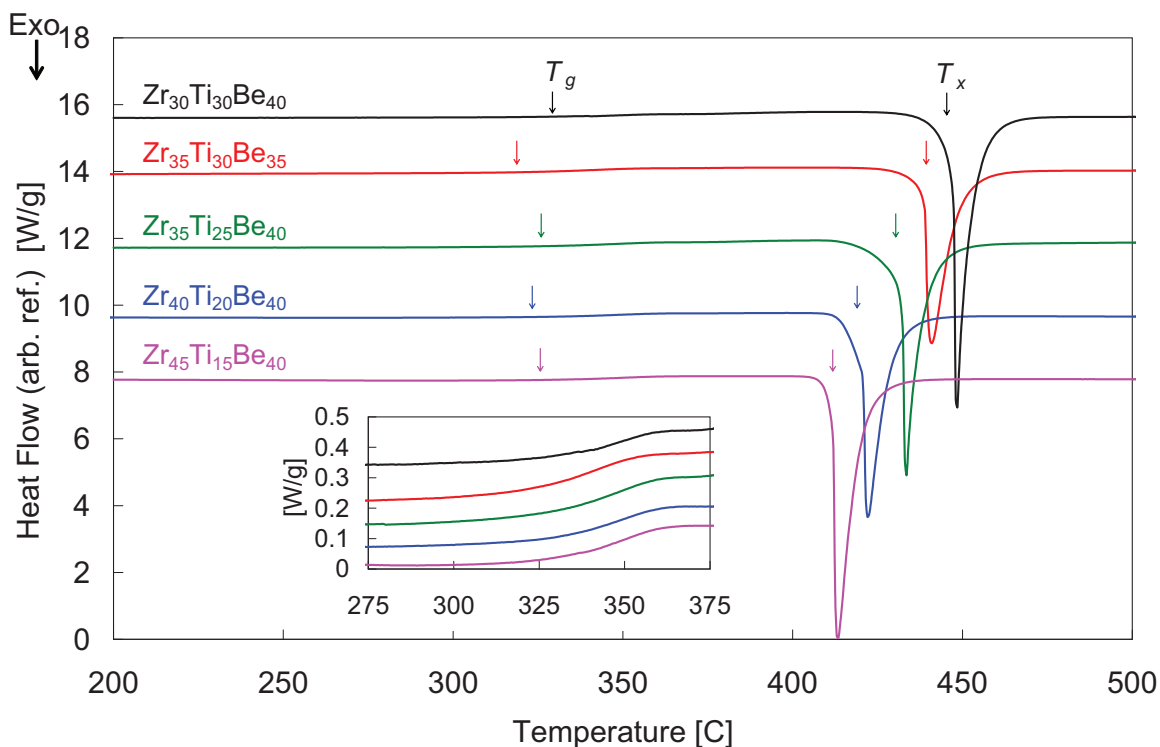


**Figure 3.3:** 20 K/min DSC scans of several alloys in the ternary ZrTiBe system. Crystallization is seen as a single exothermic peak suggesting that these alloys tend to crystallize by simultaneous crystal growth at that heating rate. Inset: Magnified view of glass transitions (temperature axes aligned); vertical order of alloys maintained.

### 3.3.1 Quaternary Alloys

Quaternary variants of Zr<sub>35</sub>Ti<sub>30</sub>Be<sub>35</sub> (Alloy K) were most thoroughly investigated because alloy K is in the best glass forming region and has the largest  $\Delta T$  while still exhibiting simultaneous crystal growth in a 20 K/min DSC scan. Al, Fe, Co, and Cu were substituted for Be and the effect on  $\Delta T$  was monitored. An increasing  $\Delta T$  resulted from additions of Fe, Co, and Cu until too high a concentration was reached. Table 3.2

lists the compositions and thermodynamic data for quaternary variants of Alloy K.

Figure 3.4 presents 20 K/min DSC scans showing the effect on thermal stability of

various additions of Cu, Co, and Fe.

**Table 3.2:** Thermodynamic data for quaternary variants of  $Zr_{35}Ti_{30}Be_{35}$  (Alloy K) obtained by substituting Cu, Co, Fe, Al for Be.

	$T_g$ [C]	$T_{x1}$ [C]	$T_{x2}$ [C]	$\Delta T$	$\Delta H_x$ (J/mol)	$T_s$ [C]	$T_L$ [C]	GFA
<b><math>Zr_{35}Ti_{30}Be_{35}</math> (Alloy K)</b>	319	439.2	-	120.2	6284	848.6	861.5	6mm
$Zr_{35}Ti_{30}Be_{30}Cu_5$	301.7	452.1	-	150.4	7549	674.5	841.2	>10mm
$Zr_{35}Ti_{30}Be_{27.5}Cu_{7.5}$	301.4	466.5	-	165.1	7446	674.4	797.5	>15mm
$Zr_{35}Ti_{30}Be_{26.75}Cu_{8.25}$	305	464	-	159	7444	674	771	>15mm
$Zr_{35}Ti_{30}Be_{25}Cu_{10}$	305.3	426.4	460.1	121.1	7449	672.4	756.7	>10mm
$Zr_{35}Ti_{30}Be_{33}Co_2$	311.1	447.8	-	136.7	7046	729	824.1	>3mm
$Zr_{35}Ti_{30}Be_{31}Co_4$	315.5	467.2	-	151.7	7418	724.7	801.9	>3mm
$Zr_{35}Ti_{30}Be_{29}Co_6$	324.1	476.2	-	152.1	7457	721.7	837.3	>15mm
$Zr_{35}Ti_{30}Be_{27.5}Co_{7.5}$	318.9	407.9	454.8	89	6154	717.8	813.7	>10mm
$Zr_{35}Ti_{30}Be_{33}Fe_2$	312.8	449.6	-	136.8	6796	770.6	827.6	>3mm
$Zr_{35}Ti_{30}Be_{31}Fe_4$	318.5	464.6	-	146.1	6297	759.4	800.5	>3mm
$Zr_{35}Ti_{30}Be_{29}Fe_6$	323.4	451.7	-	128.3	5810	747.8	842.8	>10mm
$Zr_{35}Ti_{30}Be_{27.5}Fe_{7.5}$	328.9	405.6	433.6	76.7	5370	758.2	817.8	>3mm
$Zr_{35}Ti_{30}Be_{30}Al_5$	329.3	459.6	-	130.3	6126	829.8	864.8	>3mm

Error bars are  $\pm 3$  °C on temperatures and  $\pm 5\%$  on  $\Delta H_x$ .

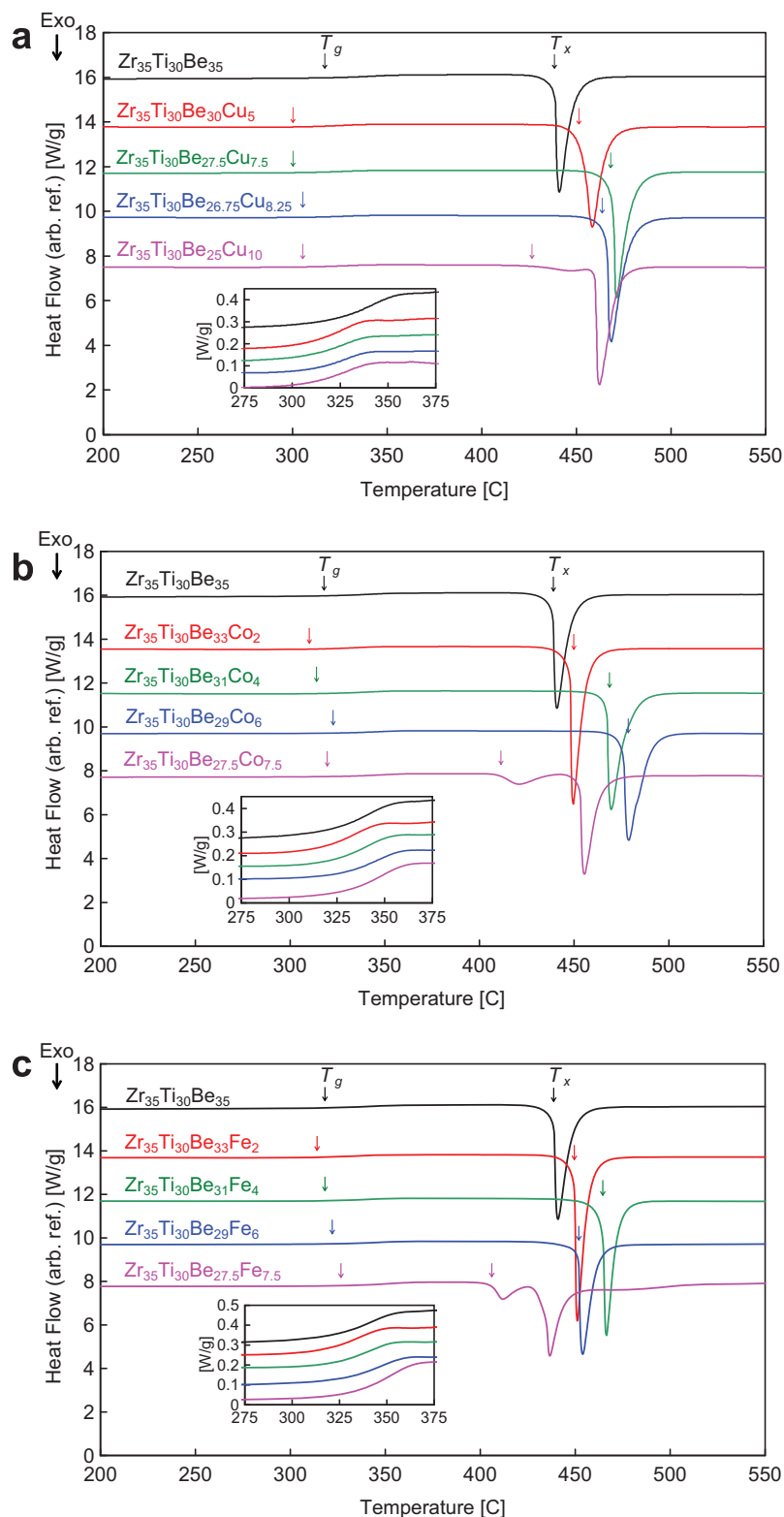


**Figure 3.4:** (a) The effect of Cu substitution for Be in  $Zr_{35}Ti_{30}Be_{35}$  (Alloy K). (b) The effect of Co substitution for Be in  $Zr_{35}Ti_{30}Be_{35}$  (Alloy K). (c) The effect of Fe substitution for Be in  $Zr_{35}Ti_{30}Be_{35}$  (Alloy K). All insets contain magnified view of glass transitions (temperature axes aligned) with vertical order of alloys maintained.

The largest  $\Delta T$  values for quaternary variants of alloy K were obtained by substituting Cu for beryllium (Figure 3.4a). The  $\Delta T$  value peaks at 165.1 °C for the alloy that has 7.5 atomic percent Cu. Co and Fe also increased  $\Delta T$  significantly, but Fe addition in alloy K was not as beneficial in terms of GFA. Since Cu was observed to have the greatest effect on GFA and  $\Delta T$ , Cu substitution for Be was performed in many of the large  $\Delta T$  ternary alloys near alloy K. Table 3.3 presents several examples of such quaternary alloys along with their thermodynamic data.

From Figure 3.4 and Tables 3.2 and 3.3 one can observe that there is an optimal late transition metal substitution for Be for each quaternary family. Substitutions smaller than optimal are shown to have a limited effect on GFA and minimally increase thermal stability, while substitutions larger than optimal tend to precipitate additional phases diminishing  $\Delta T$ . A summary of the alloys exhibiting the largest  $\Delta T$  from each of the quaternary families is presented in Figure 3.5.

**Table 3.3:** Thermodynamic data for quaternary variants of large  $\Delta T$  ternary compositions obtained by substituting Cu for Be.

	$T_g$ [C]	$T_{x1}$ [C]	$T_{x2}$ [C]	$\Delta T$	$\Delta H_x$ (J/mol)	$T_s$ [C]	$T_L$ [C]	GFA
<b>Zr<sub>40</sub>Ti<sub>25</sub>Be<sub>35</sub></b> <b>(Alloy L)</b>	300.2	409	429	108.8	5796	838	934.3	>1mm
Zr <sub>40</sub> Ti <sub>25</sub> Be <sub>29</sub> Cu <sub>6</sub>	306.5	454.9	-	148.4	7184	682.2	839.9	>10mm
Zr <sub>40</sub> Ti <sub>25</sub> Be <sub>27</sub> Cu <sub>8</sub>	306.2	464.3	-	158.1	7304	679.5	806.8	>10mm
Zr <sub>40</sub> Ti <sub>25</sub> Be <sub>25</sub> Cu <sub>10</sub>	306.2	470	-	163.8	6316	677.5	773.7	>10mm
Zr <sub>40</sub> Ti <sub>25</sub> Be <sub>23</sub> Cu <sub>12</sub>	308	389	464.5	81	9333	675.7	740.3	>10mm
<b>Zr<sub>27.5</sub>Ti<sub>35</sub>Be<sub>37.5</sub></b> <b>(Alloy P)</b>	317.4	440.2	456.5	123	7167	832.7	843	>1mm
Zr <sub>27.5</sub> Ti <sub>35</sub> Be <sub>29.5</sub> Cu <sub>8</sub>	317.7	455.4	-	137.7	5707	669.7	834.3	>10mm
<b>Zr<sub>32.5</sub>Ti<sub>30</sub>Be<sub>37.5</sub></b> <b>(Alloy Q)</b>	314.2	427.5	441.8	113.3	6469	836.8	846.8	>1mm
Zr <sub>32.5</sub> Ti <sub>30</sub> Be <sub>31.5</sub> Cu <sub>6</sub>	317.2	466.5	-	149.3	6976	673.1	>850	>10mm
Zr <sub>32.5</sub> Ti <sub>30</sub> Be <sub>29.5</sub> Cu <sub>8</sub>	314.5	471.9	-	157.4	8099	671.1	819.7	>10mm
Zr <sub>32.5</sub> Ti <sub>30</sub> Be <sub>27.5</sub> Cu <sub>10</sub>	314.6	474.2	-	159.6	8248	670.2	788	>10mm
Zr <sub>32.5</sub> Ti <sub>30</sub> Be <sub>25.5</sub> Cu <sub>12</sub>	317.1	409.1	456.2	92	7922	672.4	760.8	>10mm
<b>Zr<sub>37.5</sub>Ti<sub>25</sub>Be<sub>37.5</sub></b> <b>(Alloy R)</b>	314.1	413.2	431.4	99.1	6800	831.1	857.7	>1mm
Zr <sub>37.5</sub> Ti <sub>25</sub> Be <sub>27.5</sub> Cu <sub>10</sub>	310.8	470.9	-	160.1	7349	674.7	807	>10mm
<b>Zr<sub>30</sub>Ti<sub>30</sub>Be<sub>40</sub></b> <b>(Alloy V)</b>	330.1	447.4	-	117.3	6659	825.5	844.1	>1mm
Zr <sub>30</sub> Ti <sub>30</sub> Be <sub>32</sub> Cu <sub>8</sub>	318	462.8	-	144.8	6783	668.5	850	>1mm
Zr <sub>30</sub> Ti <sub>30</sub> Be <sub>30</sub> Cu <sub>10</sub>	322.8	467.2	-	144.4	5739	668.7	772.8	>10mm
Zr <sub>30</sub> Ti <sub>30</sub> Be <sub>27.5</sub> Cu <sub>12.5</sub>	323.1	442.7	-	119.6	7557	663.2	816.7	>10mm
<b>Zr<sub>35</sub>Ti<sub>25</sub>Be<sub>40</sub></b> <b>(Alloy W)</b>	325.5	432.4	-	106.9	6422	836.5	850	>1mm
Zr <sub>35</sub> Ti <sub>25</sub> Be <sub>32</sub> Cu <sub>8</sub>	323.3	462.2	-	138.9	7825	676.4	748	>10mm
Zr <sub>35</sub> Ti <sub>25</sub> Be <sub>30</sub> Cu <sub>10</sub>	321.8	472.9	-	151.1	8101	675.3	716	>10mm
Zr <sub>35</sub> Ti <sub>25</sub> Be <sub>28</sub> Cu <sub>12</sub>	323.1	470.8	-	147.7	8225	673	711.4	>10mm
<b>Zr<sub>40</sub>Ti<sub>20</sub>Be<sub>40</sub></b> <b>(Alloy X)</b>	324.8	415.9	-	91.1	6323	842.3	907.2	>1mm
Zr <sub>40</sub> Ti <sub>20</sub> Be <sub>26.25</sub> Cu <sub>13.75</sub>	316.3	467.6	-	151.3	7352	674.3	841.5	>10mm

Error bars are  $\pm 3$  °C on temperatures and  $\pm 5\%$  on  $\Delta H_x$ .

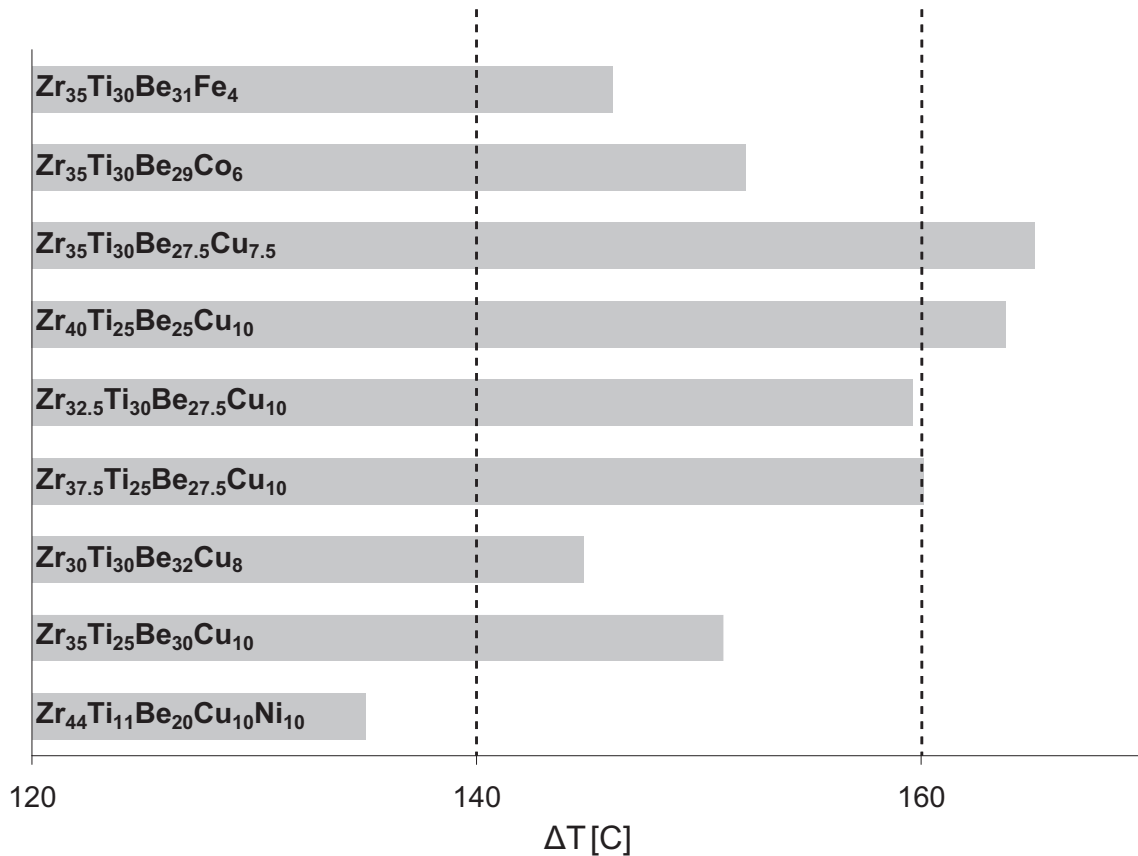


**Figure 3.5:** Bar graph showing the compositions with the largest  $\Delta T$  from each quaternary family. Alloys with  $\Delta T$  values as large as 165.1 °C are shown. Zr<sub>44</sub>Ti<sub>11</sub>Be<sub>25</sub>Cu<sub>10</sub>Ni<sub>10</sub> (Vitreloy 1b) is shown for reference.

### 3.4 Conclusion

An alloy development approach is presented, by which ZrTi based Be bearing bulk glass forming compositions were optimized for high thermal stability. From the optimization of the ternary ZrTiBe system, the following conclusions can be drawn:

- Several ternary bulk glass forming compositions were identified, capable of forming glasses with critical casting thicknesses exceeding 6mm.
- Several ternary glass forming compositions with thermal stabilities exceeding 120 °C were identified.

- The ternary alloys exhibiting good glass forming abilities and high thermal stabilities tend to undergo simultaneous or near-simultaneous crystal growth upon crystallization at 20 K/min heating rate.

The ternary alloy  $Zr_{35}Ti_{30}Be_{35}$  was found to exhibit the best combination of glass forming ability and thermal stability, and was singled out for development of high thermal stability quaternary compositions. The following conclusions can be drawn from the optimization of the quaternary alloys:

- High thermal stability quaternary glasses with good glass forming ability were obtained by substituting small fractions of Be (4 - 10 atomic percent) with late transition metals such as Cu, Co, Fe, and Al.
- Cu substitution of Be is found to yield quaternary alloys with the best combination of thermal stability and glass forming ability. For example,  $Zr_{35}Ti_{30}Be_{27.5}Cu_{7.5}$  is found to have a thermal stability exceeding 165 °C and a critical casting thickness greater than 15mm.
- The optimization strategy yielded twelve quaternary alloys with thermal stabilities >150 °C, three of which have thermal stabilities exceeding 160 °C.

Owing to the high thermal stability of their supercooled liquid states, these glasses are promising candidates for forming processes that can be performed thermoplastically in the SCLR. Furthermore, the high stability of the supercooled liquid states of these alloys will enable studies of liquid thermodynamics, rheology, atomic diffusion, and the glass transition to an extent previously not possible in metallic glass forming systems.

This alloy development strategy could be employed in other systems where ternary phase diagrams are known. Comparison of Figures 3.1 and 3.2 reveals that the

best glass formers in the ternary phase space were located near the lowest melting temperature region. Computer models designed to predict bulk glass forming compositions have enjoyed limited success to date. Perhaps the simplest approach would be to estimate ternary phase diagrams from known binary phase diagrams using a CALPHAD type approach and then check GFA of alloys near low melting temperature regions.

The authors thank the Office of Naval Research for their support of this work under ONR06-0566-22.

### Chapter 3 References

- [1] A.L. Greer, E. Ma, *MRS Bull.* 32 (2007) 611.
- [2] W.L. Johnson, *MRS Bull.* 24 (1999) 42.
- [3] A. Inoue, *Acta Mater.* 48 (2000) 279.
- [4] W.L. Johnson, *JOM* 54 (2002) 40.
- [5] J. Schroers, *JOM* 57 (2005) 35.
- [6] B. Zhang, D.Q. Zhao, M.X. Pan, W.H. Wang, A.L. Greer, *Phys. Rev. Lett.* 94 (2005) 205502.
- [7] C.A. Angell, *J. Non-Cryst. Solids* 131 (1991) 13.
- [8] J. Schroers, Q. Pham, A.J. Desai, *Micromech. Microeng.* 16 (2007) 240.
- [9] Y. Saotome, K. Imai, C. Shioda, S. Shimizu, T. Zhang, A. Inoue, *Intermetallics* 10 (2002) 1241.
- [10] J. Degmova, S. Roth, J. Eckert, H. Grahl, L. Schultz, *Mat. Sci. Eng. A* 375 (2004) 265.
- [11] K.S. Lee, Y.W. Chang, *Mat. Sci. Eng. A* 399 (2005) 238.
- [12] J. Schroers, Q. Pham, A. Peker, N. Paton, R.V. Curtis, *Scripta Mater.* 57 (2007) 341.
- [13] L.E. Tanner, R. Ray, *Acta Metall.* 27 (1979) 1727.
- [14] R.G. Hennig, A.E. Carlsson, K.F. Kelton, C.L. Henley, *Phys. Rev. B* 71 (2005) 144103.
- [15] B. Van de Moortele, T. Epicier, J.L. Soubeyroux, J.M. Pelletier, *Philos. Mag. Lett.* 84 (2004) 245.
- [16] G. Duan, A. Wiest, M.L. Lind, J. Li, W.K. Rhim, W.L. Johnson, *Adv. Mater.* 19 (2007) 4272.
- [17] L.E. Tanner, R. Ray, C.F. Cline, US Patent #4050931.
- [18] L. Kaufman, L.E. Tanner, *CALPHAD* 3 (1979) 91.
- [19] G. Duan, A. Wiest, M.L. Lind, A. Kahl, W.L. Johnson, *Scripta Mater.* 58 (2008) 465.
- [20] A. Peker, W.L. Johnson, *Appl. Phys. Lett.* 63 (1993) 2342.

## **Chapter 4 - Bulk Metallic Glass with Benchmark Thermoplastic Processability**

After discovering the large  $\Delta T$  alloys discussed in Chapter 3, we characterized the most promising of them to determine if we had made any improvements over other alloys used for thermoplastic forming (TPF). Two alloys were studied in parallel and are reported in this chapter. The data for the alloys is considered nearly interchangeable because of the similarity of compositions. The two compositions are  $Zr_{35}Ti_{30}Cu_{8.25}Be_{26.75}$  ( $\Delta T = 159$  K) and  $Zr_{35}Ti_{30}Cu_{7.5}Be_{27.5}$  ( $\Delta T = 165$  K). This chapter is based on a talk given at the MRS conference in Boston 2007 and an article entitled "Bulk Metallic Glass with Benchmark Thermoplastic Processability" [G. Duan, A. Wiest, M.L. Lind, J. Li, W.K. Rhim, and W.L. Johnson, *Adv. Mater.* 19 (2007) 4272] The article can be found at DOI: 10.1002/adma.200700969. The text has been changed in many places to reflect recent research and should be compared to the original document if all changes are of interest.

The exceptional processability and large supercooled liquid region (SCLR) of bulk amorphous metals makes them highly promising candidates for thermoplastic processing. We report a lightweight ( $\rho = 5.4$  g/cm<sup>3</sup>) quaternary glass forming alloy,  $Zr_{35}Ti_{30}Cu_{8.25}Be_{26.75}$ , having the largest supercooled liquid region,  $\Delta T = 159$  K (at 20 K/min heating rate) of any known bulk glass forming alloy. The alloy can be cast into fully amorphous rods of diameter = 1.5cm. The undercooled liquid exhibits an unexpectedly high Angell Fragility of  $m = 65.6$ . Based on these features, it is demonstrated that this alloy exhibits “benchmark” characteristics for thermoplastic processing. We report results of mechanical, thermal, rheological, and time temperature transformation (TTT) studies on this new material. The alloy exhibits high yield strength and excellent fracture toughness, and a relatively high Poisson’s ratio. Simple

microreplication experiments carried out in open air using relatively low applied pressures demonstrate superior thermoplastic processability for engineering applications. Chapter 5 will demonstrate a modified injection molding setup that allowed TPF with high strains.

Over the last two decades, the unique properties of bulk metallic glasses (BMG), such as high strength, high specific strength, large elastic strain limit, and excellent wear and corrosion resistances along with other remarkable engineering properties have made these materials of significant interest for science and industry [1-9]. Researchers have designed families of multi-component systems that form bulk amorphous alloys [4–9], among which Zr based (Vitreloy series) [4], and Pt based [8] BMG have been utilized commercially to produce items including sporting goods, electronic casings, medical devices, and fine jewelries.

The unique advantages of injection molding, blow molding, microreplication, and other thermoplastic technologies are largely responsible for the widespread uses of plastics such as polyethylene, polyurethane, PVC, etc., in a broad range of engineering applications. Powder injection molding of metals represents an effort to apply similar processing to metals, but requires blending of the powder with a plastic binder to achieve net shape forming and subsequent sintering of the powder. Given suitable materials, thermoplastic forming (TPF) would be the method of choice for manufacturing of net shape metallic glass components because TPF decouples the forming and cooling steps by processing glassy material at temperatures above the glass transition temperature ( $T_g$ ) and below the crystallization temperature ( $T_x$ ) followed by cooling to ambient temperature [10-11]. Conventional die casting requires rapid quenching to bypass the

crystallization nose, which limits the ability to make high quality casts and to create parts with complex geometries. Unfortunately, among the published metallic glasses none of the alloys used in TPF processes to date reach viscosities suitable to mimic polymer plastics formability with sufficient time to use conventional plastic processing techniques. Alloys in the expensive Pt and Pd based [8, 12-13] families have shown good thermoplastic formability reaching viscosities of around  $10^5$  Pa-s with sufficient time available for processing. Zr based metallic glasses are much less expensive than Pt and Pd based alloys. Unfortunately, Zr based BMG forming alloys have low fragilities, and low processing viscosities are only attainable in the SCLR [14-15] with alloys having large  $\Delta T$ . Strain rate effects on viscosity of amorphous alloys have been extensively studied [16-17].

An alloy optimal for TPF should have good glass forming ability, low viscosity / high fragility in the SCLR, a low processing temperature, and a long processing time at that temperature before crystallization. We studied Be bearing ZrTi based quaternary metallic glasses with compositions in the range of  $60\% \leq \text{Zr} + \text{Ti} \leq 70\%$ . We found that compared with Vitreloy alloys ( $\text{Zr} + \text{Ti} = 55\%$ ),  $T_g$  is lowered, the liquid appears to become more fragile, and the SCLR is increased. The apparent increase in fragility may be due to two phase flow effects that are further discussed in Chapter 6. Two composition regions were found with alloys that exhibit exceptional properties for TPF in the  $\text{Zr}_a\text{Ti}_b\text{Cu}_c\text{Be}_d$  system. These were  $a \approx b$  with  $c \leq 12.5\%$ , and  $a \approx 5b$  with  $d \geq 20\%$ . DSC curves of three representative alloys are presented in Figure 4.1. The alloys all exhibit a very large SCLR with a single sharp crystallization peak at which the alloy undergoes massive crystallization to a multiphase crystalline product.

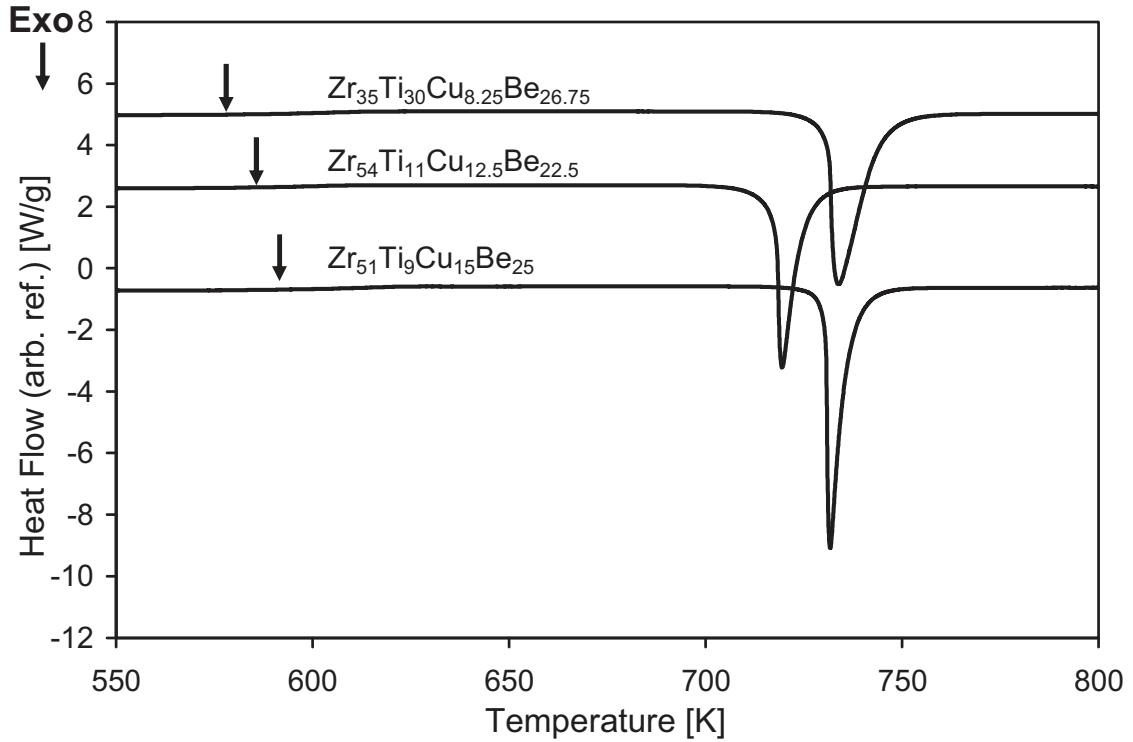


**Figure 4.1:** DSC scans of three typical bulk metallic glasses with excellent glass forming ability and extremely high thermal stability. The marked arrows represent the glass transition temperatures.

The 5 gram samples were generally found to freeze without any crystallization during preparation resulting in a glassy ingot. The  $Zr_{35}Ti_{30}Cu_{8.25}Be_{26.75}$  alloy can be cast into fully amorphous rods of diameter = 1.5cm. The amorphous nature of all the samples studied in this work has been confirmed by X-ray diffraction. A summary of thermal properties of these BMG is listed in Table 4.1 and compared with several earlier reported amorphous alloys.[4, 7-8, 12, 18–21] The variations of SCLR,  $\Delta T$  ( $\Delta T = T_x - T_g$ , in which  $T_x$  is the onset temperature of the first crystallization event), and reduced glass transition temperature  $T_{rg}$  ( $T_{rg} = T_g/T_L$ , where  $T_L$  is the liquidus temperature) are calculated. In the three newly designed alloys,  $Zr_{35}Ti_{30}Cu_{8.25}Be_{26.75}$  exhibits the lowest  $T_g$  (578 K and about 45 K lower than that of Vitreloy 1 or Vitreloy 4) and the largest  $\Delta T$

(159 K). It was further found that  $\Delta T$  of the same glass can be enlarged to be 165 K by addition of 0.5% Sn, giving the largest SCLR reported for any known bulk metallic glass.

**Table 4.1:** Thermal, mechanical, and rheological properties of various BMG forming alloys.

Material	$T_g$ [K]	$T_x$ [K]	$T_L$ [K]	$\Delta T$ [K]	$T_{rg}$ [K]	m	s	$m^* \Delta T^*_{rx}$	G [Gpa]	Y [Gpa]	$\nu$
Zr <sub>51</sub> Ti <sub>9</sub> Cu <sub>15</sub> Be <sub>25</sub>	592	730	1047	138	0.565	-	0.30	-	31.8	86.5	0.36
Zr <sub>54</sub> Ti <sub>11</sub> Cu <sub>12.5</sub> Be <sub>22.5</sub>	581	721	1035	140	0.561	-	0.31	-	30.3	82.8	0.37
Zr <sub>35</sub> Ti <sub>30</sub> Cu <sub>8.25</sub> Be <sub>26.75</sub>	578	737	1044	159	0.554	65.6	0.34	20.3	31.8	86.9	0.37
Zr <sub>41.2</sub> Ti <sub>13.8</sub> Ni <sub>10</sub> Cu <sub>12.5</sub> Be <sub>22.5</sub>	623	712	993	89	0.627	49.9	0.24	8.0	37.4	101.3	0.35
Zr <sub>46.75</sub> Ti <sub>8.25</sub> Ni <sub>10</sub> Cu <sub>7.5</sub> Be <sub>27.5</sub>	625	738	1185	113	0.527	44.2	0.20	10.0	35.0	95.0	0.35
Pd <sub>43</sub> Ni <sub>10</sub> Cu <sub>27</sub> P <sub>20</sub>	575	665	866	90	0.664	58.5	0.31	12.3	33.0	92.0	0.39
Pt <sub>60</sub> Ni <sub>15</sub> P <sub>25</sub>	488	550	804	60	0.596	67.2	0.17	12.5	33.8	96.1	0.42
Ce <sub>68</sub> Cu <sub>20</sub> Al <sub>10</sub> Nb <sub>2</sub>	341	422	643	81	0.530	-	0.26	-	11.5	30.3	0.31
Au <sub>49</sub> Ag <sub>5.5</sub> Pd <sub>2.3</sub> Cu <sub>26.9</sub> Si <sub>16.3</sub>	401	459	644	58	0.623	-	0.24	-	26.5	74.4	0.41
Pt <sub>57.5</sub> Ni <sub>5.3</sub> Cu <sub>14.7</sub> P <sub>22.5</sub>	508	606	795	98	0.639	-	0.34	-	33.4	95.7	0.43

In Figure 4.2, the temperature dependence of equilibrium Newtonian viscosity of Zr<sub>35</sub>Ti<sub>30</sub>Cu<sub>8.25</sub>Be<sub>26.75</sub> and several other metallic glass forming liquids with different Angell fragility numbers [22] are presented. The solid curve represents a Vogel-Fulcher-Tammann (VFT) fit to the viscosity data of Zr<sub>35</sub>Ti<sub>30</sub>Cu<sub>8.25</sub>Be<sub>26.75</sub>:

$$\eta = \eta_0 \exp\left(\frac{D^* * T_0}{T - T_0}\right)$$

where  $\eta_0$ ,  $D^*$ , and  $T_0$  are fitting constants.  $T_0$  is the VFT temperature and  $\eta_0 \approx 10^{-5}$  Pa-s. In the best fit,  $T_0 = 422.6$  K and  $D^* = 12.4$  are found, which yields an Angell fragility number of  $m = 65.6$ . This high fragility value could be a result of the two  $T_g$  relaxation phenomenon that will be presented in Chapter 6. No viscosity data near  $T_g$  was collected so the VFT fit used to calculate fragility, which is the slope of the  $\text{Log}[\eta(T/T_g)]$  curve at  $T_g$  (see Derivation 5), may be off. The fragility calculated from the VFT fit is quite high

when compared to fragilities for other Vitreloy glasses which are typically in the range of  $m = 30 - 40$  [23]. If we fit the data using the viscosity formula based on metallic glass physics proposed by Johnson [23] and detailed in Derivation 5 we find that  $m = 40$  and  $T_g = 539$  K. The value for  $T_g$  calculated using the Johnson formula is close to the  $T_g$  measured at 20 K/min in the DSC = 578 K and the fragility is more in line with what would be expected for a Vitreloy type alloy.

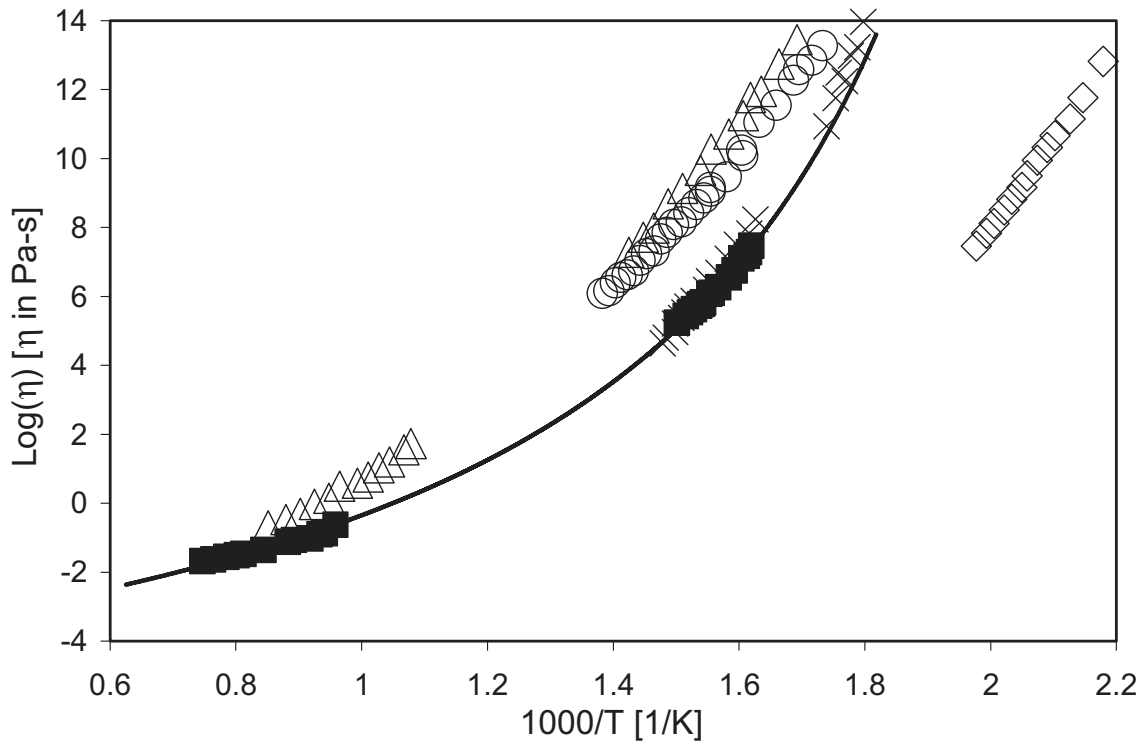


**Figure 4.2:** The temperature dependence of equilibrium viscosity of several metallic glass forming liquids:  $Zr_{41.2}Ti_{13.8}Ni_{10}Cu_{12.5}Be_{22.5}$  (Vitreloy 1) ( $\Delta$ );  $Zr_{46.25}Ti_{8.25}Cu_{7.5}Ni_{10}Be_{27.5}$  (Vitreloy 4) ( $\circ$ );  $Zr_{35}Ti_{30}Cu_{8.25}Be_{26.75}$  ( $\blacksquare$ );  $Pd_{43}Ni_{10}Cu_{27}P_{20}$  ( $\times$ );  $Pt_{60}Ni_{15}P_{25}$  ( $\diamond$ ). It is shown that the viscosity of  $Zr_{35}Ti_{30}Cu_{8.25}Be_{26.75}$  in the thermoplastic processing region is at least two orders of magnitude lower than that of Vitreloy 1 or Vitreloy 4 and is comparable to that of Pd based metallic glass and polymer glasses.

The Angell fragility parameters of Vitreloy series, Pd based, and Pt based metallic glass forming liquids [19, 24-25] are listed in Table 4.1 as well.  $Zr_{35}Ti_{30}Cu_{8.25}Be_{26.75}$  shows rather fragile behavior compared with the strong Vitreloy series of liquids. Its viscosity in the thermoplastic zone is at least two orders of magnitude lower than that of

Vitreloy 1 or Vitreloy 4 at the same temperature and is comparable to that of Pd based metallic glass. For example, the equilibrium viscosity at 683 K for  $Zr_{35}Ti_{30}Cu_{8.25}Be_{26.75}$  is measured to be only  $8 \cdot 10^4$  Pa-s, similar to that of viscous polymer melts [26]. As is known from the processing of thermoplastics, the formability is inversely proportional to viscosity. This alloy's low viscosity in the SCLR will result in a low Newtonian flow stress and high formability.

Recently, the normalized thermal stability,  $S$ , which is defined as  $\Delta T / (T_L - T_g)$ , was introduced to characterize the thermoplastic formability [10]. As indicated in Table 4.1,  $Zr_{35}Ti_{30}Cu_{8.25}Be_{26.75}$  demonstrates an  $S$  value of 0.34, which is higher than that of all the other alloys and is as good as  $Pt_{57.5}Cu_{14.7}Ni_{5.3}P_{22.5}$ . Because the  $S$  parameter is based on an oversimplified assumption of identical viscosity at  $T_L$ , a deformability parameter,  $d^* = \text{Log}[\eta(T_g^*) / \eta(T_x)]$  [19] was also proposed and correlated with Angell fragility ( $m$ ) and the reduced thermal stability,  $\Delta T_{rx}^* = (T_x - T_g^*) / T_g^*$ , where  $T_g^*$  is the glass transition temperature at which the viscosity is  $10^{12}$  Pa-s. Table 4.1 lists the calculated  $m \cdot \Delta T_{rx}^*$  values for  $Zr_{35}Ti_{30}Cu_{8.25}Be_{26.75}$ , Vitreloy 1, Vitreloy 4,  $Pd_{43}Ni_{10}Cu_{27}P_{20}$ , and  $Pt_{60}Ni_{15}P_{25}$  based on the measured viscosity data. It is seen clearly that  $Zr_{35}Ti_{30}Cu_{8.25}Be_{26.75}$  shows the largest  $m \cdot \Delta T_{rx}^*$ , which implies a superior thermoplastic workability.

In Figure 4.3, we present the measured TTT curve for  $Zr_{35}Ti_{30}Cu_{8.25}Be_{26.75}$  and other Vitreloy series alloys [27]. The TTT curve indicates a nose shape, with the minimum crystallization time of about 3 - 10 s occurring somewhere between 700 K and 950 K. The data on the bottom part of the nose was collected by heating the metallic glass from room temperature. The data on the top part of the nose was obtained by cooling the material from the melt. Because of insufficient GFA, the bottom part of the

cooling TTT curve was inaccessible with the cooling rates available to us. Both sets of data are shown on the same graph for convenience. At 683 K, where the equilibrium viscosity is about  $8 \cdot 10^4$  Pa-s, a 600 s thermoplastic processing window is available for forming.

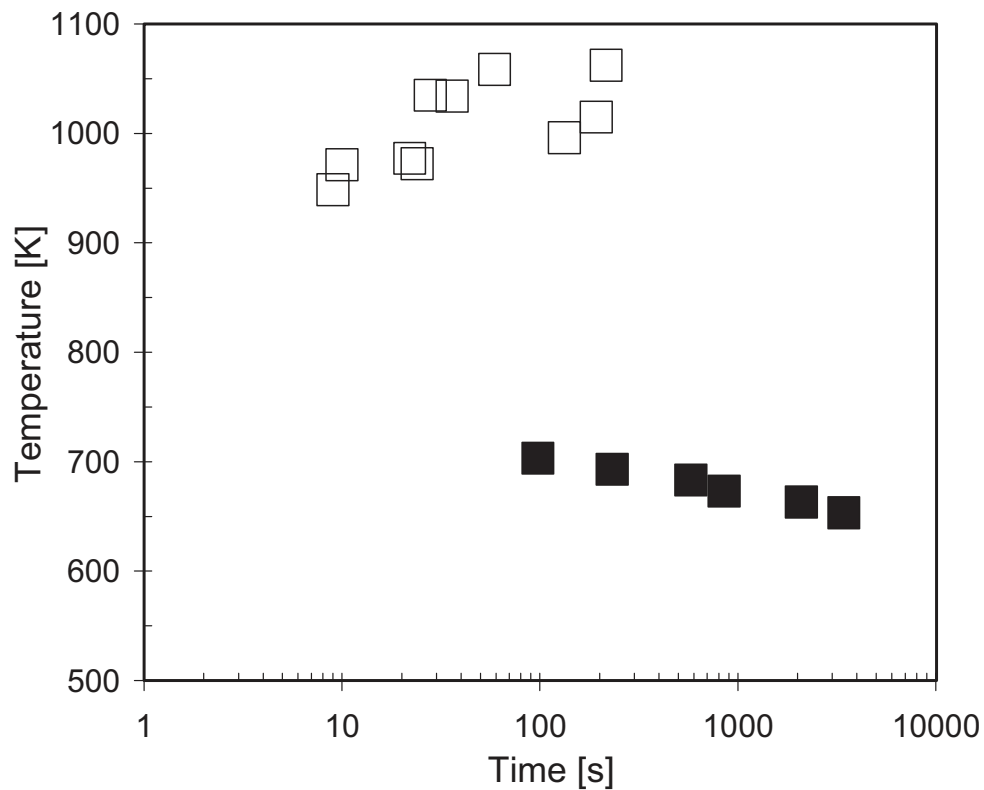


**Figure 4.3:** TTT diagrams for  $Zr_{35}Ti_{30}Cu_{8.25}Be_{26.75}$  upon heating (■), and cooling (□). The data were measured by electrostatic levitation for cooling measurements. TTT upon heating measurements were done by processing in graphite crucibles after heating from the amorphous state. At 683 K, where the equilibrium viscosity is about  $8 \cdot 10^4$  Pa-s, a 600 s thermoplastic processing window is available.

To demonstrate the strong thermoplastic processability of the  $Zr_{35}Ti_{30}Cu_{8.25}Be_{26.75}$  glassy alloy, we carried out plastic forming experiments as shown in Figure 4.4. The thermoplastic processing was done on a Tetrahedron hot press machine in air at a pressure of 25 MPa with a processing time of 45 s, followed by a water quenching step. Figure 4.4 shows the microformed impression of a United States dime (Figure 4.4b) made on TPF metallic glass ingots at about 643 K (Figure 4.4a). Minimal oxidation was

observed after processing, which is consistent with the strong oxidation resistance of Be bearing amorphous alloys. The final parts remain fully amorphous as verified by X-ray diffraction. It is found from the Rockwell hardness tests that no degradation of the mechanical properties was caused by the thermoplastic processing. Before the TPF was carried out, we produced diamond shaped microindentation patterns ( $\sim 100\mu\text{m}$ ) in the top flame of the dime using a Vickers hardness tester (Figure 4.4c). Figure 4.4d presents the successfully replicated diamond pattern in the final part. Even the scratches (on the level of several  $\mu\text{m}$ ) on the original dime are clearly reproduced. Although the induced strain was small, replication of small features is shown.

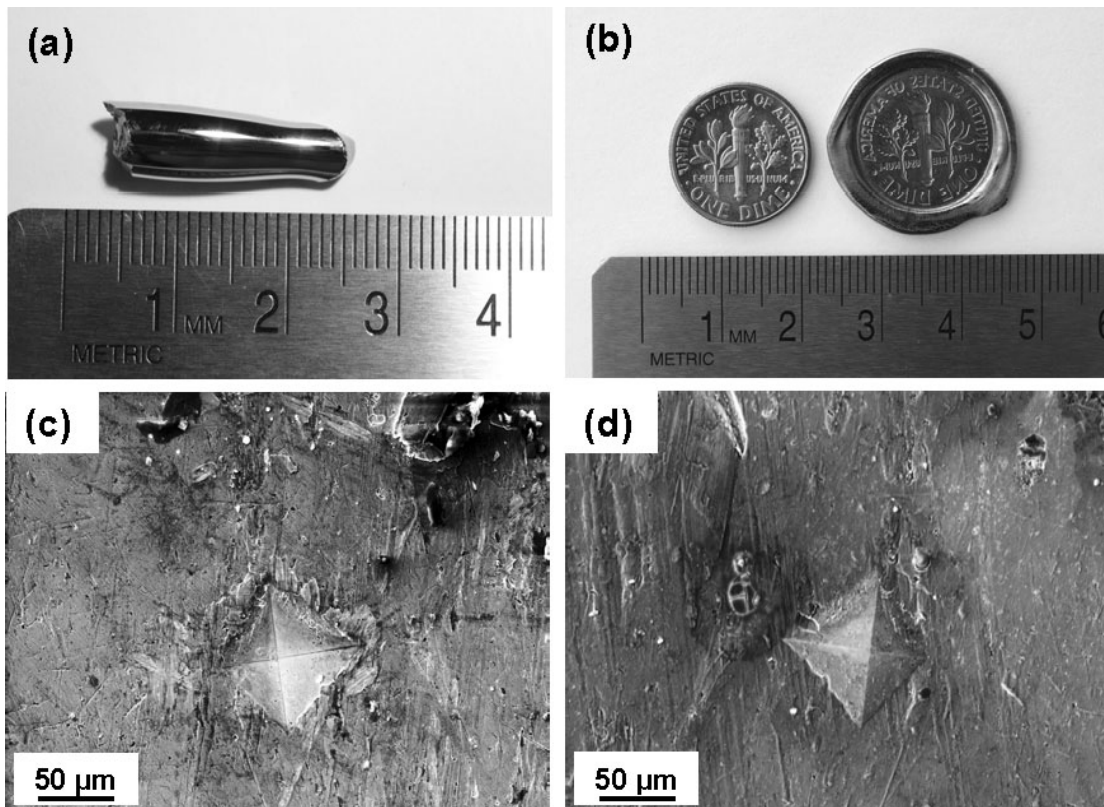
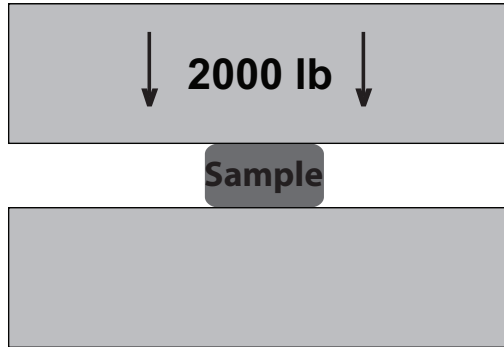


**Figure 4.4:** Demonstration of the strong thermoplastic processability of the  $\text{Zr}_{35}\text{Ti}_{30}\text{Cu}_{8.25}\text{Be}_{26.75}$  metallic glass. The ingot in (a) is pressed over a dime at 643 K for 45 s at 25 MPa to form the negative imprint of a United States dime shown in (b). A diamond shaped microindentation pattern was placed in the flame on the dime (c) and was successfully replicated in the negative imprint (d) as well.

#### 4.10

The imprinting and microreplication test on the dime required minimal thermoplastic strain. However, many TPF processes like injection molding require large strains to move material from a reservoir to a mold cavity. We used a method proposed by Schroers [28] to compare glassy alloys commonly used in TPF processes with the newly developed large  $\Delta T$  alloy for TPF processes requiring large strains. The method proposed by Schroers involves applying a constant force to a known volume of each alloy through the SCLR at a constant heating rate. We chose a force of 2000 lbs, 10 K/min heating rate, and  $0.1\text{cm}^3$  of each alloy. The alloys of interest were  $\text{Pd}_{43}\text{Ni}_{10}\text{Cu}_{27}\text{P}_{20}$ ,  $\text{Pt}_{57.5}\text{Ni}_{5.3}\text{Cu}_{14.7}\text{P}_{22.5}$ ,  $\text{Zr}_{41.2}\text{Ti}_{13.8}\text{Cu}_{12.5}\text{Ni}_{10}\text{Be}_{22.5}$  (Vitreloy 1), and  $\text{Zr}_{44}\text{Ti}_{11}\text{Cu}_{10}\text{Ni}_{10}\text{Be}_{25}$  (Vitreloy 1b). Schroers squish test is depicted in Figure 4.5 along with pictures of the squished alloys and a table of the results.

## Formability Characterization



Process in entire  $\Delta T$  region  
 $T_g < T < T_x$

$dT/dt = 10 \text{ K/min}$

Sample size =  $0.1 \text{ cm}^3$

Final Diameter indicates  
 thermoplastic formability

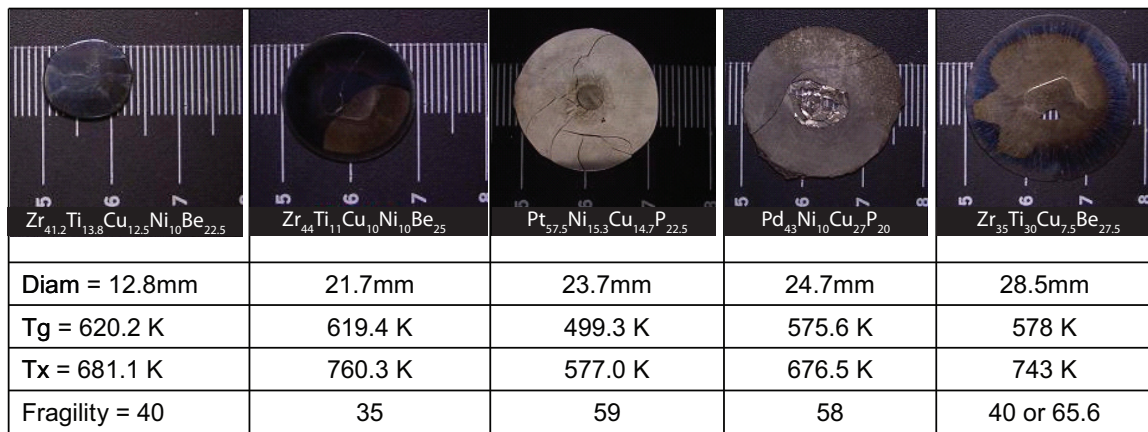


**Figure 4.5:** Squish test proposed by Schroers [28] performed on four alloys traditionally used in TPF and the new large  $\Delta T$  alloy. The largest diameter after the squish test is obtained by using the  $\text{Zr}_{35}\text{Ti}_{30}\text{Cu}_{7.5}\text{Be}_{27.5}$  alloy suggesting that it will exhibit the best flow properties in TPF processes requiring large strains.

The elastic constants of  $\text{Zr}_{35}\text{Ti}_{30}\text{Cu}_{8.25}\text{Be}_{26.75}$  and several other BMG are also shown in Table 4.1. Evidence suggests that a high Poisson's ratio is related to the ductile behavior of metallic glasses [29-34].  $\text{Zr}_{35}\text{Ti}_{30}\text{Cu}_{8.25}\text{Be}_{26.75}$  has a Poisson's ratio of  $\sim 0.37$ , higher than that of Vitreloy series alloys. The fracture toughness ( $K_{IC}$ ) of  $\text{Zr}_{35}\text{Ti}_{30}\text{Cu}_{8.25}\text{Be}_{26.75}$  was estimated to be  $\sim 85 \text{ MPa m}^{1/2}$ , while that of Vitreloy 1 is only  $\sim 20 - 45 \text{ MPa m}^{1/2}$  [35-37]. The yield strength of  $\text{Zr}_{35}\text{Ti}_{30}\text{Cu}_{8.25}\text{Be}_{26.75}$  under uniaxial compressive tests was found to be  $\sim 1.43 \text{ GPa}$ . To design this new class of BMG, a balance between strength and thermoplastic processability has to be obtained [38]. The

present series of amorphous metals possesses superior thermoplastic formability with a minimum reduction of yield strength and elastic energy storage.

In summary, we have designed a series of metallic glass forming alloys, having the combination of optimized properties for TPF, such as extraordinarily low viscosity in the thermoplastic zone, exceptional thermal stability, low  $T_g$ , and excellent GFA. These alloys demonstrate strong thermoplastic processability and excellent mechanical properties. We expect that this discovery will greatly broaden the engineering applications of amorphous metals by taking advantage of the unique properties of the newly designed BMG.

#### **4.1 Experimental Method**

Mixtures of elements of purity ranging from 99.9% to 99.99% were alloyed by induction melting on a water cooled silver boat under a Ti-gettered argon atmosphere. Typically 5 g ingots were prepared. Each ingot was flipped over and remelted at least three times in order to obtain chemical homogeneity. A Philips X'Pert Pro X-ray Diffractometer and a Netzsch 404C Pegasus Differential Scanning Calorimeter (DSC performed at a constant heating rate 0.33 K/s) were utilized to confirm the amorphous natures and to examine the isothermal behaviors in the SCLR of these alloys. The pulse-echo overlap technique with 25 MHz piezoelectric transducers was used to measure the shear and longitudinal wave speeds at room temperature for each of the samples. Sample density was measured by the Archimedean technique according to the American Society of Testing Materials standard C 693-93 [39]. The viscosity of  $Zr_{35}Ti_{30}Cu_{8.25}Be_{26.75}$  as a function of temperature in the SCLR was studied using a Perkin Elmer TMA7 Thermomechanical Analyzer (TMA) in the parallel plate geometry as described by

Bakke, Busch, and Johnson [40]. The measurement was done with a heating rate of 0.667 K/s, a force of 0.02 N, and an initial height of 0.3mm. The viscosity and TTT diagrams of  $Zr_{35}Ti_{30}Cu_{8.25}Be_{26.75}$  at high temperatures were measured in a high vacuum electrostatic levitator (ESL) [41-42]. For the viscosity measurements, the resonant oscillation of the molten drop was induced by an alternating current electric field while holding the sample at a preset temperature. Viscosity was calculated from the decay time constant of free oscillation that followed the excitation pulse. To determine the TTT curve, an electrostatically levitated molten (laser melting) droplet ( $\sim 3$ mm diameter) sample was cooled radiatively to a predetermined temperature, and then held isothermally until crystallization. The temperature fluctuations were within  $\pm 2$  K during the isothermal treatment.

The authors acknowledge the valuable discussions with Prof. Jan Schroers and Dr. Marios D. Demetriou, and the kind help from Bo Li, Dr. Boonrat Lohwangwatana, Joseph P. Schramm, and Jin-yoo Suh on taking digital and optical graphs and doing fracture toughness measurements. We also thank the support from the MRSEC Program (Center for the Science and Engineering Materials, CSEM) of the National Science Foundation under Award Number DMR - 0520565.

#### Chapter 4 References

- [1] A.L. Greer, *Science* 267 (1995) 1947.
- [2] W.L. Johnson, *MRS Bull.* 24 (1999) 42.
- [3] A. Inoue, *Acta Mater.* 48 (2000) 279.
- [4] A. Peker, W.L. Johnson, *Appl. Phys. Lett.* 63 (1993) 2342.
- [5] D.H. Xu, G. Duan, W.L. Johnson, *Phys. Rev. Lett.* 92 (2004) 245504.
- [6] V. Ponnambalam, S.J. Poon, G.J. Shiflet, *J. Mater. Res.* 19 (2004) 1320.
- [7] B. Zhang, D.Q. Zhao, M.X. Pan, W.H. Wang, A.L. Greer, *Phys. Rev. Lett.* 94 (2005) 205502.
- [8] J. Schroers, W.L. Johnson, *Appl. Phys. Lett.* 84 (2004) 3666.

- [9] Z.P. Lu, C.T. Liu, J.R. Thompson, W.D. Porter, *Phys. Rev. Lett.* 92 (2004) 245503.
- [10] J. Schroers, *JOM* 57 (2005) 35.
- [11] J. Schroers, N. Paton, *Adv. Mater. Proc.* 164 (2006) 61.
- [12] G.J. Fan, H.J. Fecht, E.J. Lavernia, *Appl. Phys. Lett.* 84 (2004) 487.
- [13] J.P. Chu, H. Wijaya, C.W. Wu, T.R. Tsai, C.S. Wei, T.G. Nieh, J. Wadsworth, *Appl. Phys. Lett.* 90 (2007) 034101.
- [14] A. Masuhr, T.A. Waniuk, R. Busch, W.L. Johnson, *Phys. Rev. Lett.* 82 (1999) 2290.
- [15] R. Busch, W.L. Johnson, *Appl. Phys. Lett.* 72 (1998) 2695.
- [16] F. Spaepen, *Acta Metall.* 25 (1977) 407.
- [17] J. Lu, G. Ravichandran, W.L. Johnson, *Acta Mater.* 51 (2003) 3429.
- [18] T.A. Waniuk, J. Schroers, W.L. Johnson, *Appl. Phys. Lett.* 78 (2001) 1213.
- [19] H. Kato, T. Wada, M. Hasegawa, J. Saida, A. Inoue, H.S. Chen, *Scripta Mater.* 54 (2006) 2023.
- [20] K. Shibata, T. Higuchi, A.P. Tsai, M. Imai, K. Suzuki, *Prog. Theor. Phys. Suppl.* 126 (1997) 75.
- [21] J. Schroers, B. Lohwongwatana, W.L. Johnson, A. Peker, *Appl. Phys. Lett.* 87 (2005) 061912.
- [22] L.M. Martinez, C.A. Angell, *Nature* 410 (2001) 663.
- [23] W.L. Johnson, M.D. Demetriou, J.S. Harmon, M.L. Lind, K. Samwer, *MRS Bull.* 32 (2007) 644.
- [24] V.N. Novikov, A.P. Sokolov, *Phys. Rev. B* 74 (2006) 064203.
- [25] D.N. Perera, *J. Phys. Condens. Matter* 11 (1999) 3807.
- [26] F.W. Billmeyer, *Text. Ploym. Sci.* (1984) 305.
- [27] T. Waniuk, J. Schroers, W.L. Johnson, *Phys. Rev. B* 67 (2003) 184203.
- [28] J. Schroers, *Acta Mater.* 56 (2008) 471.
- [29] H.S. Chen, J.T. Krause, E. Coleman, *J. Non-Cryst. Solids* 18 (1975) 157.
- [30] V.N. Novikov, A.P. Sokolov, *Nature* 431 (2004) 961.
- [31] J. Schroers, W.L. Johnson, *Phys. Rev. Lett.* 93 (2004) 255506.
- [32] W.L. Johnson, K. Samwer, *Phys. Rev. Lett.* 95 (2005) 195501.
- [33] X.J. Gu, A.G. McDermott, S.J. Poon, G.J. Shiflet, *Appl. Phys. Lett.* 88 (2006) 211905.
- [34] J.J. Lewandowski, W.H. Wang, A.L. Greer, *Philos. Mag. Lett.* 85 (2005) 77.
- [35] J.J. Lewandowski, M. Shazly, A.S. Nouri, *Scripta Mater.* 54 (2006) 337.
- [36] P. Lowhaphandu, J.J. Lewandowski, *Scripta Mater.* 38 (1998) 1811.
- [37] J.J. Lewandowski, *Mater. Trans.* 42 (2001) 633.
- [38] G. Duan, M.L. Lind, K. De Blauwe, A. Wiest, W.L. Johnson, *Appl. Phys. Lett.* 90 (2007) 211901.
- [39] M.L. Lind, G. Duan, W.L. Johnson, *Phys. Rev. Lett.* 97 (2006) 015501.
- [40] E. Bakke, R. Busch, W.L. Johnson, *Appl. Phys. Lett.* 67 (1995) 3260.
- [41] S. Mukherjee, J. Schroers, Z. Zhou, W.L. Johnson, W.K. Rhim, *Acta Mater.* 52 (2004) 3689.
- [42] S. Mukherjee, Z. Zhou, J. Schroers, W.L. Johnson, W.K. Rhim, *Appl. Phys. Lett.* 84 (2004) 5010.

## **Chapter 5 - Injection Molding Metallic Glass**

After determining that the  $Zr_{35}Ti_{30}Be_{27.5}Cu_{7.5}$  alloy shows the most promise of any known alloy for TPF processes requiring large strains, we set out to demonstrate injection molding of a metallic glass for the first time. This chapter draws heavily on "Injection Molding Metallic Glass" published in Scripta Materialia [A. Wiest, J.S. Harmon, M.D. Demetriou, R.D. Conner, W.L. Johnson, Scripta Mater. 60 (2009) 160]. Advances in alloy development produced the  $Zr_{35}Ti_{30}Be_{27.5}Cu_{7.5}$  alloy with (crystallization - glass transition temperature) =  $\Delta T = 165$  °C. This alloy's large supercooled liquid region (SCLR) provides the longest processing times and lowest processing viscosities of any metallic glass and was injection molded using tooling based on plastic injection molding technology. Injection molded beams and die cast beams were tested in three-point bending. The average modulus of rupture (MOR) was found to be similar while injection molded beams had a smaller standard deviation in MOR.

Bulk metallic glasses (BMG) are high strength, high hardness, highly elastic, low modulus, low melting temperature materials with no crystalline order that have been the subject of extensive research in recent years [1-4]. Because of their low melting temperature they are easily processed using conventional vacuum die casting and suction casting techniques. These methods require processing that is sufficiently fast to avoid crystallization, and alloys with high glass forming ability (GFA) are generally preferred. Die cast parts have somewhat unreliable mechanical properties because of porosity that often exists in the specimens due to the high flow velocities required to fill the mold cavity [5]. The cooling requirements of die casting bound the dimensions of die cast parts to no larger than can be cooled sufficiently fast to avoid crystallization and no

smaller than can be quickly filled. Parts with complex geometries, thin sections, and high aspect ratios are difficult to obtain with die casting.

Thermoplastic forming decouples the forming and cooling processes because it is carried out in the SCLR between the glass transition temperature,  $T_g$ , and the crystallization temperature,  $T_x$ . In the SCLR a BMG forming alloy exists as a viscous, deeply undercooled liquid. The viscosity of the alloy follows a hyper-Arrhenius function of temperature [6] and crystallization is forestalled due to the sluggish kinetics in the deeply undercooled liquid. Much longer processing times are available in the SCLR than are available when casting from the molten state because the alloy is resistant to crystallization below  $T_x$ . Die casting processes must shape and cool the alloy in seconds to tens of seconds while processing in the SCLR allows hundreds to thousands of seconds for forming and cooling. Time temperature transformation (TTT) diagrams measure the time to crystallization of an alloy held isothermally at a given temperature. Viscosity plots measure the Newtonian viscosity of an alloy held isothermally at a given temperature. Figure 5.1 combines data from these two kinds of plots to show attainable viscosity for a given processing time for three alloys commonly used in thermoplastic forming experiments and the alloy used in this experiment,  $Zr_{35}Ti_{30}Be_{27.5}Cu_{7.5}$  [6-9]. This plot is a viscosity time transformation plot,  $\eta$ TT. Good TTT data upon heating is not available in the literature for  $Pd_{43}Ni_{20}Cu_{27}P_{20}$  so cooling TTT data was used for the Pd alloy in the Figure 5.1. Crystallization times are known to be shorter for heating TTT plots compared to cooling TTT plots for the same alloy. Accordingly, the true heating  $\eta$ TT plot for the Pd alloy should be moved to shorter times. It is clearly seen that the  $Zr_{35}Ti_{30}Be_{27.5}Cu_{7.5}$  alloy has the lowest processing viscosity for a wide range of

processing times. Interpolation of viscosities not directly measured was done using the fit suggested by Johnson et al. [6].

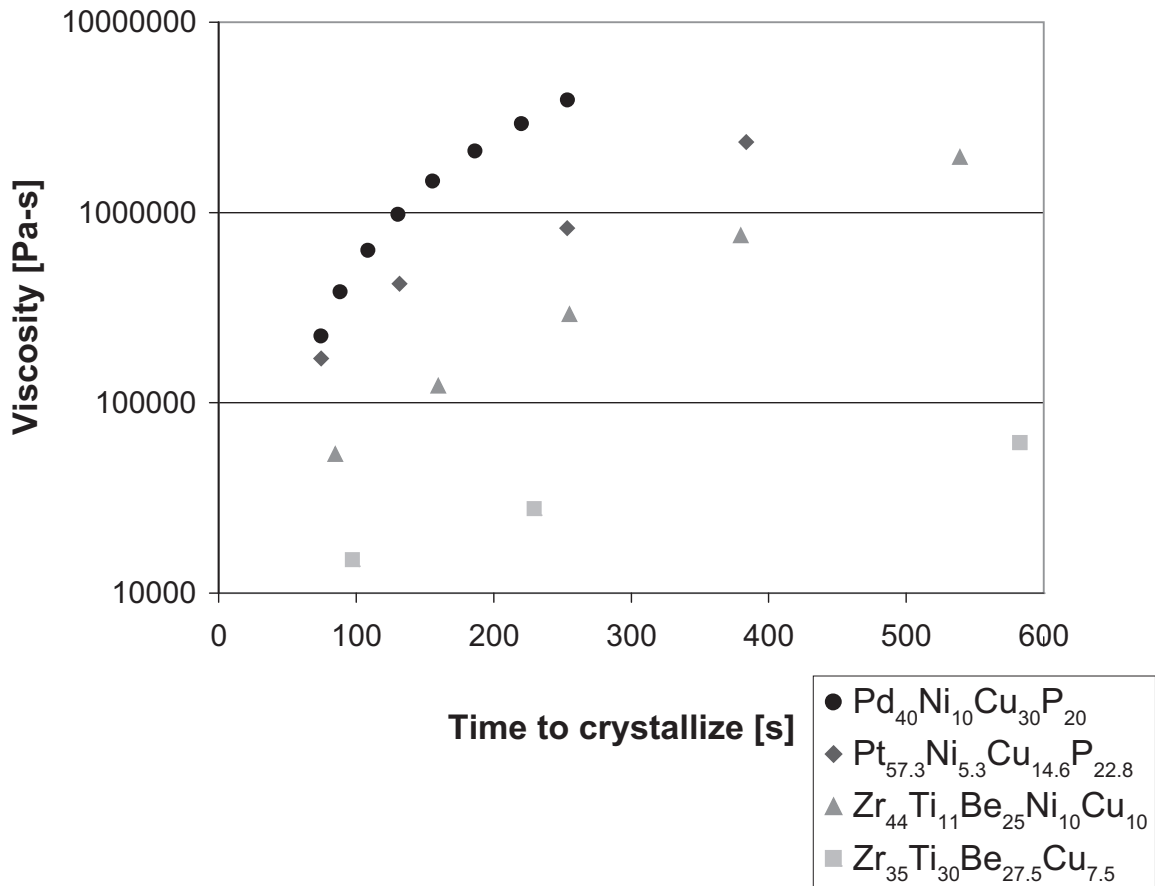


**Figure 5.1:** Time to crystallization versus viscosity plot for four thermoplastically processable alloys. This plot combines TTT and viscosity versus time data found in references [6-9] to show available processing time for a given viscosity for the alloys.

The decreasing viscosity and longer processing times available in the SCLR allow metallic glasses to be processed in ways similar to plastics which are not possible with crystalline metal alloys. Nanometer scale features with high aspect ratios have been formed in the SCLR by pressing metallic glasses into etched wells of semiconductor materials [10]. Glassy powders have been consolidated in the SCLR to form net shaped parts [11]. Hot extrusion has been demonstrated using Zr based alloys [12] and blow molding experiments using relatively low pressures yielded hemispheres with high

quality surface finish [13]. An additional benefit to processing BMG in the SCLR is the decoupling of forming and cooling steps which allows formation of parts larger than the critical casting thickness of the alloy.

A conventional processing method used in the plastics industry that has not previously been successfully demonstrated with BMG is injection molding. This is in part due to the limited viscosities and processing times available in the SCLR of known alloys. Recent discovery of alloys with SCLR ( $\Delta T = T_x - T_g$ ) as high as 165 °C makes BMG injection molding a possibility [14].

A basic injection molding machine has a heated reservoir in which plastic feedstock is softened, a piston or plunger to apply pressure to the feedstock, a nozzle or gate to restrict the flow of plastic when necessary and a mold into which the plastic is forced to form a part. A schematic drawing of the setup used in this experiment is shown in Figure 5.2b. Typical operating temperatures and pressures are 175 °C – 350 °C and 35 MPa - 150 MPa, respectively. Softened plastics used for injection molding usually have a viscosity of  $\sim 10^3$  Pa-s.

$Zr_{44}Ti_{11}Be_{25}Cu_{10}Ni_{10}$ ,  $Pd_{43}Ni_{10}Cu_{27}P_{20}$  and  $Pt_{57.5}Ni_{5.3}Cu_{14.7}P_{22.5}$  were among the most thermoplastically processable alloys known, reaching viscosities of  $\sim 10^5$  Pa-s in the SCLR before onset of crystallization. The alloy used in this experiment,  $Zr_{35}Ti_{30}Be_{27.5}Cu_{7.5}$ , can reach viscosities in the SCLR of  $\sim 3 \cdot 10^4$  Pa-s at 420 °C with  $\sim 230$  s available for thermoplastic processing at that temperature [15]. This is an order of magnitude lower viscosity than is attainable in the SCLR of previously reported metallic glasses [16-18]. However, when compared to the viscosity of plastics used for injection molding, it is an order of magnitude higher viscosity. A modified injection molding

setup was created to accommodate the higher temperatures and pressures necessary to force the more viscous  $Zr_{35}Ti_{30}Be_{27.5}Cu_{7.5}$  supercooled liquid into a mold cavity.

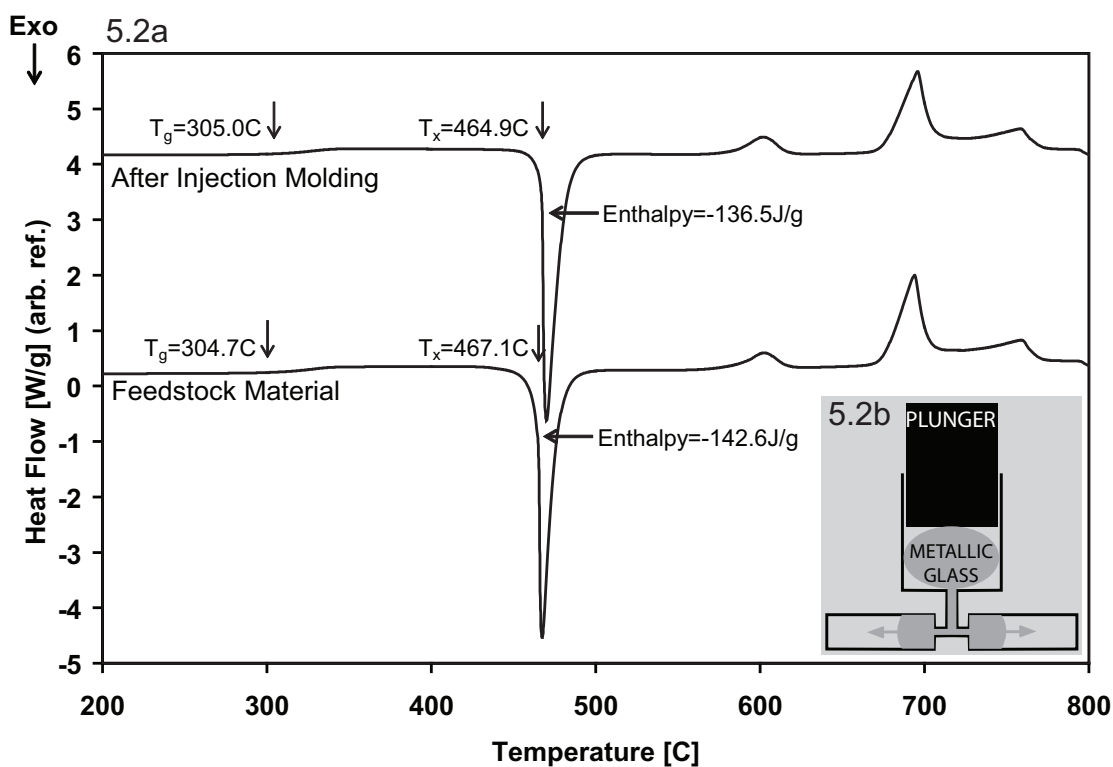


**Figure 5.2:** 2a - 20 °C/min DSC scans of feedstock material and injection molded specimen. The injection molding process appears to have had little effect on the thermodynamic properties measured in the DSC. Inset 2b - Schematic drawing of the modified injection molding setup consisting of a plunger, gates, and a heated mold and reservoir. The dimensions of the mold cavities are 2mm x 10mm x 20mm and 1.5mm x 10mm x 20mm.

The  $Zr_{35}Ti_{30}Be_{27.5}Cu_{7.5}$  feedstock material was made using >99.9% pure elements and melted thoroughly in an arc melter under a Ti-gettered argon atmosphere. Each ingot was flipped and remelted multiple times to ensure chemical homogeneity. Ingots with more than 0.1% deviation from initial weighed mass after melting were discarded. Die casting was done by radio frequency heating the alloy in a quartz nozzle and injecting the molten alloy into a copper mold using argon pressure. The amorphous nature of all material was determined using X-ray diffraction and DSC. Mechanical testing was

performed on an Instron 4204 Load Frame at a constant displacement rate of 0.5mm/min in a three-point bending geometry to determine MOR.

Suitable feedstock material was also required for the injection molding process. Various methods were tested to create amorphous feedstock material and the effect on  $\Delta T$  was measured in the DSC at 20 K/min. We noticed large variations in  $\Delta T$  depending on the method used. The results are summarized in Table 5.1. To test the variation of  $\Delta T$  with rod diameter, samples were RF melted and cast into copper molds or water quenched in quartz tubes had  $\Delta T$  values ranging from 136 °C to 170 °C but there was no systematic variation with rod diameter and the  $\Delta T = 170$  °C was only obtained once. We also tried melting the alloy in a furnace so the melting temperature could be controlled more carefully and identical diameter rods were formed. The  $\Delta T$  values ranged from 153 °C to 165 °C but the results were not systematic. Arc melted buttons showed the most uniformity in  $\Delta T$  and were chosen as the feedstock material. We removed the thin crystalline layer on the side of the ingot in contact with the copper hearth with a diamond saw and collected X-ray diffraction data on the cut samples to ensure they were completely amorphous.

A schematic drawing of the modified injection molding setup can be found in Figure 5.2b. The experimental setup consisted of a plunger used to apply force, a 19mm diameter x 20mm tall heated reservoir in which BMG feedstock material was brought to the processing temperature, an 8mm diameter x 3mm tall vertical channel opening into two perpendicular channels with dimensions 5mm x 2mm x 2mm long which restricted the flow of material into the mold cavity. The heated mold cavity on the left in Figure

5.2b is 10mm x 2mm x 60mm long and the one on the right is 10mm x 1.5mm x 60mm long.

**Table 5.1:** Effects of rod diameter and overheating above melt temperature on  $\Delta T$  as well as variation in arc melted button  $\Delta T$  are tabulated. Temperatures given in °C.

	$T_g$	$T_x$	$\Delta T$
Furnace melted samples			
7mm quartz 1235 °C	304	459	155
7mm quartz 1200 °C	303	459	156
7mm quartz 1145 °C	304	457	153
7mm quartz 930 °C	302	467	165
RF melted samples			
3mm Cu mold	305	441	136
6mm quartz	305	452	147
10mm quartz	307	477	170
15mm quartz	306	450	144
Arc Melted Ingots			
Ingot 7	305	469	164
Ingot 9	298	464	166
Ingot 11	299	467	168
Ingot 12	302	465	163
Ingot 13	306	466	160
Ingot 15	304	464	160
Ingot 16	304	467	163
Ingot 18	303	467	164
Ingot 21	306	469	163
Ingot 23	307	466	159
Ingot 25	304	468	164
Ingot 26	305	467	162
<b>Average Arc Melted Ingots</b>	<b>304</b>	<b>467</b>	<b>163</b>
<b>Standard Deviation</b>	<b>2.7</b>	<b>1.7</b>	<b>2.6</b>

A photograph of injection molding attempts is shown in Figure 5.3. The most successful run was accomplished when the mold and glassy feedstock material were heated to 420 °C with a force of 300 MPa applied to the material in the reservoir for two minutes. The material completely filled the larger mold cavity and a 0.2mm diameter flashing was formed along the perimeter due to insufficient clamping pressure. The

material that filled this cavity underwent more than 1000% strain. Minimal polishing with 320 grit sand paper removed the surface oxide layer and the beam formed in the large mold cavity was found to be glassy using X-ray diffraction. The flow was terminated in the smaller cavity due to crystallization of material near the heating element. Figure 5.3c shows the most successful metallic glass part; Figures 5.3a and 5.3b illustrate two less successful attempts, and Figure 5.3d is a part made of polyethylene shown for reference. The short fill shown in Figure 5.3a was due to the plunger binding in the reservoir. Note the parabolic flow front visible on both sides of the part.

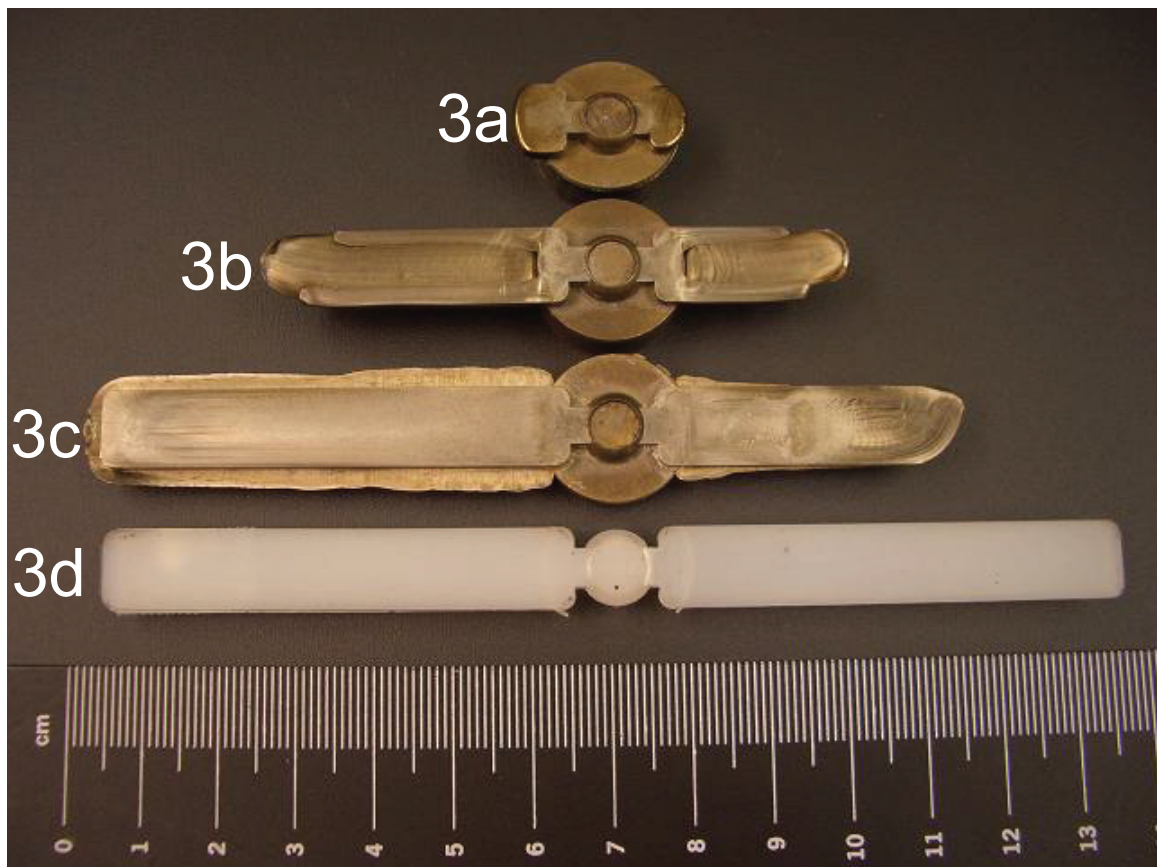


**Figure 5.3:** Photograph of injection molded parts. The top part (5.3a) was processed at 410 °C with an applied pressure of 140 MPa but the plunger jammed. The second part (5.3b) was processed at 385 °C with an applied pressure of 300 MPa for three minutes. The third part (5.3c) was processed at 420 °C with an applied pressure of 300 MPa for two minutes. The fourth part (5.3d) made of polyethylene was processed at 210 °C with an applied pressure of 35 MPa for one minute.

Using the velocity distribution of a viscous fluid flowing in a cylindrical channel assuming stick boundary conditions and laminar flow we obtain  $v = -\frac{1}{4\eta} \frac{\Delta P}{\Delta x} (R^2 - r^2)$ ,

where  $v$  is the velocity of a lamina,  $\eta$  is the viscosity,  $\Delta P$  is the pressure differential of the pipe,  $\Delta x$  is a displacement in the direction of flow,  $R$  is the diameter of the pipe, and  $r$  is the radial distance from the center of the pipe. A similar equation results for an ellipse where the lamina are elliptical cylinders instead of circular. In the limiting case of a rectangular channel, a parabolic velocity distribution is found away from the corners. The observed flow front suggests laminar flow into the mold cavity. Laminar flow is important, as it reduces the formation of voids and other flaws which weaken the part. The part shown in Figure 5.3b was processed at too low a temperature, resulting in a processing viscosity that was too high as indicated by “river marks” or flow lines. Despite the large thermal stability of  $\text{Zr}_{35}\text{Ti}_{30}\text{Be}_{27.5}\text{Cu}_{7.5}$ , approximately 10 times more force is required to form the metallic glass part than was used to form a polyethylene part of the same geometry. The polyethylene part filled both mold cavities at a processing temperature of 250 °C and a pressure of 35 MPa, while those of the BMG are 420 °C and 300 MPa.

We were able to process metallic glass parts with 10 times higher processing viscosity than polyethylene by using a higher force. It is natural to wonder if perhaps even more force could be applied to alloys with higher processing viscosities and achieve similar flow. Up to a certain point this strategy works but shortens mold life. If too high a strain rate is imposed at a given viscosity, non-Newtonian flow results and shear banding can occur in the SCLR.

## 5.10

The availability of injection molding as a potential forming process for metallic glass parts allows for the formation of parts greater than the critical casting thickness of the parent alloy. Injection molding is carried out at temperatures much lower than die casting which may improve the mold lifetime. Since processing is accomplished in the laminar flow regime, higher quality and more reliable parts can be fabricated than with current die casting technology.

DSC scans of the feedstock material and a section of the injection molded beam are overlaid in Figure 5.2a. The  $\Delta T$  value of the injection molded material is slightly smaller than the feedstock material and the enthalpies of crystallization are nearly identical.

The injection molded plate was sectioned into 2mm x 2mm x 20mm beams for mechanical testing in three-point bending. The modulus of rupture (MOR,  $\sigma_{\max}$ ) was determined for 12 beams and compared to die cast specimens of the same dimension using the formula  $\sigma_{\max} = \frac{3FL}{2ab^2}$  s where  $F$  = applied force,  $a = b = 2\text{mm}$ ,  $L$  = distance between bottom supports of the three-point bending setup = 13mm. The MOR equation for a square beam is derived in Derivation 9.

The die cast specimens were cut from three 2mm x 10mm x 20mm plates. Figure 5.4 shows the results of the three-point bend tests. Twelve specimens of each fabrication method were tested, with MOR =  $2.923 \pm 0.065$  GPa for injection molding and MOR =  $2.879 \pm 0.240$  GPa for die casting. Note that the average MOR is nearly identical for both processing methods while the standard deviation of the injection molded specimens is 73% less than that of the die cast specimens. This suggests that injection molding produces parts with more reliable mechanical properties than their die cast counterparts.

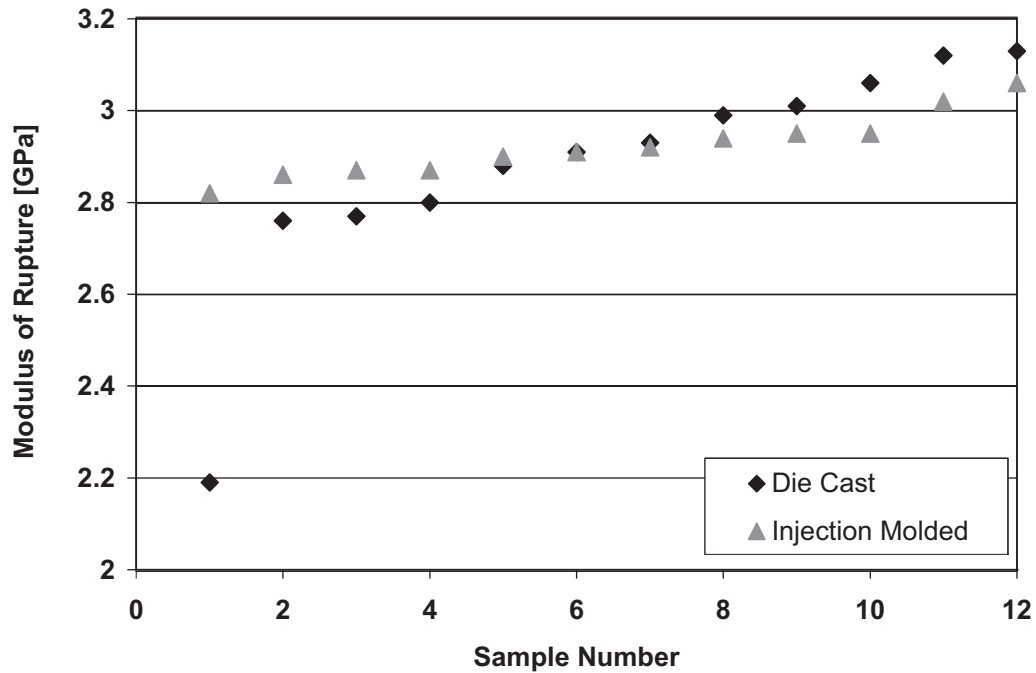


**Figure 5.4:** Plot of modulus of rupture values for injection molded and die cast samples. Die cast modulus of rupture =  $(2.879 \pm 0.240)$ GPa. Injection molding modulus of rupture =  $(2.923 \pm 0.065)$ GPa.

The discovery of the  $Zr_{35}Ti_{30}Be_{27.5}Cu_{7.5}$  alloy with viscosity in the SCLR as low as  $10^4$  Pa-s allowed injection molding of a metallic glass to be demonstrated. Tooling based on plastic injection molding machines was used, but modified to allow for the higher temperatures and pressures necessary to process the more viscous metallic glass. The material underwent strains greater than 1000% at a temperature of 420 °C and a pressure of 300 MPa applied for two minutes and formed a part 2mm x 10mm x 60mm. The injection molded part was tested mechanically in three-point bending and showed MOR equivalent to that of a die cast specimen with a standard deviation of MOR 73% less than that of die cast specimens of the same composition and dimension. The ability to injection mold high strength metal parts using methods similar to existing plastics

technology could greatly reduce processing costs, and will be the subject of future investigation.

Special thanks to Doug Hofmann, Rebecca Stevens, Glenn Garrett, Jin-Yoo Suh, and Joe Schramm for valuable discussion and heroic help quenching the 420 °C massive mold.

### Chapter 5 References

- [1] A.L. Greer, E. Ma, *MRS Bull.* 32 (2007) 611.
- [2] W.L. Johnson, *MRS Bull.* 24 (1999) 42.
- [3] A. Inoue, *Acta Mater.* 48 (2000) 279.
- [4] W.L. Johnson, *JOM* 54 (2002) 40.
- [5] K.J. Laws, B. Gun, M. Ferry, *Mat. Sci. Eng. A* 425 (2006) 114.
- [6] W.L. Johnson, M.D. Demetriou, J.S. Harmon, M.L. Lind, K. Samwer, *MRS Bull.* 32 (2007) 644.
- [7] B.A. Legg, J. Schroers, R. Busch, *Acta Mater.* 55 (2007) 1109.
- [8] J.F. Löffler, J. Schroers, W.L. Johnson, *Appl. Phys. Lett.* 77 (2000) 681.
- [9] T. Waniuk, J. Schroers, W.L. Johnson, *Phys. Rev. B* 67 (2003) 184203.
- [10] J. Schroers, Q. Pham, A. Desai, *J. Microelectromech. S.* 16 (2007) 240.
- [11] J. Degmova, S. Roth, J. Eckert, H. Grahl, L. Schultz, *Mat. Sci. Eng. A* 375 (2004) 265.
- [12] K.S. Lee, Y.W. Chang, *Mat. Sci. Eng. A-Struct.* 399 (2005) 238.
- [13] J. Schroers, Q. Pham, A. Peker, N. Paton, R.V. Curtis, *Scripta Mater.* 57 (2007) 341.
- [14] A. Wiest, G. Duan, M.D. Demetriou, L.A. Wiest, A. Peck, G. Kaltenboeck, B. Wiest, W.L. Johnson, *Acta Mater.* 56 (2008) 2625.
- [15] G. Duan, A. Wiest, M.L. Lind, J. Li, W.K. Rhim, W.L. Johnson, *Adv. Mater.* 19 (2007) 4272.
- [16] G.J. Fan, H.J. Fecht, E.J. Lavernia, *Appl. Phys. Lett.* 84 (2004) 487.
- [17] R. Busch, E. Bakke, W.L. Johnson, *Acta Mater.* 46 (1998) 4725.
- [18] H. Kato, T. Wada, M. Hasegawa, J. Saida, A. Inoue, H.S. Chen, *Scripta Mater.* 54 (2006) 2023.

## **Chapter 6 - Relaxation Phenomena in the ZrTiBe System**

### **6.1 Abstract**

The presence of two apparent glass transitions in the large  $\Delta T$  alloys prompted further investigation of flow and relaxation properties in the supercooled liquid region (SCLR). This chapter is similar to a paper entitled “Relaxation Phenomena in the ZrTiBe System” submitted to Acta Materialia. The expected authors are [A. Wiest, S. Roberts, M.L. Lind, D. Soh, D.C. Hofmann, M.D. Demetriou, C.M. Garland, W.L. Johnson]. The discovery of bulk glass forming compositions in the ZrTiBe system allowed a more thorough study of relaxation phenomena in the SCLR to be accomplished. Heat capacity measurements of glassy compositions show two discontinuities,  $\Delta c_{p1}$  and  $\Delta c_{p2}$ , in the SCLR. If the discontinuities are assumed to arise from glass transitions of two glasses with similar fragilities and different glass transition temperatures then the ratio  $\Delta c_{p1}/(\Delta c_{p1} + \Delta c_{p2})$  gives the fraction of the first glassy phase. A plot of  $\Delta c_{p1}/(\Delta c_{p1} + \Delta c_{p2})$  vs Zr concentration along an iso Be line reveals a linear relationship and rule of mixtures analysis predicts compositions that would be single phase. The predicted compositions exhibit single phase glass behavior and glass transition temperatures consistent with the two phase alloys. Viscosity vs temperature and shear modulus versus temperature measurements also reveal relaxation events at temperatures near the observed jumps in heat capacity. These relaxation events are well described by a two phase glass assumption, but microstructural evidence is lacking.

### **6.2 Introduction**

The existence of a miscibility gap in the SCLR of BMG that gives rise to phase separation upon relaxation of the glass has been claimed in many glass forming alloy

systems including AuPbSb [1-2], ZrCu [3], ZrTiBe [4-7], ZrTiCuNiBe [8-10], MgCuYLi [11], CuZrAlAg [12], TiYAlCo and ZrYAlCo [13]. Using X-ray scattering, Johnson and collaborators detected splitting of the broad amorphous spectrum in an as-spun AuPbSb glassy ribbon [1]. Additional studies using Small Angle Neutron Scattering (SANS) [9-10], Small Angle X-ray Scattering (SAXS) [10], Anomalous Small Angle X-ray Scattering (ASAXS) [11], Transmission Electron Microscopy (TEM) [13], discontinuous slopes in resistivity measurements [3], and Differential Scanning Calorimetry (DSC) [4-7] have been performed to support the apparent phase separation in many glass forming systems. In some systems, such as in the Vitreloy (ZrTiNiCuBe) system, phase separation arises by annealing the glassy phase below  $T_g$ , supporting the existence of a miscibility gap below  $T_g$  [8-10]. In other systems, such as AuPbSb and ZrTiBe, phase separation is manifested as a twin relaxation in the SCLR [1-2, 4-7], supporting the idea that the miscibility gap extends above  $T_g$ , and suggesting that perhaps two chemically separable glassy phases vitrify upon cooling the alloy below the miscibility gap.

Tanner examined the ZrTiBe system for glass forming compositions and found that many alloys could form amorphous ribbons with thickness up to  $100\mu\text{m}$  [14-15]. Heat capacity measurements using DSC revealed that some of the glassy alloys exhibit two discontinuities in heat capacity upon heating. Typically, a glassy material upon heating is expected to exhibit just one discontinuity in heat capacity that designates the increase in mobility associated with the glass relaxing to a supercooled liquid state at  $T_g$  [16]. A double jump in heat capacity, which can be interpreted as a double glass transition temperature is unusual. Tanner proposed that this anomalous feature of the heat capacity supports the coexistence of two glassy phases in the vitrified state. Other

authors who have studied this system have interpreted the second jump in specific heat as an exothermic ordering event that follows  $T_g$  and precedes crystallization [17]. To date, the precise origin of the double jump in heat capacity and the associated impact on the chemistry, structure, and rheology of the supercooled liquid remain unresolved, a fact that can be at least partly attributed to the unavailability of bulk ZrTiBe specimens.

Recently, the ZrTiBe system has been reexamined, and many compositions that exhibit the apparent two  $T_g$  phenomenon and which were previously thought to be limited to a critical casting thickness of 100 $\mu$ m could in fact be cast into bulk glassy samples with thicknesses that range from 1 - 6mm [18]. The availability of bulk ZrTiBe samples that exhibit two  $T_g$  events paves the way to a more thorough examination of this phenomenon allowing measurement of bulk flow properties and shear modulus as a function of temperature. We use bulk ZrTiBe specimens to investigate the effects of the two  $T_g$  events on the heat capacity, rheology, and rigidity of the SCLR through DSC, TMA, and ultrasonic tests.

### **6.3 Experimental Method**

Elements of 99.9% purity or higher were arc melted on a water cooled copper hearth under a Ti-gettered argon atmosphere. Zr and Ti were varied in 5 atomic percent increments along a fixed Be line and compositions were cast into 0.5mm thick plates for DSC analysis using an Edmund Buhler mini arc melter. The amorphous nature of the plates was verified using X-ray diffraction. Segments from the plates were heated in a Netzsch 404C Pegasus Differential Scanning Calorimeter at 20 K/min and 5 K/min past the crystallization temperature. The 20 K/min scans showed sharper features in heat capacity because of the larger signal produced at faster scan rates and 20 K/min scans

were used to determine the apparent glass transition temperatures and magnitude of the jumps in heat capacity. To enable the evaluation of the heat capacity jump from the 20 K/min scans, an initial baseline was taken and then subtracted from the sample run. The 5 K/min runs were used to determine the glass transition temperatures at that rate, as the viscosity and shear modulus experiments were conducted at 5 K/min. Since only  $T_g$  was of interest at 5 K/min, baseline subtraction was unnecessary.

The heat capacity features of the SCLR were analyzed in a consistent manner. A baseline heat capacity is seen at low temperatures, and two successive jumps in heat capacity are seen before the exothermic crystallization event. The lower glass transition temperature,  $T_{g1}$  is defined as the intersection between the tangent to the low temperature heat capacity baseline and the tangent to the point of steepest slope during the first heat capacity jump. The second heat capacity jump is similarly analyzed to find the second glass transition temperature,  $T_{g2}$ . The two jumps in heat capacity are denoted  $\Delta c_{p1}$  and  $\Delta c_{p2}$ , and are shown in Figure 6.1.

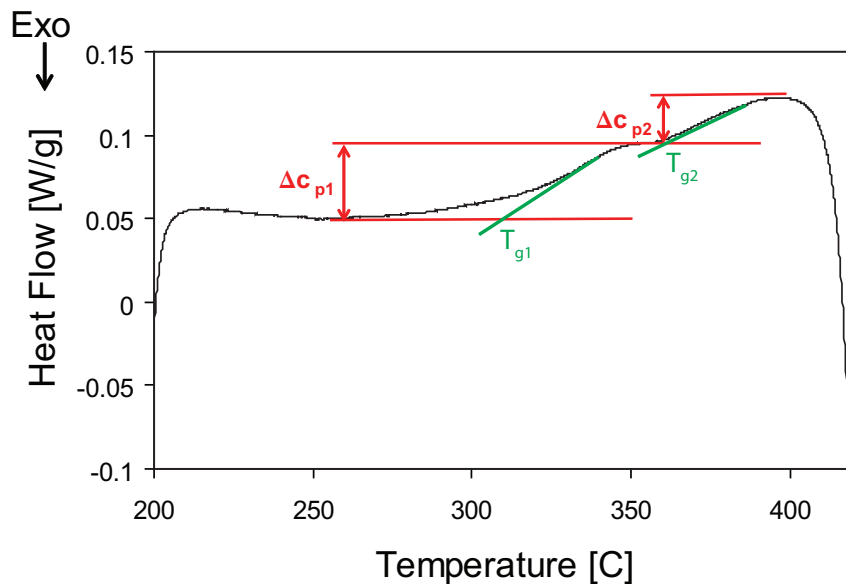


**Figure 6.1:** 20 K/min DSC scan of  $Zr_{30}Ti_{30}Be_{40}$  showing double discontinuity in heat capacity in SCLR.  $\Delta c_p$  and  $T_g$  determination method illustrated.

The viscosity was measured using the parallel plate geometry with a Perkin Elmer Diamond TMA over a temperature region spanning the two  $T_g$  events. 1mm and 3mm diameter specimens were used. The diameter to height aspect ratio was set to 1.0 for the 3mm diameter samples, and to 1.8 for the 1mm diameter samples to avoid buckling and achieve maximum deformation. A force of 1400 mN was applied resulting in a compressive stress of 1.8 MPa on the 1mm diameter specimens and a stress of 0.2 MPa on the 3mm diameter specimens. The heating rate through the SCLR was 5 K/min. The viscosity was analyzed using the displacement and the displacement time derivative data, according to the method for parallel plate rheometry also known as Stefan's equation found in Derivation 3 and [19]. The condition of zero thickness was not approximated in this study, as suggested in [19] for accurate viscosity determination. Nevertheless, despite a limited accuracy in viscosity, the relative flow behavior of different alloys, which is of interest here, is clearly revealed by the present data.

In situ pulse-echo ultrasonic measurements using 25 MHz shear transducers (Ultran) were used to measure the shear sound velocity of 8mm diameter rods heated from room temperature through 410 °C with a heating rate of approximately 5 K/min. The detailed experimental setup is fully described in Lind's Caltech PhD Dissertation [20].

Samples were prepared for TEM by dimple grinding 50 $\mu$ m thick foils from both sides and then ion milling. The ion milling was done at -100 °C, 9 degrees milling angle, 3.5kV and 7.0mA. Diffraction patterns were obtained as well as bright field and dark field images at 1400000x.

## 6.4 Results and Discussion

### 6.4.1 Heat Capacity Measurements

A DSC scan conducted at 20 K/min of a  $Zr_{30}Ti_{30}Be_{40}$  alloy is presented in Figure 6.1. If we assume two phases, then the ratio  $\Delta c_{p1}/(\Delta c_{p1} + \Delta c_{p2})$  should give some information about the fraction of phase one in the alloy. To determine what information can be gained, a brief discussion of fragility is necessary.

Fragility ( $m$ ) is a measure of a liquid's resistance to flow with temperature, or put differently, a resistance to changes in medium range order. Mathematically,

$m = \frac{\partial \text{Log}(\eta)}{\partial (T_g/T)}$  which is the slope of the  $\text{Log}(\eta(T_g/T))$  curve. A liquid with low fragility

resists flow and therefore has a lower configurational entropy ( $S_{\text{config}}$ ) than a more fragile liquid [16]. Liquids with low fragilities exhibit smaller jumps in heat capacity at the glass transition temperature because  $T^* \Delta c_p = S_{\text{config}}$ . Therefore, the fraction of phase one is given by the ratio  $\Delta c_{p1}/(\Delta c_{p1} + \Delta c_{p2})$  if the two liquids are assumed to have similar fragilities.

More thorough examination of the ZrTiBe system reveals many compositions with moderate GFA = 1 - 6mm that exhibit apparent double glass transitions, similar to the  $Zr_{36}Ti_{24}Be_{40}$  alloy, upon heating in the DSC. The alloys with the best GFA are along the  $(Zr_aTi_{1-a})_{65}Be_{35}$  composition line, but larger variations in fraction of phase 1 as a function of composition are found along the  $(Zr_aTi_{1-a})_{60}Be_{40}$  line. The data is analyzed using the similar fragility assumption so that the fraction of phase 1 =  $\Delta c_{p1}/(\Delta c_{p1} + \Delta c_{p2})$ . A plot of  $\Delta c_{p1}/(\Delta c_{p1} + \Delta c_{p2})$  versus Zr concentration is found in Figure 6.2 for the Be = 35 and Be = 40 pseudo binary lines. Linear fits are included in Figure 6.2 and have  $R^2$  values greater than 0.99. The goodness of fit of the linear relationship suggests that a rule

of mixtures analysis could be applied to determine the compositions where a single phase alloy would be expected. The compositions into which the alloy appears to be phase separating are given by  $\Delta c_{p1}/(\Delta c_{p1} + \Delta c_{p2}) = 1$  for all phase 1 and  $\Delta c_{p1}/(\Delta c_{p1} + \Delta c_{p2}) = 0$  for all phase 2.

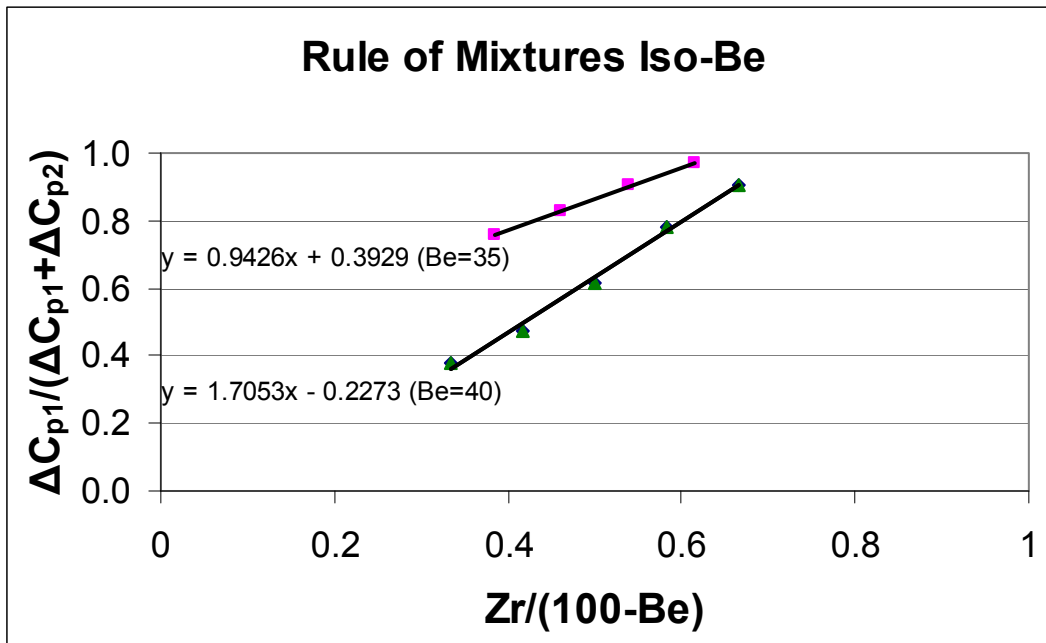


**Figure 6.2:** Plot of  $\Delta c_{p1}/(\Delta c_{p1} + \Delta c_{p2})$  versus Zr concentration gives fraction of phase 1 assuming two glassy phases with similar fragilities. Linear fits indicate rule of mixtures analysis is appropriate and suggests a metastable miscibility gap in SCLR.

Along the Be = 35 line we extrapolate to the point where  $\Delta c_{p1}/(\Delta c_{p1} + \Delta c_{p2}) = 1$  and find that the composition  $Zr_{42}Ti_{23}Be_{35}$  should exhibit a single jump in heat capacity at  $T_{g1}$  but unfortunately, the variation in  $\Delta c_{p1}/(\Delta c_{p1} + \Delta c_{p2})$  versus Zr concentration is not steep enough to find a composition where  $\Delta c_{p1}/(\Delta c_{p1} + \Delta c_{p2}) = 0$ . In Table 6.1, we see that near the composition predicted to show all phase 1 along the Be = 35 line, alloys do not have a visible second jump in heat capacity. However, along the Be = 40 line we can extrapolate to compositions where  $\Delta c_{p1}/(\Delta c_{p1} + \Delta c_{p2})$  equals 1 or 0. These compositions are  $Zr_{43}Ti_{17}Be_{40}$  for all phase 1 and  $Zr_8Ti_{52}Be_{40}$  for all phase 2. The GFA of the

Zr<sub>8</sub>Ti<sub>52</sub>Be<sub>40</sub> alloy was poor and an amorphous sample was obtainable only in thin foils. The DSC scans of Zr<sub>45</sub>Ti<sub>15</sub>Be<sub>40</sub> and Zr<sub>8</sub>Ti<sub>52</sub>Be<sub>40</sub> and a two phase glass midway along the composition line Zr<sub>30</sub>Ti<sub>30</sub>Be<sub>40</sub> are shown in Figure 6.3. The rule of mixtures analysis predicted the compositions where a single phase glass would exist and we now have some evidence of the compositions that the two phase glasses are separating into. Note that the glass transition temperatures of each phase are fairly consistent between the two phase and single phase glasses and that the overall jumps in heat capacity  $\Delta c_{p1} + \Delta c_{p2}$  are similar along each iso Be line. The Zr<sub>8</sub>Ti<sub>52</sub>Be<sub>40</sub> alloy likely exhibits a smaller  $\Delta c_{p1} + \Delta c_{p2}$  value because of early onset of crystallization. Thermodynamic data of the compositions including glass transition temperatures and  $\Delta c_p$  values is found in Table 6.1.

**Table 6.1:** DSC data for alloys considered in this article. Data shown in parentheses taken at 5 K/min. Other data taken at 20 K/min. Temperatures in °C.  $\Delta c_{p1}$  values in J/(g\*K).

Composition	T <sub>g1</sub>	$\Delta c_{p1}$	T <sub>g2</sub>	$\Delta c_{p2}$	$\Delta c_{p1}/(\Delta c_{p1} + \Delta c_{p2})$
Zr <sub>25</sub> Ti <sub>40</sub> Be <sub>35</sub>	301.7	0.275	362	0.089	0.76
Zr <sub>30</sub> Ti <sub>35</sub> Be <sub>35</sub>	304.1	0.328	364.1	0.069	0.83
Zr <sub>35</sub> Ti <sub>30</sub> Be <sub>35</sub>	305.7	0.366	364.4	0.039	0.90
Zr <sub>40</sub> Ti <sub>25</sub> Be <sub>35</sub>	303.7	0.339	367.3	0.01	0.97
Zr <sub>45</sub> Ti <sub>20</sub> Be <sub>35</sub>	303.2	0.43	N/A	0	1
Zr <sub>8</sub> Ti <sub>52</sub> Be <sub>40</sub>	N/A	0	379.9	0.25	0
Zr <sub>20</sub> Ti <sub>40</sub> Be <sub>40</sub>	324.9 (320)	0.167	377.6 (363)	0.271	0.38
Zr <sub>25</sub> Ti <sub>35</sub> Be <sub>40</sub>	319.0 (311)	0.198	379.3 (360)	0.218	0.48
Zr <sub>30</sub> Ti <sub>30</sub> Be <sub>40</sub>	323.6 (317)	0.261	375.2 (360)	0.164	0.61
Zr <sub>35</sub> Ti <sub>25</sub> Be <sub>40</sub>	312.2	0.303	377.8	0.086	0.78
Zr <sub>40</sub> Ti <sub>20</sub> Be <sub>40</sub>	319.3	0.346	374.5	0.035	0.91
Zr <sub>45</sub> Ti <sub>15</sub> Be <sub>40</sub>	323.9	0.344	N/A	0	1
Zr <sub>30</sub> Ti <sub>30</sub> Be <sub>32</sub> Cu <sub>8</sub>	(306)		(355)		

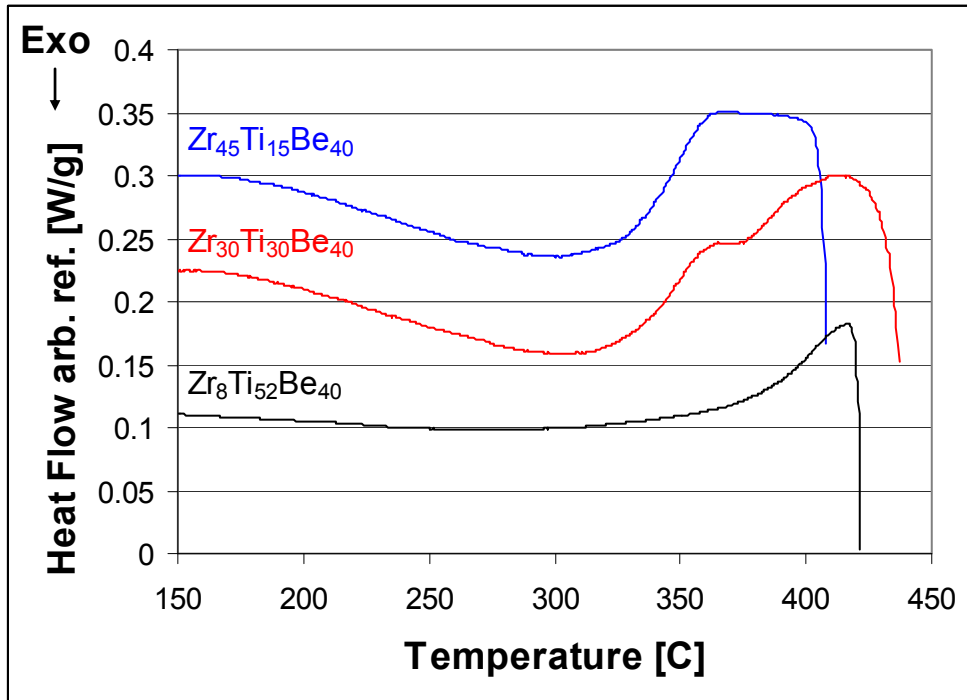


**Figure 6.3:** 20 K/min DSC scans of alloys predicted to show only one phase from rule of mixtures analysis and one intermediate two phase composition.

It is interesting to note that both the simple ZrTiBe glasses and the quinary Vitreloy compositions appear to separate into a Zr rich and a Ti rich phase. The ZrTiBe glasses differ from the Vitreloy glasses in that they exhibit the two phase behavior without any annealing in the SCLR. This suggests that the phase separation is more favorable in the ternary system. It is also likely that annealing causes the glass to relax toward the stable crystal phase as was seen in the Vitreloy glasses. This data lends itself to expression in a metastable phase diagram exhibiting a liquid miscibility gap with the endpoint compositions  $Zr_8Ti_{52}Be_{40}$  and  $Zr_{43}Ti_{17}Be_{40}$ . The metastable phase diagram is shown in Figure 6.4.

### Miscibility Gap $\text{Be} = 40$

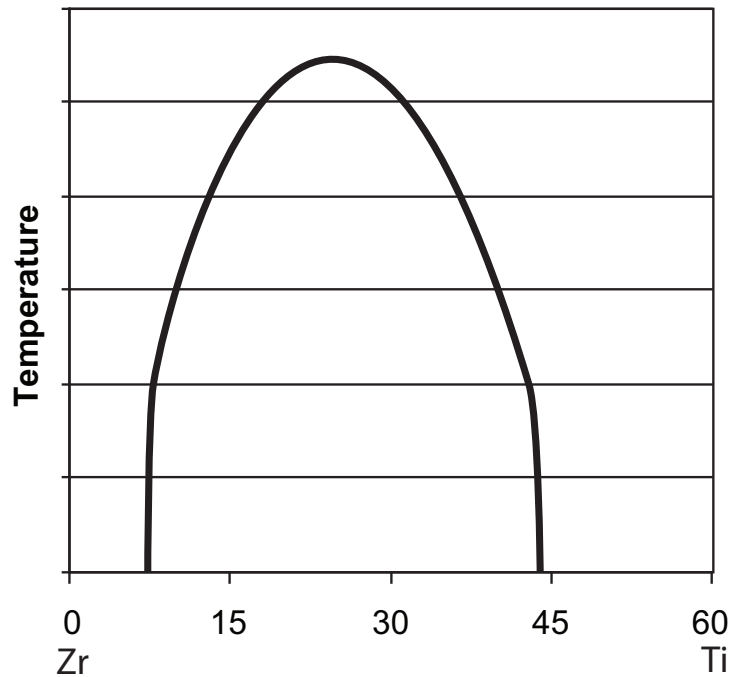


**Figure 6.4:** Sketch of the metastable miscibility gap in SCLR of  $(\text{Zr}_a\text{Ti}_{1-a})_{60}\text{Be}_{40}$ . Endpoint compositions are known, but temperature bounds are not.

The explanation of the apparent double  $T_g$  as a single  $T_g$  with an exothermic ordering event would be more plausible if only the glass exhibiting all phase 1 at  $\text{Zr}_{43}\text{Ti}_{17}\text{Be}_{40}$  had been found. In this case, one could argue that the ordering event becomes less and less thermodynamically favorable as Zr content increases until the transition disappears. However, given the discovery of the  $\text{Zr}_8\text{Ti}_{52}\text{Be}_{40}$  composition that shows only one jump in heat capacity at the temperature corresponding to the apparent  $T_{g2}$ , this exothermic ordering event explanation seems unlikely. While the present work does not prove the existence of two glassy phases in this system, it does present convincing evidence that a two phase glass is the most likely explanation. In the rest of this article, the assumption of a two phase glass is made to explain the observed phenomena.

### 6.4.2 Rheology

The flow of liquids with multiple phases is most simply divided into two limiting cases for ideal mixtures. Variations of these ideal cases have been proposed to explain the flow of other types of liquid mixtures. Very complicated analysis is possible for non-Newtonian effects and can consider interfacial energies between the layers, but we seek a qualitative picture of what to expect from viscosity as a function of temperature plots. Both cases consider a liquid mixture with parallel layers or laminae. The applied shear stress is orthogonal to the layers in Case 1. The applied shear stress is parallel to the layers in Case 2. A simple analysis of these cases can be found in Derivation 8 and [21]. The results of the analysis find that viscosities,  $\eta$ , are additive for fluid mixtures resembling Case 1, and fluidities,  $\phi = 1/\eta$ , are additive for mixtures resembling Case 2. The measured viscosity is just a volume weighted average of the individual component viscosities or fluidities depending on which case better approximates the mixture of interest. This resembles the analysis of resistors in series or parallel. In immiscible fluids, the layers resist indefinite extension and a case similar to Case 1 results [21].

In the two phase amorphous  $(Zr_aTi_{1-a})_{60}Be_{40}$  alloys, one would expect to see three regions of flow. The first region is at temperatures below  $T_{g1}$  where the sample would behave like a solid and little or no flow would be observed. The second region covers the temperature range  $T_{g1} < T < T_{g2}$ . In region 2, we should see a slope change in the viscosity versus temperature curve as the liquid + solid solution begins flow. The third region spans the temperature range  $T_{g2} < T < T_x$ . In region three, the sample should exhibit flow characteristic of a two phase liquid. The sample begins to crystallize and flow stops at  $T_x$ . Therefore, a flat  $\eta(T)$  relationship is expected in region one, followed

by a slightly decreasing  $\eta(T)$  slope in the solid + liquid solution in region 2, and finally a large decrease in the  $\eta(T)$  slope in region 3 as both liquids begin to soften and flow. Additionally, we should see a compositional effect causing lower measured values of viscosity for a given temperature in alloys with a larger fraction of the low  $T_g$  phase. The three regions should be visible in the  $\eta(T)$  plots regardless of whether the alloys exhibit flow characteristics governed by additive viscosity or additive fluidity cases.

Three alloys along the  $Be = 40$  line with moderate GFA and varying fractions of the two phases were chosen to examine the flow characteristics of the alloys in the two phase region. The chosen alloys were  $Zr_{20}Ti_{40}Be_{40}$ ,  $Zr_{25}Ti_{35}Be_{40}$ , and  $Zr_{30}Ti_{30}Be_{40}$  with 35%, 48%, 61% of phase 1 respectively (as measured by the  $\Delta c_{p1}/(\Delta c_{p1} + \Delta c_{p2})$  method). Plots of  $\eta(T)$  are shown for the three alloys in Figure 6.5. The three flow regions are visible in the plots and correlate well to the  $T_g$  values measured at the same heating rate in the DSC. We also see the composition effect causing lower measured viscosities at a given temperature for alloys with higher fractions of the low  $T_g$  phase. The horizontal region in the  $\eta(T)$  plots at  $T_{g2}$  is not understood and may be due to the small diameter of the samples tested.

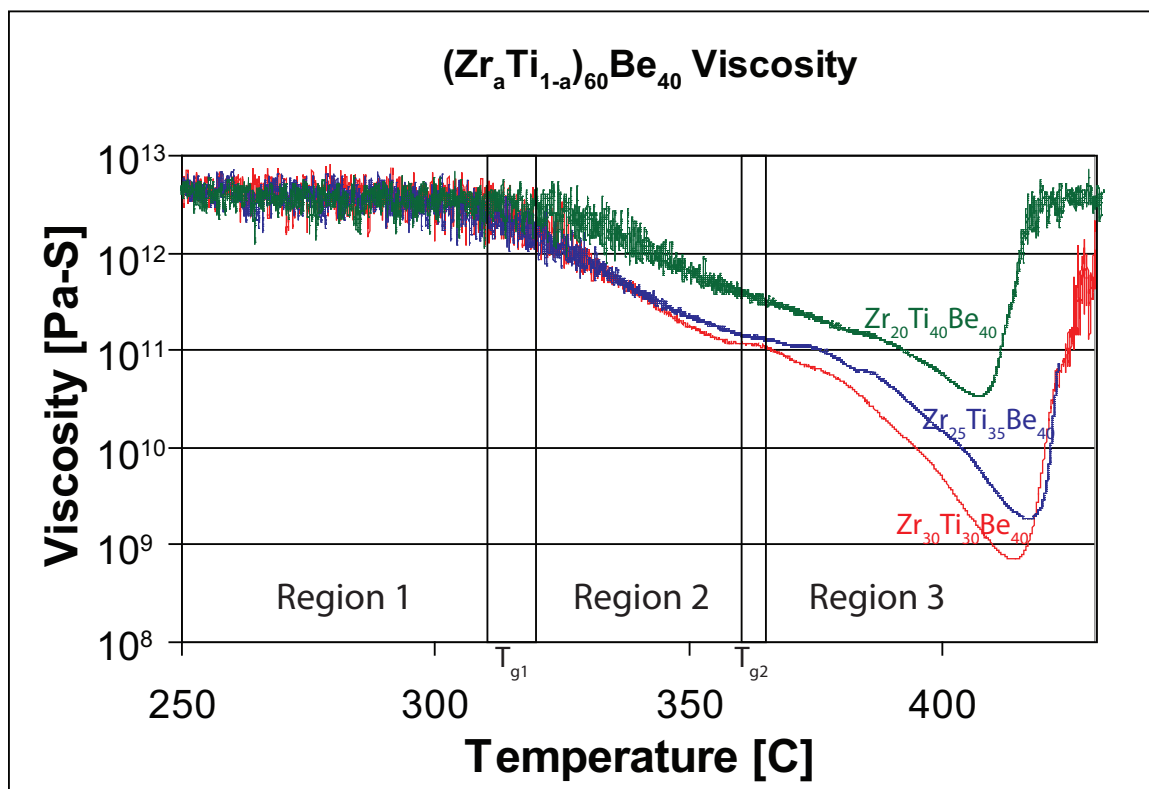


**Figure 6.5:**  $\eta(T)$  plots for three alloys with differing fractions of phase 1, showing apparent double glass transition. The test specimens were 1mm diameter x 1.8mm tall rods of  $Zr_{20}Ti_{40}Be_{40}$  (38% phase 1),  $Zr_{25}Ti_{35}Be_{40}$  (48% phase 1), and  $Zr_{30}Ti_{30}Be_{40}$  (61% phase 1) deformed under a force of 1400 mN at 5 K/min in a TMA. Region 1 corresponds to a solid-solid mixture with no deformation. Region 2 corresponds to solid-liquid mixture and minimal deformation indicated by shallow slope of  $\eta(T)$ . Region 3 is a liquid-liquid mixture with the greatest deformation rate indicated by the steepest  $\eta(T)$  slope. The scatter in first and second glass transitions as measured in 5 K/min DSC scans shown by parallel black vertical lines.

Additions of Cu were found to increase the GFA and the temperature range of the SCLR while maintaining the two discontinuities in heat capacity for some of these alloys. 3mm diameter samples of  $Zr_{30}Ti_{30}Be_{32}Cu_8$  were cast fully amorphous and  $\eta(T)$  was measured for as-cast samples and samples annealed at 410 °C for 100 s above  $T_{g2}$ .  $Zr_{30}Ti_{30}Be_{32}Cu_8$  has 63% phase 1 as measured by the  $\Delta c_{p1}/(\Delta c_{p1} + \Delta c_{p2})$  method.  $\eta(T)$  plots for the as-cast and annealed samples are shown in Figure 6.6. The  $\eta(T)$  plots are very similar for both samples. Three flow regions are again visible and the horizontal region after  $T_{g2}$  is not present. The transition from the first to the second flow region

happens at  $T_{g1}$  as expected, but the second decrease in slope of  $\eta(T)$  does not happen until 50 degrees above  $T_{g2}$ .

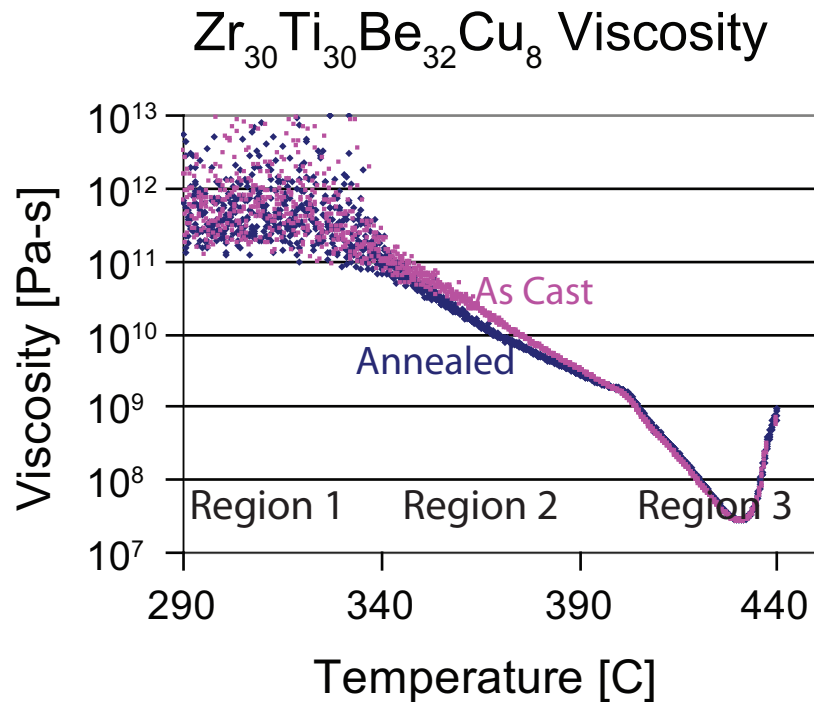


**Figure 6.6:**  $\eta(T)$  plots for as-cast and annealed samples of  $Zr_{30}Ti_{30}Be_{32}Cu_8$ . The test specimens were 3mm diameter x 3mm tall rods deformed under a force of 1400 mN at 5 K/min in a TMA. The annealed sample was heated to 410 °C for 100 s and shows a slightly lower viscosity than the as-cast sample in region 2. Both samples show similar flow behavior in the SCLR. The flow regions and glass transitions do not align for these samples as was observed for the  $(Zr_aTi_{1-a})_{60}Be_{40}$  compositions in Figure 6.5.

Viscosity versus temperature measurements show two relaxation events as would be expected by a two phase glass. These relaxation events are evidenced by changes in the slope of the viscosity vs temperature curves but the slope change does not happen at  $T_{g2}$  as one would expect.

#### 6.4.3 Shear Modulus

The shear modulus as a function of temperature  $G(T)$  provides another method to observe relaxation phenomena in the SCLR of glasses. As a glass transitions from solid-like to liquid-like behavior at the glass transition temperature, a softening in shear

modulus occurs [16]. In a two phase glass, one would expect two softening events corresponding to the two glass transition temperatures. Two in situ shear modulus measurements were conducted on the  $Zr_{30}Ti_{30}Be_{32}Cu_8$  alloy. The first measurement was masked by deformation of the glass in the SCLR because the samples height decreased as it expanded to tightly fill the holder. The second measurement gave  $G(T)$  for a sample heated past  $T_{g2}$  once. The second  $G(T)$  measurement is shown in Figure 6.7. There are two changes in the slope of  $G(T)$  roughly corresponding to the two glass transition temperatures. This is another evidence of two relaxation events in the SCLR of these alloys showing the apparent double glass transition.

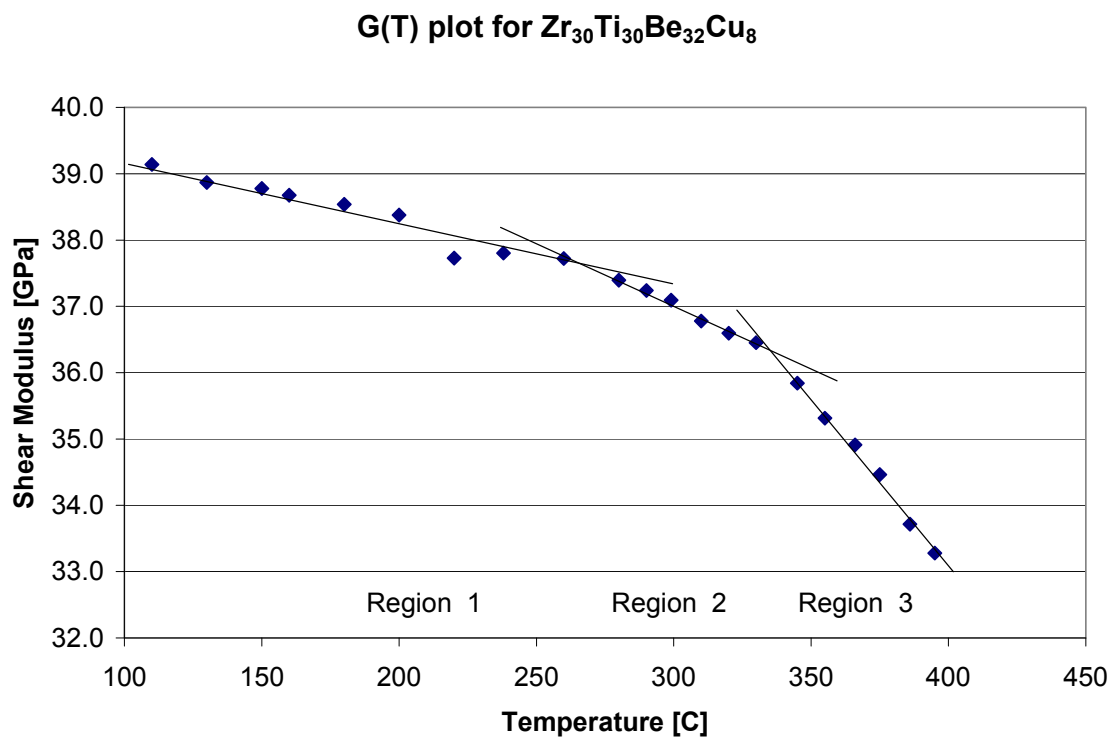


**Figure 6.7:** In situ  $G(T)$  measurements on an annealed sample of  $Zr_{30}Ti_{30}Be_{32}Cu_8$  showing two slope changes. These slope changes are indicative of two relaxation events in the alloy. The  $G(T)$  and  $\eta(T)$  relaxation temperatures do not correlate well for this sample.

It should be noted that the  $G(T)$  and  $\eta(T)$  relaxation temperatures do not correlate well with each other or with the temperatures corresponding to the heat capacity discontinuities observed in 5 K/min DSC scans. This could be an effect of differences in casting thickness between the samples. DSC and TMA samples were 3mm diameter rods and the sample cast for  $G(T)$  measurements was an 8mm rod. The relaxation events however were consistent in  $\eta(T)$  measurements for as-cast and annealed samples. Further investigation is warranted to determine the reason behind the large scatter in measured relaxation temperatures.

#### 6.4.4 Microscopy

One would expect good  $Z$  contrast in alloys separating into the Zr rich and Ti rich phases proposed in this paper. No  $Z$  contrast was visible with SEM imaging using a back scatter electron detector suggesting that phase separation may be smaller than the resolution of the SEM (about 100nm using our polishing technique). This would be consistent with the 13nm length scale phase separation found in the SANS work of Johnson [10]. A representative bright field image, dark field image, and diffraction pattern is included in Figure 6.8 for TEM observation of an ion milled  $Zr_{30}Ti_{30}Be_{40}$  specimen. The magnification on the TEM images is 1400000x.  $Z$  contrast imaging was attempted using a high angle annular dark field detector, but the lack of contrast made focusing and magnification difficult so no images were obtained. It is not clear that any broadening of the amorphous halos is present in the diffraction pattern. Elemental analysis using electron dispersive X-ray spectroscopy (EDS) in the TEM was unable to detect Be because of experimental limitations, but found that Zr concentration varied from 52 - 58 atomic percent with Ti making the balance. The alloy we imaged was

$Zr_{30}Ti_{30}Be_{40}$  so one would expect  $Zr = 50\%$  in a single phase sample, but this deviation from 50% is not statistically significant.

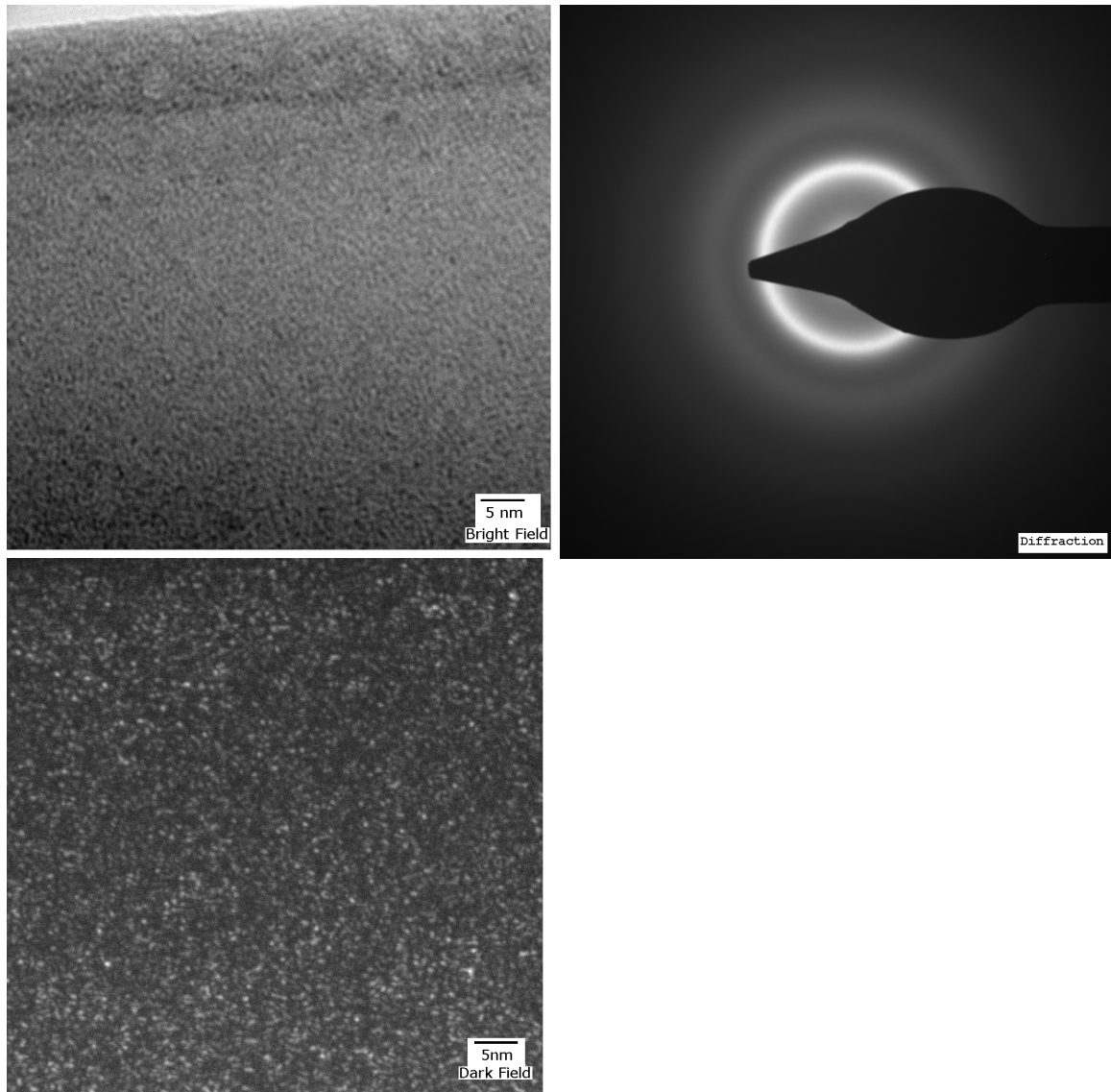


**Figure 6.8:** Dimple ground and ion milled sample imaged in TEM. Bright field and dark field images show no evidence of two phases. The diffraction pattern is characteristic of an amorphous alloy.

The lack of microscopic evidence does not preclude the existence of two phases, but it casts doubt on the likelihood that two phases are present. It is possible that ion

milling provides enough energy to randomize the two phase structure. Indeed, higher voltages and currents along with longer milling times caused another sample to nanocrystallize in regions. A well prepared, thin TEM sample is about 50nm thick. The length scale of phase separation is bounded below by the size of an STZ. If we assume a 5nm length scale, about half that observed in Vitreloy alloys, we could expect a TEM image averaged over  $\sim 10$  phase separated regions.

### 6.5 Conclusion

The discovery that many alloys in the ZrTiBe system could be cast amorphous in bulk samples allowed relaxation phenomena in the SCLR to be studied more thoroughly. Heat capacity measurements in a DSC were conducted on many compositions along the Be = 35 and Be = 40 pseudo binary lines. An anomalous double discontinuity in heat capacity in the SCLR was observed. The heat capacity discontinuities were assumed to arise from two glassy phases with different glass transition temperatures and similar fragilities. Under these assumptions, the ratio  $\Delta c_{p1}/(\Delta c_{p1} + \Delta c_{p2})$  gives the fraction of phase 1 in the glass. A plot of  $\Delta c_{p1}/(\Delta c_{p1} + \Delta c_{p2})$  versus composition reveals a linear relationship suggesting a rule of mixtures analysis would be appropriate and revealing a metastable miscibility gap in the SCLR. Extrapolating the line to  $\Delta c_{p1}/(\Delta c_{p1} + \Delta c_{p2}) = 1$  gives the composition  $Zr_{43}Ti_{17}Be_{40}$  where we would expect all phase 1. Extrapolating the line to  $\Delta c_{p1}/(\Delta c_{p1} + \Delta c_{p2}) = 0$  gives the composition  $Zr_8Ti_{52}Be_{40}$  where we would expect all phase 2. DSC scans of amorphous samples of the projected single phase compositions showed a single discontinuity in heat capacity with glass transition temperatures similar to those observed in the intermediate composition range “two phase” alloys.

Viscosity measurements as a function of temperature also revealed two relaxation phenomena.  $\eta(T)$  plots showing regions corresponding to solid-solid solutions, solid-liquid solutions, and liquid-liquid solutions were found for three  $(Zr_aTi_{1-a})_{60}Be_{40}$  compositions exhibiting the apparent two glass transitions. The  $\eta(T)$  plots also showed lower viscosities as a function of temperature for alloys with a higher concentration of the low  $T_g$ , Zr rich, phase. The temperatures at which the flow behavior changed roughly correlate to the apparent glass transition temperatures measured in the DSC. A quaternary composition exhibiting the apparent two glass transitions also showed the three regions of flow. Annealing above the second glass transition temperature did not affect the flow behavior of the quaternary glass.

In situ measurements of shear modulus as a function of temperature,  $G(T)$ , on the quaternary glass also revealed two relaxation phenomena. Decreases in the slope of the  $G(T)$  line indicated softening events and roughly correlated to measured glass transition temperatures in the DSC.

Unfortunately, attempts to image the phases in SEM and TEM were unsuccessful. If the sample thickness was larger than the length scale of phase separation, the resolution of the phases would be diminished in BF and DF imaging as electron interactions are averaged over multiple phase regions. Future work should look for evidence of composition fluctuations using small angle scattering techniques.

The low GFA of the ZrTiBe compositions makes preparation of sufficient sample for SANS difficult. SAXS and ASAXS may provide a suitable alternative method to determine the length scale of any possible phase separation. Evidence of two relaxation events in the SCLR is clear from the presented data. It is still unproven whether or not

the relaxation events arise from two glassy phases softening at  $T_g$ . It is unlikely that an explanation proposing a single glass transition with an exothermic ordering event would be sufficient to describe the relaxation phenomena observed in these experiments.

The observed double relaxation phenomena in the SCLR of the studied alloys are not yet fully understood. A two phase glass is one plausible explanation, but more microstructural evidence is needed to confirm this hypothesis.

### Chapter 6 References

- [1] M.C. Lee, J.M. Kendall, W.L. Johnson, *Appl. Phys. Lett.* 40 (1982) 382.
- [2] W.L. Johnson, *Amorphe Metallische Werkstoffe 14. Metalltagung in der DDR* (1981) 183.
- [3] R. Schulz, K. Samwer, W.L. Johnson, *J. Non-Cryst. Solids* 61 & 62 (1984) 997.
- [4] L.E. Tanner, R. Ray, *Scripta Metall.* 11 (1977) 783.
- [5] R. Hasegawa, L.E. Tanner, *Phys. Rev. B* 16 (1977) 3925.
- [6] L.E. Tanner, R. Ray, *Acta Metall.* 27 (1979) 1727.
- [7] L.E. Tanner, R. Ray, *Scripta Metall.* 14 (1980) 657.
- [8] S. Schneider, P. Thiyagarajan, U. Geyer, W.L. Johnson, *MRS Technical Report DOI 10.2172/510428* (1996).
- [9] S. Schneider, P. Thiyagarajan, U. Geyer, W.L. Johnson, *Physica B* 241 (1998) 918.
- [10] S. Schneider, U. Geyer, P. Thiyagarajan, W.L. Johnson, *Materials Science Forum Vols. 235-238* (1997) 337.
- [11] W. Liu, W.L. Johnson, S. Schneider, U. Geyer, P. Thiyagarajan, *Phys. Rev. B* 59 (1999) 11755.
- [12] Q. Zhang, W. Zhang, G. Xie, A. Inoue, *Mater. Sci. Eng. B* 148 (2008) 97.
- [13] B.J. Park, H.J. Chang, D.H. Kim, W.T. Kim, K. Chattopadhyay, T.A. Abinandanan, S. Bhattacharyya, *Phys. Rev. Lett.* 96 (2006) 245503.
- [14] L.E. Tanner, R. Ray, C.F. Cline, *US Patent #3989517*.
- [15] L.E. Tanner, R. Ray, C.F. Cline, *US Patent #4050931*.
- [16] S.R. Elliott, *Physics of Amorphous Materials*, second ed., John Wiley & Sons Inc., New York, 1990, pp. 29-69.
- [17] G. Kumar, D. Nagahama, M. Ohnuma, T. Ohkubo, K. Hono, *Scripta Mater.* 54 (2006) 801.
- [18] A. Wiest, G. Duan, M.D. Demetriou, L.A. Wiest, A. Peck, G. Kaltenboeck, B. Wiest, W.L. Johnson, *Acta Mater.* 56 (2008) 2625.
- [19] G.J. Dienes, H.F. Klemm, *J. Appl. Phys.* 17 (1946) 458.
- [20] M.L. Lind, *Dissertation, California Institute of Technology* (2008).
- [21] E.C. Bingham, *Fluidity and Plasticity*, McGraw-Hill Book Company, Inc., Ohio, 1922, pp. 81-105.

## **Chapter 7 - Conclusion**

The potential for processing metals like plastics inspired much of the research of this thesis. Some of the most important inventions and discoveries made in the course of pursuing that goal are listed below.

1. ZrTiBe + ETM increases GFA (no LTM required) (Ch2).
2. ZrTiBe + ETM alloys can be as light as Ti and as strong as tool steel (Ch2).
3. ZrTiBe alloys can be cast amorphous in 1 - 6mm diameter rods (Ch3).
4. Substitution of Be with small amounts of LTM in ZrTiBe alloys exhibiting large  $\Delta T$  values leads to alloys with even larger  $\Delta T$  values until other phases are formed with too much LTM (Ch3).
5. Cu is the most effective element at increasing  $\Delta T$  of ZrTiBe + Me alloys (Ch3).
6. The alloy with the largest  $\Delta T$  in the literature prior to my entry into grad school in 2005 was  $Zr_{44}Ti_{11}Cu_{10}Ni_{10}Be_{25}$  with  $\Delta T = 135$  °C. The current record holder.  $Zr_{35}Ti_{30}Be_{27.5}Cu_{7.5}$ , has  $\Delta T = 165$  °C and was found in the course of research for this thesis (Ch3).
7. Investigation of the viscosity and TTT properties of  $Zr_{35}Ti_{30}Be_{27.5}Cu_{7.5}$  revealed that for TPF processes requiring 60 - 300 s, this newly discovered alloy provides 10x lower processing viscosity than the other well known alloys for TPF (Ch4).
8. TTT data and  $\eta(T)$  data can be combined to give valuable processing information for TPF processes. The resulting  $\eta_{TT}$  plots tell how long one can process at a desired viscosity before crystallization (Ch5). This concept will be further discussed later in the conclusion.

9. The discovery of  $Zr_{35}Ti_{30}Be_{27.5}Cu_{7.5}$  with  $\Delta T = 165$  °C allowed injection molding of a metallic glass to be demonstrated for the first time (Ch5).
10. The discovery of bulk glass formers in the ZrTiBe system facilitated a better understanding of the SCLR of these alloys and allowed for a clear observation of two relaxation phenomena in the SCLR that is likely related to the phase separation observed in Vitreloy alloys upon annealing in the SCLR (Ch6).
11. ZrTiBe + Me compositions exhibit very low corrosion rates in 50% w/w NaOH, 0.6M NaCl, and 10x PBS (A1).
12. ZrTiBe + Me compositions have corrosion rates varying from 50 MPY to  $10^7$  MPY in 12M HCl and show a log linear relationship with half cell potential (SHE) (A1).
13. ZrTi based Be bearing alloys show evidence of good biocompatibility (A2).
14. We discovered ZrTiBe + Me compositions with 10x better corrosion resistance in ocean water than other Zr based BMG alloys in the literature and other crystalline alloys commonly used in marine environments (A3).
15. Corrosion fatigue properties are similar to other Zr based BMG alloys despite improved corrosion resistance in 0.6M NaCl (A3). This makes the use of Zr based BMG alloys unlikely in load bearing applications in saline environments like the ocean or the human body.

My optimistic hopes for broad ranging application of these materials in the orthopaedics industry compelled me to learn about corrosion, take a cell culture class, explore pertinent literature on biocompatibility, and study fatigue of materials. That

investigation culminated in the discovery of the material's terrible corrosion fatigue properties. It is disappointing to dream about endless possibilities and then find that they will not materialize as I had imagined. However, the excitement, discovery, and learning that ensued more than compensated for the occasional disappointment.

Challenging aspects of this research have yet to be fully explored. Some of this research I hope to participate in and some may keep future grad students investigating and learning.

### **7.1 Future Research Directions**

We need to determine if phase separation is happening in the ZrTiBe system. As discussed in Chapter 6, SANS is difficult with these samples due to limited GFA so SAXS is our best option. Discussion with scientists at Argonne National Laboratory is underway and if a length scale of phase separation can be found, future microscopy attempts may be more fruitful. If no phase separation is discovered then an alternate analysis of the physics behind the two  $T_g$  phenomenon observed in the SCLR of these alloys could be explored.

While we were unable to find an alloy that would work as a drop-in replacement for plastics in TPF processes, we simplified the way we think about TPF with  $\eta_{TT}$  plots and found an alloy that has 10x lower processing viscosity than the previous best alloys for conventional TPF processes requiring 60 – 300 s. An important contribution of this work to the field of metallic glasses was the discovery that new TPF processes must be completed in well under 60 s to achieve optimum formability. A major difficulty in pursuing my research was having to wait while material heated slowly in a barrel as it moved toward crystallization. This difficulty is depicted in Figure 7.1.

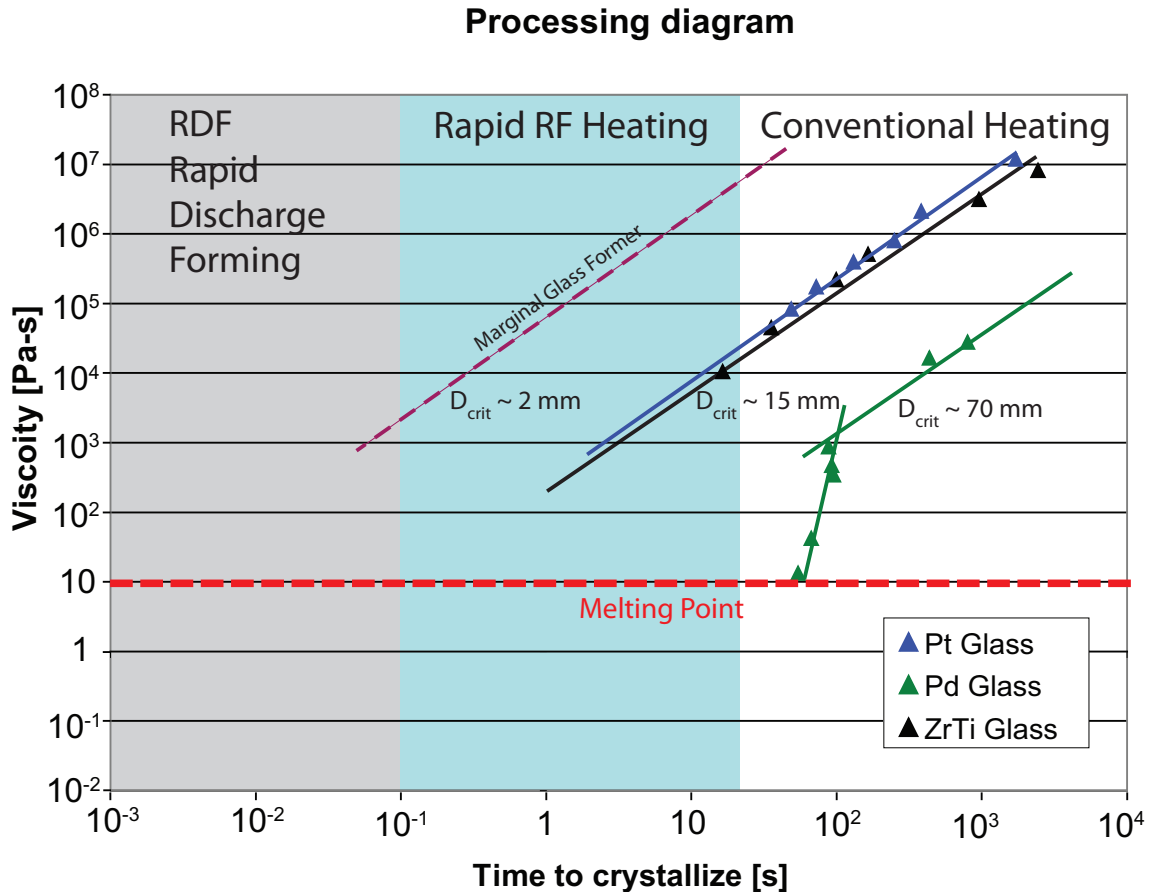


**Figure 7.1:** Heating and forming times achievable using rapid discharge forming, RF heating, and conventional heating depicted along the x axis.  $\eta_{TT}$  data for a marginal glass former is schematically represented with the dashed line.  $\eta_{TT}$  data for the Pd alloy is sketchy because it is estimated from constant heating experiments in [1-2] but shows a change in slope as the melting temperature is approached.  $\eta_{TT}$  data for Pt alloy found in [2-3], and for the Zr alloy in [2, 4].

New TPF ideas are being pursued in the Johnson group to address the need for faster processing and mainly faster heating. One way to rapidly heat metallic glass is by using RF heating. An alternating current is placed on a solenoid and the resultant eddy currents induced in nearby metallic material to counter the changing magnetic flux causes resistive heating. This method can heat a sample in under a second and with an appropriate force, the forming could be completed in less than 10 seconds depending on

part geometry. The processing window accessible using this method is shown on Figure 7.1 and labeled RF.

Another method already being explored in the Johnson group is abbreviated RDF, rapid discharge forming (not radial distribution function). It is well described in a patent application entitled “Forming of Metallic Glass by Rapid Capacitor Discharge” [5]. This method takes advantage of the unusual resistive properties of metallic glasses.

Crystalline metals usually have increasing resistances with increasing temperature. This causes crystalline material to develop hot zones near a contact with a capacitor. Metallic glasses have decreasing electrical resistance with increasing temperature. If a hot zone begins to develop in a metallic glass, the local resistance will decrease and cause the cooler regions to dissipate more of the energy resulting in uniform heating of a sample. This heating method can bring a metallic glass to a temperature in the SCLR in milliseconds. The RC time constant is the governing time scale and material can be taken all the way to the melting temperature with an appropriate sample size to capacitor energy ratio allowing access to the entire SCLR upon heating. This method theoretically allows any process viscosity up to the melt viscosity to be accessible for processing if the flow and cooling can happen quickly enough to bypass crystallization. Heating is no longer the limiting factor in process time using this processing method. This processing window is shown on Figure 7.1 and labeled RDF.

The ability to form parts with thin sections and complicated geometries is limited by the time available to heat, form, and cool them amorphous. One bonus to development of rapid heating technologies combined with large  $\Delta T$  alloys is the ability to spend much longer times in the forming step by minimizing the time required for heating.

Parts exceeding the critical casting thickness of the alloy could even be created provided sufficient time exists to cool them in the SCLR and as demonstrated in Chapter 5, the parts resulting from TPF are more reliable than die cast parts and exhibit similar strengths with less scatter in strength.

The RDF and RF methods of heating allow alloys with smaller  $\Delta T$  to be considered for TPF. Part geometries are likely more limited than larger  $\Delta T$  alloys could achieve, but alloys exhibiting desirable properties but poor GFA would become much more useful. TTT diagrams are accessible upon heating to much higher temperatures using rapid heating methods than with previous experimental methods. The SCLR of most glass forming alloys could be thoroughly explored.

I wish to close with a special thanks to Dr. Johnson for creating a fantastic atmosphere of theory and experimentation. It was exactly the education I hoped for.

### **Chapter 7 References**

- [1] J. Schroers, W.L. Johnson, R. Busch, *Appl. Phys. Lett.* 77 (2000) 1158.
- [2] W.L. Johnson, M.D. Demetriou, J.S. Harmon, M.L. Lind, K. Samwer, *MRS Bull.* 32 (2007) 644.
- [3] B.A. Legg, J. Schroers, R. Busch, *Acta Mater.* 55 (2007) 1109.
- [4] T. Waniuk, J. Schroers, W.L. Johnson, *Phys. Rev. B* 67 (2003) 184203.
- [5] W.L. Johnson, M.D. Demetriou, C.P. Kim, J.P. Schramm, US Patent application #20090236017.

**Appendix 1 - Corrosion Properties of ZrTiBe + Me Alloys in HCl**

A brief discussion about the mechanical requirements of orthopaedic hardware is presented in section 1.6.1 of the introduction. It was initially thought that many of the newly developed alloys would be ideal for orthopaedic applications from a mechanical point of view and biocompatibility considerations would be the deciding factor in whether or not the alloys could be used as implants. A survey of biocompatibility literature is daunting for a non-biologist. We verified that Ni is not biocompatible [1], but alloys containing Ni such as 316L stainless steel (13 - 15 weight % Ni) and Nitinol (55 weight % Ni) are regularly used in the body [2]. This is a striking example, but many others exist. An article by Burke [3] described 0th order biocompatibility as simply a corrosion phenomenon. If the alloy dissolves in the body then it releases ions and material that may be harmful.

We chose to do a first screening of our alloys for corrosion resistance before delving into biocompatibility. With limited equipment to test corrosion properties in our lab, we chose four highly corrosive solutions, 37% w/w HCl, 50% w/w NaOH, 0.6M NaCl, and 10x PBS, to test the corrosion resistance at 1g alloy to 30 ml static solution of three metallic glass compositions,  $Zr_{35}Ti_{30}Be_{35}$ ,  $Zr_{35}Ti_{30}Be_{29}Co_6$ , and  $Zr_{44}Ti_{11}Cu_{10}Ni_{10}Be_{25}$ , and three commonly used alloys for biomedical applications, Ti-6Al-4V, 316L Stainless Steel, and CoCrMo. Mass loss measurements were conducted at 1 week, 1 month, and 3 months and for all solutions except HCl. No mass loss was detectible until the three month time period. Inductively coupled plasma mass spectrometry (ICPMS) measurements were used to analyze the solution for dissolved elements at 3 months. 0.6M NaCl and 10x PBS solutions caused <0.1% mass loss for

## A1.2

each of the alloys after three months and ICPMS revealed no further information because the dissolved material was below the detection limit of the instrument. NaOH results did show minimal mass loss at 3 months and the results are presented in Table A1.1. It was determined that all alloys had excellent corrosion resistance in the tested solutions excluding HCl.

**Table A1.1:** Mass loss and ICPMS measurements of NaOH solution after 3 months. Solution acidified to 2% w/w HNO<sub>3</sub> as required for ICPMS.

Alloy	ZrTiBe	ZrTiBeCo	ZrTiBeCuNi	316L SS	Ti64	CoCrMo
Mass Loss	0.10%	0.10%	0.40%	<0.1%	0.20%	0.10%
Elements of Interest	Be = 75ppb	Be = 60ppb	Be = 400ppb	<50ppb	Al = 50ppb	Co,Cr=100ppb
	Zr = 1ppm	Zr = 1.7ppm	Zr = 15.7ppm		Ti = 200ppb	Mo =200ppb

Corrosion rates in HCl were enormous for most of the alloys tested.

Zr<sub>44</sub>Ti<sub>11</sub>Cu<sub>10</sub>Ni<sub>10</sub>Be<sub>25</sub> dissolved in under 10 minutes. Most of the other alloys were completely dissolved in 1 week, Zr<sub>35</sub>Ti<sub>30</sub>Be<sub>35</sub> survived for almost 1 month, and the only alloy to survive the full 3 months was CoCrMo which lost 12% of its mass. Corrosion rates in HCl were seen to vary by many orders of magnitude depending on composition. We sought to find the most corrosion resistant BMG for biological applications and given that this was an acidic chloride containing environment, we saw an opportunity to quickly differentiate corrosion resistances in a possibly biologically relevant environment. The information in this appendix is expected to be submitted as a paper entitled, "Corrosion Properties of ZrTiBe + Me Alloys in HCl," with the authors A. Wiest, S. Roberts, M.D. Demetriou, and W.L. Johnson.

### A1.1 Abstract

ZrTiBe + Me alloys, where Me is a metallic element, were immersed in concentrated HCl and the corrosion rates were measured. Depending on the fourth

### A1.3

alloying element corrosion rates from  $10^2$  -  $10^7$  MPY where MPY = 0.001 in/yr were observed. Corrosion rate and standard half cell potential of the Me element are correlated and show a log linear relationship. Surface chemistry is examined with XPS and reveals a completely oxidized surface for samples left in air and approximately 25% pure metal after 3% mass loss in HCl.

### A1.2 Introduction

Zr based bulk metallic glasses (BMG) are often noted for their high corrosion resistance [4-5]. Vitreloy 105 has corrosion rates similar to Ti-6Al-4V, CoCrMo, and 316L stainless steel in phosphate buffered saline solution. In simulated sea water (0.6M NaCl), Vitreloy 105 exhibits corrosion rates comparable to many alloys used in marine environments. The recently published  $Zr_{35}Ti_{30}Be_{35}$  and  $Zr_{35}Ti_{30}Be_{29}Co_6$  glasses have an order of magnitude higher corrosion resistance than Vit 105 in 0.6M NaCl [6].

The ZrTiBe + Me alloys where Me is an additional metallic element are the subject of this study. The corrosion resistances of the constituent elements in our base ternary alloy have been previously studied. Yau reported that “titanium is immune to all forms of corrosive attack in seawater and chloride salt solutions at ambient temperatures” in Corrosion Engineering Handbook [7]. Beryllium has been measured in oxygen free and oxygen saturated solutions at 90 °C with NaCl concentrations ranging from 28 $\mu$ M - 0.85M. Low corrosion rates are observed for oxygen free water, however the rate increases by two orders of magnitude in saturated oxygen water [8]. Zr is fully resistant to attack at temperatures up to 100 °C in saturated NaCl [7, 9]. Ti alloyed with >10% Zr is found to be more corrosion resistant in 90% H<sub>2</sub>O<sub>2</sub> solutions than pure Ti. Thus it is not surprising our alloys would exhibit high corrosion resistance in NaCl solutions.

## A1.4

In order to differentiate corrosion rates of alloys with high corrosion resistance and attempt to understand the mechanisms of corrosion better, 12M HCl was chosen as an acidic chloride containing environment. Zr has high resistance to corrosion in 12M HCl at room temperature, showing corrosion rates of  $<0.01\mu\text{m}/\text{yr}$  [9]. Ti and Be are much more susceptible in elemental form to attack in HCl. Corrosion rates spanning 5 orders of magnitude were observed for ZrTiBe + Me glasses containing 1 - 5% of an additional alloying element. Rates depended strongly on the “nobility” or standard half cell potential of the alloying element.

### **A1.3 Experimental Method**

6 - 10g master ingots were arc melted on a Cu hearth under a Ti-gettered argon atmosphere. Alloys were composed of elements  $>99.9\%$  purity and ingots with more than 0.1% variation in mass before and after melting were discarded. Alloys were cast amorphous into 2 or 3mm diameter rods depending on glass forming ability. Corrosion tests were performed in static solution of 12M HCl in loosely capped high density polyethylene bottles at room temperature using a ratio of 30 mL HCl to 1g alloy. Given the low volume of corrosive media, corrosion rates were calculated using times corresponding to mass losses of 1 - 5%.

Surface chemistry was examined using X-ray photoelectron spectroscopy (XPS). Samples of the same composition were cut from a single rod and polished to  $0.05\mu\text{m}$  surface finish. One sample from each rod was left in air to examine the passive oxygen layer. Other samples were immersed in 12M HCl until 1 - 3% mass loss was achieved. Samples were removed from 12M HCl, rinsed in methanol to minimize oxide growth, and placed in the XPS with less than 120 s of exposure to atmosphere before vacuum

pumping commenced. Final pressures were in the  $10^{-8}$  torr range. Minimal oxide growth is expected on samples immersed in HCl after removal from the corrosive solution.

#### A1.4 Results and Discussion

In order to establish a baseline corrosion rate for the ZrTiBe alloys in 12M HCl, Be was fixed at 35 atomic percent and Zr and Ti were varied in 5% increments. Be was maintained at 35% because the best glass forming region in the ternary system is along the Be = 35 line [10]. Figure A1.1 shows the corrosion rates of crystallized  $Zr_{25}Ti_{40}Be_{35}$ , and amorphous rods of  $Zr_{25}Ti_{40}Be_{35}$ ,  $Zr_{30}Ti_{35}Be_{35}$ , and  $Zr_{35}Ti_{30}Be_{35}$ . Note that the corrosion rate decreases as the Zr content of the alloy increases, and the crystalline sample has the fastest corrosion rate. The reason amorphous Zr based alloys exhibit higher corrosion resistance than identical crystalline compositions is not well understood despite other studies observing the same effect [11]. Pd40Ni40P20 shows the opposite effect with the crystalline alloy exhibiting higher corrosion resistance [12].

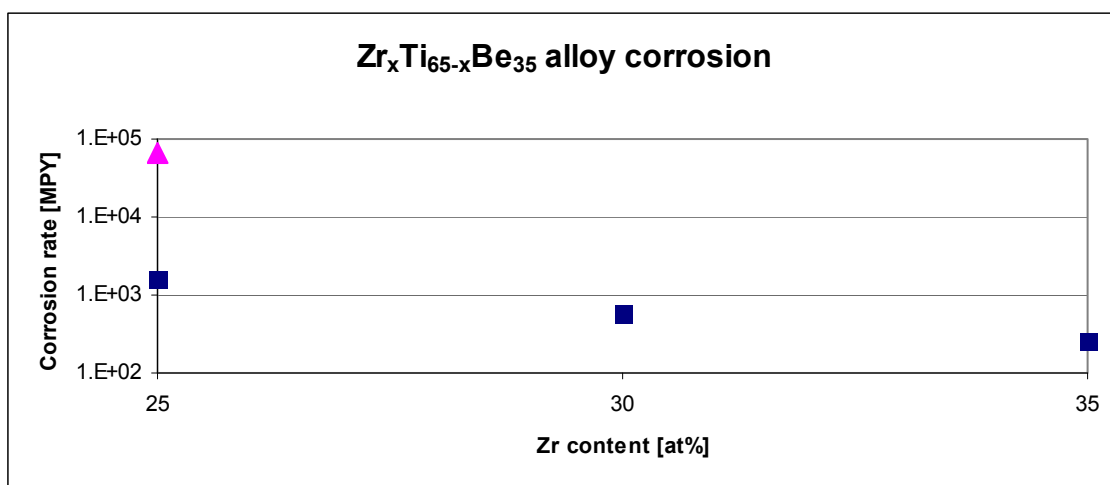


**Figure A1.1:** Corrosion rate as a function of Zr content in  $Zr_{65-x}Ti_xBe_{35}$  alloys. Squares are 2mm diameter amorphous rods. The triangle is a crystallized 2mm diameter sample.

## A1.6

$Zr_{35}Ti_{30}Be_{35-x}Me_x$  alloys, where  $x \sim 5$ , were tested in concentrated HCl. Large variations in corrosion rates were measured between different Me additions. Table A1.2 lists the alloys tested and their observed corrosion rates. Figure A1.2 plots standard half cell potential as measured against standard hydrogen electrode (SHE) of the fourth alloying element versus corrosion rate of the alloy in 12M HCl. If the Pd point is omitted, there is a nearly log linear relationship between corrosion rate and the standard half cell potential of the fourth element. With little reason to expect a log linear relationship, one can say that corrosion rate increases as nobility of the fourth alloying element increases. We see the alloy containing Al with a half cell potential  $E^0 = -1.66V$  has the lowest observed corrosion rate = 56 MPY while alloys with Pd ( $E^0 = 0.915V$ ) dissolve so quickly and violently that estimations of corrosion rate =  $10^7$  MPY are done because complete dissolution happens in under 60 s. The  $Zr_{35}Ti_{30}Be_{30}Cu_5$  alloy also exhibits very high corrosion rates =  $5 \cdot 10^4$  MPY.

**Table A1.2:** Alloy compositions and corrosion rates measured in 12M HCl.

Sample	Corrosion rate [MPY]
$Zr_{35}Ti_{30}Be_{35}$	2.6E+02
$Zr_{30}Ti_{35}Be_{35}$	5.8E+02
$Zr_{25}Ti_{40}Be_{35}$	1.6E+03
$Zr_{25}Ti_{40}Be_{35}$ crystallized	6.7E+04
$Zr_{35}Ti_{30}Be_{30}Al_5$	5.6E+01
$Zr_{25}Ti_{40}Be_{30}Cr_5$	4.3E+02
$Zr_{35}Ti_{30}Be_{29}Fe_6$	7.9E+02
$Zr_{35}Ti_{30}Be_{29}Co_6$	1.8E+03
$Zr_{35}Ti_{30}Be_{27.5}Ni_{7.5}$	2.5E+03
$Zr_{35}Ti_{30}Be_{30}Cu_5$	4.2E+04
$Zr_{35}Ti_{30}Be_{31}Ag_4$	6.4E+04
$Zr_{35}Ti_{30}Be_{31}Pd_4$	1.0E+07

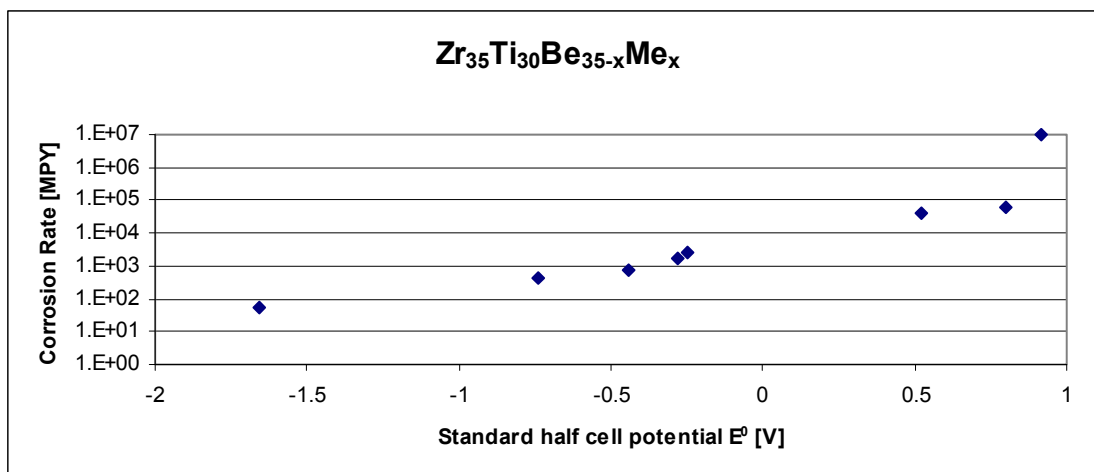


**Figure A1.2:** Plot of corrosion rate versus standard half cell potential  $E^0$  of quaternary alloying element. Table A1.2 gives compositions.

After immersion in HCl the alloy containing copper had chunks of Cu loosely adhered on the surface, particularly at the ends of the rod. Pitting corrosion was evident over the entire surface of rods removed from the HCl solution, but rods decreased uniformly in diameter and length if pit depth is neglected. Elemental Zr is known to have high corrosion rates in  $\text{CuCl}_2$  and  $\text{FeCl}_3$  solutions [9], but the measured corrosion rates for  $\text{Zr}_{35}\text{Ti}_{30}\text{Be}_{29}\text{Fe}_6 = 785$  MPY and  $\text{Zr}_{35}\text{Ti}_{30}\text{Be}_{30}\text{Cu}_5 = 42000$  MPY differ by 2 orders of magnitude. The corrosion rate may be somewhat accelerated due to the presence of dissolved Cu or Fe in the acidic chloride solution, but the nobility of the alloying element seems to be a more dominant effect. Given that Cu plates back onto the glass after dissolving into the solution, it may be beneficial to think of the corrosion process in terms of a redox reaction. Zr, Ti, and Be are all anodic elements with tough oxides, giving good corrosion resistance in many environments. When an anodic element is placed next to a cathodic element, the driving force to dissolve the anodic element is proportional to the difference in standard half cell potentials at standard conditions. Since Zr, Ti, and Be have similar half cell potentials, this difference in potential between neighbors would be

mostly dependent upon the Me added. 12M HCl is far outside standard corrosion conditions, and driving force does not predict corrosion rate, but the trend toward higher corrosion rate in alloys with large differences in standard half cell potentials of the elements suggests that the redox driving force may be an important part of the corrosion physics.

XPS was used to analyze the surface chemistry of  $Zr_{35}Ti_{30}Be_{35}$ . A polished sample left in air for 24 hours showed a fully oxidized surface. Clear oxide peaks for the  $ZrO_2$  3d<sub>3/2</sub> and 3d<sub>5/2</sub> doublet and the  $TiO_2$  2p<sub>1/2</sub> and 2p<sub>3/2</sub> peaks along with a weak BeO 1s peak were detected. Peak fitting and integration of the area determined the surface composition to be approximately  $(ZrO_2)_{42}(TiO_2)_{25}(BeO)_{33}$ . Another sample from the same rod was immersed in 12M HCl for 1 minute and then rinsed in methanol and quickly loaded into the XPS to minimize oxide growth. The surface composition was found to be  $(ZrO_2)_{45}(TiO_2)_{24}(BeO)_{31}$ . These surface compositions are quite similar and different from the bulk sample composition. Ti and Be are slightly deficient in the surface with Zr dominating the chemistry. It appears that 1 min in HCl is not long enough to alter the surface chemistry of this alloy. Another sample was polished and immersed in 12M HCl for 12 hours resulting in 3% mass loss. This sample was rinsed in methanol and quickly placed in the XPS to minimize time for oxide growth in air and a new surface chemistry was observed. Zr and Ti peaks were visible separate from the oxide peaks and accounted for approximately 25% of the surface chemistry. Figure A1.3 shows the Zr and Ti oxide peaks for the sample left in air and the oxide + metallic peaks for the sample immersed in HCl for 12 hours. Despite 3% mass loss, the oxide is still the dominant surface feature of the sample.

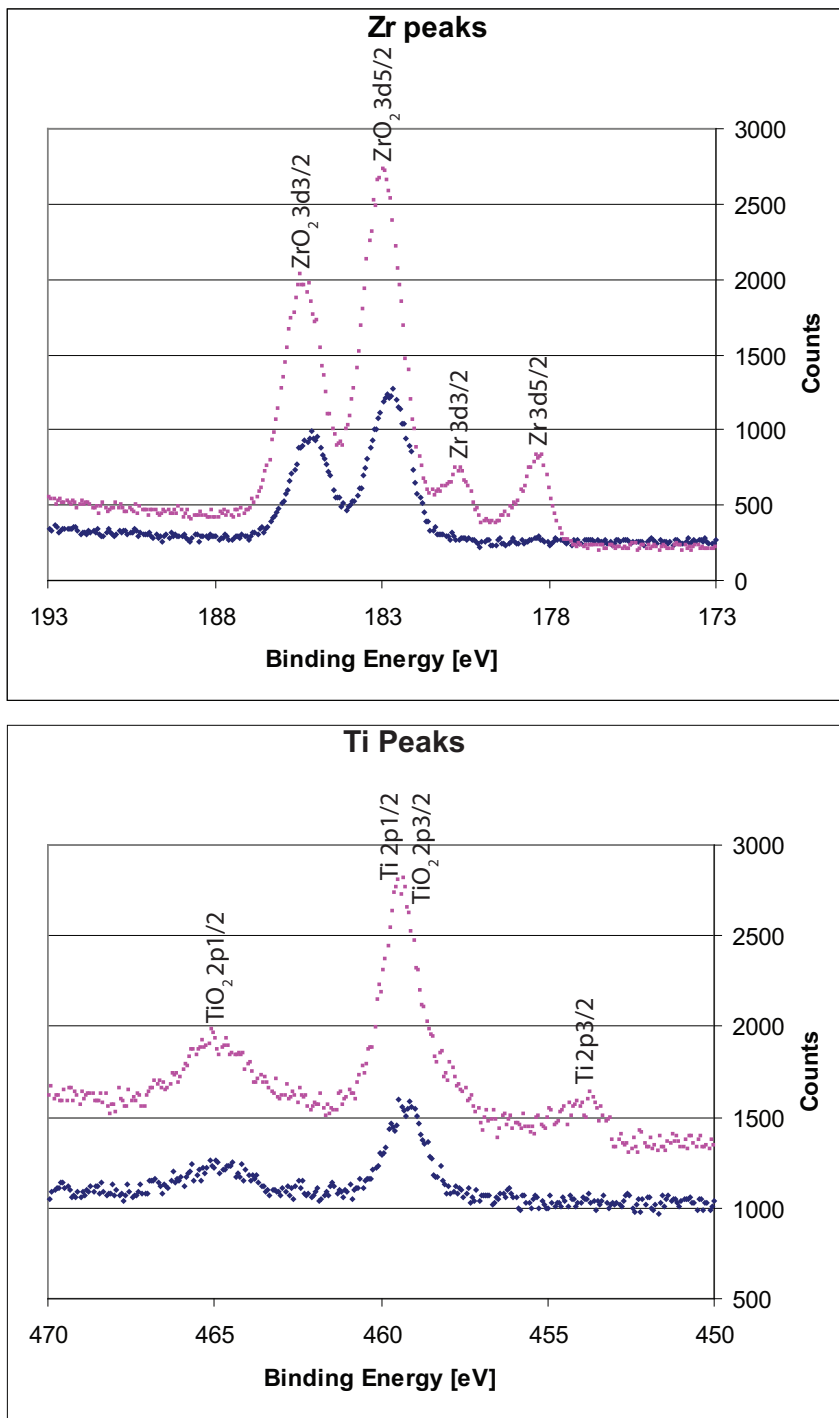


**Fig A1.3:** High resolution XPS scans of  $Zr_{35}Ti_{30}Be_{35}$  after sitting in air for 24 hours (blue) and after being immersed in 12M HCl for 12 hr resulting in 3% mass loss (pink).

**A1.5 Conclusion**

ZrTiBe alloys are shown to have higher corrosion resistance as the Zr content is increased. A crystallized rod of the  $Zr_{25}Ti_{40}Be_{35}$  composition exhibits much higher corrosion rates than the glassy rods. Corrosion rates from 56 MPY to  $10^7$  MPY are observed when approximately 5% of a metallic element is substituted for Be in  $Zr_{35}Ti_{30}Be_{35}$  compositions. The Log of the corrosion rate seems linearly correlated with standard half cell potential or nobility of the alloying element where, counterintuitively, more noble elements cause higher corrosion rates. XPS reveals a completely oxidized surface with surface chemistry differing from the bulk alloy. After dissolution in HCl resulting in 3% mass loss, the surface reveals approximately 25% of the metal is in the unoxidized state.

**Appendix 1 References**

- [1] M. Uo, F. Watari, A. Yokoyama, H. Matsuno, T. Kawasaki, *Biomaterials* 20 (1999) 747.
- [2] J.F. Burke, P. Didisheim, D. Goupil, J. Heller, J.B. Kane, J.L. Katz, S.W. Kim, J.E. Lemons, M.F. Refojo, L.S. Robblee, D.C. Smith, J.D. Sweeney, R.G. Tompkins, J.T. Watson, P. Yager, M.L. Yarmush, in: B.D. Ratner, A.S. Hoffman, F.J. Schoen, J.E. Lemons (Eds.), *Biomaterials Science: An Introduction to Materials in Medicine*, Academic Press, California, 1996, pp. 283-297.
- [3] G.L. Burke, *Can. Med. Assoc. J.* (1940) 125.
- [4] M.L. Morrison, R.A. Buchanan, P.K. Liaw, B.A. Green, G.Y. Wang, C.T. Liu, J.A. Horton, *Mater. Sci. Eng. A* 467 (2007) 198.
- [5] M.L. Morrison, R.A. Buchanan, R.V. Leon, C.T. Liu, B.A. Green, P.K. Liaw, J.A. Horton, *J. Biomed. Mater. Res. Part A* 74A (2005) 430.
- [6] A. Wiest, G.Y. Wang, L. Huang, S. Roberts, M.D. Demetriou, P.K. Liaw, W.L. Johnson, *Scripta Mater.* in review.
- [7] T.L. Yau, in: P.A. Schweitzer (Ed.), *Corrosion Engineering Handbook*, Marcel Dekker, Inc., New York, 1996, pp. 158-163, 195-252.
- [8] J.L. English, in: D.W. White, J.E. Burke (Eds.), *The Metal Beryllium*, The American Society for Metals, Ohio, 1955, pp. 533-548.
- [9] L.B. Golden, in: *Zirconium and Zirconium Alloys*, The American Society for Metals, Ohio, 1953, pp. 305-326.
- [10] A. Wiest, G. Duan, M.D. Demetriou, L.A. Wiest, A. Peck, G. Kaltenboeck, B. Wiest, W.L. Johnson, *Acta Mater.* 56 (2008) 2625.
- [11] S. Hiromoto, A.P. Tsai, M. Sumita, T. Hanawa, *Corros. Sci.* 42 (2000) 1651.
- [12] Y.F. Wu, W.C. Chiang, J. Chu, T.G. Nieh, Y. Kawamura, J.K. Wu, *Mater. Lett.* 60 (2006) 2416.

**Appendix 2 – One Year Rabbit Implantation Study of a Zirconium Based Beryllium Bearing Metallic Glass**

Aaron Wiest<sup>1</sup>, Theodore A. Waniuk<sup>2</sup>

1. Keck Engineering Laboratories, California Institute of Technology, Pasadena, California 91125, US

2. Liquidmetal Technologies, 30452 Esperanza, Rancho Santa Margarita, CA 92688, US

Zr<sub>35</sub>Ti<sub>30</sub>Be<sub>35</sub> and Zr<sub>35</sub>Ti<sub>30</sub>Be<sub>29</sub>Co<sub>6</sub> were chosen for further biocompatibility testing.

Zr<sub>35</sub>Ti<sub>30</sub>Be<sub>35</sub> exhibited one of the best corrosion resistances in HCl, had moderate GFA = 6mm, had a moderate  $\Delta T = 120$  °C and good strength to weight ratio. Zr<sub>35</sub>Ti<sub>30</sub>Be<sub>29</sub>Co<sub>6</sub> had good corrosion resistance, but much better GFA = 15mm,  $\Delta T = 155$  °C, and showed good potential for TPF. Samples were sent to a testing company, NAMSA, and short term *in vitro* and *in vivo* studies were done to assess biocompatibility. Both alloys performed as well as the control specimen and were considered biocompatible in these short term trials. A cell culture class at PCC provided me with the opportunity to test the cytotoxicity of the 10x PBS solutions in which the metals were tested for corrosion resistance over a period of three months. The solution was diluted to 1x strength and no visible damage to the cells resulted after they were exposed to the media and allowed to grow to 90% confluence. We became aware of extensive biocompatibility testing performed for Liquidmetal Technologies on samples of Vitreloy 1 and a glassy composite material called LM2 as part of Liquidmetal's effort to obtain FDA approval. Liquidmetal Technologies kindly agreed to let me summarize and publish the results of the tests. The summary was submitted to the Journal of Materials Science: Materials in Medicine under the title “One Year Rabbit Implantation Study of a Zirconium Based Beryllium Bearing

## A2.2

Metallic Glass,” but was not accepted. The reviewer stated that the paper seemed more appropriate for a technological review and was likely correct. It is included here because it presents important findings about the biocompatibility of ZrTiNiCuBe alloys.

### **A2.1 Abstract**

A one year implantation study in specific pathogen free New Zealand White Rabbits was performed to test the local response of bone and muscle tissue to a zirconium based beryllium bearing bulk metallic glass, LM1, and a toughened glassy composite material, LM2. Short term *in vitro* and *in vivo* studies conducted prior to the implantation study are summarized and show that both LM1 and LM2 elicit responses similar to the negative control material in each study. The implantation study shows LM1 elicits a mild but worsening response with time while LM2 is statistically similar to 316L stainless steel used as control. LM1 and LM2 have highly desirable mechanical properties including low Young’s modulus, yield strengths double those of titanium alloys, and elastic limits 5-10 times greater than crystalline metals.

### **A2.2 Introduction**

Bulk metallic glasses, BMG, are relatively new highly elastic materials with high hardness, high strength, and low modulus [1-3]. BMG are alloys composed of mixtures of elements that frustrate crystallization pathways sufficiently that samples greater than 1mm in all dimensions can be cast completely amorphous. Unlike crystalline materials which have periodic arrangements of atoms or molecules, the atoms of glasses solidify into a random structure. Crystalline materials have much higher theoretical strengths than are ever observed in nature. This is because all crystals have defects, and the defects dramatically weaken the material. Glasses, on the other hand, have near theoretical

### A2.3

properties because the structure is random and atom-size defects are nonexistent. A commercially available BMG called Vitreloy1 or LM1 with composition  $Zr_{62.6}Ti_{11.0}Cu_{13.2}Ni_{9.8}Be_{3.4}$  (weight percent) is of particular interest to the BMG community because of its exceptional glass forming ability (parts with sections >1 inch thickness can be cast) and good mechanical properties [4]. LM1 has a tensile yield stress of  $\sim 1.9$  GPa and a Vicker's hardness of  $\sim 600$  Kg/mm<sup>2</sup> (double that of 316L stainless steel). It has an elastic limit of 2% (10 times greater than most crystalline metals) and a Young's modulus of  $\sim 90$ GPa (less than half the value of 316L stainless steel and 20% lower than titanium alloys) [5]. The disadvantage of LM1 is that it fails catastrophically if the yield strength is exceeded. Such stresses would never be observed in biological environments, but efforts have been made to avoid the catastrophic failure mode. Another commercially available alloy, LM2 ( $Zr_{71.9}Ti_{9.2}Cu_{6.2}Ni_{4.6}Be_{1.6}Nb_{6.5}$ ), is a composite material with a glassy matrix and soft crystalline inclusions that absorb energy when failure initiates, allowing for graceful failure and plastic elongation of up to 5% in tension [6]. This material yields at 1.4 GPa. Both LM1 and LM2 have been studied in fatigue loading conditions and values ranging from 60 MPa - 700 MPa at  $10^7$  cycles have been reported, so no conclusive statements can be made about the fatigue endurance limit [7-9]. This, along with corrosion fatigue characterization, is an area where more research is needed.

In the simplest approximation, cytotoxicity can be thought of as a corrosion problem [10]. Given the high cytotoxicity of metallic salt forms of nickel, copper and beryllium [11], it may seem surprising that a material containing all three would be tested for biocompatibility. However, due to the high corrosion resistance of these alloys, both

## A2.4

LM1 and LM2 performed as well as the negative control in a wide range of *in vitro* and *in vivo* tests. Zr based BMG exhibit excellent corrosion resistance in saline environments. In a study conducted by Morrison et al., a Zr based BMG was shown to have corrosion resistance higher than 316L stainless steel and comparable to CoCrMo and Ti-6Al-4V in a saline environment [12].

### **A2.3 Experimental Method**

Biological testing was performed by AppTec Laboratory Services or Louisiana State University Health Sciences Center Department of Orthopaedics. Studies were conducted in compliance with U.S. Good Laboratory Practice (GLP) regulations set forth in 40 CFR Part 160, 40 CFR Part 792, or 21 CFR Part 58. Samples obtained from Liquidmetal Technologies were either chemically sterilized or sterilized with steam. All extractions to obtain leachable materials from LM1 and LM2 were performed while maintaining the ratio of 60cm<sup>2</sup> to 20mL.

Samples for *in vitro* and *in vivo* tests were produced by Liquidmetal Technologies. >99% pure elements were melted under an inert argon atmosphere in a water cooled crucible and cast into plates or rods. The amorphous nature of the material was verified using X-ray spectroscopy. The material was cut and polished into specimens with the dimensions and surface finish specified by AppTec Laboratory Services or Louisiana State University Health Sciences Center Department of Orthopaedics.

### **A2.4 Preliminary Tests and Results**

The cytotoxicity of both materials was assessed using two different methods set forth in ISO10993-5. In one study, LM1 and LM2 were extracted in Eagle's Minimal

## A2.5

Essential Medium (E-MEM), supplemented with 5% (v/v) Fetal Bovine Serum (FBS) and one or more of the following: L-glutamine, HEPES, gentamicin, penicillin, vancomycin, and Fungizone at  $37 \pm 1$  °C and  $5 \pm 1\%$  CO<sub>2</sub> for 24 hours. A ratio equivalent of 60.0cm<sup>2</sup> test article and 20mL E-MEM + 5% FBS was maintained in the extraction process. L929 mouse fibroblast cells obtained from ViroMed Laboratories, Inc., Minnetonka, MN, were grown and used as monolayers in disposable tissue culture labware at  $37 \pm 1$  °C and  $5 \pm 1\%$  CO<sub>2</sub>. After the extraction period, the maintenance culture media was removed from the test culture wells and replaced with test media/extract and control media. Positive and intermediate controls were media spiked with CdCl<sub>2</sub> and negative control was normal media. All samples were tested in triplicate and cultures were evaluated for cytotoxic effects by microscopic observation after 24, 48, and 72 hour incubation periods at  $37 \pm 1$  °C and  $5 \pm 1\%$  CO<sub>2</sub>. Positive control showed nearly complete destruction of the cell layer. Intermediate control showed no extensive cell lysis or empty areas between cells, but 20 - 50% of cells were round and devoid of intracytoplasmic granules. Negative control, LM1 and LM2 showed no reactivity. In the other study, leachable extracts were allowed to diffuse through an agarose barrier and contact cultured cells. The agar was composed of 1% agarose, 1X E-MEM, and 5% FBS + supplements listed in the first study. The maintenance media was removed from the L929 cells cultured as in the first study and it was replaced with the agar mixture. The cultures were held at room temperature until the agarose solidified, and the test material was placed directly onto the agar surface for 1 hour and incubated as in the first study. At the completion of the incubation period the perimeter of the test articles was outlined in indelible ink and then removed. All cultures were flooded with 0.01% neutral red stain, incubated for 1 hour

## A2.6

and then observed microscopically. LM1, LM2 and the negative control, dram vial cap, showed no detectible zone under or around specimen, and the positive control, Davol Penrose Drain Tubing, showed definitive cytotoxic effects in a zone greater than 1cm beyond the edge of the specimen.

The propensity of the materials to cause mutation was determined by three methods outlined in ISO 10993-3. The first test was conducted on five strains of *Salmonella typhimurium*. The positive and negative controls behaved as expected and saline extracts of LM1 and LM2 showed no statistically significant tendency to induce histidine (his) reversion in *S. typhimurium* (his- to his+) caused by base changes or frameshift mutations in the genome of tester organisms.

The second test, conducted on L5178Y mouse lymphoma cells, determines the ability of a test article to induce forward mutation at the thymidine kinase (TK) locus in the presence of trifluorothymidine (TFT). TK is an enzyme that allows cells to salvage thymidine from the surrounding medium for DNA synthesis. If the thymidine analog TFT is included in the growth medium, the analog will be phosphorylated via the TK pathway and will cause cellular death by inhibiting DNA synthesis. Cells which are heterozygotes at the TK locus (TK+/-) may undergo a single-step forward mutation to the TK-/- genotype in which little or no TK activity remains. These mutants are as viable as the heterozygotes in normal medium because DNA synthesis proceeds by *de novo* synthesis pathways that do not involve thymidine as an intermediate. TK-/- mutants cannot utilize toxic analogs of thymidine. Cells which may grow to form colonies in the presence of TFT are therefore assumed to have mutated, either spontaneously or as a result of exposure to the test article, at the TK+/- locus. Neither test article extract (either

## A2.7

with or without metabolic activation) induced appreciable differences in cell density throughout the expression and recovery period as compared to the concurrent negative control.

The third test was an *in vivo* mouse micronucleus assay. The Mouse Micronucleus Assay evaluated the potential of 0.9% sodium chloride for injection (saline) and cottonseed oil (CSO) extracts of the test article to induce *in vivo* clastogenic events or damage to the mitotic spindle in polychromatic erythrocytes obtained from mouse bone marrow of CD-1 mice.

Male and female CD-1 mice were treated with one of the test article extracts, or negative or positive controls. Twenty-four and forty-eight hours after treatment, the animals were sacrificed and the bone marrow harvested. All negative control treated preparations demonstrated normal levels of spontaneously occurring aberrations while positive control treated cultures demonstrated dramatic, dose-dependant increases in aberrant cells. None of the mice treated with the test article preparations exhibited overt signs of toxicity either immediately post-treatment or during the induction period. The levels of micronucleated cells were within normal negative ranges. Based on the criteria and conditions outlined in the study protocol, the results indicate that the test article is non-mutagenic in this test system.

Hemolytic activity of LM1 and LM2 was investigated by placing the metals in direct contact with New Zealand White Rabbit blood for 1 hour, removing the test article, centrifuging, and analyzing the absorbance of the supernatant at 545nm using a standard laboratory spectrophotometer. LM1 and LM2 showed the same hemolytic activity as

## A2.8

isotonic saline and are therefore considered non-hemolytic under the test conditions employed.

In a test where isotonic saline extracts were injected intravenously into Specific Pathogen Free New Zealand White Rabbits, body temperature was measured at 30 minute intervals for 3 hours and no evidence of pyrogenicity was found.

Allergic reactions and evidence of edema or erythema induced by direct contact with the metal or injection/contact with extracts were tested according to three methods detailed in ISO 10993-10. In one study adult Hartley strain guinea pigs had topical applications of isotonic saline extracts and direct contact with the material on shaved regions of their back for 24 hours as well as intradermal injections in the back of extracts of LM1, LM2, and positive chlorodinitrobenzene and negative 316L stainless steel controls. Edema and erythema were evaluated at 24, 48, and 72 hours after treatment. LM1, LM2, and 316L stainless steel elicited no visible skin edema or erythema while the positive control showed deep lesions at the same stages validating the methodology. LM1 and LM2 showed no allergic potential in either bulk or extracted form. In the second and third tests specific Pathogen Free New Zealand White Rabbits were tested. In the second test, rabbits were treated with isotonic saline extracts of LM1 and LM2 applied via gauze patches to the flank for four hours and no local irritation or sensitization was observed. In the third test, isotonic saline and cottonseed oil extracts of LM1 and LM2 were injected intradermally into the backs of the rabbits. No local irritation in the dermal tissues of the rabbits was observed at 24, 48, or 72 hours.

An ISO10993-11 Test for Systemic Toxicity was also performed. In this test Specific Pathogen Free Albino Swiss Mice were injected intravenously with saline

extracts of LM1, LM2, or were injected intraperitoneally with cottonseed oil extracts of the materials. Control injections were saline and cottonseed oil with no extract.

Extraction was performed at 37 °C for 72 hours and dosage was 0.05mL/g. Body weight and general health were evaluated at 4, 24, 48, and 74 hours. Based on the observations it was concluded that LM1 and LM2 do not contain leachable materials that cause toxic effects as a result of a single-dose injection in mice.

Given the promising results of these *in vitro* and *in vivo* short term trials, a one year implantation study in 21 Specific Pathogen Free New Zealand White Rabbits was done to test for local effects after implantation.

### **A2.5 Long Term Implantation Study**

The tissue response to polished and bead blasted samples of LM1 and LM2 was compared to the control material, 316L stainless steel (SST) by implanting specimens into specific pathogen free New Zealand White Rabbits.

Twenty-one specific pathogen free New Zealand White Rabbits were purchased from Harlan World Headquarters, Indianapolis, IN. Animals of both sexes were used. This test method and species have historically been used to assess systemic safety in determining the biocompatibility of materials used in medical devices. The animal species, number and route of test article administration were as recommended in ISO 10993-6:1995.

Each animal was anesthetized with a 50+5 mg/kg Ketamine/Xylazine cocktail, according to SOP-0001. At the initial injection, a 0.1 mg/kg of acepromazine was added. Subsequently a surgical plane of anesthesia was maintained by injections of 50 mg/kg of Ketamine. Sterilized cylindrical implants of the two test materials and stainless steel

## A2.10

controls were implanted into the paraspinal musculature and distal femora of 21 New Zealand White Rabbits using sterile surgical technique according to SOP-0012. Each animal received two types of implants – one test material on the left side and a different one on the right side. The total number of implants per animal was 12: four in the right and four in the left paravertebral musculature, and two unicortical implants placed into each femur. Paravertebral implants were cylindrical in shape, 3mm diameter x 10mm length. Bone implants were also cylindrical in shape, 2mm diameter x 7mm length.

All animals survived the implantation procedures and through to their planned sacrifice time with no major complications. Animals were followed postoperatively daily for two weeks and then at a minimum of bi-weekly until their sacrifice date. Animals were sacrificed at 3, 6 and 12 month intervals. At the time of sacrifice, blood was withdrawn for complete blood counts and chemical analysis. Part of the liver and one kidney were retrieved for histological examination and were observed for gross evidence of abnormalities. Implants in both muscle and bone were retrieved for histological examination with some surrounding tissue. Tissues were observed for gross evidence of rejection such as necrosis, cysts or extended granulation tissues. Histologically, muscle and bone implants were evaluated and graded according to the criteria listed in Table A2.1. Transcribed results from the histological evaluations and blood chemistry and CBC are included in the supplementary materials section.

Gross examination of the implants and surrounding tissues revealed no overt signs of rejection such as cysts or necrosis and no gross evidence of local inflammation. The only significant findings were three muscle implants that had migrated to the fatty tissues. One of these was surrounded by hemorrhage without overt inflammation or necrosis.

## A2.11

Additionally, one bony implant was placed on the proximal tibia rather than the distal femur due to technical error. All retrieved kidneys and livers appeared grossly normal.

The histological data regarding bone implants show no fibrosis, degeneration or inflammatory reaction with direct apposition of bone on all three materials, and remodeling to partially or completely surround the implant. As is shown in the statistical analyses in Tables A2.2 - A2.7, these responses had no association with the implanted material. Thus for all materials, excellent compatibility with bone is in evidence.

Statistical analysis of the implant local reaction data were performed using non-parametric methods (Kruskal-Wallis); statistically significant post-hoc Student Neuman Keuls comparisons are reported where appropriate (i.e., where there is significant main effect and a post-hoc result with statistical significance). All evaluations are performed at a 0.05 significance.

The histological data regarding muscle implants show what appears to be evolving tissue responses. Histological examination showed stable encapsulation of muscle implants with minimal to mild intracapsular inflammation for all materials, but adverse response to the LM1 test material was greater than the control material at 6 and 12 months. Statistical analyses were performed on the results of the histologic analysis of the slides. The first stage of the analyses shown in Tables A2.2 - A2.7 examines the effect of materials at each time interval.

Because there were significant effects on muscle implants of fibrosis thickness, intracapsular inflammation, degeneration, extracapsular inflammation grade and distance at the 12 month time period, interaction analyses (multi-way analysis of variance) were performed to assess combined effects on the materials (SST, LM1, LM2), finish

(polished, bead blasted), and time post-implantation (3, 6, 12 months). Statistically significant post-hoc Student Neuman Keuls comparisons are reported where appropriate (i.e., when there is a significant main effect and a post-hoc result with statistical significance). Similarly, interaction trends are described where significant in Tables A2.8 – A2.12.

The results of this study suggest that LM2 creates a local tissue response that is essentially similar to that of the control material. LM1 creates a local tissue response that is substantially greater than that of the control material. Although local tissue responses of LM1 were within the mild category, trends indicated that local degeneration would continue to evolve through the one year endpoint for this material.

## **A2.6 Conclusion**

High strength Zr based Be bearing BMG and composite materials show good evidence of biocompatibility despite the presence of Cu, Ni, and Be. This is attributed to the high corrosion resistance of Zr based BMG. In short term *in vitro* and *in vivo* trials, LM1 and LM2 elicited biological responses similar to control materials. Only in the long term implantation study were statistically significant differences apparent. It was found that, independent of surface finish, LM2 creates a local tissue response similar to 316L stainless steel. LM1, however, creates a mild response worse than either SST or LM2 that appears to be increasing with time. When the compositions of LM1 and LM2 are compared, one will note that LM2 contains about half the Cu, Ni, and Be as is found in LM1 and additionally LM2 contains Nb. The data collected in these studies does not indicate which elements caused the most adverse effects, but the decrease of Cu, Ni, Be, and/or the addition of Nb improved the local tissue response to the material LM2. Given

the excellent mechanical properties of these materials and the good biocompatibility in evidence here, LM1 and LM2 may find utility as biomaterials in the future.

## Appendix 2 References

- [1] A.L. Greer, E. Ma, MRS Bull. 32 (2007) 611.
- [2] W.L. Johnson, MRS Bull. 24 (1999) 42.
- [3] A. Inoue, Acta. Mater. 48 (2000) 279.
- [4] A. Peker, W.L. Johnson, Appl. Phys. Lett. 63 (1993) 2342.
- [5] J. Black, Biological Performance of Materials: Fundamentals of Biocompatibility, fourth ed., CRC Press, Taylor & Francis Group, Florida, 2006, pp. 127-129.
- [6] C.C. Hays, C.P. Kim, W.L. Johnson, Phys. Rev. Lett. 84 (2000) 2901.
- [7] K.M. Flores, W.L. Johnson, R.H. Dauskardt, Scripta Mater. 49 (2003) 1181.
- [8] B.C. Menzel, R.H. Dauskardt, Scripta Mater. 55 (2006) 601.
- [9] G.Y. Wang, P.K. Liaw, A. Peker, B. Yang, M.L. Benson, W. Yuan, W.H. Peter, L. Huang, M. Freels, R.A. Buchanan, C.T. Liu, C.R. Brooks, Intermetallics 13 (2005) 429.
- [10] G.L. Burke, Can. Med. Assoc. J., Aug (1940) 125.
- [11] A. Yamamoto, R. Honma, M. Sumita, J. Biomed. Mater. Res. 39 (1998) 331.
- [12] M.L. Morrison, R.A. Buchanan, R.V. Leon, C.T. Liu, B.A. Green, P.K. Liaw, J.A. Horton, J. Biomed. Mater. Res. 74A (2005) 430.

**Table A2.1:** Muscle and bone implant histological grading criteria.

<b>Parameter</b>	<b>Grade</b>	<b>Description</b>
Fibrosis	0	None
	1	< 1/3 circumference
	2	1/3 < 1/2 circumference
	3	1/2 < 3/4 circumference
	4	> 3/4 circumference
		Thickness ( $\mu\text{m}$ )
Intracapsular Inflammation	0	None
	1	1-5 cells/high powered field
	2	6-10 cells/high powered field
	3	11-25 cells/high powered field
	4	26-50 cells/high powered field
	5	> 50 cells/high powered field
Degeneration	None	None
	Mild	Minimal changes - nuclear pyknosis and/or minimal loss of striation
	Moderate	Nuclear karyorhexis/karyolysis and/or extensive loss of striation
	Severe	Coagulation necrosis
Fatty Infiltration	None	None
	Mild	Focal, interfascicular and/or intermyocyte
	Moderate	Multifocal, interfascicular and/or intermyocyte
	Severe	> 3/4 Circumferential, interfascicular and/or intermyocyte
Extracapsular Inflammation	0	None
	1	1-5 cells/high powered field
	2	6-10 cells/high powered field
	3	11-25 cells/high powered field
	4	26-50 cells/high powered field
	5	> 50 cells/high powered field
	Distance ( $\mu\text{m}$ ) inclusive from implant interface	
Granulomatous Inflammation	None	None
	Mild	Focal, unicellular histiocytes or < 5 cell aggregates
	Moderate	Multifocal, unicellular histiocytes or > 5 cell aggregates
	Severe	Sheets of histiocytes and/or foreign body giant cells
Bone Remodeling	None	None - cortical hole present with or without periosteal lining
	Minimal	Focal osteoblastic/osteoclastic activity with < 1/3 encasement of the implant and/or cortex resorption
	Moderate	1/3 - 1/2 encasement of the implant and/or cortex resorption
	Extensive	> 1/2 encasement of the implant and/or cortex resorption
Necrosis	No	No evidence of necrosis
	Yes	Nuclear debris and/or capillary wall breakdown

**Table A2.2:** 3 Month Muscle Implants: Significance of Material Type vs Parameter.

Parameter		P-value	Significant Post Hocs (if applicable)
Fibrosis	Grade	0.368	N/A
	Thickness	0.093	N/A
Intracapsular Inflammation		0.075	N/A
Degeneration		0.155	N/A
Fatty Infiltration		0.553	N/A
Extracapsular Inflammation	Grade	0.227	N/A
	Distance	0.146	N/A
Granulomatous Inflammation		0.138	N/A
Necrosis		(none observed)	N/A

**Table A2.3:** 3 Month Bone Implants: Significance of Material Type vs Parameter.

Parameter		P-value	Significant Post Hocs (if applicable)
Fibrosis	Grade	(none observed)	N/A
	Thickness	(none observed)	N/A
Inflammation		(none observed)	N/A
Degeneration		(none observed)	N/A
Granulomatous Inflammation		(none observed)	N/A
Bone Remodeling		0.955	N/A
Necrosis		(none observed)	N/A

**Table A2.4:** 6 Month Muscle Implants: Significance of Material Type vs Parameter.

Parameter		P-value	Significant Post Hocs (if applicable)
Fibrosis	Grade	0.360	N/A
	Thickness	0.108	N/A
Intracapsular Inflammation		0.010	LM1>SST
Degeneration		0.560	N/A
Fatty Infiltration		0.331	N/A
Extracapsular Inflammation	Grade	0.136	N/A
	Distance	0.242	N/A
Granulomatous Inflammation		(none observed)	N/A
Necrosis		0.643	N/A

## A2.16

**Table A2.5:** 6 Month Bone Implants: Significance of Material Type vs Parameter.

Parameter		P-value	Significant Post Hocs (if applicable)
Fibrosis	Grade	(none observed)	N/A
	Thickness	(none observed)	N/A
Inflammation		(none observed)	N/A
Degeneration		(none observed)	N/A
Granulomatous Inflammation		(none observed)	N/A
Bone Remodeling		0.153	N/A
Necrosis		(none observed)	N/A

**Table A2.6:** 12 Month Muscle Implants: Significance of Material Type vs Parameter.

Parameter		P-value	Significant Post Hocs (if applicable)
Fibrosis	Grade	0.091	N/A
	Thickness	0.0485	LM1>LM2
Intracapsular Inflammation		0.003	LM1>SST; LM1>LM2
Degeneration		0.018	LM1>SST; LM1>LM2
Fatty Infiltration		0.061	N/A
Extracapsular Inflammation	Grade	0.003	LM1>SST; LM1>LM2
	Distance	0.0002	LM1>SST; LM1>LM2
Granulomatous Inflammation		(none observed)	N/A
Necrosis		0.145	N/A

**Table A2.7:** 12 Month Bone Implants: Significance of Material Type vs Parameter.

Parameter		P-value	Significant Post Hocs (if applicable)
Fibrosis	Grade	(none observed)	N/A
	Thickness	(none observed)	N/A
Inflammation		(none observed)	N/A
Degeneration		(none observed)	N/A
Granulomatous Inflammation		(none observed)	N/A
Bone Remodeling		0.460	N/A
Necrosis		(none observed)	N/A

**Table A2.8:** Fibrosis Thickness Interaction Analysis: Muscle Implants by Time, Finish, and Material.

<b>Factor</b>	<b>P-value</b>	<b>Post Hoc (Or Interaction Tendencies)</b>
Material	0.336	N/A
Finish	0.137	N/A
Time	0.886	N/A
Material * Finish	0.471	N/A
Material * Time	0.129	N/A
Finish * Time	0.764	N/A
Material * Finish * Time	0.428	N/A

**Table A2.9:** Intracapsular Inflammation Interaction Analysis: Muscle Implants by Time, Finish, and Material.

<b>Factor</b>	<b>P-value</b>	<b>Post Hoc (Or Interaction Tendencies)</b>
Material	0.0001	LM1>SST; LM1>LM2
Finish	0.041	Bead Blasted > Polished
Time	0.046	12 months > 3 months
Material * Finish	0.167	N/A
Material * Time	0.001	LM1 increases with time
Finish * Time	0.386	N/A
Material * Finish * Time	0.797	N/A

**Table A2.10:** Degeneration Interaction Analysis: Muscle Implants by Time, Finish, and Material.

<b>Factor</b>	<b>P-value</b>	<b>Post Hoc (Or Interaction Tendencies)</b>
Material	0.885	N/A
Finish	0.026	Bead Blasted > Polished
Time	0.866	N/A
Material * Finish	0.894	N/A
Material * Time	0.006	LM1 increases; SST decreases
Finish * Time	0.644	N/A
Material * Finish * Time	0.039	Material and finish affect time response

## A2.18

**Table A2.11:** Extracapsular Inflammation Grade Interaction Analysis: Muscle Implants by Time, Finish, and Material.

<b>Factor</b>	<b>P-value</b>	<b>Post Hoc (Or Interaction Tendencies)</b>
Material	0.0003	LM1>SST; LM1>LM2
Finish	0.0027	Bead Blasted > Polished
Time	0.404	N/A
Material * Finish	0.063	N/A
Material * Time	0.088	N/A
Finish * Time	0.356	N/A
Material * Finish * Time	0.878	N/A

**Table A2.12:** Extracapsular Inflammation Distance Interaction Analysis: Muscle Implants by Time, Finish, and Material.

<b>Factor</b>	<b>P-value</b>	<b>Post Hoc (Or Interaction Tendencies)</b>
Material	0.340	N/A
Finish	0.048	Bead Blasted > Polished
Time	0.209	N/A
Material * Finish	0.429	N/A
Material * Time	0.359	N/A
Finish * Time	0.204	N/A
Material * Finish * Time	0.445	N/A

# Supplementary Materials for Appendix 2

**Specific Pathogen Free New Zealand White Rabbit Blood Chemistry and CBC**

Parameter	12 Month			6 Month			3 Month																	
	Ref. Low	Ref. High	B-71	B-51	B-52	B-53	B-54	B-55	B-56	B-57	B-58	B-59	B-60	B-61	B-62	B-63	B-64	B-65	B-66	B-67	B-68	B-69	B-70	B-71
Rabbit ID#	B-51		B-71	B-51	B-52	B-53	B-54	B-55	B-56	B-57	B-58	B-59	B-60	B-61	B-62	B-63	B-64	B-65	B-66	B-67	B-68	B-69	B-70	B-71
Glucose	74	148		123	248	127	251	136	138	139	169	209	174	273	201	143	151	167	175	138	176	132	163	136
AST	33	99		10	19	10	14	15	154	11	17	20	18	64	32	69	20	34	32	12	19	25	30	17
ALT	25	65		27	23	17	23	18	35	14	28	24	49	46	19	46	21	52	35	25	45	31	34	26
Alk. Phosphatase	10	86		22	18	10	23	23	***	22	32	52	55	18	57	41	33	48	41	62	48	41	59	38
Ck (CPK)				1200	1467	1616	1511	2712	1747	1846	1023	4770	748	5479	5155	4382	2430	934	1244	374	908	1138	1136	1925
Total Bilirubin	0.2	0.5		0.1	0.2	0.1	0.1	0.1	0.4	0.1	0.1	0.1	0.1	0.1	0.1	0.1	0.1	0.1	0.1	0.1	0.1	0.1	0.1	0.1
Total Protein	5	7.5		5.3	5	5.6	5.5	5.6	9.8	5.7	5.6	5.9	5.4	5.3	5.7	5.1	5.2	5	5.4	5	5.2	4.8	4.9	4.9
Albumin	2.7	5		4.4	4.2	4.6	4.5	4.3	8.8	4.5	4.3	4.6	4.3	4.3	4.6	4	4.2	4.1	4.3	4.1	4.4	4	4.1	4.2
Globulin	1.5	2.7		0.9	0.8	1	1	1.3	1	1.2	1.3	1.3	1.1	1	1.1	1.1	1	0.9	1.1	0.9	0.8	0.8	0.8	0.7
Cholesterol	10	100		36	28	21	46	22	351	18	13	25	16	24	38	54	24	56	43	88	33	42	46	41
Urea Nitrogen	5	25		18	20	21	22	20	21	18	21	20	22	20	17	19	17	24	22	25	20	21	25	34
Creatinine	0.5	2.6		1.1	1.2	1.1	1.1	1.2	1.3	1.2	0.9	0.9	0.9	0.9	0.9	0.9	1.2	1.5	1.4	1.2	1.2	1.2	1.4	1.3
Calcium				14.2	13.5	14.6	14.2	14	12.4	14	13.7	14.2	14	13.4	14.4	13.2	14.1	13.8	14.2	12.8	13.3	13.7	13.6	13.4
Phosphorus	4	6		2.6	3.6	3	4.2	3.2	6.4	3	3.1	4	3.1	3.5	3.1	3	3.1	4.1	4.4	4	3.7	2.9	4.1	4.3
Sodium	125	150		141	139	141	142	141	121	141	144	142	143	142	144	140	143	141	143	143	143	142	142	140
Potassium	3.7	7		5.9	7	6.9	6.9	5.9	15***	5.8	4.6	4.6	4.6	4.4	4.2	4.5	4.7	4.5	4.9	5.7	5.2	4.7	6.3	5.9
Chloride	92	120		101	100	102	98	103	94	101	105	100	99	100	98	102	105	101	104	104	108	105	103	103
TCO2				26.9	27.5	23.9	24.9	27.5	12.6	31.5	26.7	26.8	29.8	29.3	28.2	24.9	23.6	24.1	21.3	26.7	25.6	28	26.9	28.1
Anion Gap				19	18.5	22	26	16.4	29.4	14.3	16.9	19.8	18.8	17.1	22	17.6	19.1	20.4	22.6	18	14.6	13.7	18.4	14.8
Erythrocytes	5.3	6.8		5.75	6.13	6.63	5.71	6.18	5.63	6.11	6.65	5.91	6.48	6.59	5.95	5.39	5.61	6.39	6.45	4.65	6.32	5.65	5.7	5.03
Hemoglobin	9.8	14		12.9	14	14.6	13.4	12.9	12.7	13.5	14.2	12.5	13.7	14.5	13.8	13.1	12.2	13.4	13.5	10.9	12.9	11.6	12	11.2
Hematocrit				36.6	40.1	41.5	38.1	37.5	36.4	38.9	42.6	37.6	41.1	43	40.9	38.2	35.7	40.6	41.8	32.4	39.9	36.2	37.3	35.3
MCV	60	69		63.8	65.5	62.5	66.9	60.7	64.7	63.7	64	63.6	63.5	66.2	68.7	70.8	61.4	63.6	64.3	69.6	63.2	64	65.4	70.1
MCH	19	23		22.4	22.9	22	23.5	20.9	22.6	22	21.4	21.2	21.1	22	23.2	24.3	21	21	20.9	23.4	20.4	20.5	21.1	22.3
MCHC	31	35		35.1	34.9	35.2	35.2	34.5	35	34.6	33.3	33.2	33.3	33.7	33.7	34.3	34.2	33	32.3	33.6	32.3	32	32.2	31.7
Platelets	158	650		272	396	304	414	392	149	337	275	277	221	226	153	190	174	320	353	324	264	285	303	342
Plasma Protein				6	5.3	6.3	6.6	5.6	6.2	6	5.7	6.1	5.7	5.6	6.3	5.9	5.1	5.2	5.7	5.5	5.5	5.2	5.2	5.3
PCV	34	43		38	40	42	38	39	34	40	42	35	39	42	40	38	37	38	40	32	39	35	37	35
Total Leucocytes	5.1	9.7		6.9	4.9	5.4	5.5	7.9	7.6	7.8	7.5	7.3	8.6	8.2	7.7	7.6	7.6	6.6	5.3	10.7	3.9	2.8	9.9	8.1
Heterophils (%)	25	46		28	24	33	23	27	32	33	67	41	28	38	26	38	47	34	25	46	25	30	14	30
Lymphocytes (%)	39	68		65	69	63	73	69	61	65	27	55	69	59	72	57	49	59	65	51	73	61	79	65
Monocytes (%)	1	9		7	6	3	2	1	7	0	3	3	3	4	2	3	4	3	5	2	2	4	6	4
Basophils (%)	2	5		0	1	0	1	3	0	2	2	1	0	0	0	2	0	4	5	1	0	5	1	1

## A2.21

All Animals Histology Data - Liver and Kidney					
ID#	Organ	Inflam- tion	Fatty Changes	Acute Tubular Necrosis	Comment
51	Kidney	0	---	0	
51	Liver	0	1	---	1
52	Kidney	0	---	0	
52	Liver	0	0	---	
53	Kidney	0	---	0	
53	Liver	0	0	---	
54	Kidney	0	---	0	
54	Liver	0	1	---	
55	Kidney	0	---	0	
55	Liver	0	0	---	
56	Kidney	0	---	0	
56	Liver	0	0	---	
57	Kidney	0	---	0	
57	Liver	0	0	---	
58	Kidney	0	---	0	
58	Liver	0	1	---	
59	Kidney	0	---	0	
59	Liver	0	1	---	
60	Kidney	0	---	0	
60	Liver	0	1	---	
61	Kidney	0	---	0	
61	Liver	0	0	---	
62	Kidney	0	---	0	
62	Liver	0	2	---	
63	Kidney	0	---	0	
63	Liver	0	1	---	
64	Kidney	0	---	0	
64	Liver	0	0	---	
65	Kidney	0	---	0	
65	Liver	2	0	---	
66	Kidney	0	---	0	
66	Liver	0	0	---	
67	Kidney	0	---	0	
67	Liver	0	0	---	
68	Kidney	0	---	0	
68	Liver	1	1	---	
69	Kidney	0	---	0	
69	Liver	0	0	---	
70	Kidney	0	---	0	
70	Liver	0	0	---	2
71	Kidney	0	---	0	3
71	Liver	0	0	---	
Comment	1	Fatty change in the liver was minimal and around the portal vein/venule regions			
	2	Mild autolytic changes			
	3	Frequent deposits of dystrophic calcification in cortical distal tubule. Significance unknown			

3 Month Sacrifice Histology Data - Bone Samples												
Rabbit ID	Slide ID	Material	Finish	Fibrosis Grade	Inflammation	Degeneration	Fatty Infiltration	Granulomatous Inflammation	Bone Remodeling	Necrosis	Comment	
				Thickness								
65	BR-1	LM1	Polished	0	0	0	0	0	2	0		
65	BR-2	LM1	Bead Blasted	0	0	0	0	0	2	0		
65	BL-1	316-L	Polished	0	0	0	0	0	3	0		
65	BL-2	316-L	Bead Blasted	0	0	0	0	0	0	0		
66	BR-1	LM1	Polished	0	0	0	0	0	1	0		
66	BR-2	LM1	Bead Blasted	0	0	0	0	0	1	0		
66	BL-1	316-L	Bead Blasted	0	0	0	0	0	0	0		
66	BL-2	316-L	Polished	0	0	0	0	0	0	0	1	
67	BR-1	LM2	Bead Blasted	0	0	0	0	0	1	0		
67	BR-2	LM2	Polished	0	0	0	0	0	0	0		
67	BL-1	316-L	Polished	0	0	0	0	0	1	0		
67	BL-2	316-L	Bead Blasted	0	0	0	0	0	3	0		
68	BR-1	LM2	Polished	0	0	0	0	0	0	0		
68	BR-2	LM2	Bead Blasted	0	0	0	0	0	0	0	1	
68	BL-1	316-L	Polished	0	0	0	0	0	0	0		
68	BL-2	316-L	Bead Blasted	0	0	0	0	0	0	0	1	
69	BR-1	LM1	Polished	0	0	0	0	0	0	0		
69	BR-2	LM1	Bead Blasted	0	0	0	0	0	1	0		
69	BL-1	LM2	Bead Blasted	0	0	0	0	0	0	0		
69	BL-2	LM2	Polished	0	0	0	0	0	0	0		
70	BR-1	LM1	Bead Blasted	0	0	0	0	0	0	0		
70	BR-2	LM1	Polished	0	0	0	0	0	1	0		
70	BL-1	LM2	Bead Blasted	0	0	0	0	0	1	0		
70	BL-2	LM2	Polished	0	0	0	0	0	2	0		
71	BR-1	LM1	Bead Blasted	0	0	0	0	0	0	0		
71	BR-2	LM1	Polished	0	0	0	0	0	0	0		
71	BL-1	LM2	Polished	0	0	0	0	0	3	0		
71	BL-2	LM2	Bead Blasted	0	0	0	0	0	2	0		

Comment 1 Recut requested on original samples - no improved visualization on recut noted

3 Month Sacrifice Histology Data - Muscle Samples													
Rabbit ID	Slide ID	Material	Finish	Fibrosis		Intracaps Inflamm	Degeneration	Fatty Infiltration	Extracapsular Inflammation		Granulomatous Inflammation	Necrosis	Comment
				Grade	Thickness				Grade	Distance			
65	MR-1	LM1	Polished	0	0	0	0	0	0	0	0	0	
65	MR-2	LM1	Bead Blasted	1	11	0	0	2	0	0	0	0	
65	MR-3	LM1	Polished	4	117	0	0	1	0	0	0	0	
65	MR-4	LM1	Bead Blasted	1	72	1	0	1	4	116	0	0	2
65	ML-1	316-L	Polished	4	32	0	0	2	0	0	0	0	
65	ML-2	316-L	Bead Blasted	4	8	0	0	1	0	0	0	0	
65	ML-3	316-L	Polished	2	9	0	0	0	0	0	0	0	
65	ML-4	316-L	Bead Blasted	1	3	0	0	1	0	0	0	0	
66	MR-1	LM1	Polished	4	61	0	0	1	0	0	0	0	
66	MR-2	LM1	Bead Blasted	3	33	0	0	0	0	0	0	0	
66	MR-3	LM1	Polished	2	42	0	0	1	0	0	0	0	
66	MR-4	LM1	Bead Blasted	4	153	2	0	2	3	85	0	0	
66	ML-1	316-L	Bead Blasted	0	0	0	0	0	0	0	0	0	
66	ML-2	316-L	Polished	3	26	0	0	0	0	0	0	0	
66	ML-3	316-L	Bead Blasted	4	157	0	1	1	0	0	0	0	1
66	ML-4	316-L	Polished										
67	MR-1	LM2	Bead Blasted	3	36	0	0	1	0	0	0	0	
67	MR-2	LM2	Polished	0	0	0	0	1	0	0	0	0	
67	MR-3	LM2	Bead Blasted	4	79	1	0	1	1	210	0	0	
67	MR-4	LM2	Polished	4	206	0	0	2	1	62	0	0	3
67	ML-1	316-L	Polished	1	5	0	0	2	0	0	0	0	
67	ML-2	316-L	Bead Blasted	0	0	0	0	1	0	0	0	0	
67	ML-3	316-L	Polished	2	11	0	0	1	0	0	0	0	
67	ML-4	316-L	Bead Blasted	4	85	2	0	1	2	105	0	0	
68	MR-1	LM2	Bead Blasted										1
68	MR-2	LM2	Polished	1	17	0	0	0	0	0	0	0	
68	MR-3	LM2	Bead Blasted	1	258	1	1	2	1	121	0	0	3
68	MR-4	LM2	Polished	4	291	2	0	2	2	161	0	0	4
68	ML-1	316-L	Bead Blasted	3	26	0	0	0	0	0	0	0	
68	ML-2	316-L	Polished	4	12	0	0	4	0	0	0	0	
68	ML-3	316-L	Bead Blasted	1	9	0	0	2	0	0	0	0	
68	ML-4	316-L	Polished	3	21	0	0	2	0	0	0	0	
69	MR-1	LM1	Bead Blasted	1	22	0	0	0	0	0	0	0	
69	MR-2	LM1	Polished	0	0	0	0	1	0	0	0	0	
69	MR-3	LM1	Bead Blasted	1	236	1	0	2	1	2000	0	0	5
69	MR-4	LM1	Polished	0	0	0	0	2	0	0	0	0	



6 Month Sacrifice Histology Data - Bone Samples												
Rabbit ID	Slide ID	Material	Finish	Fibrosis		Inflammation	Degeneration	Fatty Infiltration	Granulomatous Inflammation	Bone Remodeling	Necrosis	Comment
				Grade	Thickness							
58	BR-1	LM1	Polished	0	0	0	0	0	0	1	0	
58	BR-2	LM1	Bead Blasted	0	0	0	0	0	0	1	0	
58	BL-1	316-L	Polished	0	0	0	0	0	0	1	0	
58	BL-2	316-L	Bead Blasted	0	0	0	0	0	0	2	0	
59	BR-1	LM1	Polished	0	0	0	0	0	0	3	0	
59	BR-2	LM1	Bead Blasted	0	0	0	0	0	0	2	0	
59	BL-1	316-L	Bead Blasted	0	0	0	0	0	0	2	0	
59	BL-2	316-L	Polished	0	0	0	0	0	0	0	0	
60	BR-1	LM2	Bead Blasted	0	0	0	0	0	0	0	0	
60	BR-2	LM2	Polished	0	0	0	0	0	0	0	0	
60	BL-1	316-L	Polished	0	0	0	0	0	0	0	0	
60	BL-2	316-L	Bead Blasted	0	0	0	0	0	0	0	0	
61	BR-1	LM2	Polished	0	0	0	0	0	0	1	0	
61	BR-2	LM2	Bead Blasted	0	0	0	0	0	0	0	0	
61	BL-1	316-L	Polished	0	0	0	0	0	0	2	0	
61	BL-2	316-L	Bead Blasted	0	0	0	0	0	0	2	0	
62	BR-1	LM1	Polished	0	0	0	0	0	0	3	0	
62	BR-2	LM1	Bead Blasted	0	0	0	0	0	0	3	0	
62	BL-1	LM2	Bead Blasted	0	0	0	0	0	0	3	0	
62	BL-2	LM2	Polished	0	0	0	0	0	0	3	0	
63	BR-1	LM1	Bead Blasted	0	0	0	0	0	0	3	0	
63	BR-2	LM1	Polished	0	0	0	0	0	0	1	0	
63	BL-1	LM2	Bead Blasted	0	0	0	0	0	0	1	0	
63	BL-2	LM2	Polished	0	0	0	0	0	0	1	0	
64	BR-1	LM1	Bead Blasted	0	0	0	0	0	0	1	0	
64	BR-2	LM1	Polished	0	0	0	0	0	0	2	0	
64	BL-1	LM2	Polished	0	0	0	0	0	0	2	0	
64	BL-2	LM2	Bead Blasted	0	0	0	0	0	0	1	0	

6 Month Sacrifice Histology Data - Muscle Samples													
Rabbit ID	Slide ID	Material	Finish	Fibrosis		Intracaps Inflamm	Degeneration	Fatty Infiltration	Extracapsular Inflammation		Granulomatous Inflammation	Necrosis	Comment
				Grade	Thickness				Grade	Distance			
58	MR-1	LM1	Polished	0	0	0	0	0	1	0	0	0	0
58	MR-2	LM1	Bead Blasted	3	9	0	0	0	0	0	0	0	0
58	MR-3	LM1	Polished	3	146	1	0	0	0	0	0	0	0
58	MR-4	LM1	Bead Blasted	0	0	0	0	0	2	0	0	0	0
58	ML-1	316-L	Polished	4	8	0	0	0	1	0	0	0	0
58	ML-2	316-L	Bead Blasted	3	9	0	0	0	0	0	0	0	0
58	ML-3	316-L	Polished	2	146	0	0	0	2	0	0	0	0
58	ML-4	316-L	Bead Blasted	0	0	0	2	0	0	0	0	0	0
59	MR-1	LM1	Polished	0	0	0	0	0	0	0	0	0	0
59	MR-2	LM1	Bead Blasted	4	161	4	0	0	1	0	0	0	2
59	MR-3	LM1	Polished	0	0	0	0	0	3	0	0	0	0
59	MR-4	LM1	Bead Blasted	4	112	5	0	0	0	3	65	0	3
59	ML-1	316-L	Polished	0	0	0	0	0	1	0	0	0	0
59	ML-2	316-L	Bead Blasted	0	0	0	0	0	2	0	0	0	0
59	ML-3	316-L	Polished	4	82	0	0	0	1	0	0	0	0
59	ML-4	316-L	Bead Blasted	3	11	0	0	0	1	0	0	0	0
60	MR-1	LM2	Polished	4	152	2	0	0	2	0	0	0	4
60	MR-2	LM2	Bead Blasted	0	0	0	0	0	1	0	0	0	0
60	MR-3	LM2	Polished	2	17	0	0	0	2	0	0	0	0
60	MR-4	LM2	Bead Blasted	0	0	0	0	0	2	0	0	0	0
60	ML-1	316-L	Polished	4	131	0	0	0	3	0	0	0	0
60	ML-2	316-L	Bead Blasted	0	0	0	0	0	1	0	0	0	0
60	ML-3	316-L	Polished	3	22	0	0	0	2	0	0	0	0
60	ML-4	316-L	Bead Blasted	4	13	0	0	0	3	0	0	0	0
61	MR-1	LM2	Bead Blasted	4	219	3	0	0	3	2	43	0	5
61	MR-2	LM2	Polished	2	8	0	0	0	0	0	0	0	0
61	MR-3	LM2	Bead Blasted	0	0	0	0	0	1	0	0	0	0
61	MR-4	LM2	Polished	0	0	0	0	0	1	0	0	0	0
61	ML-1	316-L	Bead Blasted	0	0	0	0	0	2	0	0	0	0
61	ML-2	316-L	Polished	0	0	0	0	0	0	0	0	0	0
61	ML-3	316-L	Bead Blasted	3	9	0	0	0	1	1	51	0	0
61	ML-4	316-L	Polished	4	13	0	0	0	0	0	0	0	6
62	MR-1	LM1	Bead Blasted	0	0	0	0	0	0	0	0	0	0
62	MR-2	LM1	Polished	4	123	2	0	0	0	0	0	0	4
62	MR-3	LM1	Bead Blasted	4	102	2	0	0	0	2	31	0	4
62	MR-4	LM1	Polished	4	188	5	0	0	2	5	0	1	7









### **Appendix 3 - Corrosion and Corrosion Fatigue of Vitreloy Glasses Containing Low Fractions of Late Transition Metals**

The text and figures of this appendix draw heavily on a paper submitted and under review in Scripta Materialia entitled “Corrosion and Corrosion Fatigue of Vitreloy Glasses Containing Low Fractions of Late Transition Metals.” The authors are A. Wiest, G.Y. Wang, L.Huang, S. Roberts, M.D. Demetriou, P.K. Liaw, and W.L. Johnson.

Corrosion resistance and fatigue performance of Vitreloy glasses with low fractions of late transition metals (LTM) in 0.6M NaCl are investigated and compared to a traditional Vitreloy glass and other crystalline alloys. Low LTM Vitreloy glasses exhibit 1/10 the corrosion rates of the other alloys. Corrosion fatigue performance of present alloys is found to be <10% of their yield strength at  $10^7$  cycles. The poor corrosion fatigue performance of the present alloys is likely due to low fracture toughness of the passive layer.

Owing to the lack of long range order in their atomic structure and the absence of microscopic defects such as vacancies, dislocation, or grain boundaries that typically arise in crystalline microstructures, bulk metallic glasses (BMG) demonstrate a unique combination of mechanical properties, such as high strength, high hardness, and a high elastic strain limit [1-4]. The lack of electrochemically active sites, provided by the absence of microstructural defects, has long been thought to give rise to exceptional resistance to corrosion and chemical attack. Some BMG alloys based on noble metals indeed demonstrate superb corrosion resistance [5], however, the resistance to corrosion is not universally high for all BMG alloys. Zr based BMG of the Vitreloy alloy family

### A3.2

were found to exhibit corrosion resistance in saline solutions higher than most crystalline engineering metals, however on par with the most advanced corrosion resistant metals. For example, the corrosion resistance of ZrTiNiCuAl glass (Vitreloy 105) in phosphate buffered saline (PBS) was found to be on par or slightly lower than widely used metallic biomaterials such as stainless steels, Ti-6Al-4V, and CoCrMo [6]. Despite the generally good corrosion behavior of Vitreloy type BMG, their behavior in stress corrosion environments, specifically cyclic stress (fatigue) corrosion environments, is rather poor. The stresses at which Vitreloy type BMG endure  $10^7$  cycles in saline solutions was found to be just 10 - 20% of their corresponding values in air [7,8]. We investigate the corrosion and corrosion fatigue behavior of certain Vitreloy alloy variants in a 0.6M saline environment (simulated sea water) and contrast it to traditional Vitreloy alloys and other metals used in marine applications. We demonstrate that small variations in the Vitreloy alloy composition can lead to dramatic improvements in corrosion resistance. The improvement in corrosion resistance, however, is not accompanied by an analogous improvement in corrosion fatigue endurance, thereby revealing that the two processes are controlled by different physical mechanisms.

A series of Vitreloy type BMG compositions with low atomic fractions of LTM have recently been reported [9]. Many of these alloys were found to exhibit a combination of exceptionally large supercooled liquid region (SCLR) and good glass forming ability. Notable examples include the ternary  $Zr_{35}Ti_{30}Be_{35}$  and quaternary  $Zr_{35}Ti_{30}Be_{29}Co_6$ , with SCLR of 120 °C and 150 °C and critical casting thicknesses of 6mm and 15mm, respectively. Owing to the low LTM atomic fractions, these compositions were thought to also exhibit good corrosion characteristics. The corrosion and corrosion fatigue

### A3.3

behavior of  $Zr_{35}Ti_{30}Be_{35}$  and  $Zr_{35}Ti_{30}Be_{29}Co_6$  is investigated here, and is contrasted to  $Zr_{52.5}Cu_{17.9}Ni_{14.6}Al_{10}Ti_5$ , a traditional Vitreloy alloy (Vit105) with a much higher LTM atomic fraction. The measured values are also contrasted to three traditional metallic alloys used in sea water environments: 18/8 stainless steel, Monel (Cu-Ni-based), and Alclad (Al-based) [10].

Alloys  $Zr_{35}Ti_{30}Be_{35}$  and  $Zr_{35}Ti_{30}Be_{29}Co_6$  were prepared by arc melting elements of >99.9% purity on a water cooled Cu plate in Ti-gettered argon atmosphere. 3mm diameter amorphous rods of  $Zr_{35}Ti_{30}Be_{29}Co_6$  and 2mm diameter amorphous rods of  $Zr_{35}Ti_{30}Be_{35}$  were cast using an Edmund Buhler mini arc melter suction casting setup. The amorphous nature of the rods was verified using X-ray diffraction and differential scanning calorimetry (DSC).

Cyclic anodic polarization experiments were conducted on unloaded samples of  $Zr_{35}Ti_{30}Be_{35}$  and  $Zr_{35}Ti_{30}Be_{29}Co_6$  in 0.6M NaCl solution at a scan rate of 0.167 mV/s. Data for Vit 105 was gathered from the study of Morrison et al. [7].  $E_{pit}$ , the pitting potential, and  $E_{corr}$ , the steady state corrosion potential, were measured multiple times for each sample. In between measurements, samples were polished with 1200 grit sandpaper in order to remove the reaction layer. Corrosion rates were calculated from corrosion current density measurements. A more detailed description of the experimental method can be found in [6-7]. The averaged cyclic anodic polarization curves for the three alloys are presented in Figure A3.1. Average  $E_{pit}$  and  $E_{corr}$  values for each alloy along with corrosion rates are tabulated in Table A3.1.

## Cyclic Anodic Polarization

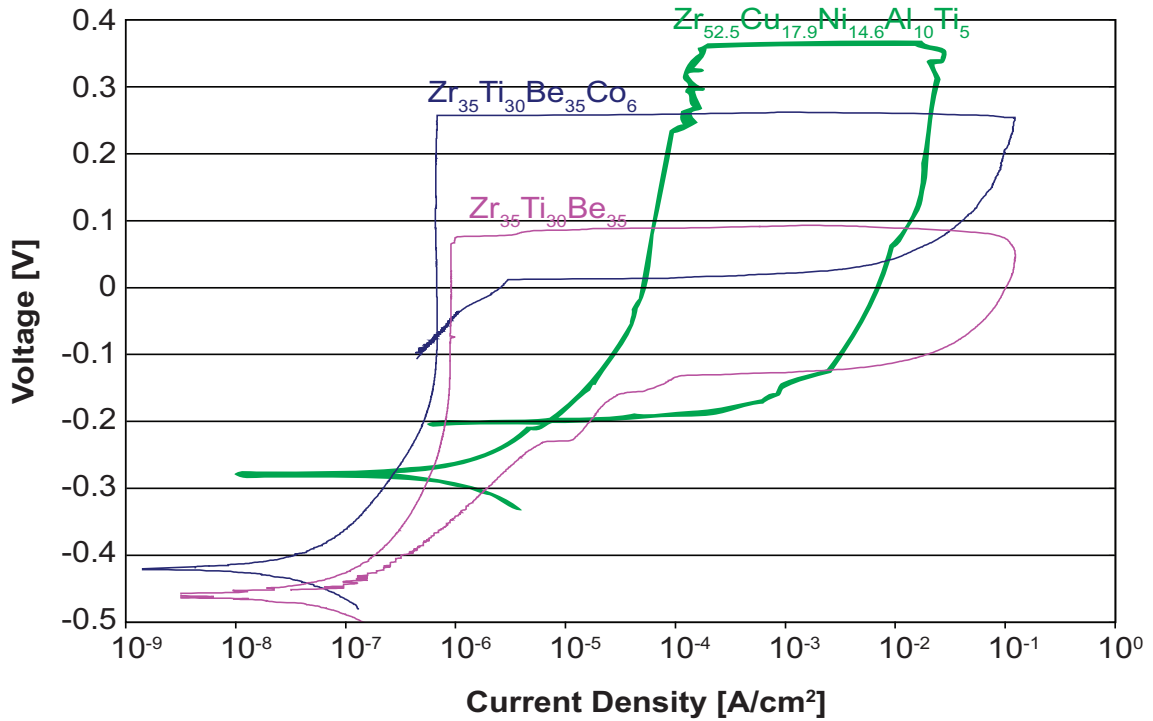


**Figure A3.1:** Cyclic anodic polarization curves of  $Zr_{52.5}Cu_{17.9}Ni_{14.6}Al_{10}Ti_5$ ,  $Zr_{35}Ti_{30}Be_{29}Co_6$ , and  $Zr_{35}Ti_{30}Be_{35}$  in 0.6M NaCl solution at a scan rate of 0.167 mV/s.

**Table A3.1:** Data for corrosion and corrosion fatigue in 0.6M NaCl. Fatigue values are the stress amplitudes at which the samples endured  $10^7$  loading cycles normalized by the material yield strength. The yield strengths of  $Zr_{35}Ti_{30}Be_{35}$ ,  $Zr_{35}Ti_{30}Be_{29}Co_6$ , and  $Zr_{52.5}Cu_{17.9}Ni_{14.6}Al_{10}Ti_5$  are 1850 MPa [22], 1800 MPa [22], and 1700 MPa [7], respectively. Corrosion data for 18/8 Stainless Steel, annealed Monel, and Alclad 24S-T are taken from [10], while data for fatigue in air and 0.6M NaCl are taken from [11-15].

	$E_{corr}$ [mV]	$E_{pit}$ [mV]	corrosion rate [ $\mu\text{m}$ per year]	Fatigue (Air) [% strength]	Fatigue (0.6M NaCl) [%strength]
$Zr_{35}Ti_{30}Be_{35}$	-445±42	84.5±23.5	0.871 ±.266	27%	8%
$Zr_{35}Ti_{30}Be_{29}Co_6$	-424±8	257±64	0.544 ±.215	28%	6%
$Zr_{52.5}Cu_{17.9}Ni_{14.6}Al_{10}Ti_5$	-264	324	29±6	25%	6%
18/8 Stainless Steel			13	25%	15%
Monel - Annealed			15.2	40%	35%
Alclad 24S-T			11.2	20%	10%

Fatigue and corrosion fatigue measurements were conducted on 3mm diameter x 6mm tall rods of  $Zr_{35}Ti_{30}Be_{29}Co_6$  and 2mm diameter x 4mm tall rods of  $Zr_{35}Ti_{30}Be_{35}$  in a compression-compression loading geometry at 10 Hz using a stress ratio

$R = \sigma_{\min}/\sigma_{\max} = 0.1$ . For Vit 105, four-point bending fatigue and corrosion fatigue data from the study of Morrison et al. [7] were utilized. Even though compression-compression and four-point bending fatigue experiments often result in somewhat different endurance limits, the relative drop in the endurance limits between air and saline environments, which is of interest here, is not expected to be dramatically different in the two tests. The S/N curves for the three alloys in air and saline environments are presented in figure A3.2. The ratio of fatigue limit to yield stress in air and in saline solution for the three BMG are listed in Table A3.1. Data for 18/8 stainless steel, Alclad 24S-T and Monel taken from Atlas of Fatigue Curves and other sources [11-15] are also displayed in Table A3.1.

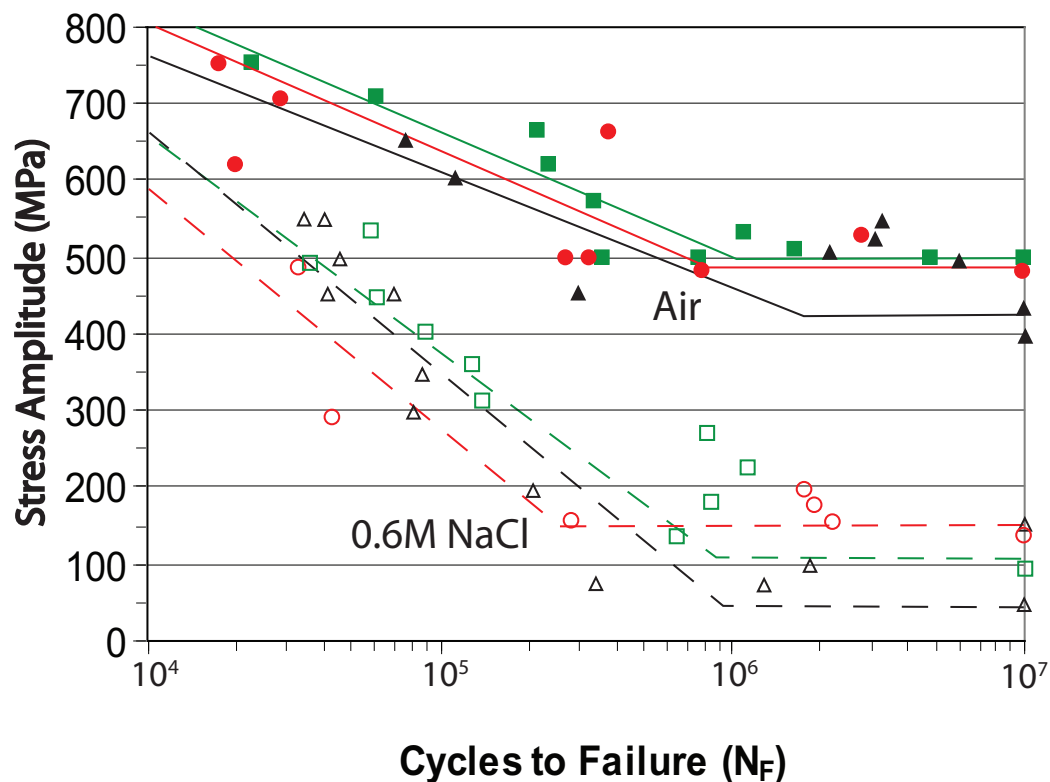


**Figure A3.2:** Fatigue performance in air ( $\blacktriangle$   $Zr_{52.5}Cu_{17.9}Ni_{14.6}Al_{10}Ti_5$ ,  $\blacksquare$   $Zr_{35}Ti_{30}Be_{29}Co_6$ , and  $\bullet$   $Zr_{35}Ti_{30}Be_{35}$ ) and in 0.6M NaCl ( $\triangle$   $Zr_{52.5}Cu_{17.9}Ni_{14.6}Al_{10}Ti_5$ ,  $\square$   $Zr_{35}Ti_{30}Be_{29}Co_6$ , and  $\circ$   $Zr_{35}Ti_{30}Be_{35}$ ) at a frequency of 10 Hz and  $R = 0.1$ .  $Zr_{52.5}Cu_{17.9}Ni_{14.6}Al_{10}Ti_5$  is tested in four-point bending geometry (data taken from [9]).  $Zr_{35}Ti_{30}Be_{29}Co_6$  and  $Zr_{35}Ti_{30}Be_{35}$  are tested in compression-compression geometry (present study).

### A3.6

Analysis of the cyclic anodic polarization data, presented in figure A3.1, reveals that the pitting potential of Vit 105 is the greatest, followed by  $Zr_{35}Ti_{30}Be_{29}Co_6$  and  $Zr_{35}Ti_{30}Be_{35}$ . This suggests that the  $Zr_{35}Ti_{30}Be_{35}$  is the most susceptible and  $Zr_{52.5}Cu_{17.9}Ni_{14.6}Al_{10}Ti_5$  the least susceptible to attack by pitting in 0.6M NaCl. However, the corrosion current densities of the alloys with low LTM fraction are approximately two orders of magnitude lower than  $Zr_{52.5}Cu_{17.9}Ni_{14.6}Al_{10}Ti_5$  in the range between  $E_{corr}$  and  $E_{pit}$ . A higher corrosion current density naturally leads to a higher corrosion rate. The corrosion rate of Vit 105 in 0.6M NaCl is reported to be  $29 \pm 6 \mu\text{m}/\text{yr}$  [7]. By contrast, the corrosion rates of  $Zr_{35}Ti_{30}Be_{29}Co_6$  and  $Zr_{35}Ti_{30}Be_{35}$  in the same solution and under the same conditions were measured in this study to be  $0.5 \pm 0.2 \mu\text{m}/\text{yr}$  and  $0.9 \pm 0.3 \mu\text{m}/\text{yr}$ , respectively. These rates are lower than that of  $Zr_{52.5}Cu_{17.9}Ni_{14.6}Al_{10}Ti_5$  by factors of  $\sim 150$  °C and  $\sim 30$  °C, respectively. Corrosion rates for 18/8 stainless steel, Alclad 24S-T, and annealed Monel in sea water are reported to be 13, 11.2 and  $15.9 \mu\text{m}/\text{yr}$ , respectively [10]. These rates are slightly lower than that of Vit 105, but more than an order of magnitude higher than the rates of  $Zr_{35}Ti_{30}Be_{35}$  and  $Zr_{35}Ti_{30}Be_{29}Co_6$ .

The results of fatigue testing differ markedly from the corrosion results. The tested metallic glasses have similar yield strengths (1700 - 1800 MPa) and, as shown in Figure A3.2, the fatigue values at  $10^7$  cycles are also very close in each environment given the experimental scatter. In Table A3.1, fatigue values are presented as a fraction of the material yield strength. It is interesting to observe how each material's fatigue strength, at  $10^7$  cycles, diminishes in saline solution compared to air. The tested metallic glasses retain 25 - 28% of their yield strength at  $10^7$  cycles in air, but drop to 6 - 8% of their yield

### A3.7

strength in saline solution. Alclad also has a low strength in NaCl decreasing from 20% to 10%. Similar to metallic glasses, steel exhibits 25% of its strength at  $10^7$  cycles in air, but only drops to 15% in saline solution. Annealed Monel starts with a low yield strength, but retains the largest fractions of its yield strength surviving  $10^7$  cycles at 40% of its yield strength in air and 35% in saline solution.

Crack growth rates of traditional Vitreloy alloys undergoing cyclic loading in saline solutions are found to approach  $1\mu\text{m}/\text{cycle}$  at high stress intensities [8], a value substantially higher than in air. Owing to the dramatically improved corrosion resistance demonstrated by  $\text{Zr}_{35}\text{Ti}_{30}\text{Be}_{29}\text{Co}_6$  and  $\text{Zr}_{35}\text{Ti}_{30}\text{Be}_{35}$  over the traditional Vit 105, one would expect to observe an analogous improvement in corrosion fatigue endurance as well. As seen in Table A3.1 however, no statistically significant improvement in corrosion fatigue endurance is attained. This suggests that the corrosion resistance and corrosion fatigue endurance of Vitreloy alloys are governed by distinctly different mechanisms.

When exposed in a chemical environment, Zr, the base metal for Vitreloy glasses, is known to rapidly form a passive layer several atomic distances thick that protects the bulk of the material against chemical dissolution [16-17]. Likewise, glassy Vitreloy alloys based on Zr also tend to passivate rapidly when exposed in chemical environments. The thermodynamic and chemical stability of the formed passive layer controls the rate of corrosion of these glasses and is known to be a measure of their overall corrosion resistance [18-21]. Preliminary X-ray Photoelectron Spectroscopy (XPS) studies of ZrTiBe alloys show a passive layer comprised of oxides of the base elements in ratios similar to the bulk sample [22]. This layer is stable in NaCl solutions in stress free

environments and protects the bulk sample from dissolution [20]. It is therefore reasonable to assume that the improvement in corrosion resistance demonstrated by the low LTM Vitreloy glasses ( $Zr_{35}Ti_{30}Be_{29}Co_6$  and  $Zr_{35}Ti_{30}Be_{35}$ ) over traditional Vitreloy glasses ( $Zr_{52.5}Cu_{17.9}Ni_{14.6}Al_{10}Ti_5$ ) is due to the low fraction or complete absence of late transition metals such as Ni and Cu. The presence of late transition metals in Vitreloy glasses is known to interfere with the formation of chemically stable passive layers. For example, XPS studies of Vitreloy glasses containing Cu show that the surface composition includes Cu compounds which are not as resistant to chemical attack [22]. Under stress (or cyclic stress) corrosion conditions however, the mechanical stability of the passive layer is also important. Mechanical properties of the passive layer such as its fracture strength and fracture toughness are critical in determining the structural integrity of the layer under stress and the sustained protection of the material against chemical dissolution. While the fracture strength and fracture toughness of the passive layer of these alloys is not known, the ceramics  $ZrO_2$  and  $TiO_2$  have fracture strengths of 550 MPa and 52 MPa respectively, and fracture toughnesses of less than  $10 \text{ MPa}\cdot\text{m}^{1/2}$  [23]. These low fracture strength and fracture toughness values suggest that the passive layer is brittle and prone to cracking under low applied stresses.

Mechanical rupture of the passive layer can be expected to lead to severe chemical attack concentrated at the extending crack tip. Indeed, stress assisted cracking or anodic dissolution is identified to be the dominant mechanism of corrosion fatigue failure of Vitreloy glasses [7-8, 24]. Hence independent of its chemical stability, a brittle passive layer can lead to early corrosion fatigue failure despite its ability to protect against corrosion in stress free environments. Therefore, the poor corrosion fatigue performance

### A3.9

demonstrated by  $Zr_{35}Ti_{30}Be_{29}Co_6$  and  $Zr_{35}Ti_{30}Be_{35}$ , despite their superior corrosion resistance in stress free environment, can be attributed to the formation of a passive layer with high chemical stability but low fracture toughness.

In conclusion, the corrosion resistance and corrosion fatigue performance of low LTM Vitreloy glasses  $Zr_{35}Ti_{30}Be_{29}Co_6$  and  $Zr_{35}Ti_{30}Be_{35}$  in 0.6M NaCl were investigated and compared to traditional Vitreloy glass  $Zr_{52.5}Cu_{17.9}Ni_{14.6}Al_{10}Ti_5$  and to other crystalline engineering alloys used widely in saline environments such as 18/8 stainless steel, Alclad 24S-T, and annealed Monel. The low LTM Vitreloy glasses were found to exhibit corrosion rates of less than  $1\mu\text{m}$  per year, which are lower by more than one order of magnitude compared to the traditional Vitreloy glass and the conventional engineering metals. The high corrosion resistance of the present alloys is attributed to the low fraction or complete absence of LTM elements facilitating the formation of a chemically stable passive layer. Despite their superb corrosion resistance, the corrosion fatigue performance of  $Zr_{35}Ti_{30}Be_{29}Co_6$  and  $Zr_{35}Ti_{30}Be_{35}$  is found to be rather poor, as less than 10% of their yield strength is retained at  $10^7$  cycles, a value comparable to traditional Vitreloy glasses but significantly lower than conventional crystalline alloys. The poor corrosion performance of the present alloys is likely due to the fracture toughness of the passive layer being relatively low, providing little protection against chemical dissolution after being fractured in a corrosive environment.

Valuable discussions with Dr. Vilupanur A. Ravi are gratefully acknowledged. This work is supported by the NSF International Materials Institutes Program under DMR-0231320, with Drs. C. Huber, U. Venkateswaran, and D. Finotello as contract monitors, and by the Office of Naval Research under ONR06-251 0566-22.

**Appendix 3 References**

- [1] A.L. Greer, E. Ma, *MRS Bull.* 32 (2007) 611.
- [2] W.L. Johnson, *MRS Bull.* 24 (1999) 42.
- [3] A. Inoue, *Acta Mater.* 48 (2000) 279.
- [4] W.L. Johnson, *JOM* 54 (2002) 40.
- [5] Y.F. Wu, W.C. Chiang, J. Chu, T.G. Nieh, Y. Kawamura, J.K. Wu, *Mater. Lett.* 60 (2006) 2416.
- [6] M.L. Morrison, R.A. Buchanan, R.V. Leon, C.T. Liu, B.A. Green, P.K. Liaw, J.A. Horton, *J. Biomed. Mater. Res. Part A* 74A (2005) 430.
- [7] M.L. Morrison, R.A. Buchanan, P.K. Liaw, B.A. Green, G.Y. Wang, C.T. Liu, J.A. Horton, *Mater. Sci. Eng. A* 467 (2007) 198. Correspondence with the Liaw group verified that the corrosion rate value is  $29 \pm 6 \mu\text{m/yr}$ , not  $29 \pm 60 \mu\text{m/yr}$  as reported.
- [8] V. Schroeder, C.J. Gilbert, R.O. Ritchie, *Mater. Sci. Eng. A* 371 (2001) 145.
- [9] A. Wiest, G. Duan, M.D. Demetriou, L.A. Wiest, A. Peck, G. Kaltenboeck, B. Wiest, W.L. Johnson, *Acta Mater.* 56 (2008) 2625.
- [10] C.V. Brouillette, *Corrosion Rates in Sea Water at Port Hueneme, California, for Sixteen Metals*, AD81212 Armed Services Technical Information Agency, 1954.
- [11] H.E. Boyer, *Atlas of Fatigue Curves*, American Society for Metals, Ohio, 1986, pp. 37-38, 66, 177-180, 319, 321, 327, 391-392.
- [12] H.W. Russell, L.R. Jackson, H.J. Grover, W.W. Beaver, *Fatigue Strength and Related Characteristics of Aircraft Joints*, National Advisory Committee for Aeronautics Technical Note No. 1485, 1948.
- [13] A.C. Bond, *Fatigue Studies of 24S-T and 24S-T Alclad Sheet with Various Surface Conditions*, Master's Thesis, Georgia Institute of Technology, 1948.
- [14] T.W. Crooker, R.E. Morey, E.A. Lange, *Low Cycle Fatigue Crack Propagation Characteristics of Monel 400 and Monel K-500 Alloys*, NRL Report 6218, 1965.
- [15] *Monel Alloy R-405*, Technical Brochure, UNS N04405, [www.specialmetals.com](http://www.specialmetals.com).
- [16] P.A. Schweitzer, *Corrosion Engineering Handbook*, Marcel Dekker, Inc., New York, 1996, pp. 157-163, 195-252.
- [17] D.W. White Jr., J.E. Burke, *The Metal Beryllium*, The American Society for Metals, Ohio, 1955, pp. 530-547.
- [18] K. Hashimoto, K. Asami, M. Naka, T. Masumoto, *The Research Institute for Iron, Steel and Other Metals* 1694 (1979) 237.
- [19] K. Hashimoto, K. Asami, M. Naka, T. Masumoto, *The Research Institute for Iron, Steel and Other Metals* 1695 (1979) 246.
- [20] S. Hiromoto, A.P. Tsai, M. Sumita, T. Hanawa, *Corros. Sci.* 42 (2000) 1651.
- [21] S. Hiromoto, A.P. Tsai, M. Sumita, T. Hanawa, *Corros. Sci.* 42 (2000) 2193.
- [22] Unpublished Work.
- [23] <http://www.ceramics.nist.gov/srd/summary/ftmain.htm>.
- [24] Y. Nakai, Y. Yoshioka, *JSMS* 3 (2009) 219.

## Appendix 4 – Derivations

### Derivation 1 - Fourier Heat Equation

We begin with the Fourier heat equation.

$$\frac{\partial U(x, y, z, t)}{\partial t} = a \nabla^2 T$$

Where  $U$  is the temperature of the sample at every point in space and time,  $a$  is

a constant, and  $\nabla^2 = \frac{\partial^2}{\partial x^2} + \frac{\partial^2}{\partial y^2} + \frac{\partial^2}{\partial z^2}$ .

We could solve this equation for many geometries, but the simplest solution is for an infinite plane of material in the  $y, z$  directions with thickness  $L$  in the  $x$  direction. This reduces the problem to 1D and approximates a cast plate where the thickness is much smaller than the other two dimensions. The equation reduces to:

$$\frac{\partial U(x, t)}{\partial t} = a \frac{\partial^2 U}{\partial x^2}$$

Boundary conditions

1. Let us assume that the temperature of the mold is absolute zero so  $U(0, t) = U(L, t) = 0$ . This is a reasonable 0th order approximation if  $T_g \gg T_{\text{mold}}$  where  $T_g$  is the glass transition temperature where the liquid material becomes a glass, and  $T_{\text{mold}}$  is the temperature of the mold.
2. Let us assume that the temperature of the material when it is cast into the mold at  $t = 0$  is  $U(x, 0) = T_L$  or the liquidus temperature.

We must also assume that  $T(x, t) = T(t)X(x)$  so separation of variables applies. This gives

$$\frac{T'(t)}{aT(t)} = \frac{X''(x)}{X(x)} = -\lambda$$

The solutions for  $\lambda \leq 0$  force  $U = 0$  and for  $\lambda > 0$  we find

$$T(t) = Ae^{-\lambda at}$$

and  $X(x) = B \sin(x\sqrt{\lambda}) + C \cos(x\sqrt{\lambda})$  where  $\lambda = n\pi / L$

Applying boundary conditions gives

$$U(x, t) = \sum_{n=1}^{\infty} D_n \left( \sin \frac{n\pi x}{L} \right) e^{-\frac{n^2 \pi^2 at}{L^2}}$$

Where  $D_n = \frac{2}{L} \int_0^L T_L \sin\left(\frac{n\pi x}{L}\right) dx = T_L \frac{2 - 2 \cos(n\pi)}{n\pi}$

The critical cooling rate is the time required to cool the centerline to  $T_g$ .

Critical cooling rate =  $U(L/2,t)=T_g$ .

$$T_g = T_L \sum_{n=1}^{\infty} \frac{2 - 2 \cos(n\pi)}{n\pi} \sin\left(\frac{n\pi}{2}\right) e^{-\frac{n^2 \pi^2 a t}{L^2}}$$

We can solve this for  $n = 1$  for the first order approximation and find that

$$t = \frac{L^2}{\pi^2 a} \ln \frac{T_L}{T_g}$$

The important message from this derivation is that the critical cooling rate goes like the thickness squared ( $L^2$ ).

### Derivation 2 - Implications of Slope Change in Thermodynamic Variables

Assume a slope change in the entropy  $S(T)$  or enthalpy  $H(T)$  of a material. Call the temperature where the slope change occurs  $T_g$ . We know from thermodynamics that

$$c_V = T \left( \frac{\partial S}{\partial T} \right)_V \quad \text{and} \quad c_P = T \left( \frac{\partial S}{\partial T} \right)_P = \left( \frac{\partial H}{\partial T} \right)_P$$

If either  $H$  or  $S$  changes slope at  $T_g$  then

$$\left( \frac{\partial S(T_g^+)}{\partial T} \right)_V \neq \left( \frac{\partial S(T_g^-)}{\partial T} \right)_V \quad \text{and} \quad \left( \frac{\partial S(T_g^+)}{\partial T} \right)_P \neq \left( \frac{\partial S(T_g^-)}{\partial T} \right)_P$$

and we would expect a discontinuous  $c_V$  and  $c_P$ . Similarly if the slope of  $P(T)$  changes at  $T_g$  then we would expect discontinuities in the compressibility. These slope changes are observed in glass forming liquids and the discontinuities in  $c_P$  as measured in a DSC provide a way to determine the glass transition temperature.

### Derivation 3 - Stefan's Equation for Parallel Plate Viscometer

The viscosity equation for a parallel plate viscometer geometry is called Stefan's Equation. It is solved fully in "Theory and Application of the Parallel Plate Plastometer" [G.J. Dienes, H.F. Klemm, J. Appl. Phys. 17 (1946) 458]. The derivation takes four journal pages and the basic strategy is given here.

Begin with the equation of motion for a viscous fluid. Neglect body forces. Transform to cylindrical coordinates and consider a cylinder with height  $\ll$  radius. Assume no slippage at the plates and a parabolic flow front.

General expression for motion of a Newtonian fluid of viscosity  $\eta$  neglecting body forces is

$$\rho \frac{d\vec{v}}{dt} + \rho \vec{v} \cdot \nabla \vec{v} = -\nabla p + \eta \nabla^2 \vec{v} + \frac{1}{3} \eta \nabla \nabla \cdot \vec{v}$$

assuming incompressibility requires  $\nabla \cdot \vec{v} = 0$

assuming velocity is small we neglect  $\rho \vec{v} \cdot \nabla \vec{v}$

and are left with 
$$\rho \frac{d\vec{v}}{dt} = -\nabla p + \eta \nabla^2 \vec{v}$$

In cylindrical coordinates we have three equations

$$\rho \frac{dv_r}{dt} = -\frac{dp}{dr} + \eta \nabla^2 v_r$$

$$\rho \frac{dv_\theta}{dt} = -\frac{1}{r} \frac{dp}{d\theta} + \eta \nabla^2 v_\theta$$

$$\rho \frac{dv_z}{dt} = -\frac{dp}{dz} + \eta \nabla^2 v_z$$

The parallel plates are located at  $z = 0$  and  $z = h$

circular symmetry requires  $v_\theta = 0$

assuming a short sample lets us assume  $v_z \sim 0$

assuming no slippage and steady state flow means

$$v_r(z=0) = v_r(z=h) = 0 \text{ and } \frac{dv_r}{dz} = 0$$

ASSUMPTIONS ARE GREAT!!!!!! We are left with

$$\frac{dp}{dr} = \eta \frac{d^2 v_r}{dz^2}$$

Integrate twice and apply the boundary conditions

$$v_r = \frac{1}{2\eta} \frac{dp}{dr} (z-h)z$$

consider flow through a surface element  $r d\theta dz = r d\theta dz v_r$

$$U = \text{flow per unit arclength} = \int_0^h v_r dz = \frac{1}{2\eta} \frac{dp}{dr} \int_0^h z^2 - zh dz$$

$$U = -\frac{h^3}{12\eta} \frac{dp}{dr}$$

next we let the plates move towards each other at a rate  $\frac{dh}{dt}$

a volume element  $r dr d\theta dz$  changes volume at a rate  $r dr d\theta \frac{dh}{dt}$

since the fluid is incompressible the rate of decrease of volume must equal the outward flow rate. Thus,

$$-r dr d\theta \frac{dh}{dt} = \frac{\partial}{\partial r} (r d\theta U) dr \rightarrow \frac{12\eta}{h^3} \frac{dh}{dt} r = \frac{\partial}{\partial r} \left( r \frac{\partial p}{\partial r} \right)$$

Integrating and requiring that  $p$  is finite for  $r = 0$  and  $p(r=R) = \text{atmospheric pressure}$  gives

$$p = -\frac{3\eta}{h^3} \frac{dh}{dt} (R^2 - r^2) + 1 \text{ atm}$$

We must balance the forces on the plate in steady state flow.

$$\text{Downward force applied to top plate} = F + \int_0^R 1 \text{ atm} * 2 \pi r \, dr$$

$$\text{Sample applies this force upwards} = \int_0^R p 2 \pi r \, dr$$

$$\text{We arrive at } F = -2 \pi \frac{dh}{dt} \frac{3 \eta}{h^3} \int_0^R (R^2 - r^2) r \, dr$$

solving for the case where radius of plate (R) = radius of sample (a) we obtain

$$F = -\frac{3 \pi \eta a^4}{2 h^3} \frac{dh}{dt}$$

Solving for the case where we assume the plates are larger than the diameter of the cylinder we are squishing and we find:

$$F = \frac{-3 \eta V^2}{2 \pi h^5} \frac{dh}{dt}$$

Where F is the applied force,  $\eta$  is the viscosity, V is the volume, h is the height, dh/dt is the time derivative of the height of the specimen which is assumed to be incompressible.

#### Derivation 4 – Vogel-Fulcher-Tammann Viscosity

Some liquids are observed to exhibit Arrhenius type behavior. This means that their flow properties as a function of temperature can be well described by

$\eta(T) = \eta_0 e^{\frac{T_0}{T-T_0}}$  where  $\eta_0$  is the high temperature viscosity limit  $\approx 10^{-5}$  Pa-s, and  $T_0$  is the temperature at which no flow occurs. Deviations from this behavior are observed for many liquids. The deviation usually results in a steeper drop of viscosity with temperature than the Arrhenius relationship predicts. This is called hyper-Arrhenius behavior. To allow for this, the Vogel-Fulcher-Tammann (VFT) fit to the viscosity data has a multiplier in the exponent as seen below.

$$\eta = \eta_0 \exp \frac{D^* T_0}{T-T_0}$$

where  $D^*$  is a fitting constant and  $\eta_0$  and  $T_0$  are defined as before.  $T_0$  is also called the VFT temperature.

#### Derivation 5 - Viscosity of BMG from Potential Energy Landscape Perspective

Flow of a metallic glass is described as barrier crossing events in “Rheology and Ultrasonic Properties of Metallic Glass-Forming Liquids” published in Materials Research Society Bulletin [W.L. Johnson, M.D. Demetriou, J.S. Harmon, M.L. Lind, K. Samwer, MRS Bull. 32 (2007) 644].

A barrier to flow is argued to be a function of STZ volume ( $\Omega(T, P)$ ) and the energy barrier to shear flow of the STZ which is shear modulus ( $G(T, P)$ ). The total barrier to flow is  $W \sim G \cdot \Omega$ . The barrier to flow at the glass transition temperature is  $W_g$ .

Experimental data suggests that the contributions of the shear modulus and STZ volume barriers are similar and can be well represented by

$$W = W(G(T), \Omega(T)) = W_g \left( \frac{T_g}{T} \right)^n \left( \frac{T_g}{T} \right)^p$$

$$W \sim W_g (T_g / T)^{2n}$$

Taking the barrier crossing rate normalized by an attempt frequency to follow a Boltzmann distribution (equivalently, thermally activated hopping), one arrives at a viscosity law that takes the form

$$\frac{\eta}{\eta_\infty} = \text{Exp}[-W / kT]$$

Because these flow barriers give rise to the observed viscosity, The exponents are shown to be related to the fragility as follows.

$$m = (1 + 2n) \text{Log}(\eta_g / \eta_\infty)$$

where

$$m = \left( \frac{\partial \text{Log} \eta}{\partial (T_g / T)} \right)_{T_g = T}$$

and

$$W_g = kT_g \ln(\eta_g / \eta_\infty) .$$

We can combine terms

$$\frac{\eta}{\eta_\infty} = \text{Exp} \left[ \frac{W_g}{kT} \left( \frac{T_g}{T} \right)^{2n} \right]$$

$$\text{Ln} \left[ \frac{\eta}{\eta_\infty} \right] = \frac{W_g}{kT} \left( \frac{T_g}{T} \right)^{2n} \text{ solve for } T_g$$

$$\text{Ln} \left[ \frac{\eta_g}{\eta_\infty} \right] = \frac{W_g}{kT_g} \left( \frac{T_g}{T_g} \right)^{2n} \rightarrow W_g = K T_g \text{Ln} \left[ \frac{\eta_g}{\eta_\infty} \right] \text{ plugging back in}$$

$$\text{Ln} \left[ \frac{\eta}{\eta_\infty} \right] = \text{Ln} \left[ \frac{\eta_g}{\eta_\infty} \right] \left( \frac{T_g}{T} \right)^{2n+1}$$

$$\text{Log} \left[ \frac{\eta}{\eta_\infty} \right] = \frac{\text{Ln} \left[ \frac{\eta_g}{\eta_\infty} \right]}{\text{Ln}[10]} \left( \frac{T_g}{T} \right)^{m / \text{Log}(\eta_g / \eta_\infty)}$$

If we let

$$A = \text{Log}(\eta_g / \eta_\infty)$$

we arrive at the expression

$$\text{Log} \left[ \frac{\eta}{\eta_\infty} \right] = A \left( \frac{T_g}{T} \right)^{m/A}$$

**Derivation 6 - Thermoplastic Formability Parameter**

Starting with the result of Derivation 5:  $\text{Log} \left[ \frac{\eta}{\eta_{\infty}} \right] = \mathbf{A} \left( \frac{\mathbf{T}_g}{\mathbf{T}} \right)^{m/\mathbf{A}}$

We integrate as shown in Figure A4.1 by oversimplifying BMG physics and assuming all BMG exhibit the same viscosity at  $T_x$ .

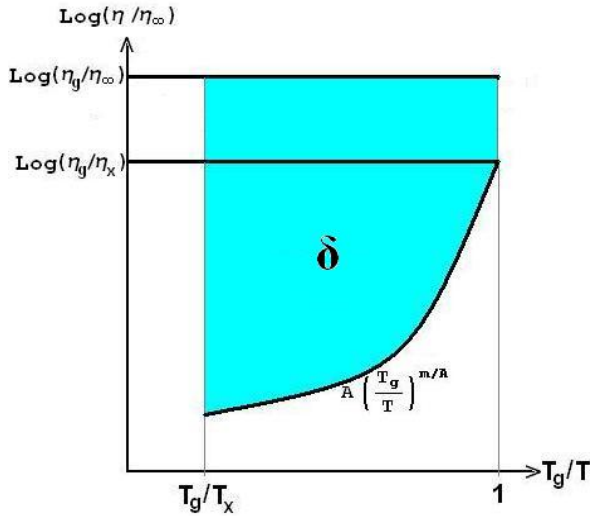


**Figure A4.1:** Thermoplastic formability parameter  $\delta$  found by integrating as shown.

In reality, the square region may be different from alloy to alloy.

$$\delta = \int_{T_g/T_x}^1 [A - \text{Log} (\eta / \eta_{\infty}) ] d (T_g / T)$$

$$\delta = \int_{T_g/T_x}^1 \left[ A - A \left( \frac{T_g}{T} \right)^{m/A} \right] d (T_g / T)$$

$$\delta = A \left( 1 - \frac{T_g}{T_x} \right) - \frac{A}{1 + \frac{m}{A}} \left[ 1 - \left( \frac{T_g}{T_x} \right)^{1+m/A} \right]$$

Squish data and correlation with  $\delta$  are detailed in Figure A4.2.

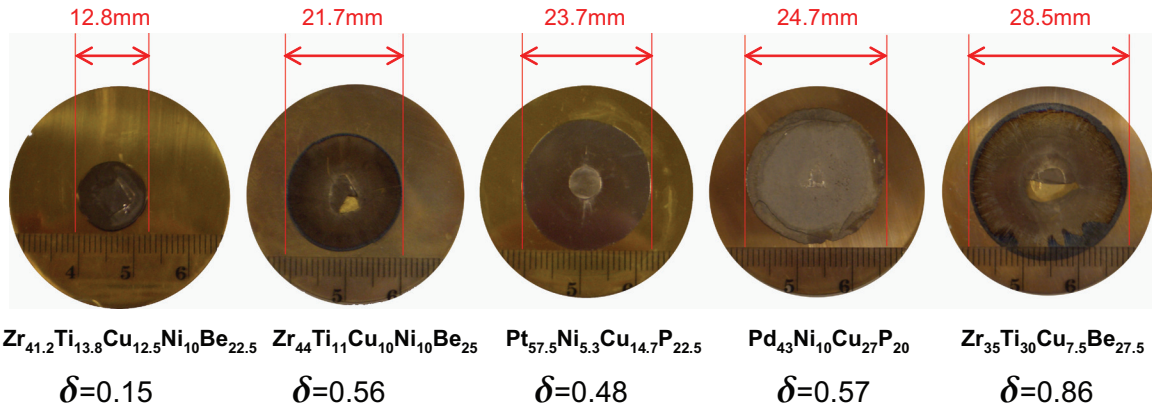


**Figure A4.2:** Squish test data for 5 TPF candidate alloys shows  $\delta$  is a decent predictor of TPF potential.

### Derivation 7 - Composition Counting

To determine the number of compositions one must create for 1 - 5 element alloys assuming 5% composition steps. There is a constraint that the sum of the elements = 100.

One element: There is only one choice with 100% of that element.

Two elements: Give the alloys shown in Table A4.1.

**Table A4.1:** All possible two component compositions with 5% composition steps.

Alloy #	1	2	3	4	5	6	7	8	9	10	11	12	13	14	15	16	17	18	19	20	21
%element1	100	95	90	85	80	75	70	65	60	55	50	45	40	35	30	25	20	15	10	5	0
%element2	0	5	10	15	20	25	30	35	40	45	50	55	60	65	70	75	80	85	90	95	100

We see 21 possible compositions.

Three elements: This case is best thought of with a ternary phase diagram as shown in Figure A4.3. This can be drawn in 2D because of the constraint that the sum of the elements = 100. The alloy's composition is determined by drawing lines orthogonal to the corners. In the Ti corner, the alloy would have 100% Ti. Horizontal lines orthogonal to the Ti corner are drawn in 5% composition steps. The lines slanting downward are drawn orthogonal to the Be corner in 5% composition steps. Intersections of the lines form a grid in the triangle where the Zr composition = 100 - Ti - Be. There are 21 compositions along the bottom of the triangle going from the Be corner to the Zr corner with Ti = 0%. There are 20 compositions possible along the line Ti = 5% just above the bottom of the triangle. This continues until we reach the Ti corner with 1 possible composition. The total number of compositions is  $21 + 20 + 19 + \dots + 2 + 1 = 231$ .

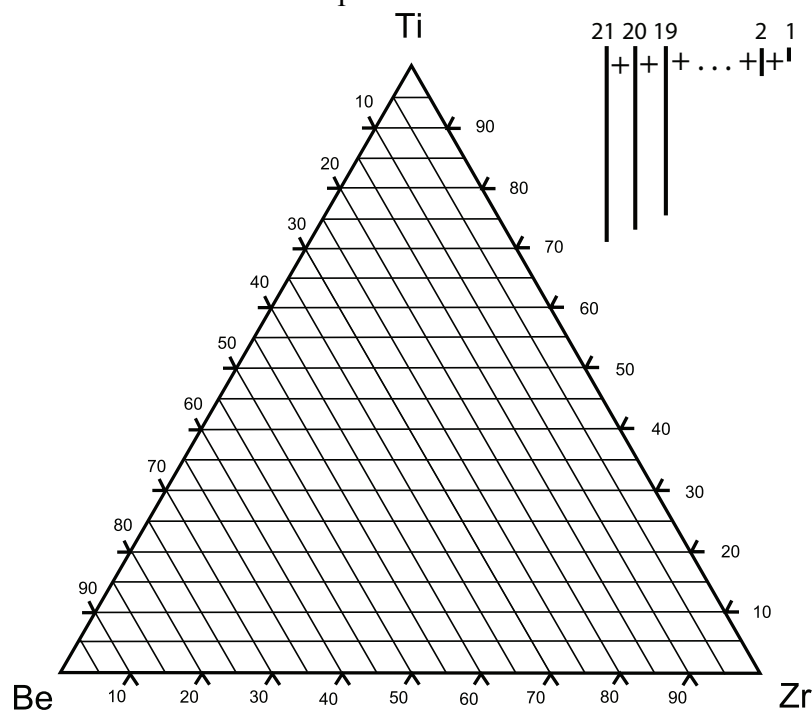


**Figure A4.3:** All possible three component compositions with 5% composition steps found at line intersections.

Four elements: This case is best approached with a quaternary phase diagram drawn in 3D because of the constraint as shown in Figure A4.4. In this case the phase diagram is an equilateral pyramid with compositions determined by a plane orthogonal to each corner. Instead of adding line elements, we add equilateral triangle elements as shown below. A table with the math is included after the 5 element analysis.

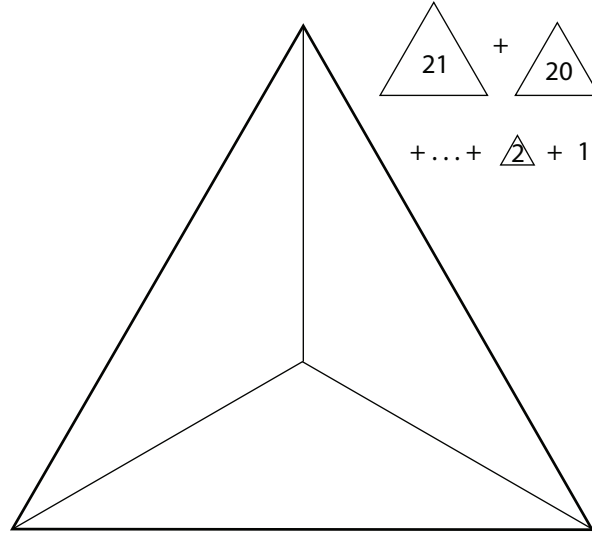


**Figure A4.4:** Four component phase diagram is an equilateral pyramid / tetrahedron.

Five elements: This case can't be drawn and occupy a 4D phase diagram that is an equilateral hyperpyramid as shown in Figure A4.5. Instead of adding equilateral triangles for composition steps, we now add equilateral pyramid elements shrinking in size as shown below. The counting follows.

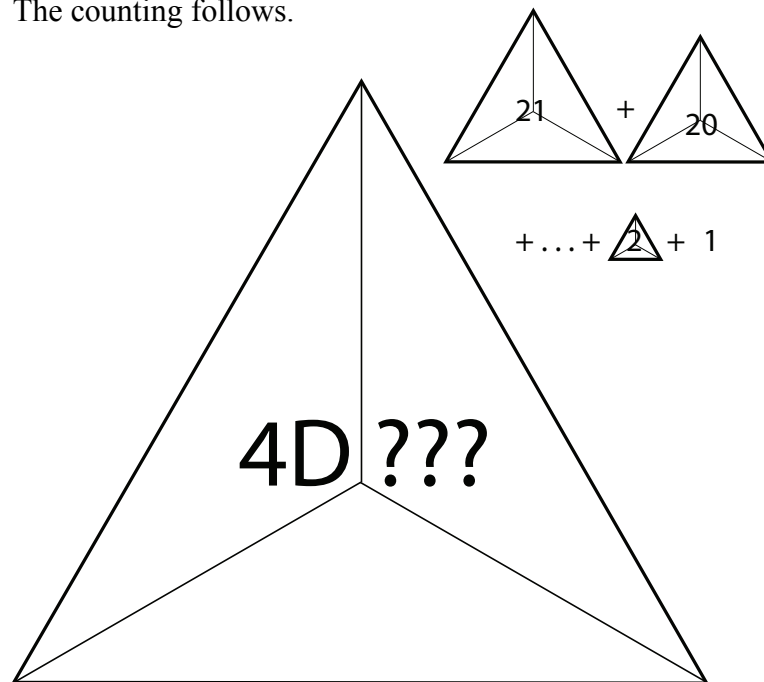


**Figure A4.5:** Five component phase diagram is a 4D equilateral hyperpyramid.



### Derivation 8 - Limiting Cases of Two Phase Liquid Flow

A recent study of amorphous alloys in the ZrTiBe system showed the possibility of a miscibility gap in the supercooled liquid region along the Be = 40 pseudo binary line, but no microscopic evidence of the two phases was obtained. The two phase glasses are thought to separate into a Zr rich phase with a glass transition temperature  $T_{g1} \sim 320$  °C and a Ti rich phase with  $T_{g2} \sim 375$  °C. If there are indeed two glasses, one would expect to see flow, or more precisely viscosity, as a function of temperature characteristic of a two phase liquid.

The flow of liquids with multiple phases was a phenomenon studied extensively in the early 1900s. Two limiting cases were solved for ideal mixtures. Variations of these ideal cases were postulated to explain the flow of other types of liquid mixtures. Both cases consider a liquid mixture with parallel layers or laminae. The applied shear stress is orthogonal to the layers in Case 1 as shown in Figure A4.6. The applied shear stress is parallel to the layers in Case 2 as shown in Figure A4.7.

The fundamental law governing viscous flow is

$$\frac{dv}{dr} = \frac{F}{\eta} \quad (1)$$

Where  $F$  is the applied shear stress,  $\eta$  is the viscosity, and  $\frac{dv}{dr}$  is the spatial derivative of the velocity orthogonal to the shear direction.

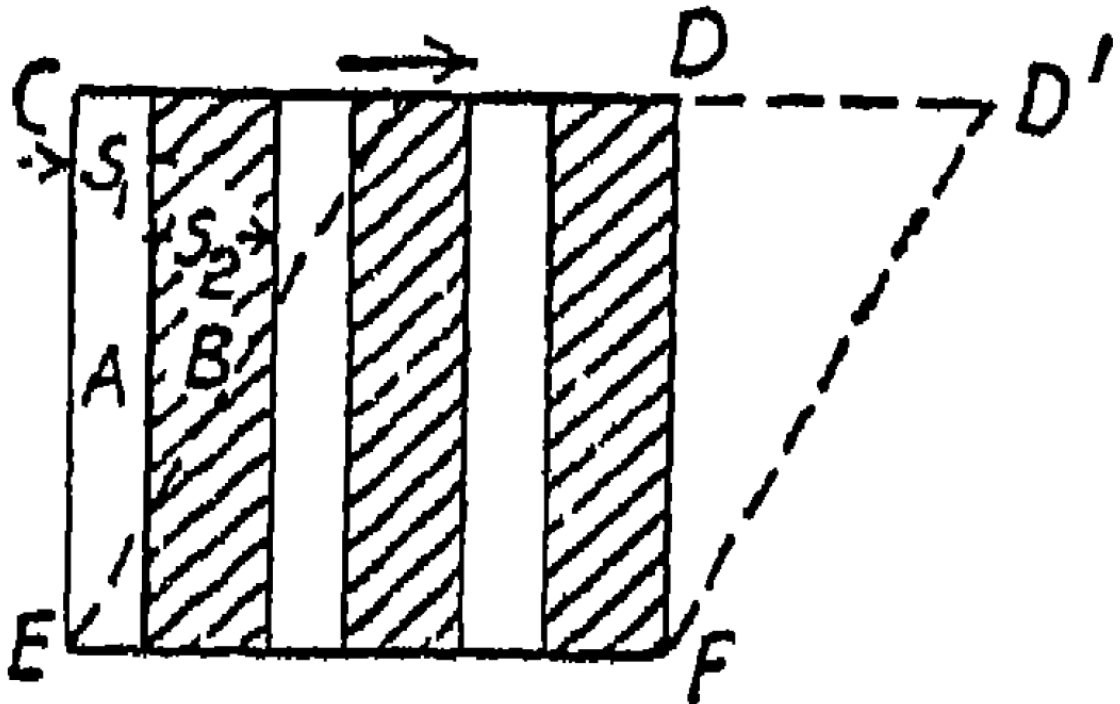


Figure A4.6: Case 1 showing laminae of two fluids orthogonal to shear direction.

Case 1 constrains the layers to have the same velocity. For simplicity consider a liquid with alternating laminae  $A, B, \dots$  with viscosities  $\eta_A$  and  $\eta_B \dots$ , and laminae thicknesses  $s_A$  and  $s_B \dots$ , and shear stresses per unit area  $P_A$  and  $P_B \dots$ . Since we are considering only a simple shear stress, we can integrate equation 1 and find

$$v = \frac{RP}{H} = \frac{RP_A}{\eta_A} = \frac{RP_B}{\eta_B}$$

Where  $R$  is the distance between horizontal planes,  $H$  is the viscosity of the mixture, and  $P$  is the average shear stress over the entire distance  $S$ .  $PS = P_A s_A + P_B s_B + \dots$ . Hence

$$H = \frac{R}{v} \left( \frac{P_A s_A + P_B s_B + \dots}{S} \right)$$

Because  $s_A/S$  is the fraction by volume of substance A in the mixture, we can use the volume fraction  $c_i$  for the  $i$ th substance in the mixture and find viscosities are additive for Case 1.

$$H = \sum_i c_i \eta_i \quad (2)$$

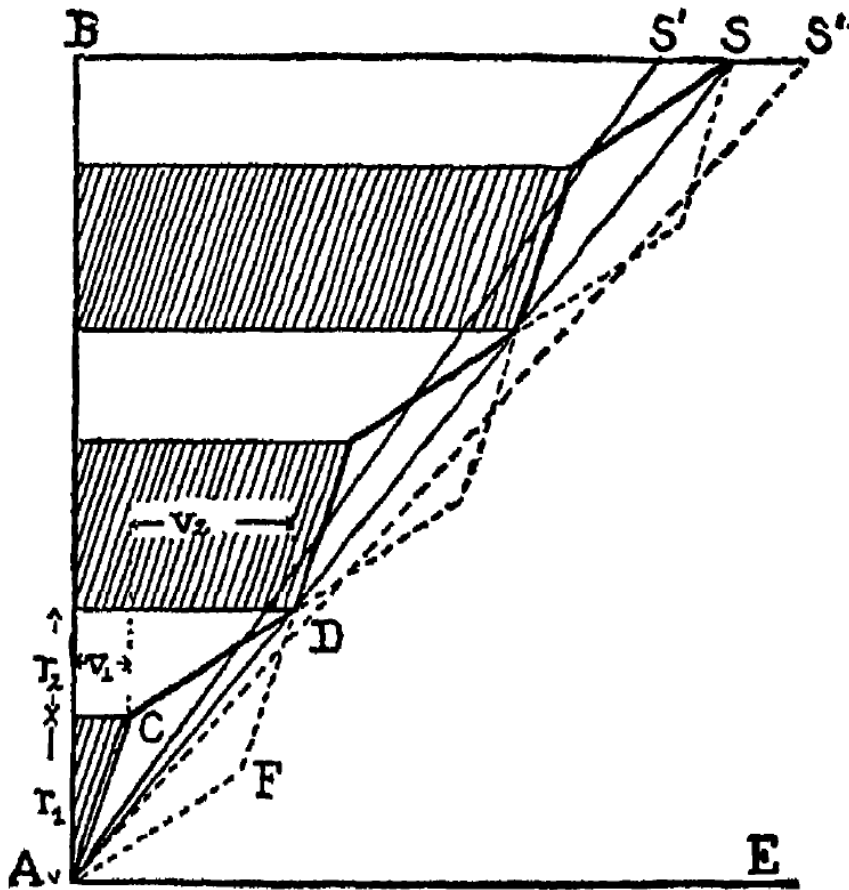


Figure A4.7: Case 2 showing laminae of two fluids parallel to shear direction.

The constraint in Case 2 requires the shearing stress to be constant across the layers such that

$$P = \frac{\eta_A v_A}{r_A} = \frac{\eta_B v_B}{r_B} = \dots \quad (3)$$

where the  $v_A$  and  $v_B$  are the partial velocities, and  $r_A$  and  $r_B$  are the thicknesses of the A and B laminae. The measured viscosity may be determined by the velocity of the top plane relative to the bottom one such that

$$P = \frac{Hv}{R} \quad (4).$$

The partial velocities of each layer are additive and combining equations 3 and 4 gives

$$\frac{PR}{H} = \sum_i v_i = \sum_i \frac{Pr_i}{\eta_i}.$$

Substituting in the fluidity,  $\Phi$ , which is defined to be the  $1/\eta$ , we find that

$$PR\Phi = P(r_A\phi_A + r_B\phi_B + \dots).$$

But  $r_A/R$  is the volume fraction of substance A in the mixture and can be replaced by  $c_i$ . We find that fluidities are additive in Case 2.

$$\Phi = \sum_i c_i\phi_i \quad (5)$$

A similar derivation can be found in [1]. In immiscible fluids, the layers A and B resist indefinite extension and flow resembling Case 1 results. See page 87 of [1].

In the two phase amorphous  $(Zr_aTi_{1-a})_{60}Be_{40}$  alloys, one would expect to see three regions of flow. The first region is at temperatures below  $T_{g1}$  where the sample would behave like a solid and little or no flow would be observed. The second region covers the temperature range  $T_{g1} < T < T_{g2}$ . In region 2, we should see a slope change in the viscosity versus temperature curve as the liquid-solid solution begins flow. The third region spans the temperature range  $T_{g2} < T < T_x$ . In region three, the sample should exhibit flow characteristic of a two phase liquid. At  $T_x$  the sample begins to crystallize and flow stops.

It is difficult to predict the flow properties of the  $(Zr_aTi_{1-a})_{60}Be_{40}$  system in a quantitative manner. First we don't know the fragilities of the phases in the alloys. These will be assumed similar to Vitreloy type alloys with  $m = 40$ . Also, the flow in region 2 depends not only on volume fraction of the solid phase, but also the size distribution, which is unknown. There are many theoretical models predicting measured viscosity of a liquid solid mixture with known viscosity and solid phase fraction, but they vary by orders of magnitude in their predictions [2]. They are not presented here. A schematic picture of flow is desired. As such, the Johnson viscosity model [3] will be used and a solid will be assumed to have a viscosity =  $10^{12}$  Pa-s. At  $T_{g1}$ , the first phase is assumed to soften and at  $T_{g2}$ , the second phase is assumed to soften and flow according to the Johnson model.

## A4.13

We will assume  $T_g$  values measured in the DSC are correct and also assume a fragility of 40 which is reasonable for Vitreloy type alloys.

We will look at flow predicted by both Case 1 and Case 2 for a glass similar to  $Zr_{30}Ti_{30}Be_{40}$  with about 60% of the low  $T_g$  phase. Assume  $T_{g1} = 310$  °C,  $T_{g2} = 360$  °C,  $m = 40$ .

Case 1: Additive viscosities:

$$\text{Region 1: } \eta(T < 310 \text{ °C}) = 0.6 * 10^{12} + 0.4 * 10^{12}) \text{ Pa-s}$$

$$\text{Region 2: } \eta(310 \text{ °C} < T < 360 \text{ °C}) = \left( 0.6 * \eta_{\infty} * 10^{A \left( \frac{310}{T} \right)^{m/A}} + 0.4 * 10^{12} \right) \text{ Pa-s}$$

$$\text{Region 3: } \eta(360 \text{ °C} < T < T_x) = \left( 0.6 * \eta_{\infty} * 10^{A \left( \frac{310}{T} \right)^{m/A}} + 0.4 * \eta_{\infty} * 10^{A \left( \frac{360}{T} \right)^{m/A}} \right) \text{ Pa-s}$$

These equations are taken from the final equation of derivation 5 and solved for  $\eta$ .

$$\text{Case 2: Additive fluidities so } \frac{1}{\eta} = \phi = c_1 \phi_1 + c_2 \phi_2 = \frac{c_1}{\eta_1} + \frac{c_2}{\eta_2}$$

$$\text{Solving for } \eta \text{ gives } \eta = \frac{\eta_1 * \eta_2}{c_1 \eta_1 + c_2 \eta_2}$$

$$\text{Region 1: } \eta(T < 310 \text{ °C}) = \left( \frac{10^{12} * 10^{12}}{0.6 * 10^{12} + 0.4 * 10^{12}} \right) \text{ Pa-s} = 10^{12} \text{ Pa-s}$$

$$\text{Region 2: } \eta(310 \text{ °C} < T < 360 \text{ °C}) = \left( \frac{\eta_{\infty} * 10^{A \left( \frac{310}{T} \right)^{m/A}} * 10^{12}}{\left( 0.6 * \eta_{\infty} * 10^{A \left( \frac{310}{T} \right)^{m/A}} + 0.4 * 10^{12} \right)} \right) \text{ Pa-s}$$

$$\text{Region 3: } \eta(360 \text{ °C} < T < T_x) = \left( \frac{\eta_{\infty} * 10^{A \left( \frac{310}{T} \right)^{m/A}} * \eta_{\infty} * 10^{A \left( \frac{360}{T} \right)^{m/A}}}{\left( 0.6 * \eta_{\infty} * 10^{A \left( \frac{310}{T} \right)^{m/A}} + 0.4 * \eta_{\infty} * 10^{A \left( \frac{360}{T} \right)^{m/A}} \right)} \right)$$

The two limiting cases for two phase liquid flow are plotted in Figure A4.8.

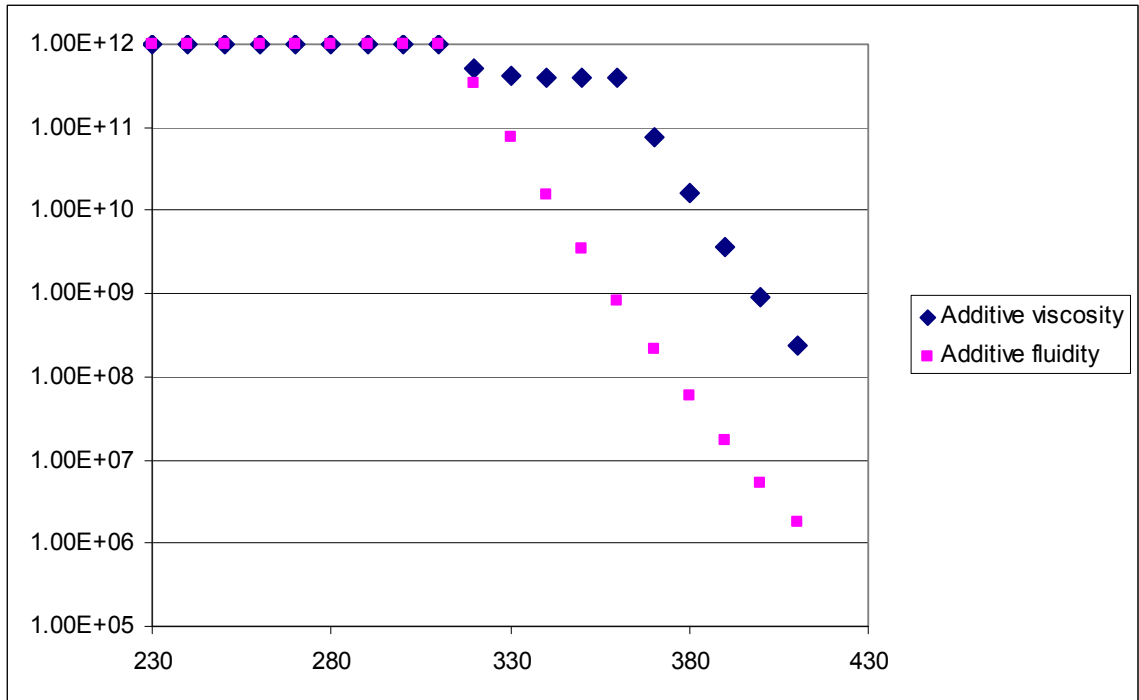


**Figure A4.8:** Additive fluidity cases and additive viscosity cases on three flow regions of a glass with 60% low  $T_g$  phase are shown. It is interesting to note that the theoretical additive viscosity case resembles the flow seen in figure 6.5 suggesting that we may approach the immiscible fluids resisting indefinite extension case proposed in [1] on page 87.

### Derivation 9 - Modulus of Rupture Equation for Rectangular Beam

Modulus of Rupture for beam bending

$$\sigma = \frac{M * y}{I} = \frac{3 * F * L}{2 * b * h^2}$$

Where

$\sigma$  = stress parallel to neutral axis

M = bending moment

y = distance from neutral axis

I = second moment of area

We begin by considering a strain in the x direction which is related to the distance from the neutral axis as follows

$$\epsilon_x = -\kappa y$$

The resulting stress is

$$\sigma_x = E \epsilon_x = -E \kappa y$$

$$dM = -\sigma_x y dA$$

$$M = \int E \kappa y^2 dA$$

$$I = \int y^2 dA = \int_{-b/2}^{b/2} \int_{-h/2}^{h/2} y^2 dy dz$$

$$I = \frac{bh^3}{12}$$

$$M = E \kappa I = \frac{\sigma_x I}{y}$$

$$\sigma_{x\max} = \frac{My}{I} = \frac{\frac{F}{2} * \frac{L}{2} * \frac{h}{2}}{\frac{bh^3}{12}} = \frac{3FL}{2bh^2}$$

#### Appendix 4 References

- [1] E.C. Bingham, Fluidity and Plasticity, McGraw-Hill Book Company, Inc., Ohio, 1922, pp. 81-105.
- [2] C. Journeau, G. Jeulain, L. Benyahia, J.F. Tassin, P. Abélard, Rhéologie 9 (2006) 28.
- [3] W.L. Johnson, M.D. Demetriou, J.S. Harmon, M.L. Lind, K. Samwer, MRS Bull. 32 (2007) 644.